TESIS DE LA UNIVERSIDAD DE ZARAGOZA
2024
60

Beatriz Parejo Alonso

Harnessing Metabolic Plasticity and Extracellular Signaling to Target Cancer Stem Cell Functions: Role of PPAR-delta and ALK in Pancreatic Ductal Adenocarcinoma

Director/es
Sancho Andrés, Patricia

ISSN 2254-7606

Prensas de la Universidad
Universidad Zaragoza

ISSN 2254-7606

Universidad Zaragoza
1542

Tesis Doctoral

HARNESSING METABOLIC PLASTICITY AND EXTRACELLULAR SIGNALING TO TARGET CANCER STEM CELL FUNCTIONS: ROLE OF PPAR-DELTA AND ALK IN PANCREATIC DUCTAL ADENOCARCINOMA

Autor

Beatriz Parejo Alonso

Director/es

Sancho Andrés, Patricia

UNIVERSIDAD DE ZARAGOZA
Escuela de Doctorado

Programa de Doctorado en Bioquímica y Biología Molecular

2023

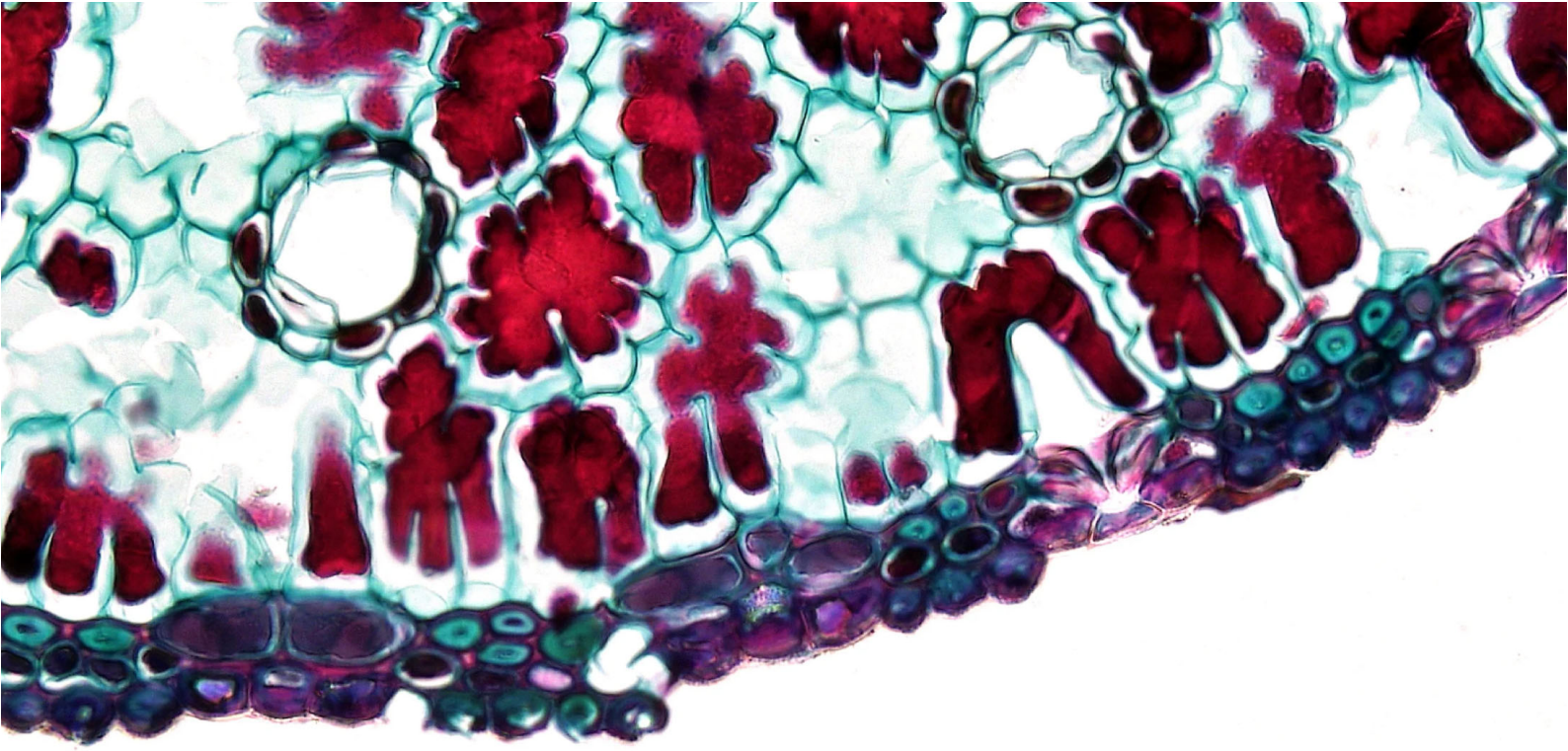

DOCTORAL THESIS

Harnessing Metabolic Plasticity and Extracellular Signaling to Target Cancer Stem Cell Functions: Role of PPAR-delta and ALK in Pancreatic Ductal Adenocarcinoma

Universidad de Zaragoza

Beatriz Parejo Alonso

Zaragoza, 2023

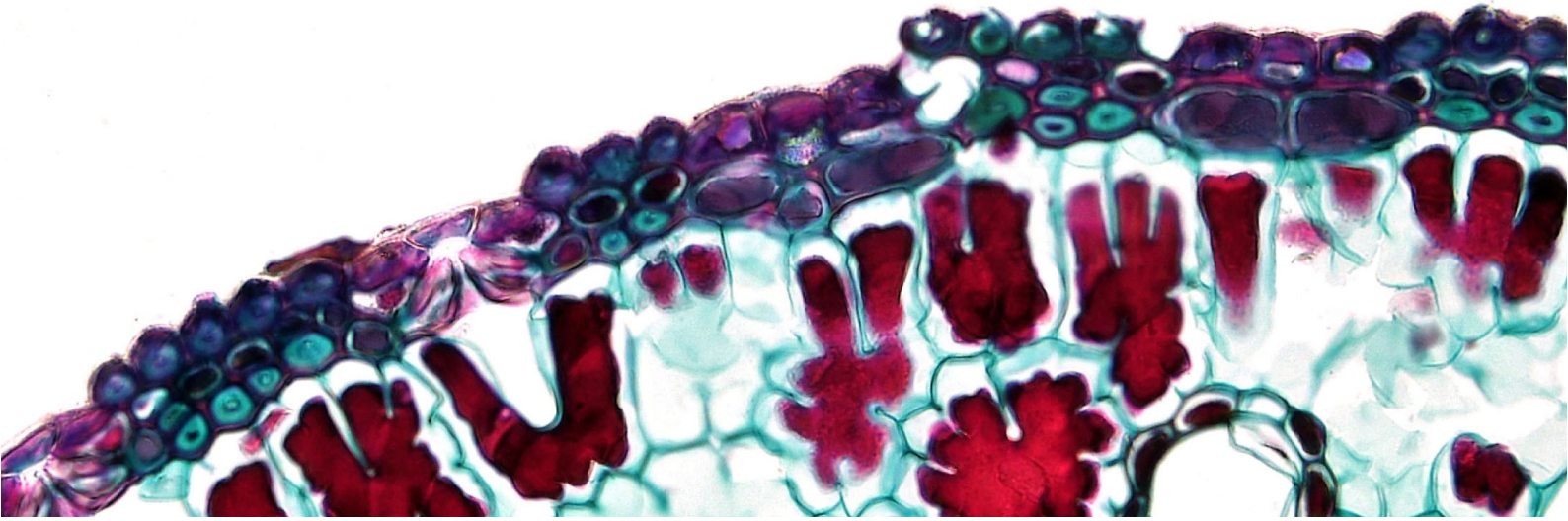

TESIS DOCTORAL

Aprovechamiento de la Plasticidad Metabólica y la Señalización Celular para Atacar las Funciones de Célula Madre Tumoral: Papel de PPAR-delta y ALK en el Adenocarcinoma Ductal de Páncreas

Harnessing Metabolic Plasticity and Extracellular Signaling to Target Cancer Stem Cell Functions: Role of PPAR-delta and ALK in Pancreatic Ductal Adenocarcinoma

Directora:

Dra. PATRICIA SANCHO ANDRÉS

Memoria presentada por **BEATRIZ PAREJO ALONSO** para optar

al Grado de Doctor por la Universidad de Zaragoza

Zaragoza, 2023

Instituto de Investigación Sanitaria Aragón

Universidad Zaragoza
1542

This research was funded by the Health Institute Carlos III (refs.: CP16-00121, PI17-00082 and PI20-00921), the Worldwide Cancer Research Foundation with the Spanish Association Against Cancer (AECC, ref.: 190250) and a crowdfunding supported by the platform Precipita from the Spanish Science and Technology Federation (FECYT). Dª. Beatriz Parejo Alonso was granted with the V fellowship Ford Motor Company-Apadrina la Ciencia Foundation.

Esta investigación ha sido financiada por el Instituto de Salud Carlos III (refs.: CP16-00121, PI17-00082 y PI20-00921), la Fundación Worldwide Cancer Research junto con la Asociación Española Contra el Cáncer (AECC, ref.: 190250) y una campaña de micromecenazgo a través de la plataforma Precipita de la Federación Española para la Ciencia y la Tecnología (FECYT). Dª. Beatriz Parejo Alonso recibió la V beca Ford Motor Company-Fundación Apadrina la Ciencia.

“Champions are made from something they have deep inside them:
a desire, a dream, a vision.
They have to have the skill and the will,
but the will must be stronger than the skill”.

Muhammad Ali

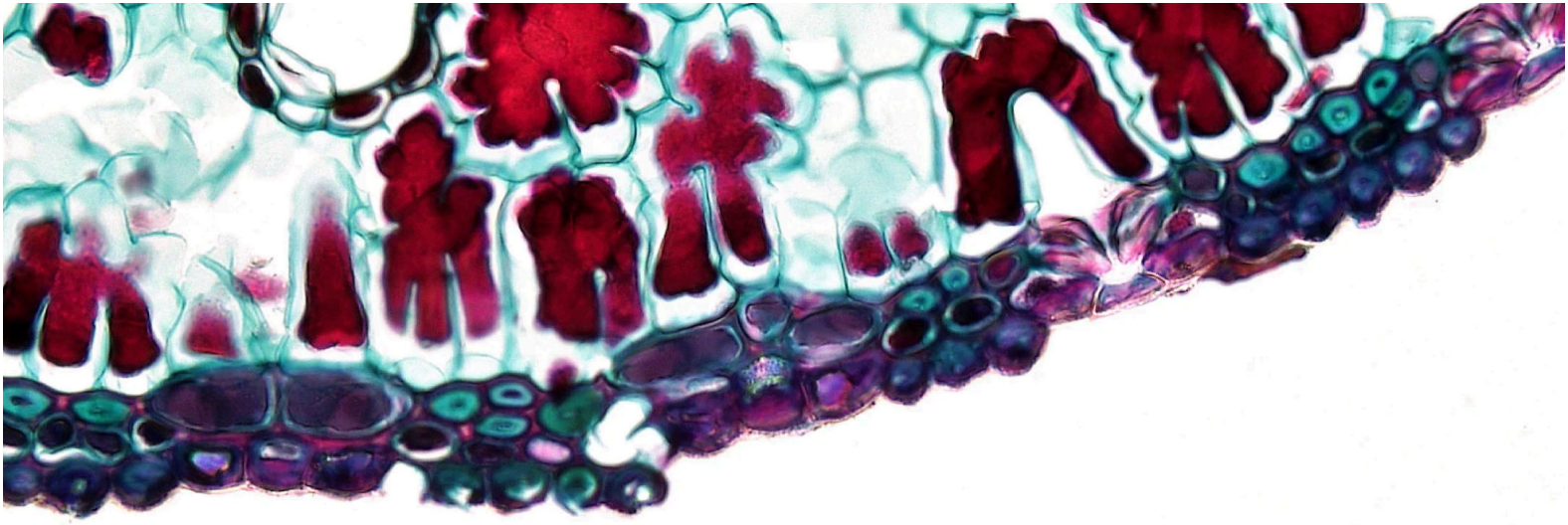

SUMMARY / RESUMEN

Pancreatic ductal adenocarcinoma (PDAC) is an extremely aggressive disease characterized by its metastatic potential and chemoresistance. These traits are partially attributable to the highly tumorigenic pancreatic cancer stem cells (PaCSCs). Interestingly, these cells show unique features in order to sustain their identity and functionality, some of them amenable for therapeutic intervention. Importantly, our group has previously described that the ratio between MYC and peroxisome proliferator-activated receptor gamma coactivator-1 alpha (PGC1α) controls the oxygen phosphorylation (OXPHOS)-dependent metabolic phenotype of PaCSCs to maintain their pluripotent status. This scenario, apparently, renders PaCSCs highly sensitive to mitochondrial inhibition with Metformin. However, different clones of PaCSCs with distinct levels of MYC/PGC1α arise upon such metabolic stress situation, thereby generating resistance to this compound. Therefore, we hypothesize that deciphering the mechanisms underlying PaCSCs biology bears the potential to find novel targets amenable for therapeutic intervention against this extremely chemoresistant subpopulation with tumor-initiating properties. To that end, the main aim of this doctoral thesis is to study the specific traits of PaCSCs that contribute to their inherent aggressiveness in order to identify novel targetable orchestrators of their functionality.

On the one hand, compiling data from our group suggests that peroxisome proliferator-activated receptor delta (PPAR-δ) correlates with pancreatic cancer progression and metastatic dissemination in response to energy deprivation and microenvironmental cues derived from tumor-associated macrophages (TAMs). However, the mechanistic basis of this regulation remains elusive. Here, we demonstrate that *PPARD* was consistently upregulated in response to different metabolic stressors (i.e., macrophage-derived conditioned medium or low dose Etomoxir) prior to epithelial-to-mesenchymal transition (EMT)-related functional changes. Intriguingly, treatment with various PPAR-δ agonists induced enhanced invasiveness. In addition, both experimental approaches increased the MYC/PGC1α ratio, suggesting that the metabolic modulation that takes place in PaCSCs is orchestrated upstream by PPAR-δ. The increased aggressiveness found *in vitro* was translated into enhanced metastatic dissemination *in vivo*. Mechanistically, *PPARD* overexpression or incubation with the agonist GW0742 induced an early activation of the *MYC* promoter, reducing the activity of

PGC1A promoter. Moreover, MYC therapeutic targeting blocked the invasion induced by PPAR-δ, suggesting its pro-metastatic effects were dependent on MYC/PGC1α. Conversely, pharmacological targeting of PPAR-δ inhibited the invasive capacity conferred by MCM or Etomoxir, or basal invasiveness in highly metastatic cells. Importantly, *in vivo* treatment with the PPAR-δ antagonists GSK3787 or GSK0660 showed decreased liver metastases incidence, which strongly supports the pro-metastatic role of PPAR-δ in PDAC.

On the other hand, screening of phospho-receptor tyrosine kinases revealed that PaCSCs harbored increased activation of anaplastic lymphoma kinase (ALK). We subsequently demonstrated that oncogenic ALK signaling contributes to tumorigenicity in PDAC patient-derived xenografts (PDXs) by promoting stemness through ligand-dependent activation. Indeed, the ALK ligands midkine (MDK) or pleiotrophin (PTN) increased self-renewal, clonogenicity and CSC frequency in several *in vitro* local and metastatic PDX models. Conversely, treatment with the clinically-approved ALK inhibitors Crizotinib and Ensartinib decreased PaCSC content and functionality, including invasiveness, *in vitro* and *in vivo*, by inducing cell death. Strikingly, ALK inhibitors sensitized chemoresistant PaCSCs to Gemcitabine, as the most used chemotherapeutic agent for PDAC treatment. Consequently, ALK inhibition delayed tumor relapse after chemotherapy *in vivo* by effectively decreasing the content of PaCSCs. In summary, our results demonstrate that targeting the MDK/PTN-ALK axis with clinically-approved inhibitors impairs *in vivo* tumorigenicity and chemoresistance in PDAC.

Taken together, our data strongly suggests that blockade of PaCSCs specific characteristics with pharmacologic inhibitors by different means, such as modulating their metabolic phenotype or targeting specific signaling pathways, decreases the metastatic incidence, tumorigenicity and chemoresistance in PDAC.

El adenocarcinoma ductal de páncreas (PDAC, del inglés *pancreatic ductal adenocarcinoma*) es una enfermedad extremadamente agresiva caracterizada por su potencial metastásico y quimioresistencia. Estas características se atribuyen parcialmente a unas células altamente tumorigénicas denominadas células madre tumorales pancreáticas (PaCSCs, del inglés *pancreatic cancer stem cells*). Estas células presentan unas características únicas que les permiten mantener su identidad y funcionalidad y pueden representar oportunidades terapéuticas. Nuestro grupo ha descrito con anterioridad que el balance entre MYC y el coactivador del receptor gamma-1 alfa activado por el proliferador de peroxisomas (PGC1α, del inglés *peroxisome proliferator-activated receptor gamma coactivator-1 alpha*) controla el fenotipo metabólico dependiente de fosforilación oxidativa (OXPHOS, del inglés *oxygen phosphorylation)* para sustentar su estado de pluripotencia. Aparentemente, este escenario hace que las PaCSCs sean altamente sensibles a la inhibición mitocondrial con Metformina. Sin embargo, diferentes clones de PaCSCs con distintos niveles de MYC/PGC1α surgen ante tal situación de estrés metabólico, generando así resistencia a este compuesto. Por lo tanto, nuestra hipótesis es que descifrar los mecanismos que subyacen a la biología de las PaCSCs tiene el potencial de encontrar novedosas dianas susceptibles de intervención terapéutica contra esta subpoblación extremadamente quimiorresistente con propiedades iniciadoras de tumores. Considerando lo anterior, el principal propósito de esta tesis doctoral es el estudio de las características específicas de las PaCSCs que contribuyen a su inherente agresividad con el fin de identificar novedosos reguladores de su funcionalidad que puedan ser bloqueados.

Por un lado, la recopilación de datos de nuestro grupo sugiere que el receptor delta activado por proliferadores de peroxisomas (PPAR-δ, del inglés *peroxisome proliferator-activated receptor delta*) se correlaciona con la progresión del cáncer de páncreas y la diseminación metastásica en respuesta a la deprivación energética y señales microambientales derivadas de macrófagos asociados a tumores (TAMs, del inglés *tumor-associated macrophages*). Sin embargo, el mecanismo de esta regulación sigue sin conocerse. Aquí, demostramos que *PPARD* se reguló al alza de forma consistente en respuesta a diferentes estresores metabólicos (i.e., medio

condicionado derivado de macrófagos o dosis bajas de Etomoxir) antes de los cambios funcionales relacionados con la transición epitelio-mesénquima (EMT, del inglés *epithelial-to-mesenchymal transition*). Curiosamente, el tratamiento con varios agonistas de PPAR-δ indujo un incremento en la capacidad invasiva de las células. Además, ambas estrategias experimentales (estresores metabólicos y activación directa de PPAR-δ) incrementó la relación MYC/PGC1α, lo que sugiere que la modulación metabólica que tiene lugar en las PaCSCs está orquestada por PPAR-δ. El aumento de la agresividad encontrado *in vitro* se tradujo en mayor diseminación metastásica *in vivo*. En cuanto al mecanismo, la sobreexpresión de *PPARD* o la incubación con el agonista GW0742 indujo una activación temprana del promotor de *MYC*, reduciendo la actividad del promotor de *PGC1A*. Además, el bloqueo terapéutico de MYC redujo la invasión inducida por PPAR-δ, sugiriendo que sus efectos pro-metastásicos dependen de MYC/PGC1α. Por el contrario, el bloqueo farmacológico de PPAR-δ inhibió la capacidad invasiva conferida por MCM o Etomoxir, o la invasividad basal en células altamente metastásicas. Es importante destacar que el tratamiento *in vivo* con los antagonistas de PPAR-δ GSK3787 o GSK0660 resultó en una disminución de la incidencia de metástasis hepáticas, lo que apoya firmemente el papel pro-metastásico de PPAR-δ en PDAC.

Por otra parte, el cribado de fosfo-receptores tirosina quinasa reveló que las PaCSC albergaban una mayor activación de la quinasa del linfoma anaplásico (ALK, del inglés *anaplastic lymphoma kinase*). Posteriormente, demostramos que la señalización oncogénica de ALK contribuye a la tumorigenicidad de los xenoinjertos derivados de pacientes (PDXs, del inglés *patient-derived xenografts*) de PDAC al promover la pluripotencia mediante la activación dependiente de ligando. De hecho, los ligandos de ALK, midkina (MDK) o pleiotrofina (PTN), aumentaron la autorrenovación, la clonogenicidad y la frecuencia de CSC en varios modelos *in vitro* de PDXs locales y metastásicos. Por el contrario, el tratamiento con los inhibidores de ALK ya aprobados para su uso clínico, Crizotinib y Ensartinib, redujo el contenido y la funcionalidad de las PaCSCs, incluida su capacidad de invasión, *in vitro* e *in vivo*, al inducir su muerte celular. Sorprendentemente, los inhibidores de ALK sensibilizaron a las PaCSCs quimiorresistentes a la Gemcitabina, el agente quimioterapéutico más utilizado

para el tratamiento del PDAC. En consecuencia, la inhibición de ALK retrasó la reaparición tumoral tras la quimioterapia *in vivo* al disminuir eficazmente el contenido de PaCSCs. En resumen, nuestros resultados demuestran que atacar el eje MDK/PTN-ALK con inhibidores clínicamente aprobados disminuye la tumorigenicidad y la quimiorresistencia *in vivo* en PDAC.

En síntesis, nuestros datos sugieren firmemente que la neutralización de la funcionalidad de las PaCSCs por diferentes medios, como la modulación de su fenotipo metabólico o la inhibición de vías de señalización específicas, disminuye la incidencia metastática, la tumorigenicidad y la quimiorresistencia en PDAC.

TABLE OF CONTENTS

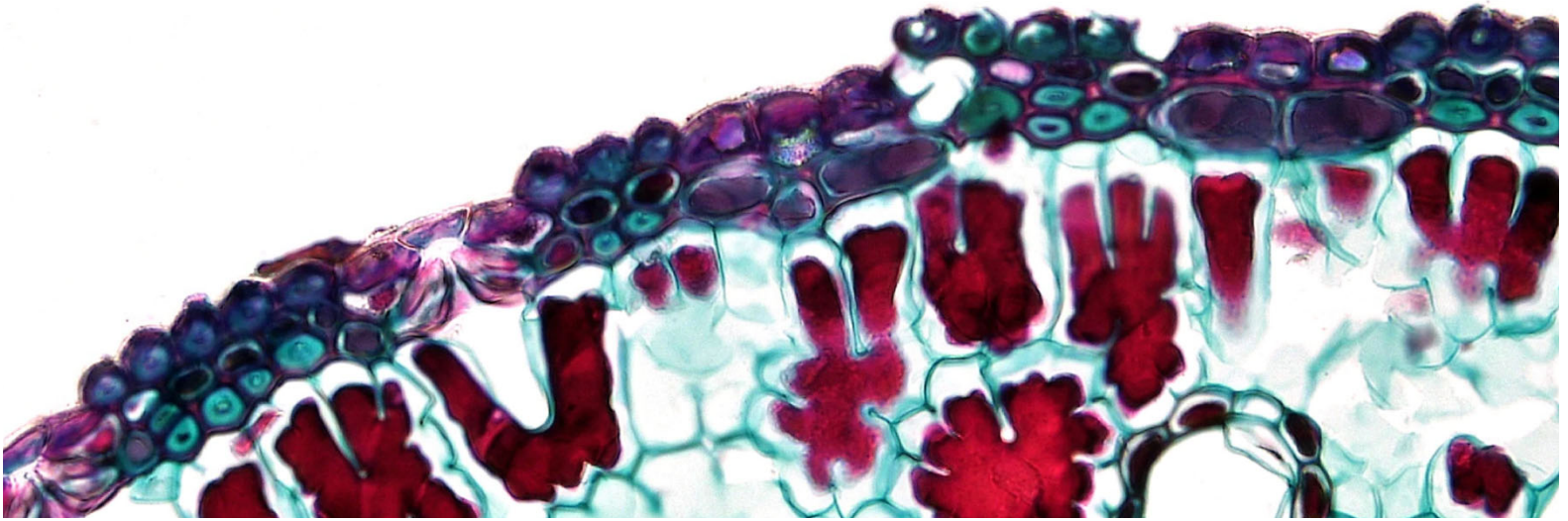

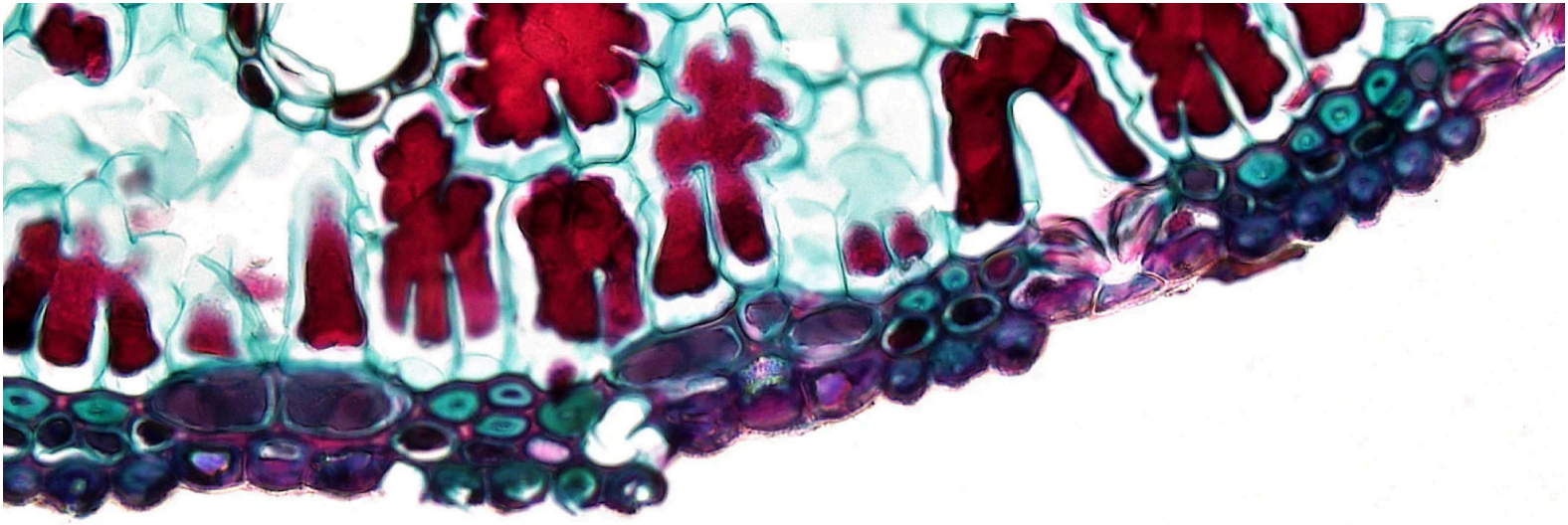

ABBREVIATIONS

ABC	ATP-binding cassette
Abx	Abraxane
Acetyl CoA	Acetyl coenzyme A
Adh	Adherent cultures
ADM	Acinar-to-ductal metaplasia
ALCL	Anaplastic large-cell lymphoma
ALK	Anaplastic lymphoma kinase
ANOVA	Analysis of variance statistical test
APC	Allophycocyanin fluorophore
ATP	Adenosine triphosphate
BCL-6	B-cell lymphoma 6
c-MET	Hepatocyte growth factor receptor
CAFs	Cancer-associated fibroblasts
CD133	Prominin-1
CDKN2A	Cyclin-dependent kinase inhibitor 2A
cDNA	Complementary deoxyribonucleic acid
CFA	Colony formation assay
CK-19	Cytokeratin-19
CPT1a	Carnitine palmitoyl-transferase 1a
CRIZO	Crizotinib
CSCs	Cancer stem cells
CTCs	Circulating tumor cells
CXCR4	Chemokine receptor type 4
DNA	Deoxyribonucleic acid
ECM	Extracellular matrix
EGFR	Epidermal growth factor receptor

ELDA	Extreme limiting dilution assay
ELISA	Enzyme-linked immunosorbent assay
EMA	European medicines agency
EMT	Epithelial-to-mesenchymal transition
ENS	Ensartinib
EpCAM	Epithelial cell adhesion molecule
ERK 1/2	Extracellular signal-regulated kinase 1/2
ESA	Epithelial specific antigen
ETC	Electron transport chain
Eto	Etomoxir
FACS	Fluorescence activated cell sorting
FAM150A	Family with sequence similarity 150 member A
FAM150B	Family with sequence similarity 150 member B
FAO	Fatty acid oxidation
FAs	Fatty acids
FBS	Fetal bovine serum
FDA	American food and drug administration
FGFb	Fibroblast growth factor basic
FITC	Fluorescein fluorophore
Fluo	Autofluorescent cells
Gem	Gemcitabine
GEMM	Genetically engineered mouse models
GFP	Green fluorescence protein
GSEA	Gene set enrichment analysis
GTEx	Genotype-tissue expression dataset
HCC	Hepatocellular carcinoma
hGAPDH	Human glyceraldehyde-3-phosphate dehydrogenase

HSC	Hematopoietic stem cells
i.p.	Intraperitoneal
i.v.	Intravenous
IFNs	Interferons
IHC	Immunohistochemistry
ISG15	IFN-stimulated gene 15
IVIS®	*In vivo* imaging system
JAK/STAT	Janus kinase/signal transducers and activators of transcription
K-RAS	Kristen rat sarcoma virus
KD	Knockdown
KLF4	Krüppel-like factor 4
KO	Knockout
LDLa	Lipoprotein receptor class a
LDs	Lipid droplets
LOXL2	Lysyl oxidase homolog 2
luc	Firefly luciferase
MAM	Meprin, A-5 protein, receptor protein-tyrosine phosphatase mu domain
MCM	Macrophage conditioned medium
MDK	Midkine
MET	Mesenchymal-to-epithelial transition
mRNA	Messenger ribonucleic acid
nab-Paclitaxel	Albumin-bounded Abraxane
NMPA	Chinese national medical products administration
Non-CSCs	Non cancer stem cells
NPM	Nucleophosmin

nRTKs	Non-receptor tyrosine kinases
NSCLC	Non-small cell lung cancer
NSG	NOD SCID gamma
OXPHOS	Oxygen phosphorylation
PaCSCs	Pancreatic cancer stem cells
PanIN	Pancreatic intraepithelial neoplasia
PBS	Phosphate buffered saline
PD-1	Programmed cell death protein-1
PD-L1	Programmed cell death protein-1 ligand
PDAC	Pancreatic ductal adenocarcinoma
PDXs	Patient-derived xenografts
PE	Phycoerythrin fluorophore
PGC1α	Peroxisome proliferator-activated receptor gamma coactivator-1 alpha
PPARs	Peroxisome proliferator-activator receptors
PPREs	PPAR responsive elements
PTN	Pleiotrophin
RIPA	Radioimmunoprecipitation assay buffer
RNA	Ribonucleic acid
RNAseq	RNA sequencing analysis
ROS	Reactive oxygen species
RTKs	Receptor tyrosine kinases
RTqPCR	Real time quantitative polymerase chain reaction
scRNAseq	Single cell RNA sequencing analysis
SEM	Standard error of the mean
SFA	Sphere formation assay
shRNA	Short hairpin ribonucleic acid

SMAD4	SMA- and MAD-related protein 4
SOC	Standard-of-care
SOX2	Sex determining region Y-box 2
SOX9	SRY-box transcription factor 9
Sph	Spheroid cultures
TAMs	M2-polarized protumoral macrophages
TCA cycle	Tricarboxylic acids cycle
TCGA	The cancer genome atlas dataset
TGFβ	Transforming growth factor beta
TKi	Tyrosine kinase inhibitors
TKs	Protein tyrosine kinases
TME	Tumor microenvironment
TP53	Tumor protein 53
WNT	Wingless/integrated
ZEB1	Zinc-finger E-box-binding homeobox 1

INTRODUCTION

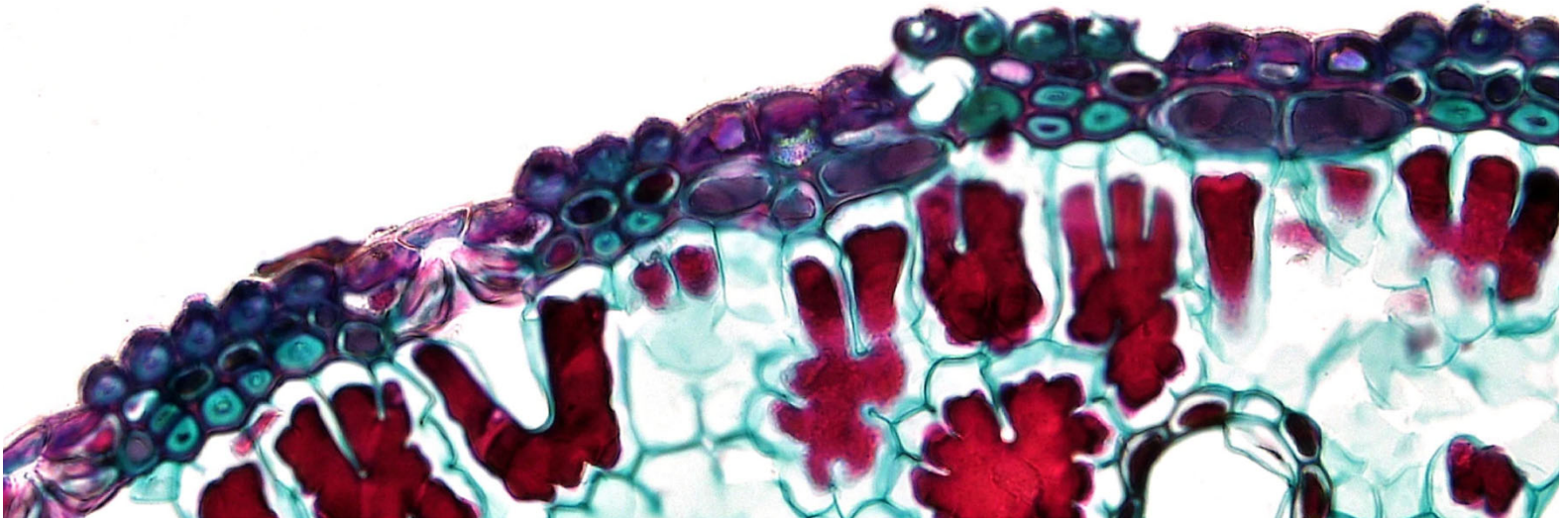

1. PANCREATIC CANCER

The pancreas, an essential organ with important roles for normal body functioning, is a dual gland composed by both endocrine and exocrine parenchymas. On the one hand, the endocrine secretory tissue –also known as islets of Langerhans– represents 1-2% of the total pancreas mass and is composed by different cell types, including beta cells. These cells secrete the insulin necessary to maintain blood glucose homeostasis. On the other hand, the remaining exocrine pancreatic mass is comprised of acinar and ductal cells that produce different enzymes necessary for the proper digestive function[1] (**Figure 1**).

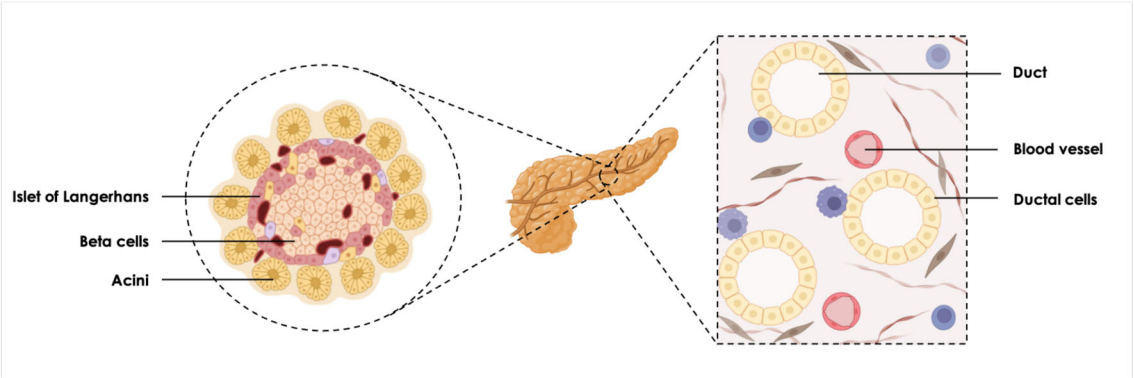

Figure 1. Schematic representation of the healthy pancreas. The pancreatic parenchyma is composed by endocrine and exocrine glands. The endocrine tissue, or Islets of Langerhans, contains, among others, the beta cells responsible of insulin secretion. The exocrine tissue contains the acini and the ducts, where digestive enzymes are produced.

Pancreatic Ductal Adenocarcinoma (PDAC) is the most represented pancreatic cancer with an increasing incidence and an extremely poor 5-year overall survival of 10% and 7% in Spanish females and males, respectively[2]. Despite PDAC low incidence rate as compared to other cancer-related malignancies, its mortality rate continues to rise, making it potentially the second deadliest cancer by 2030[3,4]. PDAC may be originated from both ductal and acinar cells, being the latter the most common cell-of-origin[5]. In this case, PDAC arise from acinar cells that suffer acinar-to-ductal metaplasia (ADM) or ductal reprogramming, a process by which these cells transdifferentiate and acquire ductal identity. Consequently, acinar cells following ADM display enhanced expression of ductal markers, such as cytokeratin-19 (CK-19) and SOX9[6]. Therefore, ADM is considered the precursor lesion of pancreatic intraepithelial neoplasia (PanIN) which, in turn, is the main pathological process triggering

PDAC[7]. In most cases, along PDAC evolution from ADM, mutations in key genes occur without distinction between duct- and acinar-derived PDACs[5]. *K-RAS* is the main driver mutation, being present in >95% of the cases and responsible for the ADM, followed by loss of the tumor suppressors $p16^{INK4A}$ (*INK4A*), *CDKN2A*, *TP53* and *SMAD4*[8,9] (**Figure 2**). Nonetheless, not all of these mutations occur in all PDAC patients; the combination of two of them, usually *K-RAS* and another one, is sufficient to trigger oncogenic transformation.

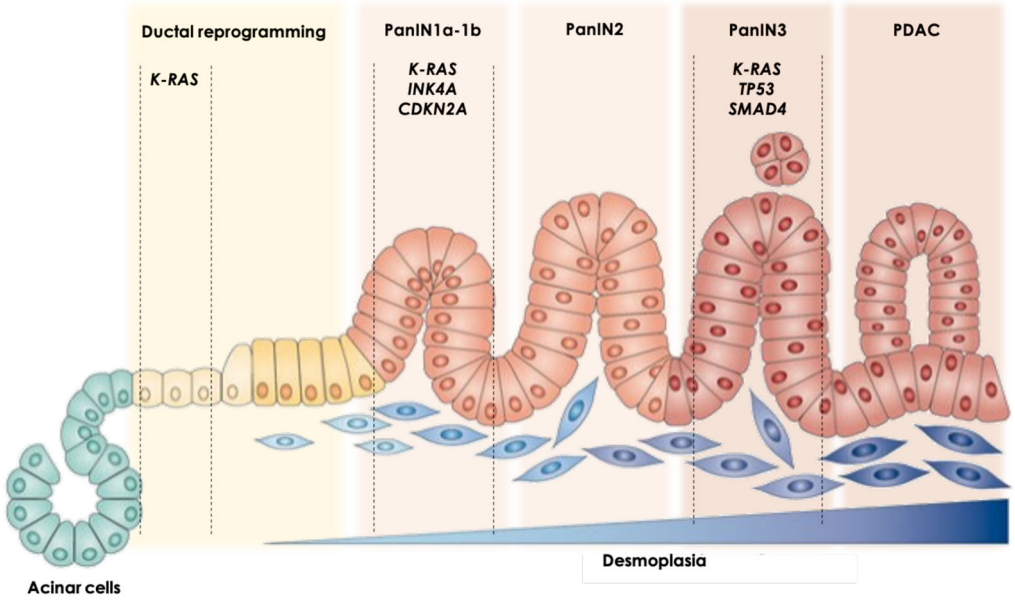

Figure 2. Schematic representation of PDAC evolution and the key mutation drivers during tumor progression. The most common genes mutated along PDAC development are represented. K-RAS hyperactivity may drive acinar cells into ductal reprogramming, thereby further establishing the PanIN state. Further mutations in *INK4A*, *CDKN2A*, *TP53* and *SMAD4* genes may contribute to PDAC development. However, mutations in all these genes do not occur always. In addition, concomitant increasing desmoplasia occurs along pancreatic tumoral transformation. *Adapted from Morris et al., 2010.*

Risk factors associated to pancreatic malignant transformation consist of smoking, alcohol consumption, obesity, occupational exposure to certain metals and chemical agents, age, gender, ethnicity, diabetes and family history[4]. Contrast-enhanced computed tomography (CT) is the imaging tool of choice under pancreatic cancer suspicion. In addition to this, the only serum biomarker used nowadays for pancreatic cancer is CA 19-9. However, while it only may help to confirm the diagnosis, it is not sufficiently sensitive nor specific as an individual screening tool for asymptomatic patients[10]. The neoplastic evolution of PDAC in early stages is not concomitant to symptoms occurrence. Thus, in the vast majority of cases (80-90%) it is diagnosed when the metastatic events, which

are mainly restricted to the liver, have already occurred. Commonly, symptoms at the time of diagnose include jaundice, abdominal and back pain, nausea, unexplained weight loss, changed bowel habits, depression, deep vein thrombosis and new onset of diabetes not associated to weight gain[11]. While PDAC is mostly diagnosed at an advanced/metastatic stage, only 10-15% of the patients will be eligible for surgical resection which are precisely the ones presenting the disease at early stages. On the contrary, the standard-of-care (SOC) in the case of advanced disease is chemoradiotherapy with Gemcitabine plus nab-Paclitaxel (albumin-bounded Abraxane) for patients with poor health or FOLFIRINOX (Folinic acid, 5-Fluoracil, Irinotecan and Oxaliplatin) for patients with otherwise good health[12]. However, the European overall median survival for metastatic PDAC undergoing treatment is 4.6 months[13]. Indeed, PDAC treatment remains a supreme challenge since, despite the possible initial remission, most of PDAC patients ultimately display resistance to current therapeutic strategies following tumor relapse[14]. As a consequence, limited progress has been made in the past decades concerning PDAC treatment. To date, countless targeted compounds have been tested and failed in clinical trials for pancreatic cancer[15], yet few exhibited moderate promising results[16]. In 2007, the American Food and Drug Administration (FDA) approved Erlotinib, an inhibitor of the epidermal growth factor receptor (EGFR), in combination with Gemcitabine as a first line SOC for metastatic PDAC patients[17]. However, the last major breakthrough occurred more than 10 years later when, in 2019, approval of the poly ADP-ribose polymerase (PARP) inhibitor Olaparib represented a four months increase in $BRCA^+$ PDAC patients survival[18].

Regardless of this, extensive research has permitted the identification of the main source of PDAC inherent chemoresistance. Mounting evidence point PDAC-associated chemotherapy failure to a small but unique subpopulation of cells within the tumor known as pancreatic cancer stem cells (PaCSCs). As such, these cells have self-renewal capacity and tumor-initiating properties, which make them capable of initiating and sustaining tumor growth. In addition to this, they are able to survive after chemotherapy as a consequence of their intrinsic chemoresistance, thus promoting recurrence[19,20].

Therefore, in addition to delayed detection, lack of effective therapeutic options due to the presence of highly chemoresistant PaCSCs make PDAC an

extremely aggressive disease. Having acknowledged PaCSCs as the source of PDAC aggressiveness and understanding CSCs biology is crucial in order to finding new targets amenable for therapeutic intervention with the final goal of efficiently control this lethal disease.

2. INTRATUMOR HETEROGENEITY AND THE CANCER STEM CELL CONCEPT

While large progress has been achieved concerning cancer therapy, outcomes are widely divergent across cancer types and, most importantly, from patient to patient with the same tumor. Efforts in finding a unique effective cancer therapy had been shaded by what we know as tumor heterogeneity. This is the inherent ability of a single tumor to evolve, and so leading to systematic therapy failure that results in tumor progression, recurrence and greater mortality. The use of next-generation sequencing has denoted a major breakthrough in understanding cancer as independent and completely different disorders across types and patients. Importantly, spatial and temporal sequencing of a single tumor throughout progression have deciphered that conversion of non-malignant to malignant cells is the final outcome of a sequential acquisition of genetic and epigenetic alterations in key cellular processes that contribute to an increasing intratumor heterogeneity. While this phenomenon can be remarkably variable across cancer types and patients, it is well recognized now that is the main responsible for therapeutic failure and recurrence[21–24]. Thus, understanding the origin of such intratumor heterogeneity has become a major priority in cancer biology. Indeed, three principles lay the foundation to explain the underlying mechanisms of such heterogeneity: genetic driver mutations, hierarchical organization and the influence of the tumor microenvironment (TME). While their nature diverges from one another, they are not mutually exclusive and contemplating them as a whole has the potential to facilitate the understanding of the intricate ecosystem of cancer disease[25].

First proposed by Peter Nowell in 1976[26], the "stochastic" clonal evolution model comprises a series of genetic advantageous mutations, that lead to clonal and sub-clonal selection of transformed cancer cells across different tumor regions[27–29]. This principle implies that cancer initiation, development and progression obey the "Theory of Evolution by Natural Selection" of Charles

Darwin, by which differentiated cancer cells acquire heritable mutations that will attribute their progeny with survival advantages over the cells lacking these mutations. These mutations, called oncogenic drivers, are accumulative and beneficial for cancer cells, ultimately promoting the expansion of selected clones which further contribute to the evolving intratumor heterogeneity[25] (**Figure 3A**).

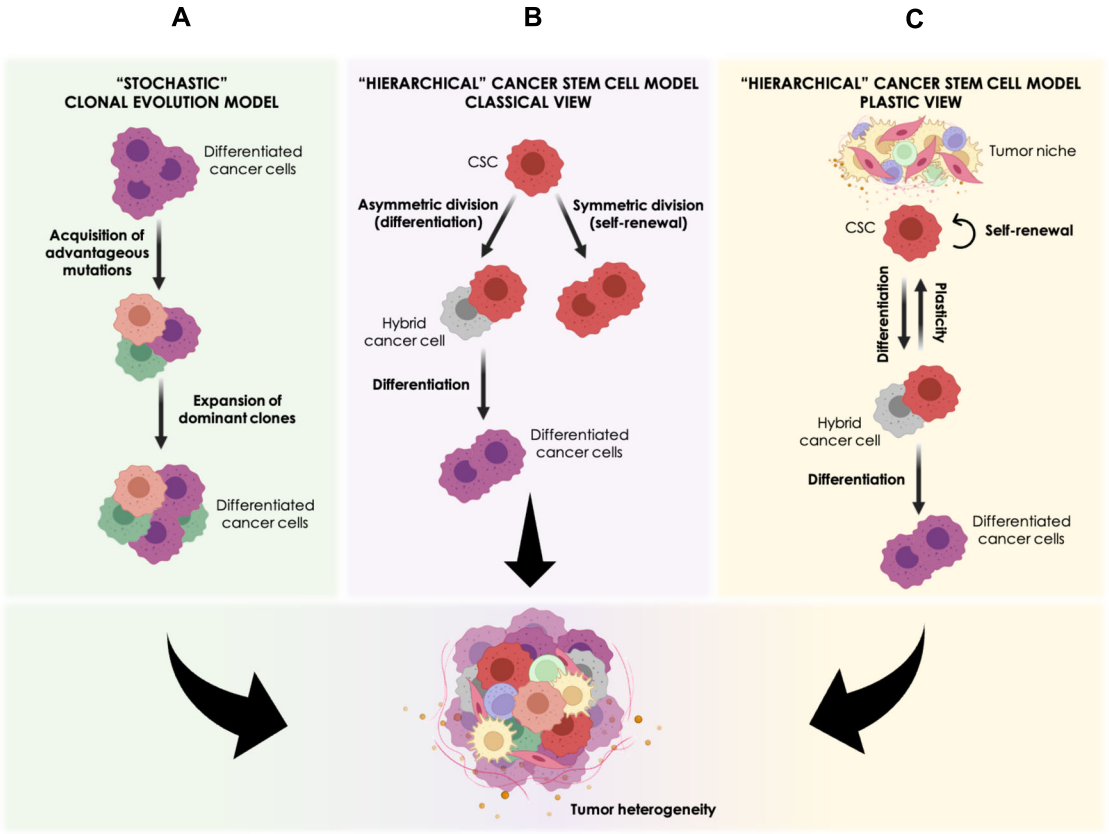

Figure 3. Schematic representation of the different models of acquisition of tumor heterogeneity. A) In the "stochastic" clonal evolution model, tumor heterogeneity is achieved by the selection and expansion of specific clones of differentiated cells that suffered genetic mutations. **B, C)** While the classical view of the "hierarchical" CSC model supports that CSCs undergo symmetric and asymmetric divisions to promote differentiation and perpetuate its linage (self-renewal), respectively **(B)**, the plastic view states that CSCs are capable of swinging between different grades of stemness (CSC-hybrid) and differentiation states under signals derived from the tumor microenvironment **(C)**. *Adapted from Dagogo-Jack et al., 2017 and Valle et al., 2018.*

However, oncogenic driver mutations are not sufficient to fully explain intratumor heterogeneity. To this regard, studies in leukemia have permitted to learn two lessons: 1. there are different clones that contribute to tumor evolution, and 2. in terms of response to therapy and recurrence, subclonal variability exists as well. In other words, not all the subclones respond equally to the same therapy. In fact, the blood system is formed by a complex hierarchy in which

hematopoietic stem cells (HSC) give rise to diversified pools of cells with distinct grades of differentiation and function. This branched out structure, rather than being dependent of the HSC genetic status, is based on sophisticated developmental programs, and the resulting organization is necessary for the proper function of the blood system. Then, functional heterogeneity in normal tissue evolution is based in non-genetic modulation and tells us that, without this diversity, the functionality of the entire system would be compromised. That is, for instance, without HSC, it would be impossible to have a functional immune system[25]. Certainly, upon their very first discovery in acute myeloid leukemia by Tsvee Lapidot[30] almost 30 years ago, the CSC theory has gained enormous momentum to explain cancer origin and intratumoral heterogeneity. The "hierarchical" CSC model, then, implies that this heterogeneity is consequence of a hierarchically organized structure in which CSCs are on top of a phenotypic and functional pyramid. In spite of being a small proportion of the total tumor mass, these unique cells with self-renewal capacity and tumor initiating properties coexist as different clones that are able to sustain the intratumoral heterogeneity by undergoing symmetrical and asymmetrical divisions. As a consequence, the cells within the tumor show differences in morphology, state of differentiation, proliferation, gene expression, metabolism and invasive, metastatic and angiogenic potential. CSC have similar features to their non-tumoral counterparts, as they retain the unlimited ability of self-renewal and dedifferentiation characteristics of a stem cell, though in a deregulated manner. Likewise, each subclone is a (epi-) genetically distinct entity that can give rise to different progenitor cells that will lead to tumor growth in the context of such heterogeneity[31] (**Figure 3B**). Lapidot demonstrated his hypothesis using fluorescence activated cell sorting (FACS) by separating $CD34^+/CD38^-$, $CD34^+/CD38^+$ and $CD34^-$ cell fractions and further injecting them in immunocompromised mice. With this elegant experiment, Lapidot evidenced the presence of what he called leukemia initiating cells confined to the $CD34^+/CD38^-$ subset[30]. This early study served as a precedent to demonstrate the CSC hypothesis in solid malignancies such as breast[32], brain[33], head and neck[34], pancreas[19,20], lung[35], prostate[36,37], colon[38,39] and sarcoma[40]. Importantly, all of these reports used tumor engraftment as a way to validate one of the main characteristics featured by CSCs, the tumor initiating potential.

Interestingly, theories explaining the intratumor heterogeneity continue to evolve and a second hypothesis included in the "hierarchical" model has already been proposed: the plastic CSC view. This new perspective implies that a single CSC is able to epigenetically modulate its phenotype according to microenvironmental cues, hence being forced to adapt in order the tumor to survive and progress[41]. Therefore, CSC self-renew or differentiate into plastic hybrid cancer cells that will further differentiate or dedifferentiate according to specific signals from their niche. Indeed, as far as nutrient availability is concerned, glucose and oxygen levels diminish in the milieu as malignant cells grow and the TME expands, the pH becomes acid and reactive oxygen species (ROS) and inflammatory mediators accumulate. Considering that differentiated tumor cells are fully glycolytic in order to cope with their enhanced proliferative demands (i.e., Warburg effect), this scarce scenario obliges CSCs to become metabolically and functionally plastic in order to survive and detoxify their microenvironment from ROS. However, CSCs preferentially use oxygen phosphorylation (OXPHOS) or glycolysis depending on the tumor type and model used[42] and this lack of consensus could be explained, at least in part, by CSCs intrinsic plasticity. Then, hybrid cancer cells and CSCs are continuously sensing a selective pressure that will ultimately force them to either adapt and progress or otherwise extinguish completely, thus promoting the survival of the fittest clones. Apart from metabolic mediators, there are other microenvironmental stimuli maintaining the tumoral evolution and progression. Indeed, the tumor niche becomes the perfect stage where the communication between cancer (stem) cells and stromal cells takes place. This crosstalk befalls in an accurate bidirectional cascade of events that, among other phenomena, promotes the scape from the natural mechanisms of immune surveillance[43] (**Figure 3C**).

Concurrently to the discrepancies in explaining tumor heterogeneity, and especially related to the "hierarchical" model, the hypothesis of CSCs emergence remains still unclear since it might vary between malignancies. One theory arises from the observed similarities between CSCs and their homologous adult tissue resident stem cells (SCs) suggesting that the latter may suffer a malignant transformation during the physiological regeneration program that maintains tissue homeostasis[44]. Other hypothesis entails the acquisition of stemness-related properties by differentiated cancer cells. On the one hand, it

has been suggested that differentiated cancer cells undergoing epithelial-to-mesenchymal transition (EMT) can also acquire stem-like properties[45]. On the other hand, microenvironmental signals from stromal cells may mediate dedifferentiation of non-CSCs, thus conferring serf-renewal, tumorigenic abilities and chemoresistance[46,47]. A dual scenario in which tissue resident SCs and differentiated cancer cells originate new CSCs is present in chemoresistant pancreatic[48] and lung[49] cancer cells as well.

Therefore, although the "hierarchical" model was controversial for more than a century[50], mounting evidence over the past decades supports the presence of highly tumorigenic CSCs with self-renewal capacity and functional plasticity to the extent of becoming the most suitable and recognized theory to understand and characterize intratumor heterogeneity.

3. TRAITS OF PANCREATIC CANCER STEM CELLS

PaCSCs were first isolated and characterized almost two decades ago by two independent groups based on the differential expression of distinct cell surface biomarkers (**Figure 4**), as previously demonstrated in many other malignancies. First of all, Li *et al*.[20] defined a highly tumorigenic population expressing the cell surface markers CD44, CD24 and epithelial specific antigen (ESA, also known as epithelial cell adhesion molecule EpCAM) by implanting primary PDAC xenografts in immunocompromised mice. In this study, the authors demonstrated that, while $CD44^+/CD24^+/ESA^+$ cells represented a very small proportion of the total cellularity (<0.8%), it clearly featured stemness-related properties. Afterwards, Hermann *et al*.[19] not only demonstrated the presence of $CD133^+$ PaCSCs with increased tumorigenicity and chemoresistance, but also dissected the presence of $CD133^+/CXCR4^+$ metastatic PaCSCs in the invading edge. Indeed, $CD133^+$ CSCs have been reported in other cancer types, such as brain[51], liver[52], colon[38,39], prostate[53] and breast[54] cancers, further validating this surface protein as a biomarker for this cell population. CD133 (cluster of differentiation 133) is also known as Prominin-1. Despite its specific function remains still elusive, the AC133 epitope of human Prominin-1 was first discovered as a marker of HSCs[55]. Several studies have demonstrated the role of Prominin-1 in CSC-related properties, as reviewed by Shmelkov *et al.*[55]. In addition to

CD133, Miranda-Lorenzo *et al*.[56] identified a CSC-exclusive autofluorescence compartment capable of discriminating stem-like populations from the differentiated counterparts (**Figure 4**). Additionally, several other biomarkers have been proposed for the identification and isolation of PaCSCs, including aldehyde dehydrogenase 1 (ALDH1)[57], the anthrax toxin receptor 1 (ANTXR1)[58], CD9[59] and hepatocyte growth factor receptor c-MET[60], among others (**Figure 4**). Certainly, the use of all these biomarkers have helped to understand PaCSCs biology and raise awareness that, indeed, the differences in their functionality are the reflection of differences at the molecular, metabolic and signaling pathways levels. Therefore, exploring this distinctness in order to find novel therapeutic targets against PaCSCs bears the potential for developing new clinical strategies with the final aim of effectively control this aggressive disease.

Beyond the surface biomarkers mentioned above, the expression of specific genes has been reported and accepted for the molecular characterization of PaCSC. The increased expression of specific genes in PaCSC *versus* differentiated cells has been recognized as a pluripotency gene expression signature characteristic of enhanced stemness. *KLF4*, *NANOG*, *OCT3/4* and *SOX2* are the main genes composing this signature for the study of PaCSCs[61–64] (**Figure 4**). On the one hand, *NANOG*, *OCT3/4* and *SOX2* are very important factors that sustain pluripotency and self-renewal in embryonic stem cells (ESCs) during the first stage of embryonic development[65]. Indeed, these three pluripotency factors are commonly expressed in all four types of pluripotent cells: ESCs, adult stem cells (ASCs), induced pluripotent stem cells (iPSCs) and CSCs[65]. The role of these three core pluripotency genes in PDAC, whose activity orchestrates the pluripotent state by regulating the subsequent expression of several other crucial genes involved in this specific cell state, was summarized by Herreros-Villanueva and collaborators[66]. On the other hand, *KLF4* was firstly described as one of the four Yamanaka factors essential for the formation of iPSCs, together with *OCT3/4*, *SOX2* and *MYC*[67]. Further investigations reported an essential role of KLF4 in acinar-to-duct cell reprograming in PDAC early carcinogenic stages[68,69].

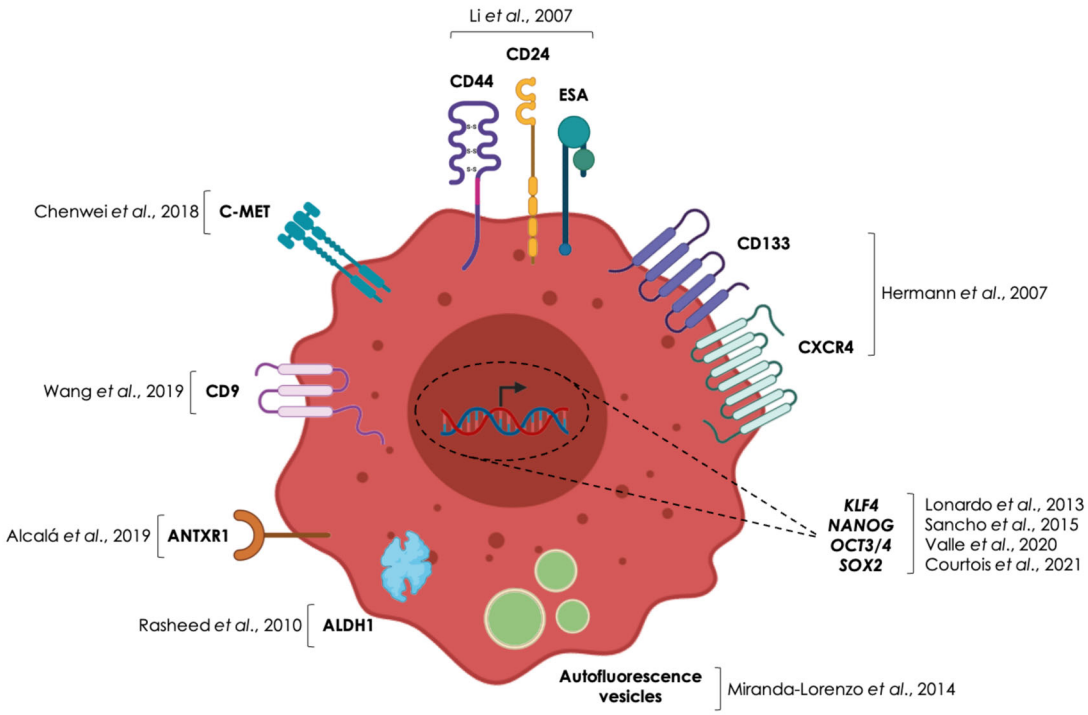

Figure 4. Schematic representation of the most common biomarkers and genes used to study the PaCSCs compartment. The research studies in which these biomarkers and genes were originally described are referenced.

In summary, the expression of different genes and surface biomarkers have permitted PaCSCs isolation for their study and characterization, further allowing for the design of therapeutic strategies aiming to target this aggressive subpopulation. In addition to this, it is worth noticing that previous studies from our group and others have shown that PaCSCs bear unique features essential to maintain their properties and functionality, such as increased mitochondrial metabolism (i.e., OXPHOS), metabolic plasticity (i.e., ability to use other metabolic substrates for energy production), enhanced mesenchymal-like phenotype primed to invade, increased immunoevasive properties and an inherent ability to induce chemotherapeutic failure. These characteristics, in principle, are amenable for therapeutic intervention and will be further explained.

3.1. Metabolic plasticity

Differentiated cancer cells have been recognized for more than a century for showing exclusive aerobic glycolytic metabolism (the Warburg effect) concomitant to dysfunctional mitochondrion[70,71]. However, increasing evidence now demonstrates that cancer cells may also relay on OXPHOS according to nutrient and oxygen availability at a given time[72]. This phenomenon has been termed as "metabolic reprogramming" or "metabolic plasticity" and has been recently acknowledged as one of the cancer hallmarks[73]. However, our group has reported that mitochondrial OXPHOS coupled to the tricarboxylic acids (TCA) cycle appears to be the preferred pathway for energy production in PaCSCs[61], as described for CSCs in other malignancies[42,62]. This metabolic disparity between non-CSCs and CSCs may be explained by the increased proliferative demands of differentiated cancer cells. Despite more efficient in terms of ATP production per molecule of glucose, mitochondrial respiration requires more biochemical reactions, thus rendering the process slower than aerobic glycolysis. For that reason, fast proliferating cells such as differentiated cancer cells prefer aerobic glycolysis, a faster although less efficient pathway for energy production, while slow proliferating CSCs would lean towards a more diversified mitochondria-dependent metabolism. In fact, this may be as well considered as a metabolic adaptation in response to the nutrient shortage characteristic of the TME, since several substrates may be recycled to enter the TCA cycle. This is the case of, for instance, lipids or amino acids present in the TME or obtained *via* autophagy or the lactate resulted from the aerobic glycolysis performed by differentiated cancer cells. This dual scenario may be exploited to benefit PDAC patients with strategies combining chemotherapeutics targeting fast-proliferating bulk differentiated cancer cells with compounds against PaCSCs mitochondria for the ablation of this highly tumorigenic relapse-responsible subpopulation[74].

We have provided proof-of-concept for the efficacy of metabolic inhibition for PaCSCs targeting in animal models[61,62,64,75,76], but further clinical translation has remained challenging due to lack of clinically effective compounds. On the one hand, we have recently demonstrated that PaCSCs subpopulation may be compromised by targeting mitochondrial dynamics, a key mechanism necessary for its homeostasis. Specifically, PaCSC rely on mitochondrial fission

and its inhibition with Mdivi-1 affected the energetic balance in these cells by accumulating dysfunctional mitochondria, further leading to cell death and diminishing CSC-related functions in consequence[64]. However, the use of metabolism-based therapies targeting PaCSCs have proven a big challenge in their way to the clinics. On the one hand, the proposed compounds showed poor bioavailability for their use in complex organisms[74]. On the other hand, our group has previously demonstrated that the metabolic phenotype in PDAC stem-like cells is not completely homogeneous and that different phenotypes co-exist within PaCSCs[62]. Therefore, although the vast majority of PaCSC rely on OXPHOS and are very sensitive to mitochondrial inhibition by the antidiabetic agent Metformin[61], a small portion of PaCSCs with low mitochondrial amount ($CD133^{+}/Mito^{LOW}$) becomes resistant to this inhibition while maintains its self-renewal status[62]. Importantly, the OXPHOS-dependency of PaCSCs directly relies on the balance between the protooncogene c-MYC and the master regulator of mitochondrial biogenesis PGC1α (peroxisome proliferator-activated receptor gamma coactivator-1 alpha). In a physiological context, PGC1α is a transcriptional coactivator that binds specific nuclear receptors serving as an anchor platform to trigger metabolism-related gene transcription. As a result, PGC1α acts as a metabolic sensor of environmental stress and finely tunes energetic metabolism. On the one hand, it coordinates both genomic and mitochondrial DNA expression to promote mitochondrial biogenesis[77]. On the other hand, PGC1α promotes glycogen storage by inducing the expression of glucose transporter 4 (GLUT4), thus increasing glucose uptake while inhibiting glycolysis[78,79]. In PDAC, c-MYC modulates stemness through PGC1α activity by binding to its promoter. Therefore, increased levels of c-MYC correlate with PGC1α inhibition and cell differentiation, while c-MYC downregulation directly influence PGC1α upregulation to unleash PaCSC phenotype[62] (**Figure 5**).

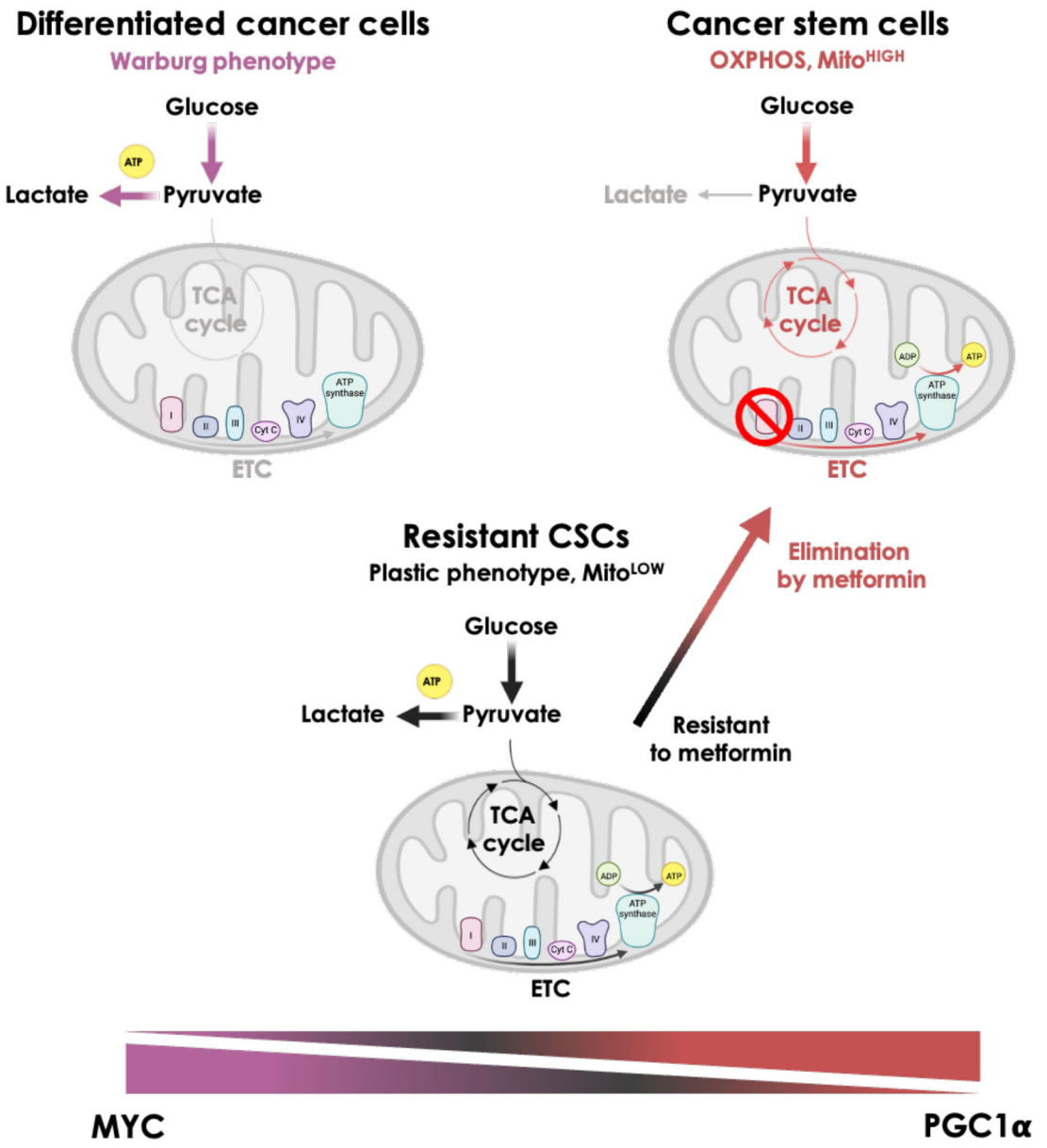

Figure 5. Schematic representation of the heterogeneity of the CSCs pool in PDAC. While differentiated cancer cells display a Warburg phenotype characterized by MYC-dependent enhanced glycolysis, PaCSC are mainly PGC1α-mediated OXPHOS-dependent, a situation that, in principle, renders them very sensitive to mitochondrial inhibition by Metformin. However, the presence of PaCSCs resistant to this compound revealed the metabolic heterogeneity that exists within this aggressive subpopulation. ETC: electron transport chain. *Adapted from Sancho et al., 2015*.

In addition to the functions above mentioned, PGC1α regulates the expression of genes involved in the fatty acids (FAs) oxidation (FAO) process, thereby promoting OXPHOS[80]. Importantly, PGC1α is a transcriptional coactivator of a superfamily of receptors involved in FAs metabolism, the peroxisome proliferator-activator receptor family (PPARs)[81–83]. In line with what

we mentioned above about the CSC-diversified mitochondrial metabolism, several studies have proved that lipid metabolism is required to maintain the CSC pool in several malignancies[84–86], including PDAC[87], not only concerning energy production, but also being directly implicated in the formation of the cell membrane, as well as acting as signaling molecules[88]. Importantly, accumulating evidence indicates that CSCs accumulate higher amount of lipids into lipid droplets (LDs) than their more differentiated progenies, further reinforcing the notion that lipid metabolism modulates cancer aggressiveness[89]. Indeed, the acetyl coenzyme A (acetyl CoA) resulting from the FAO serves to replenish the TCA cycle in the absence of glucose, thereby contributing to the OXPHOS-dependent PaCSC metabolism in scarce scenarios[74]. Several preclinical studies have used Etomoxir, an inhibitor of the lipid transporter into the mitochondria CPT1a (carnitine palmitoyl-transferase 1a), to demonstrate how FAs modulate CSC-related properties[74].

3.2. Immunoevasion

The immune system has a proved dual implication in tumorigenesis. On the one hand, the natural immunity provides host-protecting mechanisms. On the other hand, the immune system has tumor-shaping effects, defined as the ability to promote tumor progression by escaping from the immunosurveillance mechanisms. Several cells and factors are differentially linked to the immunoevasion process in distinct cancer types. This dual scenario led to define the concept of cancer immunoediting, which includes three processes known as the "three Es": elimination, equilibrium and escape. The elimination process, indeed, corresponds to the immunosurveillance phase. In the equilibrium phase, the immune system shapes the tumor and promotes the selection of cancer cell clones with enhanced survival opportunities upon an immune response against them. Finally, the escape phase is characterized by the expansion of the immune-shaped tumor[43]. In addition to this, tumors are defined as "hot" or "cold" whether they are prone to trigger a strong antitumoral immune response or not, respectively. Importantly, PDAC is considered an immunotolerant "cold" tumor in which several factors contribute to the immunosuppression mechanisms that explain why immunotherapy results ineffective in these patients (**Figure 6**). On the one hand, the extremely desmoplastic histopathological reaction

characteristic of the PDAC microenvironment is characterized by a dense stroma composed by cancer-associated fibroblasts (CAFs), which are thought to come from pancreatic stellate cells (PSCs). CAFs contribute to PDAC immunoevasive properties by producing the extracellular matrix (ECM) deposits, among other functions. The tightly-packed ECM limits the proper vascularization, thus creating a hypoxic TME that impedes antitumoral immune cells recruitment and chemotherapeutic agents' bioavailability to the targets. On the other hand, the PDAC immune landscape is characterized by infiltration of M2-polarized protumoral macrophages (TAMs), myeloid-derived suppressor cells (MDSCs) and regulatory T cells (Tregs)[90]. In addition to this, there are other components that also contribute to PDAC's immunosuppressive phenotype. Secreted factors or cytokines produced by cancer (stem) cells, CAFs, TAMs and the rest of immune cells present in PDAC stroma mediate this immunotolerant TME. These include, but are not limited to, interleukin 10 (IL-10) and transforming growth factor beta (TGFβ)[91]. Likewise, the expression of specific surface proteins, such as programmed cell death protein-1 (PD-1) and its ligand (PD-L1), as well as the antiphagocytic signal CD47, also promote PDAC immunosuppressive phenotype. PD-L1 protein expression in cancer (stem) cells promotes self-tolerance by regulating effector T cell activity and viability through PD-1 interaction. Moreover, cancer-expressed PD-L1 avoids regulatory T cell-mediated apoptosis[92]. Other important components of the antitumoral immune response are interferons (IFNs), which may have both immunostimulant and immunosuppressive impact depending, at least in part, by the exposure time. During a chronic stimulation phase, IFN-γ is associated to what is known as adaptive immune resistance. Under these circumstances, IFN-γ induces PD-1 and PD-L1 expression in PDAC and other cancers[93,94]. For all these reasons, every attempt of clinical trials with current immunotherapy has failed in obtaining favorable results. However, deciphering the immunoediting mechanisms have gained a big momentum in PDAC research.

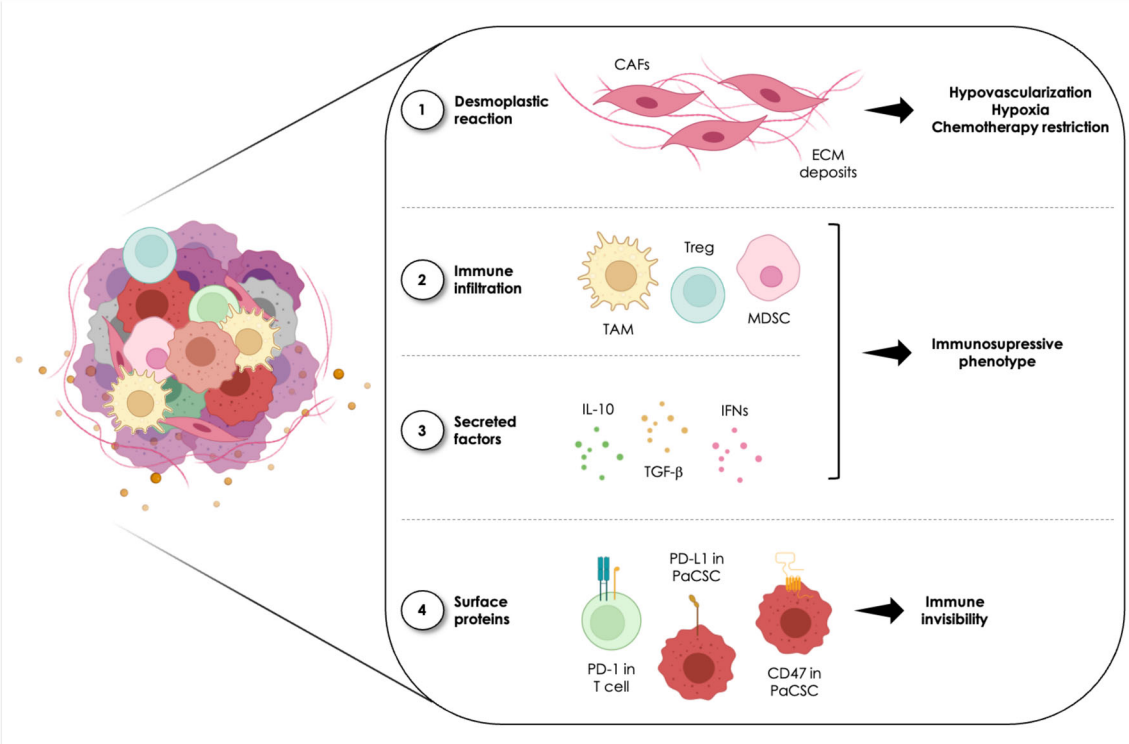

Figure 6. Schematic representation of the main components contributing to PDAC immunoevasive phenotype. The strong desmoplasia, the infiltration of immunosuppressive cells and the cytokines secreted, together with the expression of surface markers that make pancreatic cancer (stem) cells imperceptible to the immune cells promote the immunoediting process in PDAC.

In addition to the above mentioned, the strong correlation found between CSCs markers expression and the infiltration of immunosuppressive cells have provided clear insights on the importance of this phenomenon for tumor progression[95,96]. Particularly in PDAC, enhanced immunoevasive properties may be induced by shaping cell metabolism towards OXPHOS-dependent CSCs-enriching conditions[63]. Indeed, PaCSCs exhibit upregulation of PD-L1 which correlates with poor prognosis[97]. Despite the mechanisms underlying PaCSCs-mediated immunoevasion remains poorly understood, a recent study demonstrated the implication of PaCSCs in promoting immunoediting by upregulating PD-L1 and CD47[63]. IFNs are also involved in the maintenance of PaCSCs properties. On the one hand, an early study demonstrated that IFN-α enhances the expression of CSC markers *in vitro* and *in vivo* while promoting invasiveness and metastasis[98]. On the other hand, a more recent study further reinforced the notion that IFNs modulate PaCSCs functionality. In this study, PaCSCs-secreted IFN-β promoted IFN-stimulated gene 15 (ISG15) secretion by TAMs which, in turn, fostered PaCSCs maintenance and activity[99]. Therefore,

despite little advances have been made towards the use of immunotherapy in PDAC compared to other malignancies, the knowledge about the immunosuppressive phenotype of PaCSCs is now increasing, thereby shedding light on this previously discouraging field.

3.3. EMT, invasiveness and metastasis

Metastasis, the final step of cancer progression, is also the deadliest event of the disease. During the metastatic course, cancer (stem) cells undergo a dynamic and reversible stepwise process characterized by escape from the primary tumor site, intravasation and dissemination through the blood and/or lymphatic system, extravasation at distant organs, metastatic seeding, colonization and tumor outgrowth in the metastatic niche (**Figure 7**). This exceptionally complex sequence of events is finely regulated by the initiation of transcriptional programs, whose execution will lead to cell migration. Basically, two different programs have been described to mediate cancer cell migration and invasion: amoeboid migration, which is the main mechanism used for individual cell migration, and mesenchymal migration, which is mainly featured by cell clusters[100]. Despite its complexity, the mesenchymal migration process has been comprehensibly studied. It is characterized by the induction of the EMT program. While being essential in the embryonic developmental process, the EMT program also plays a key role in tissue repair, tumorigenesis and metastasis formation, being especially relevant in PDAC, since >90% of patients are diagnosed when metastatic events have already occurred[101]. It comprises different transitory intermediate states along the whole epithelial-mesenchymal phenotype spectrum (partial/hybrid E-M, **Figure 7**) upon activation of certain transcription factors such as Snail, Slug, Twist and Zeb[102]. In PDAC, the expression of several genes is a well-accepted approach for the study of the EMT program induction. These included *SNAIL*, *SLUG*, *ZEB1*[64,99,103] and, later on, *LOXL2*[104] (**Figure 7**). Another gene that has been intimately linked to cancer cell migration and invasion is *MYC*[105,106]. However, a direct role of deregulated MYC activity controlling invasiveness in PDAC has not been described to date. As a result of the activation of the EMT transcriptional program, the cells undergo morphological changes concomitant to increased motility and resistance to apoptosis, as well as higher ability to degrade the extracellular matrix[101,107,108].

Once cancer cells had reached the metastatic niche, they are subjected to the opposite process termed mesenchymal-to-epithelial transition (MET, **Figure 7**) which may explain why metastases perfectly resemble the original tumor from which they arose, both at the molecular and histopathological level.

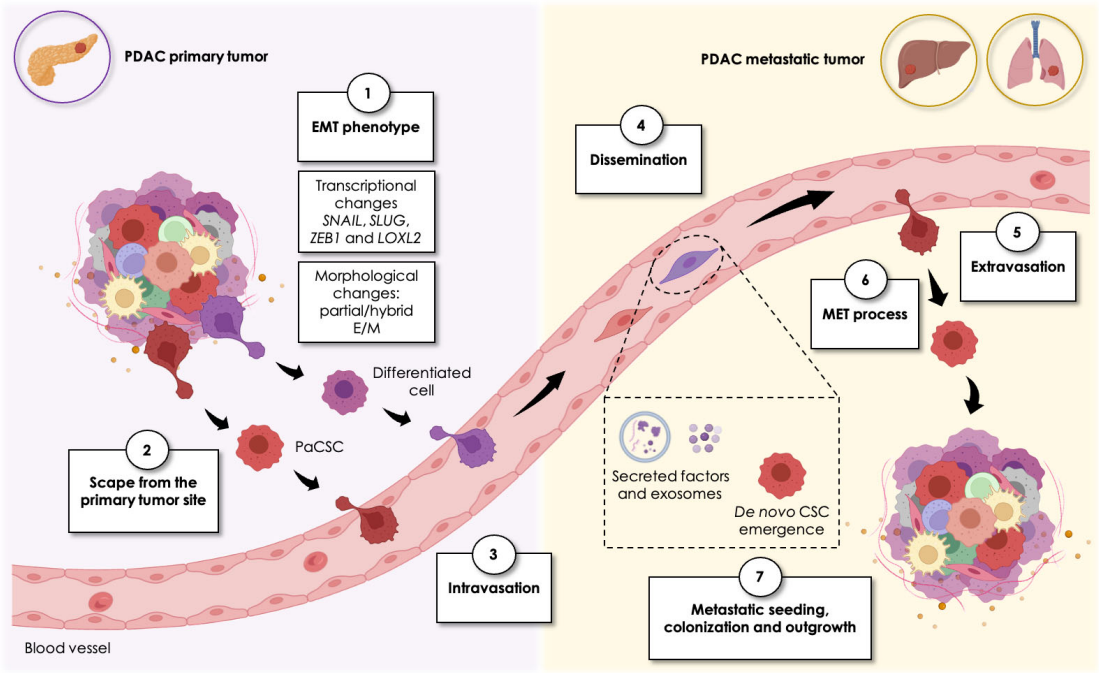

Figure 7. Schematic representation of the metastatic dissemination in PDAC. The metastatic process comprises a finely tuned consecutive events led by the induction of the EMT transcriptional program followed by mesenchymal-like morphological changes (1). This phenomenon precedes the scape from the primary tumor site mediated by increased migration and invasion abilities (2, 3) that will promote the dissemination of cancer (stem) cells through the blood vessels (4). When the cells arrive to distant organs, mainly liver and lungs, PaCSCs extravasate from the blood vessels (5) and undergo the opposite mesenchymal-to-epithelial transition process (6). Then, metastatic seeding occurs leading to colonization and secondary tumor outgrowth (7). On the other hand, migrating non-CSCs are thought to contribute to the metastatic niche formation by secreting factors and exosomes or by emerging as newly-made stem-like cells.

Single cell transcriptomic analyses on PDAC genetically engineered mouse models (GEMM) and human samples demonstrated that the EMT program contributes as well to tumor heterogeneity. This study proved the presence of cellular clusters with different gene expression patterns corresponding to epithelial or mesenchymal phenotypes, as well as hybrid subpopulations with intermediate phenotypes, all of them well-qualified for the dissemination process[109]. These paradoxical results require the additional notion that metastatic spreading commanded by the EMT program is rather a complex process in which multifactorial components are involved. Importantly,

understanding the association of the EMT program with the CSC phenotype is essential to comprehend this complexity. However, while both non-CSCs and CSCs have the ability to undergo EMT and MET processes, only CSCs will have the ultimate capacity of colonizing the secondary site to successfully establish a metastasis, and this is due to their inherent self-renewal and tumor initiating properties[101]. Importantly, a great percentage of circulating tumor cells (CTCs) express CSC markers in their surface[110,111]. While it is now well-accepted that CSCs are the sole cell entity responsible for the initiation of the metastatic tumor[19], the role of differentiated cancer cells without tumor initiating capability in the metastatic process is becoming a major issue as well. On the one hand, it is known that they may contribute to the formation of the pre-metastatic niche by secreting tumor-derived factors and exosomes that will reach secondary sites, paving the way for the successful metastatic colonization[112]. On the other hand, some studies have demonstrated that non-CSCs undergoing EMT acquire CSCs-related properties during the process, thus associating the EMT program with the *de novo* CSC emergence mentioned in the previous section[45] (**Figure 7**).

Lastly, TAMs' implication in tumor evolution goes far beyond their association to the immunoevasive phenotype, but rather they also have an impact in the metastatic process. Importantly, an enhanced EMT phenotype in PDAC cells spatially overlaps with inflammation, while treatment with anti-inflammatory agents abrogates metastatic spreading in mice. In this early study, the authors also demonstrated by tagging and tracking PDAC cells that these events occur before the histological detection of the pathology[110], therefore, supporting the notion that EMT takes place in early stages of the tumorigenic outgrowth, including the pre-neoplastic lesions. In PDAC, secreted factors from cancer cells confer a pro-metastatic phenotype in macrophages by modulating monocyte metabolism towards increased glycolysis[113]. In turn, TAMs promote invasiveness in PaCSCs[99]. Hence, the intricate crosstalk between pancreatic cancer (stem) cells and their niche fosters aggressiveness not only by immunoediting mechanisms, but also by enhancing the invasive abilities of cancer cells.

3.4. Chemoresistance

Chemotherapy failure remains the Achilles heel concerning PDAC –and other aggressive cancers– management in the pursuit of long-lasting treatment responses that increase patients' survival. While common chemotherapeutic agents are quite efficient in eliminating bulk differentiated tumor cells, CSCs are able to escape from the treatment due to their inherent chemoresistance. Different mechanisms, reviewed by Abdullah and Chow[114], define this CSC-intrinsic characteristic and include, but are not limited to, overexpression of ATP-binding cassette (ABC) transporters and hyperactivation of CSC-related signaling pathways such as Hedgehog, PI3K/Akt, Notch, WNT/β-catenin, and MYC, among others.

ABC transporters are especially known by their ability to efflux toxic agents as chemotherapeutics out of cancer cells, thereby contributing to cancer chemoresistance and cytoprotection. Importantly, ABC transporters expression is enhanced in CSCs, including PaCSCs[115], thus, representing both potential biomarker for CSCs detection and target for anti-CSCs therapy. In addition to this, ABC transporters have a side function dedicated to release active biomolecules into the extracellular milieu. Nevertheless, ABC transporters are not exclusively located in the cell membrane and can be found in the membranes from cytoplasmic vesicles as well. As an example, *ABCG2* is overexpressed in CSCs from PDAC and other tumoral malignancies and serves to pump in and accumulate ABCG2-dependent substrates, such as the autofluorescence riboflavin (vitamin B2), and drugs, such as Mitoxantrone. This scenario not only potentiates chemotherapeutic failure as PaCSCs avoid Mitoxantrone's effects by accumulating it in intracellular vesicles, but also allows for the detection and isolation of fluorescence PaCSCs[56] (**Figure 8**).

Many signaling pathways have been linked to CSC-intrinsic chemoresistance in PDAC. For instance, TET1, as the most important demethylating enzyme implicated in chemoresistance, induces the expression of CHL1 (neural cell adhesion molecule L1-like protein, also known as close homolog of L1) that will further downregulate the Hedgehog pathway, thus favoring chemosensitivity[116]. Additionally, the natural compound Berberine reverted Rap1/PI3K-Akt-mediated Gemcitabine resistance in both PDAC cell lines and patient-derived organoids (PDOs)[117]. Another pathway implicated in chemoresistance in PDAC is Notch.

On the one hand, PSCs mediate chemotherapy failure by promoting the expression of the stemness regulator transcription factor *HES1 via* Notch-1 receptor activation[118]. On the other hand, the cytokine midkine (MDK) induced *ABCC1* and *ABCC2* expression[119] and activated Notch-2 signaling to inhibit Gemcitabine sensitivity[120]. Likewise, in osteosarcoma, enhanced WNT/β-catenin signaling displayed increased resistance to doxorubicin through the WNT/β-catenin pathway by inducing the expression of *ABCB1* transporter in a PTN/ALK-dependent manner[121]. This indicates that, apart from the traditional signaling pathways, others such as ALK may also play a pivotal role in mediating chemoresistance (**Figure 8**).

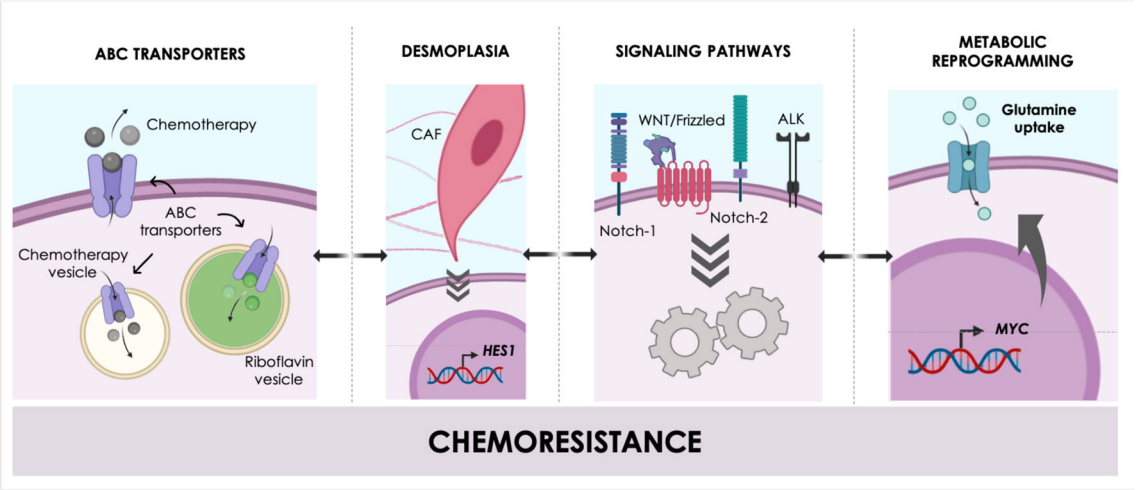

Figure 8. Schematic representation of the different events contributing to PDAC-intrinsic chemoresistance. ABC transporters control chemotherapy efflux of the cell or influx in intracellular vesicles to neutralize toxicity, as well mediate riboflavin accumulation in fluorescence vesicles that facilitate CSCs detection and isolation. CAFs-mediated desmoplasia induces the expression of the pluripotent factor *HES1*. Different signaling pathways increase resistance to distinct chemotherapeutic agents. The protooncogene MYC promotes chemotherapy failure by inducing a metabolic reprogramming featured by enhanced glutamine usage. However, these four mechanisms are interrelated and not mutually exclusive.

Finally, mounting evidence described the link between metabolic reprogramming by MYC signaling and resistance to chemotherapy. In a murine model of PDAC, Gemcitabine enhanced the expression of Muc5ac, a protein previously related to chemoresistance. Muc5ac promoted β-catenin translocation to the nuclei to unleash Myc expression which, in turn, increased glutamine uptake and utilization. Either glutamine deprivation or glutaminolysis inhibition overcame Muc5ac-mediated resistance to Gemcitabine[122]. In another study, the link between MYC and nab-Paclitaxel resistance was

described in primary PDAC cells. In this study, resistant nab-Paclitaxel cells were generated *in vitro* from treatment-*naïve* PDAC patients' cells to demonstrate in animal models that *MYC* expression was sustained long after nab-Paclitaxel withdrawal[123]. Therefore, the chemoresistance process goes beyond an acute state that rather produces long-lasting effects in the cells undergoing it. Indeed, the notion that MYC is a key regulator of stemness in PDAC[62], further reinforces its link with chemoresistance (**Figure 8**).

Hence, while chemotherapy resistance continues to be a real challenge, our knowledge continues to increase. Indeed, several approaches, such as ABC transporters blockade or inhibition of CSC-related signaling pathways, may be useful to successfully overcome PaCSCs-intrinsic chemoresistance.

4. PEROXISOME PROLIFERATOR-ACTIVATED RECEPTORS

Peroxisome proliferator-activated receptors (PPARs) comprise a family of proteins belonging to the nuclear hormone receptor superfamily of transcription factors (TFs) that, after being activated by specific ligands, extensively regulate gene expression through direct binding to PPAR responsive elements (PPREs) in the DNA[124]. The PPARs structure consists of four main regions: 1. A/B or ligand-independent domain, which includes the AF1 region important for subtype-specific activity; 2. C or DNA-binding domain (DBD); 3. D or docking cofactors domain; and 4. E or ligand-binding domain (LBD). The LBD is quite similar to other nuclear receptor except for being larger, which may facilitate the interaction with a wider range of compounds harboring an acidic head group compared to other nuclear receptors[125]. Three different PPAR isoforms have been described to date: PPAR-α (also known as NR1C1), PPAR-δ (also known as PPAR-β or NR1C2) and PPAR-γ (also known as NR1C3). Characterization of the LBD of each isoform revealed that, while PPAR-α and PPAR-γ have pretty similar ligand-binding pocket in terms of size and shape, the one of PPAR-δ is significantly smaller. This peculiarity my explain the observed ligand restriction in PPAR-δ *versus* the other two isoforms. The endogenous ligands activating all three PPARs are all kinds of FAs and FA-derived molecules. Likewise, several synthetic compounds are currently available for PPARs modulation, although none of the PPAR-δ agonists/antagonists are approved for clinical use nowadays[124]. Upon ligand-

dependent activation, all PPARs heterodimerize with the retinoid X receptor (RXR), which belongs to the same receptor superfamily, and the LBD stabilizes acquiring a conformation that promotes binding of coactivator or corepressor proteins. Then, the PPAR:RXR heterodimer plus the coactivator or corepressor bind to the PPREs present in the promoters of the target genes and, subsequently, activate or repress their expression[126]. PPARs function is isotype-specific and varies across tissues in a context-dependent manner. In broad terms, all three PPARs are involved in energy homeostasis through lipid sensing, while PPAR-δ additionally regulates cell proliferation, differentiation, survival and tissue repair. On the other hand, mounting evidence associates all PPARs with tumorigenesis, thereby rendering them excellent candidates for therapeutic intervention[124,127].

4.1. PPAR-delta

PPAR-β/δ was first identified 30 years ago in *Xenopus* and named PPAR-β[128]. A year later, a similar protein with apparent incomplete homology to PPAR-β was isolated from mouse and termed PPAR-δ[129]. Further studies eventually demonstrated that, indeed, PPAR-β and PPAR-δ are homologous. In humans, PPAR-δ is encoded by the gene *PPARD* and is expressed broadly, especially in organs with high FAs metabolism, reproductive organs and the cardiovascular, endocrine and immune systems, with increased basal levels in the gastrointestinal tract and the skeletal muscle[125].

Unsaturated FAs are natural ligands for PPAR-δ, including derivatives from linoleic acid. However, the effect of endogenous ligand-dependent activation of PPAR-δ is, in fact, tissue-specific depending also on the relative presence of coactivators and corepressors. For instance, 13-HODE (13-hydroxyoctadecadienoic acid) has been reported to inhibit PPAR-δ in colorectal cancer cells to induce apoptosis[130], while in pre-adipocytes it acts as an agonist enhancing lipid detoxification[131]. Additionally, PPAR-δ may be exogenously activated with FAs from outside the cell or synthetic ligands. On the one hand, for instance, the flavonoid ombuine (ombuin-3-O-beta-D-glucopyranoside) is a dual agonist of PPAR-α and PPAR-δ able to decrease lipids concentration in hepatocytes and macrophages[132]. On the other hand, several chemical PPAR-δ modulators have been developed to date. The very first PPAR-δ agonist L-

165041 or the compound GW0742, among others, are the most used PPAR-δ inducers nowadays for *in vitro* experiments. Conversely, GSK0660 as the first selective PPAR-δ antagonist, GSK3787 as irreversible PPAR-δ inhibitor, or DG172 are considered inverse agonists since they are able to recruit corepressor proteins to downregulate PPAR-δ target genes[125]. Certainly, it is important to highlight the notion that both endogenous and exogenous signals may trigger PPAR-δ signaling with different downstream effects. PPAR-δ activation results in the phosphorylation of several consensus sites by protein kinase A (PKA), regardless of the presence or absence of a ligand, thereby increasing basal and ligand-dependent activity to unleash gene expression or repression of PPAR-δ target genes. Conversely, negative regulation of PPAR-δ is mediated by ubiquitin-induced proteolysis[133].

As mentioned in the general introduction for PPARs, PPAR-δ exerts a wide range of physiological functions in a tissue-specific manner, most of them related to lipid metabolism. In the pancreas, *PPARD* knockout (KO) increased insulin secretion, while systemic treatment of obese (ob/ob)[134] and diabetic (db/db)[135] mice with PPAR-δ agonists enhanced glucose-stimulated insulin secretion and normalized pancreatic islet hypertrophy. In the liver, one of the most important organs implicated in energy homeostasis, PPAR-δ promotes lipogenesis and activates the pentose phosphate pathway (PPP) to increase glucose utilization, while *PPARD* null mice exhibit glucose intolerance[136].

In cancer, however, the role of PPAR-δ has remained a subject of controversy among malignancies probably due to tissue contextualization. Even more disturbing is the fact that this controversy is found within the same malignancy, although this is most likely a consequence of the diversity of the models used[137]. For instance, *PPARD* knockdown (KD) promoted colon cancer progression and resistance to treatment[138], while PPAR-δ signaling endowed intestinal organoid- and tumor-initiating properties induced by a high-fat diet (HFD) in the same malignancy[139] (**Figure 9**). Another example of controversy is the one found in liver carcinoma. On the one hand, *PPARD*$^{-/-}$ mice were more susceptible to develop induced hepatocellular carcinoma (HCC) and, subsequently, *PPARD* overexpression in HCC cell lines inhibited proliferation, migration and invasion while enhanced apoptosis in these cells[140]. Conversely, a different study correlated increased PPAR-δ activity to treatment resistance in HCC providing

proof of concept of the potential benefits of PPAR-δ targeting to improve chemosensitivity[141] (**Figure 9**). Contradictory results have been published also for breast cancer, reporting both PPAR-δ-dependent inhibition of tumorigenicity[142] and survival and metastatic advantages in harsh metabolic conditions[143] (**Figure 9**). Likewise, this controversy is also found in PDAC. In previous reports, PPAR-δ was found to regulate B-cell lymphoma 6 (BCL-6)-dependent matrix metalloproteinase 9 (MMP-9) activity, thus inhibiting the ability of PDAC cells to invade[144]. Further studies demonstrated that PPAR-δ and BCL-6 counteract the anti-inflammatory state characteristic in the transition from pancreatitis to PDAC[145] (**Figure 9**).

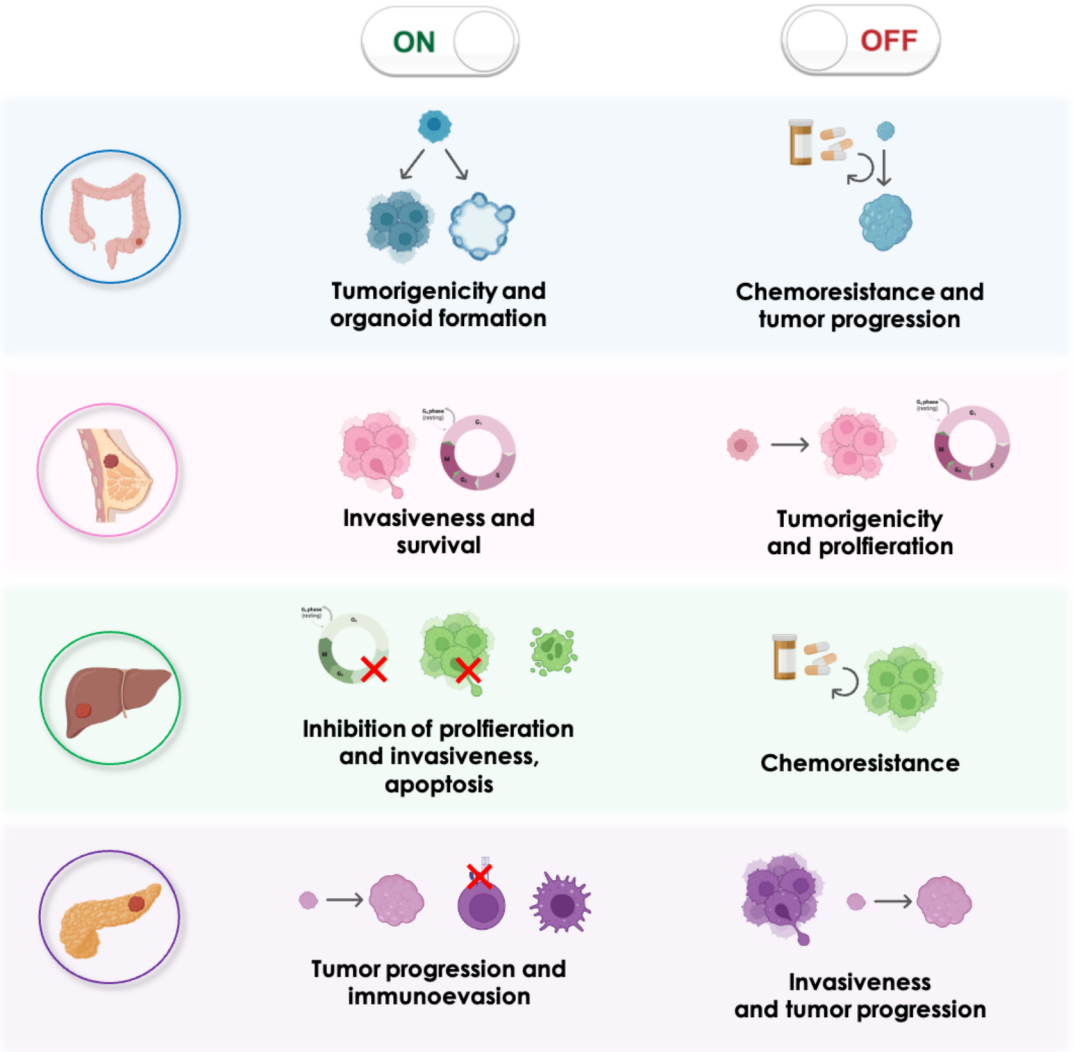

Figure 9. Controversies described in PPAR-δ implication across tumoral malignancies. Different studies have reported contradictory effects of PPAR-δ activation or repression, not only among cancer types, but also within the same tumor entity, most likely due to the different models used.

However, the role of PPAR-δ in PDAC progression and metastasis has gained more attention lately. An early study already correlated *PPARD* expression with increased *in vitro* EMT, migration and invasion, as well as *in vivo* metastasis in several cancers, including PDAC[146]. This was not only recently confirmed, but also a link between PPAR-δ and immunoevasion in PDAC was reported. On the one hand, PPAR-δ activation with a chemical agonist or with HFD significantly accelerated PDAC progression from PanINs *via* CCL2-mediated immunosuppression[147]. Additionally, direct FA binding to the mitochondrial glutamic-oxaloacetic transaminase 2 (GOT2) promoted PPAR-δ activity to inhibit T cell effector recruitment in the TME, thus promoting an immunoevasive scenario[148]. Importantly, *PPARD* is expressed in hepatic resident macrophages (also known as Kupffer cells). In this situation, PPAR-δ is responsible for macrophage polarization towards a M2 anti-inflammatory and protumoral phenotype[149], thus confirming the role of PPAR-δ in Immunoevasion (**Figure 9**).

In summary, despite an apparent lack of consensus when attributing the anti- or pro-tumoral role of PPAR-δ, accumulating evidence suggest that, in PDAC, this transcription factor has an important role in promoting tumor progression, immune system scape and metastasis. Therefore, PPAR-δ targeting hold promise to substantially improve PDAC patient's outcome.

5. RECEPTOR TYROSINE KINASES

The human protein kinase complement or "kinome" comprises over 500 protein kinases that represents the 1.7% of the total human genome. Protein kinases modulate other protein activity by transferring phosphate groups from ATP to amino acids residues[150,151]. Protein kinases are classified into nine major groups, each of them further divides into different families and, frequently, subfamilies[152]. One of the most studied groups is the one known as protein tyrosine kinases (TKs) which, as its own name suggests, phosphorylates tyrosine aminoacidic residues in the target proteins. A total of 90 TKs has been identified to date, among which 58 are receptor tyrosine kinases (RTKs) and 32 correspond to non-receptor tyrosine kinases (nRTKs)[153]. Both RTKs and nRTKs activation converges into signal transduction pathways inside the cells that control basic cellular functions such as cell proliferation, differentiation, survival and

metabolism and are frequently overexpressed and/or hyperactivated in many cancer types[154,155]. Indeed, the neoplastic progression process comprises a multistep course of events commonly induced by dysregulated cellular signal transduction pathways mediated by protein TKs. Cancer cells interact with surrounding non-malignant cells and other components of the TME in an intricate crosstalk involving cell-cell and cell-matrix contacts, as well as paracrine and endocrine regulations based on ligand-receptor interactions, being the latter typically orchestrated by RTKs[156,157]. In addition to the above-mentioned cellular processes, RTKs are also involved in the induction of angiogenesis[158] and migratory/invasive capacity[159]; such processes are especially relevant in tumor progression by restoring nutrient and oxygen accessibility in the typically scarce TME and potentiating metastatic dissemination, respectively. Even more interesting for us is the implication of several TKs in promoting stemness in different tumor types, such as EGFR in breast cancer[160,161], FGFR in prostate cancer[162], EphR in brain tumors[163,164], melanoma[165] and lung cancer[166], as well as the nRTK SRC in pancreatic cancer[167].

Therefore, one of the most explored avenues to design new targeted treatment strategies is, precisely, the inhibition of TKs. Notably, several TK inhibitors (TKi) are currently under evaluation in clinical trials for PDAC, including Erlotinib (EGFR inhibitor, phase III) or Masitinib (c-kit/PDGFR inhibitor, phase III)[15]. Hence, RTKs may also be potential candidates for targeting PaCSCs.

5.1. Anaplastic Lymphoma Kinase

Anaplastic lymphoma kinase (ALK) is one of the 58 RTKs described to date that was first discovered in 1994 in anaplastic large-cell lymphoma (ALCL) as the fusion protein NPL-ALK following chromosomal rearrangement[168]. Subsequently, ALK was shown to be aberrantly expressed and/or activated in several cancer types[169–172]. Some years before its discovery, in 1997, the first *ALK* wild-type characterization was reported by two groups simultaneously[173,174]. The ALK receptor belongs to a two-member RTK subfamily and shows a high homology with the other member of the subfamily, the leukocyte tyrosine kinase (LTK). *ALK* is predominantly expressed in several regions of both the central and the peripheral nervous system (CNS and PNS, respectively) with increased levels in

the neonatal brain[173]. This indicates that ALK plays an important physiological role in neural development[169,173].

Human *ALK*, or CD246 (cluster of differentiation 246), gene is located at region p23.2-p23.1 of chromosome 2[174]. It contains 26 exons that encode different protein isoforms. The full-length ALK is formed by 1620 amino acids (aa) and, as the rest of RTKs, it contains three domains: intracellular tyrosine kinase domain (ICD), a single transmembrane domain (TMD) and extracellular ligand binding domain (ECD). However, ALK is an unusual RTK since it has a unique structure in the ECD which is not present in any of the other RTKs, including LTK: two MAM (meprin, A-5 protein, receptor protein-tyrosine phosphatase mu) domains, which are thought to participate in cell adhesion, separated by a low-density lipoprotein receptor class a (LDLa) domain, whose function remains unknown[174].

Full-length ALK protein may suffer post-translational *N*-glycosylation, a process by which the molecular weight of ALK increases from 180 to 220 kDa. Besides this, the 220 kDa glycosylated full-length ALK protein can be cleaved in the ECD to give a 140 kDa truncated ALK and an 80 kDa free fragment released into the extracellular compartment (**Figure 10**). It has been described that both glycosylation and cleavage take place during normal ALK function[171].

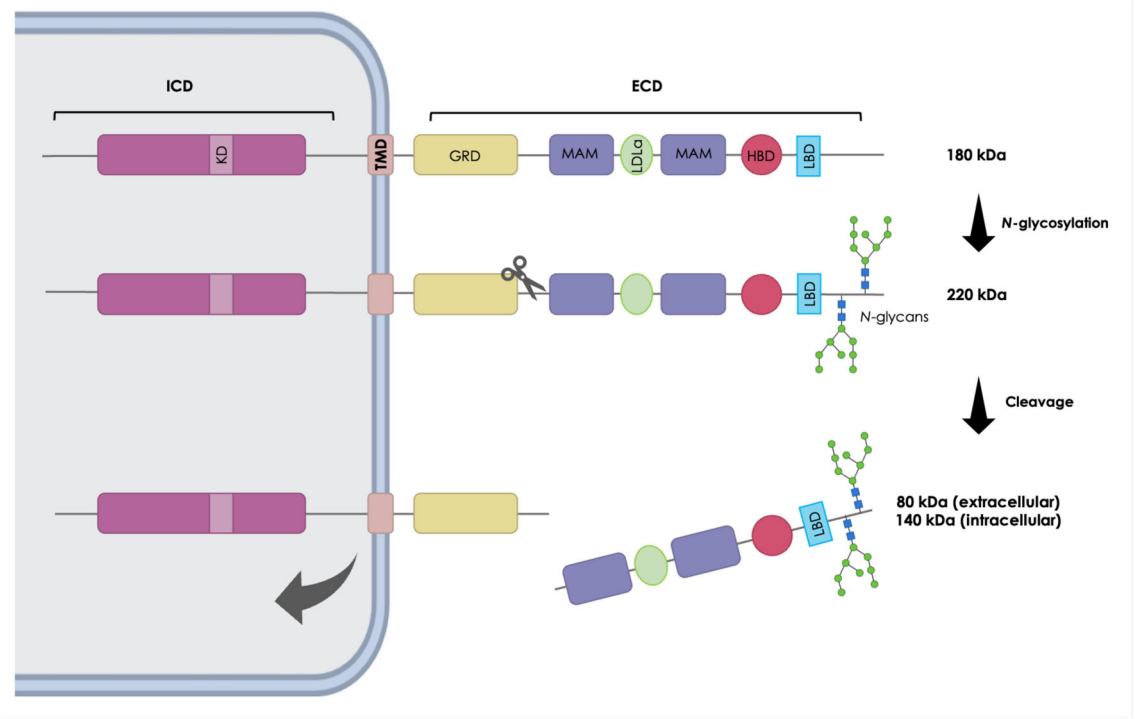

Figure 10. Schematic representation of the ALK receptor structure and its main post-translational modifications. ALK receptor consists of an intracellular domain (ICD) which contains the kinase domain (KD), a transmembrane domain (TMD) and an extracellular domain (ECD). The ECD contains different subdomains important for ALK activation and function, such as the glycine-rich domain (GRD), two MAM domains separated by a LDLa domain, a heparin binding domain (HBD) and the ligand binding domain (LBD). The 180 kDa full length ALK protein may be *N*-glycosylated, a fact that increases its molecular weight to 220 kDa. Finally, both 180 and 220 kDa ALK may be cleaved resulting in an extracellular 80 kDa portion and an intracellular 140 kDa fragment that will be further internalized.

While ALK remained an orphan receptor for many years, different molecules have been recently proposed as potential ALK activating ligands. However, this is still a matter of great controversy. While some studies point to midkine (MDK) and pleiotrophin (PTN)[170,175], others suggest the cytokines family with sequence similarity 150 members A and B (FAM150A and B, also known as ALKAL1 and 2)[176] as main activators of the ALK pathway. MDK and PTN are heparin-binding growth factors with multiple regulatory functions in biological processes such as proliferation, differentiation, migration and neural development through binding to different receptors, including ALK[177,178] Indeed, the ECD of the full-length ALK protein contains a heparin binding motif and heparin was reported to physically bind to the ALK receptor, thus activating it[179] (**Figure 10**). Conversely, FAM150A and B were first described as LTK ligands[180] and their activity on ALK was

demonstrated later on given the reported high homology between both RTKs[176,181].

ALK receptor physiological activation triggers different intracellular signaling pathways involved in proliferation, survival and metabolism, including JAK/STAT and Ras/ERK[171,182,183]. However, ALK function is better studied and acknowledged in disease. As mentioned before, although mammalian ALK receptor is involved in neural development, it also has been linked to oncogenic signaling caused by three main different mechanisms: translocations, gain-of-function mutations and amplification. On the one hand, ALK rearrangements generate a wide range of fusion proteins upon chromosomal translocation of the ALK gene with other genes. The most common cancer-related malignancies with ALK translocations are ALCL[168] and NSCLC (non-small cell lung cancer)[184], which fusion partners are nucleophosmin (NPM) and echinoderm microtubule-associated protein-like 4 (EML4), respectively. Despite this, many other translocations have been described to occur in these and other tumoral malignancies[183,185]. On the other hand, ALK activating mutations have been reported in glioblastoma[186], among others adult cancer types[183], as well as pediatric cancers such as neuroblastoma[187] and rhabdomyosarcoma[188]. Finally, amplification has been demonstrated in a wide range of cancers, including but not limited to NSCLC and melanoma[183]. Therefore, oncogenic ALK has gained substantial interest due to its raising detection in human malignancies. However, in PDAC, this receptor has been completely overlooked. The possible cause points to the lack of mRNA overexpression in bulk tumor cells when compared with normal pancreas or the low level of chromosomal rearrangements of the ALK gene found in PDAC tumors[189,190].

Oncogenic ALK signaling has also been described to regulate stemness[191–194]. For instance, in glioblastoma, ALK signaling modulates self-renewal and tumorigenicity through SOX2-mediated PTN activation[191]. A more recent study on the same malignancy reported that, in turn, the modulation of these CSC features takes places through SOX9-mediated MDK activation[192], thus highlighting the importance of the ALK pathway in controlling the pluripotent status in glioblastoma. Another example is the one found in ovarian high-grade serous carcinoma (HGSC) in which ALK amplification promotes the maintenance of the aggressive phenotype by enhancing CSC features[194]. Another stemness-

related feature in which ALK signaling has been found deregulated is the prometastatic events. In neuroblastoma, both MYCN and c-MYC regulate ALK expression to enhance invasiveness[195,196].

Several small molecules have been used in the clinics to block ALK activity for years. Currently, six ALK inhibitors classified into three generations are approved for their use in NSCLC patients. Crizotinib was the first-in-class first-generation ALK inhibitor authorized by the FDA in 2011 as second line therapeutic strategy for this disease. It was approved later on by the European Medicines Agency (EMA) in 2012 and the Chinese National Medical Products Administration (NMPA) in 2013. In 2015, Crizotinib was approved by the EMA as first line treatment for NSCLC[197]. Crizotinib completely transformed ALK+ NSCLC management as a trivalent TKi against ALK, c-MET and ROS1[198–200]. However, Crizotinib presented poor blood-brain barrier penetration, thereby favoring metastatic dissemination to the brain as the main organ of NSCLC progression site[201]. In addition to this, NSCLC patients rapidly showed resistance to Crizotinib due to mutations in the ALK receptor that led to inefficient Crizotinib-ALK binding[202]. As a consequence, second-generation ALK inhibitors were developed, such as Ensartinib, which exhibited a potent response in Crizotinib-resistant ALK+ NSCLC patients[203]. This led to its approval by the Chinese NMPA in 2020 as second-line treatment[197]. Unfortunately, second-generation ALK inhibitors induced further resistance due to other mutations in the ALK receptor. In 2021, Lorlatinib, was approved as a third-generation ALK inhibitor by the American FDA and, in 2022 by the EMA, as first-line therapy in NSCLC. Importantly, diverse studies in NSCLC have linked resistance to ALK inhibitors with EMT. On the one hand, resistance to ALK inhibitors conferred by mutations in the receptor promotes the acquisition of the EMT phenotype, thereby enhancing migration and invasion abilities[204,205]. On the other hand, a very recent study showed that, indeed, the EMT process promotes cross-resistance to new-generation ALK inhibitors through TGFβ, and that this phenomenon is less pronounced in cancer cells with partial/hybrid E-M transition state. The authors of this study demonstrated that inhibition of TGFβ-mediated EMT with silibinin overcomes resistance to new-generation ALK inhibitors in NSCLC cells with stronger mesenchymal phenotype[206]. Currently, fourth-generation ALK inhibitors are being investigated to reduce ALK TKi-resistant mutations susceptibility[197].

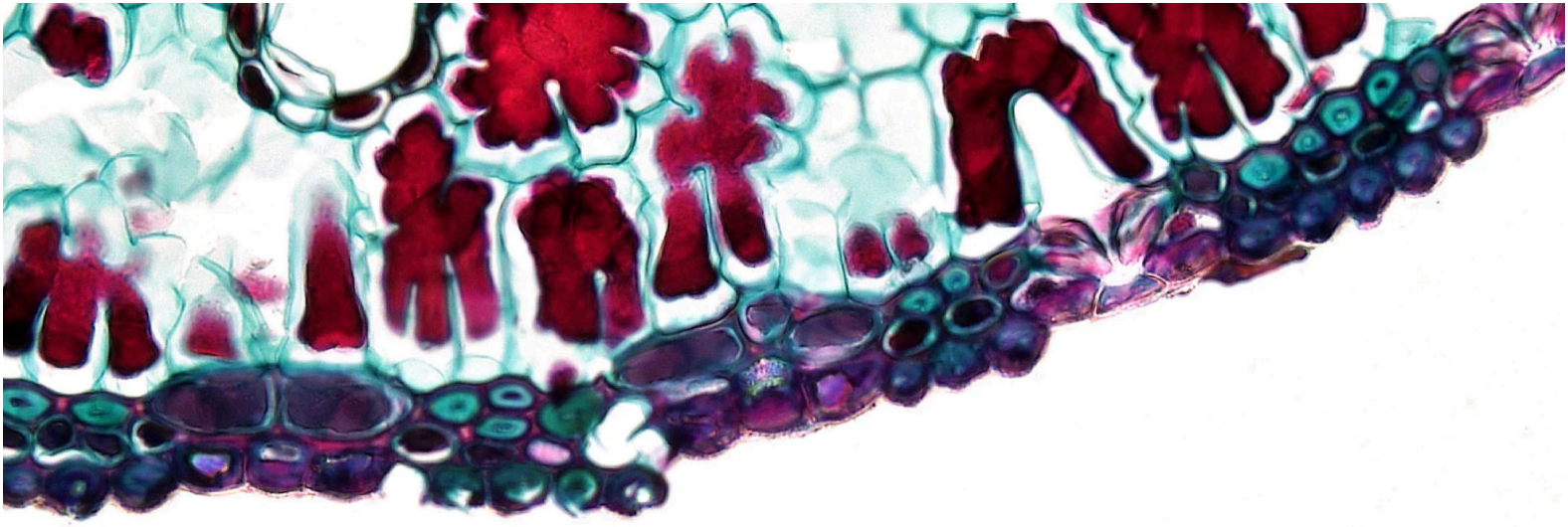

HYPOTHESIS & OBJECTIVES

PDAC aggressiveness is, to a large extent, the consequence of the presence of a small portion of cells with stem-like properties known as pancreatic cancer stem cells (PaCSCs). Thanks to their inherent self-renewal capacity, tumor-initiating properties and chemoresistance, these cells are the sole cell entity responsible for tumor formation, metastatic dissemination and disease relapse. Notably, PaCSCs harbor unique characteristics, such as enhanced mitochondrial metabolism or hyperactivation of specific signaling pathways. Bearing this in mind, the general hypothesis on which the present doctoral thesis has been developed is the following:

The identification of distinct metabolic routes and signaling pathways used by pancreatic cancer (stem) cells may serve to pinpoint new targets amenable for therapeutic intervention.

Based on this hypothesis, the main aim of this doctoral thesis was to interrogate the role of the nuclear hormone receptor PPAR-δ and the surface receptor tyrosine kinase ALK in orchestrating PaCSCs-specific functions. In order to accomplish this general aim, the following specific objectives were proposed:

1. To assess PPAR-δ/ALK status in PDAC patients and patient-derived xenograft (PDX) models.
2. To evaluate the functional effects of PPAR-δ/ALK activation upon specific experimental conditions.
3. To appraise, *in vitro* and *in vivo*, the consequences of PPAR-δ/ALK inhibition on PaCSCs features.

MATERIALS & METHODS

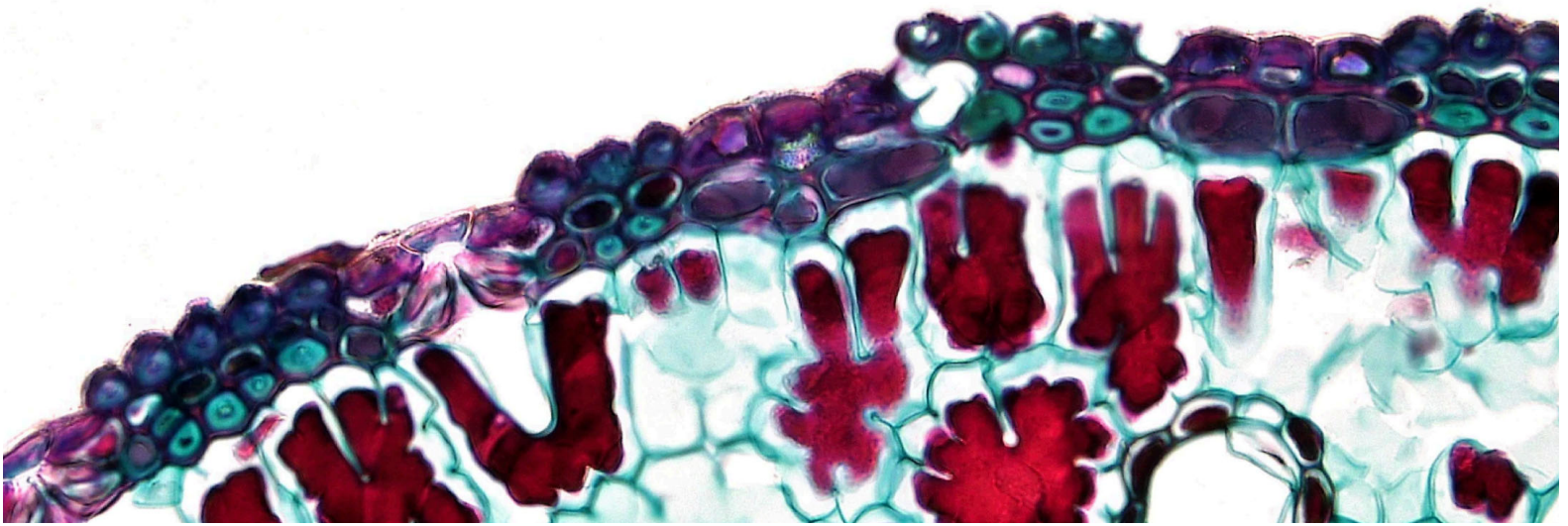

1. Cell culture

1.1. Patient-Derived Xenografts (PDXs) and Circulating Tumor Cells (CTCs)

PDX185, PDX215, PDX253, PDX265, PDX354 and PDXA6L were obtained through the Biobank of the Spanish National Cancer Research Center (CNIO, Madrid, Spain; CNIO20-027). Tumor pieces underwent several amplification passages in mice prior to establishing primary cultures. Tumor dissociation and establishment of *in vitro* primary cultures was performed as previously described[207]. The metastatic model CTCA was established from circulating tumor cells and obtained through the Barts Pancreas Tissue Bank of the Barts Cancer Institute (https://www.bartspancreastissuebank.org.uk/; BCI, London, United Kingdom; 2019/02/IISA/PS/E/Cell-cultures). Cells were submitted to a maximum of 15 passages in complete RPMI 1640 GlutaMAX™ medium supplemented with 10% fetal bovine serum (FBS) and 50 U/mL penicillin/streptomycin (all from Gibco, Life Technologies, Carlsbad, CA, USA). For experiments, the medium was changed to DMEM/F-12 GlutaMAX™ medium supplemented with 2% B27 (Gibco), 50 U/mL penicillin/streptomycin, and 20 ng/mL fibroblast growth factor (FGF)-basic (Pan-Biotech, Aidenbach, Germany). All PDXs were grown in a humidified incubator at 37°C with 5% CO_2 and regularly tested for mycoplasma at the Technical and Scientific Services Unit from the Health Sciences Institute of Aragón (IACS).

1.2. Cell lines

AsPC1, BxPC3, MiaPaCa2, Panc1 and Su8686 were purchased from the American Type Culture Collection (ATCC, Manassas, VA, USA). Cells were submitted to a maximum of 30 passages in the same conditions as the primary cultures described above (**section 1.1**). HEK 293T were purchased from ATCC and submitted to a maximum of 30 passages in DMEM medium supplemented with 10% FBS, 50 U/mL penicillin/streptomycin, 6 mM glutamine, 1X pyruvate and 1X non-essential amino acids (all from Gibco).

1.3. Adherent *versus* spheroids

PDAC PDXs cells were cultured in adherence as per 1.1. or anchorage-independent conditions at 10^5 cells/mL with DMEM/F-12 GlutaMAX™ medium supplemented as described above (**section 1.1.**). First generation spheroids were grown up to seven days, dissociated with trypsin (Corning, Oneonta, NY, USA)

and regrown at 10^5 cells/mL for five more days. Flasks were coated with 10% poly(2-hydroxyethyl methacrylate) (Sigma-Aldrich, Saint Louis, MO, USA) in 96% ethanol and left at 37ºC until all the liquid was evaporated. Flasks were rinsed once with 1X PBS prior to their utilization. When adherent cells reached around 70% of confluence, medium was changed to complete DMEM/F-12 GlutaMAX™ for 72 hours. After the indicated times, supernatants from both adherent and spheroid cells were collected and cells or spheroids were harvested for further analyses.

1.4. Primary human macrophages and conditioned medium

Leucocyte cones from anonymous healthy donors were obtained from the National Blood Transfusion Service (UK) according to City and East London Research Ethics Committee (17/EE/0182). Cones were stored at 4ºC and used within 24 hours of delivery to maintain cell viability. Monocyte-derived human macrophage culture, polarization into M2-like macrophages and generation of conditioned medium were performed as previously described[99]. Monocyte-derived human macrophage cultures were maintained in IMDM (Gibco) supplemented with 10% human AB serum (Corning) and polarized to M2-like phenotype by incubation with 0.5 ng/mL of macrophage colony-stimulating factor for 48 hours (MCSF; PeproTech). To generate conditioned medium (MCM), macrophages were then washed with 1X PBS and cultured for additional 48 hours in complete DMEM/F12 GlutaMAX™ medium. Medium was then collected, centrifuged and supernatant stored at -80ºC.

2. *In vitro* treatments

2.1. EMT induction with Etomoxir and MCM

Etomoxir was purchased from Sigma-Aldrich and dissolved in ultrapure RNase and DNase free water (Gibco) following the manufacturer's instructions. Cells were treated for 48 hours at low-dose Etomoxir (20-40 µM) to avoid toxicity.

MCM was obtained as described above (**section 1.4**) and PDAC cells were then incubated for 48 hours.

2.2. PPAR-δ agonists, antagonists and inverse agonists

GW0742 (agonist), GSK3787 (antagonist) and L165 (agonist) were purchased from Cayman Chemical (Ann Arbor, MI, USA). GSK0660 was purchased from Sigma-Aldrich. DG172 (inverse agonist) was purchased from Tocris Bioscience (Bristol, UK). All compounds were dissolved in DMSO (Sigma-Aldrich) following the manufacturer's instructions. Cells were treated for 48 hours with GW0742 or L165 at 5 μM, GSK3787 or GSK0660 at 10 μM or DG172 at 2.5 μM.

2.3. MYC inhibitors

Mycro3 was purchased from Aobious INC (Gloucester, MA, USA) and dissolved in DMSO following the manufacturer's instructions. Cells were treated for 48 hours with Mycro3 at 25 μM, with DMSO compensation when needed.

2.4. ALK ligands and inhibitors

Midkine and pleiotrophin were purchased from PeproTech (London, UK) and dissolved following the manufacturer's instructions. Cells were treated at 1, 10 or 100 ng/mL for the indicated time points in each individual experiment. Crizotinib and Ensartinib were purchased from Selleckchem (Munich, Germany) and dissolved in DMSO following the manufacturer's instructions. Cells were treated at concentrations ranging 0.5 to 10 μM for the indicated time points in each individual experiment, with DMSO compensation when needed.

2.5. Chemotherapy

Gemcitabine 0.9% sodium chloride (Eli Lilly and Company, IN, USA) was used at concentrations ranging from 1 to 750 nM for 24 to 72 hours.

3. Cell viability, toxicity and proliferation

3.1. Resazurin (viability assay)

Cells were seeded in triplicate in 96-well plates 24 hours before treatment. At zero and 72 hours, medium was discarded and Resazurin (Alfa Aesar) was added to the cells at 10 μM in 1X PBS and incubated for one hour in a humidified incubator at 37ºC with 5% CO_2. Fluorescence was then read according to manufacturer's instructions by using a Synergy HT (BioTek Instruments, Santa Clara, CA, USA) plate reader. The IC_{50} was calculated using GraphPad Prism 8.

3.2. MultiTox-Fluor Multiplex Cytotoxicity Assay (toxicity assay)

Cells were seeded in triplicate in 96-well plates 24 hours before treatment. At zero and 72 hours, assay was performed by incubating with MultiTox reagents (Promega, Madison, WI, USA) and fluorescence was then read according to manufacturer's instructions by using a Synergy HT plate reader.

3.3. Crystal violet (proliferation assay)

After Resazurin or MultiTox technique, the cells were rinsed once with 1X PBS and incubated for 30 minutes with crystal violet. The plates were rinsed carefully with tap water and dried for at least 24 hours. After dissolution in 1% SDS, the absorbance at 590 nm was read using a Synergy HT plate reader. The IC_{50} was calculated using GraphPad Prism 8.

4. RNA analyses

4.1. RNA extraction

Cell pellets were homogenized in TRIzol reagent (Invitrogen, Carlsbad, CA, USA) and RNA was extracted according to manufacturer's instructions and quantified using Nanodrop™ 2000 (ThermoFisher Scientific).

4.2. cDNA synthesis

1 µg of RNA was retrotranscribed into cDNA using Maxima H minus cDNA synthesis Master Mix with dsDNase kit for regular RTqPCR analysis (ThermoFisher Scientific) following manufacturer's instructions.

4.3. Real Time quantitative Polymerase Chain Reaction (RTqPCR)

RTqPCR was performed using PowerUp™ SYBR Green Master Mix (Applied Biosystems, ThermoFisher Scientific) according to manufacturer's instructions. The human primers used are listed below (**Table 1**). Human HPRT was used as endogenous housekeeping gene.

GENE	FORWARD PRIMER	REVERSE PRIMER
HPRT	TGACCTTGATTTATTTTGCATACC	CGAGCAAGACGTTCAGTCCT
PPARD	CTCTATCGTCAACAAGGACG	GTCTTCTTGATCCGCTGCAT
VIM	GACAATGCGTCTCTGGCACGTCTT	TCCTCCGCCTCCTGCAGGTTCTT
ZEB1	GATGATGAATGCGAGTCAGATGC	CTGGTCCTCTTCAGGTGCC
SLUG	GTGTTTGCAAGATCTGCGGC	TTCTCCCCCGTGTGAGTTCT
LOXL2	GGCACCGTGTTGCGATGACGA	GCTGCAAGGGTCGCCTCGTT
SNAIL	GCTCCTTCGTCCTTCTCCTC	TGACATCTGAGTGGGTCTGG
GAPDH	TCCTGTTCGACAGTCAGCCGC	ACGACCAAATCCGTTGACTCCG
ALK	CGAGCTGTTCAGTTGGTGGA	AGGAGCTATGACCAGTCCCG
MDK	GGTCCCGCGGGTTATACAG	CCGCCCTTCTTCACCTTATCTTT
PTN	CAGTCCAAAAATCCCGCCAA	AGCCTGCATTTTTGAGTTGGAA
KLF4	ACCCACACAGGTGAGAAACC	ATGTGTAAGGCGAGGTGGTC
OCT3/4	CTTGCTGCAGAAGTGGGTGGAGGAA	CTGCAGTGTGGGTTTCGGGCA
NANOG	AGAACTCTCCAACATCCTGAACCT	TGCCACCTCTTAGATTTCATTCTCT
SOX2	AGAACCCCAAGATGCACAAC	CGGGGCCGGTATTTATAATC
PD-L1	TGCAGGGCATTCCAGAAAGA	ACCGTGACAGTAAATGCGTTC

Table 1. List of primers used for the RTqPCR assays.

4.4. *MYC* and *PGC1A* reporter assay

293T cells were transfected with either an empty promoter, *c-MYC* promoter (HBM-luc, plasmid #16604; Addgene, Watertown, MA, USA) or *PGC1A* promoter, all coupled to luciferase expression, using Lipofectamine™ 2000 (Invitrogen) and Opti-MEM™ medium (Gibco). In parallel, two experimental conditions were set: *PPARD* OE and PPAR-δ activation. To do so, 293T cells were either transfected with the empty vector *TRIPZ* or *TRIPZ-PPARD* OE vector, or treated with 5 μM GW0742. After 12 hours, medium was changed and treatment with GW0742 was maintained. Likewise, doxycycline treatment was started at 2 μg/mL. Cells were harvested at different time points and lysed with RIPA buffer as per 5.1. subsection. *MYC* and *PGC1A* promoters' activity was then analyzed by using the Pierce™ Firefly Luciferase Glow Assay Kit (ThermoFisher Scientific) following the manufacturer's instructions. Luminescence was detected using the Synergy HT plate reader. Samples were normalized for total protein amount as per 5.2.

5. Protein analyses

5.1. Protein extraction

Cell pellets were lysed in RIPA buffer (Sigma-Aldrich) supplemented with protease and phosphatase inhibitors (both from Alfa Aesar, ThermoFisher Scientific) for 30 minutes ice-rocking. Cell lysates were then centrifuged at 12000 x *g* for 30 minutes and protein-containing supernatants were kept at -80ºC.

5.2. Protein quantification

After extraction, proteins were quantified using the Pierce™ BCA Protein Assay Kit (ThermoFisher Scientific) by reading the absorbance with the Synergy HT plate reader.

5.3. Protein separation and detection by Western Blot

Proteins were separated in Novex™ WedgeWell™ 10% Tris-Glycine precast gels using BenchMark™ pre-stained protein ladder (both from Invitrogen) and transferred into PVDF membranes (ThermoFisher Scientific). Membranes were blocked in 5% BSA-1X PBS-0.1% Tween 20 (ThermoFisher Scientific) for 1 hour at room temperature and incubated overnight at 4ºC with the following primary antibodies: PPAR-δ (1:1000), PGC1α (1:1000) (both from Santa Cruz), ALK (1:1000),

pALK (Tyr1604, 1:1000), ERK 1/2 (1:3000) (all from Cell Signaling Technology, Danvers, MA, USA), pERK 1/2 (T202-Y204, 1:3000, Abgent, San Diego, CA, USA), and vinculin (1:10000) or β-actin (clone AC-74, 1:10000) (both from Sigma-Aldrich) as loading controls. After several washes with 1X PBS-0.5% Tween 20, membranes were incubated with peroxidase-conjugated goat anti-rabbit (1:5000) or goat anti-mouse (1:50000) (both from Invitrogen). Pierce™ ECL Western Blotting Substrate was used to detect protein-antibody complexes prior to visualization on CL-X Posure™ films. Band intensities were analyzed using ImageJ software (https://imagej.nih.gov/ij/). Likewise, protein from sorted CD133 and autofluorescence cells extracted for the RTK array were separated, transferred and visualized as described for normal Western Blot.

5.4. PPAR-δ Transcription Factor Assay Kit

The specific binding of PPAR-δ to the PPAR response element was quantified following manufacturer's instructions. Briefly, nuclear extracts from different experimental conditions (MCM, Etomoxir, GW0742) were obtained and incubated on top of PPAR response element-coated in the assay 96-well plate overnight. After several washes, anti-PPAR-δ primary antibody was added following HRP-conjugated secondary antibody incubation. Afterwards, absorbance was detected using the Synergy HT plate reader.

5.5. Proteome Profiler™ Array

Cells were sorted by autofluorescence and CD133 expression using the SH800S Cell Sorter as described below (**section 6.2.**) and pellets were lysed according to manufacturer's instructions. The samples were further processed following the Human Phospho-Receptor Tyrosine Kinase Kit (R&D Systems Europe, Ltd., Abingdon OX14 3NB, UK) manufacturer's instructions. Pierce™ ECL Western Blotting Substrate was used to detect protein-antibody complexes prior to visualization on CL-X Posure™ films (both from ThermoFisher Scientific, Waltham, MA, USA). The resulting dots were analyzed using ImageJ software (National Institutes of Health, Bethesda, MD, USA).

5.6. Enzyme-Linked Immunosorbent Assay (ELISA)

MDK levels in supernatants from cell cultures and fresh tumor pieces, as well as plasma from mice bearing orthotopic tumors were determined using the MDK DuoSet ELISA kit (R&D systems, Minneapolis, MN, USA) as per manufacturer's

instructions. For MDK determination in tumor pieces, freshly extracted subcutaneous or orthotopic tumors were minced, and pieces of around 1 mm^3 were incubated for 24 hours in 1 mL of complete DMEM/F-12 GlutaMAX™ medium.

6. Flow Cytometry

6.1. Apoptosis

Cell pellets were rinsed once with 1X PBS and incubated on ice for 15 minutes in 2% FBS-0.5% BSA-1X PBS blocking solution. PE-conjugated CD133 antibody or the corresponding control immunoglobulin G1 were added at 1:400 in blocking solution. Cells were stained on ice for 30 minutes and protected from light. Then, the antibody or IgG1 excess was rinsed and pellets were resuspended in APC-conjugated Annexin V at 1:20 in Annexin V buffer solution plus Zombie Violet dye at 1:400 (all antibodies and probes are from Biolegend, San Diego, CA, USA). Samples were transferred into FACS tubes and incubated for 20 minutes at room temperature protected from light prior to their analysis by FACS Canto II (BD, Franklin Lakes, NJ, USA). Flowing 2 software (Turku Bioscience Centre, Turku, Finland) was used for data analysis.

6.2. Fluorescence Activated Cell Sorting (FACS)

Cells were blocked and stained for CD133 as described above (**section 6.1.**). For autofluorescence sorting, a previously described protocol was followed[56]. After staining, pellets were resuspended in Zombie Violet dye at 1:400 in 1X PBS and incubated for 20 minutes at room temperature protected from light. Viable cells corresponding to CD133 or autofluorescence negative and positive populations were sorted using the SH800S Cell Sorter (Sony Biotechnology, San José, CA, USA) and collected into 5 mL tubes containing complete RPMI medium. Pellets were stored at -80ºC for further processing.

7. *In vitro* functional assays for CSCs

7.1. Invasion assay

After 48 hours of treatment with PPAR-δ activators/inhibitors or ALK inhibitors, 10^5 cells were seeded in DMEM/F-12 GlutaMAX™ medium without supplements

on top of Matrigel-coated 24-well 0.8 µm PET membrane invasion chambers (Corning). After 12-24 hours, invasion towards a 20% FBS gradient was tested by staining invading cells with Diff Quick staining (PanReac AppliChem, Barcelona, Spain) following manufacturer's instructions and counting using an inverted microscopy (Nikon Eclipse TS100).

7.2. Sphere Formation Assay (SFA)

10^4 cells were seeded in triplicate in complete DMEM/F-12 GlutaMAX™ medium using polyhema-coated 24-well plates in the presence of different treatments. When indicated, cells were pre-treated in adherence for 48 hours in complete DMEM/F-12 GlutaMAX™ medium prior to being seeded without treatments in anchorage-independent conditions as described above (**section 1.3.**). In both cases, the spheroids were counted after seven days using an inverted microscope at 20X magnification.

7.3. Colony Formation Assay (CFA)

Cells were seeded in complete RPMI medium in 6-well plates at a density of 500 or 1000 cells/well. After 24 hours, treatments were added in complete DMEM/F-12 GlutaMAX™ medium. Medium and treatments were changed every seven days. After 21 days, colonies were stained with crystal violet dye (Acros Organics, ThermoFisher Scientific). Colonies were then counted manually, dissolved in 1% sodium dodecyl sulfate (SDS, ThermoFisher Scientific) and the absorbance at 590 nm was read using the plate reader Synergy HT.

7.4. Extreme Limiting Dilution Assay (*in vitro* ELDA)

10^3 cells per condition were mixed with DMEM/F-12 GlutaMAX™ medium plus treatments and serial dilutions were then seeded in sextuplicate in polyhema-coated 96-well plates. After seven days, the presence or absence of, at least, one spheroid was assessed using an inverted microscope. Further analysis was done by the Walter+Eliza Hall Bioinformatics online tool for ELDA analysis (http://bioinf.wehi.edu.au/software/elda/)[208].

7.5. Wound Healing Assay (WHA)

Cells were seeded in 6-well plates and cultured until obtaining a confluent monolayer when a mechanical cell-free gap was made by scratching the monolayer with a 200 µL pipette tip. Cells were then washed twice with 1X PBS to remove detached cells. Cells were treated with Crizotinib or Ensartinib in DMEM/F-12 GlutaMAX™ medium for up to 48 hours and pictures were taken every 12 hours using an inverted microscope at 10X magnification.

8. *In vivo* experiments

8.1. Experimental metastasis assay

PDX354 cells stably expressing either a doxycycline-inducible non-targeting shRNA (NT) or a shRNA against *PPARD* (sh#1 PAPRD) coupled to the expression of the green fluorescence protein (GFP) were pre-treated *in vitro* with 2 µg/mL doxycycline and/or 40 µM Etomoxir for 48 hours. Afterwards, GFP expression was checked by flow cytometry prior injection of 10^5 of these cells into the spleen of immunodeficient NOD SCID gamma (NSG) mice under isofluorane-induced anesthesia. Mice were then provided with doxycycline in the drinking water and treated intraperitoneally with 15 mg/kg of Etomoxir or vehicle for seven days. Next, splenectomies were performed and tumor growth was followed up by palpation. After nine weeks post intrasplenic surgeries, all mice were euthanatized and livers were processed to check GFP expression by RTqPCR.

8.2. Spontaneous metastasis assay

CTCA-GFP-luc or PDX265 were pre-treated *in vitro* with the PPAR-δ inducer GW0742 at 5 µM or antagonists GSK3787 or GSK0660 at 10 µM for 48 hours. Cells were then orthotopically injected in the pancreas of NSG mice under isofluorane-induced anesthesia. One week post-surgeries, intraperitoneal treatment with the drugs was started at 3 mg/kg/day and continued for up to nine weeks. Tumor growth was followed up by IVIS® or palpation twice a week. Then, mice were euthanized and both pancreas and livers were processed for RNA or histology.

8.3. Tumorigenicity assay (*in vivo* ELDA)

Cells were pre-treated *in vitro* for 48 hours. Two cell densities (10^4 and 10^3) diluted in 50:50 complete DMEM/F-12 GlutaMAX™ medium:Matrigel™ (Corning)

were subcutaneously injected into both the top and bottom flanks of six weeks-old Foxn1nu nude mice of both sexes (n=4 mice per group, n=8 injections per group) under isofluorane-induced anesthesia. Tumor size was monitored once a week using a caliper and volumes were calculated using the formula (length*width^2)/2. After six weeks, when control mice had reached humane endpoint criteria, mice were euthanized, tumors were collected and pictures were taken. The number of tumors at end point was analyzed using the Walter+Eliza Hall Bioinformatics online tool, considering tumors >50 mm^3 that were growing for 3 weeks in a row, the rest were excluded from the analysis. Tumors corresponding to the injections with 10^4 cells from PDX354 were dissociated and stained with EpCAM-FITC, CD133-PE and CD44-APC antibodies for FACS analysis as described above (**section 6.2.**).

8.4. *In vivo* treatment assay

Tumor pieces of about 15 mm^3 were soaked in Matrigel™ prior subcutaneous implantation in both flanks of six weeks-old Foxn1nu nude female mice (n=4 mice per group, n=8 implants per group) under isofluorane-induced anesthesia. When tumor size was about 300 mm^3, mice were treated with one cycle of chemotherapy as follows: 30 mg/kg Abraxane (i.v.) twice a week plus 70 mg/kg Gemcitabine (i.p.) once a week during three weeks and one week of rest. After the chemotherapy cycle, mice were randomized and treated with 25 mg/kg Crizotinib or the corresponding dose of vehicle (hydroxypropyl methyl cellulose, Sigma Aldrich) (oral gavage) twice a day until endpoint. Tumor size was monitored twice a week using a caliper and volumes were calculated using the formula (length*width^2)/2. After 10.5 weeks, when control tumors had reached humane endpoint criteria, mice were euthanized, tumors were collected and weighted and pictures were taken. A small piece of the tumors was processed for RNA to assess pluripotency gene expression by RTqPCR as described above (**section 4**). The rest of the tumors was dissociated as previously reported[207] and stained with EpCAM-FITC, CD133-PE and CD44-APC antibodies for FACS analysis as described above (**section 6.2.**).

9. Bioinformatic analyses

9.1. GEPIA2 webserver

Expression data from human PDAC tissue and normal pancreatic tissue were analyzed using the webserver GEPIA2 (TCGA and the GTEx project databases; http://gepia2.cancer-pku.cn/)[209]. The Pearson correlation coefficient was calculated to study the association of the individual genes corresponding to *ALK* or ALK ligands with 1) a stemness signature defined by the combined expression of the pluripotency-related genes *KLF4*, *OCT3/4*, *NANOG* and *SOX2*; or 2) a EMT signature defined by the combined expression of the EMT-related genes *ZEB1*, *SLUG*, *SNAIL* and *LOXL2*. Likewise, *ALK* overexpression (OE) signature previously described in Mazzeschi *et al*.[210] was used to analyzed its association with ALK ligands expression. The correlation between *PD-L1* and a TAMs infiltration signature previously described in PDAC by Xia *et al*.[211] with *ALK*, *ALK* OE signature, *MDK* and *PTN* was also analyzed.

9.2. cBioPortal Webserver

ALK mutational status was assessed using the webserver cBioPortal (Pancreas UTSW, Pancreas TCGA PanCan 2018, Pancreas TCGA, Pancreas ICGC and Pancreas QCMG 2016 project datasets; https://www.cbioportal.org)[212].

9.3. Gene Set Enrichment Analysis (GSEA)

PDX354 cells untreated or treated with Etomoxir were compared in GSEA for the Hallmark glycolysis. PDAC samples of the TCGA dataset classified into high and low *ALK* expression were compared in GSEA for a stemness signature previously described in Ai *et al*.[213]. The GSEA module of the GenePattern suite from the Broad Institute was used with 1000 permutations and FDR < 25% was considered statistically significant.

10. Statistical Analyses

Data are represented as mean ± SEM of, at least, three independent experiments unless otherwise specified. Data were analyzed using GraphPad Prism 8. Student's t-test or Mann-Whitney test were performed for two-group comparisons, while one-way ANalysis Of VAriance (ANOVA) or Kruskal-Wallis tests

were performed for multiple group comparisons, depending on the results of the Shapiro-Wilk normality test, with post hoc Bonferroni's or Dunn's tests, respectively. Differences were considered significant when $p < 0.05$.

11. Other experimental procedures

The bellow-listed experimental procedures were externally performed in collaboration with other facilities or laboratories according to their own protocols.

PROCEDURE	FIGURE	FACILITY OR LABORATORY
Bulk RNAseq	Figure I.7	Christopher Heeschen's lab Shanghai Jiao Tong University School of Medicine, China
IHC	Figure I.8C and D	CIBA (Center of Biomedical Research from Aragon), technical scientific services CNIO (Spanish National Cancer Research Center), technical scientific services
scRNAseq	Figure II.11	Álvaro Curiel (Kenneth P. Olive's lab) Columbia University Irving Medical Center, New York, USA

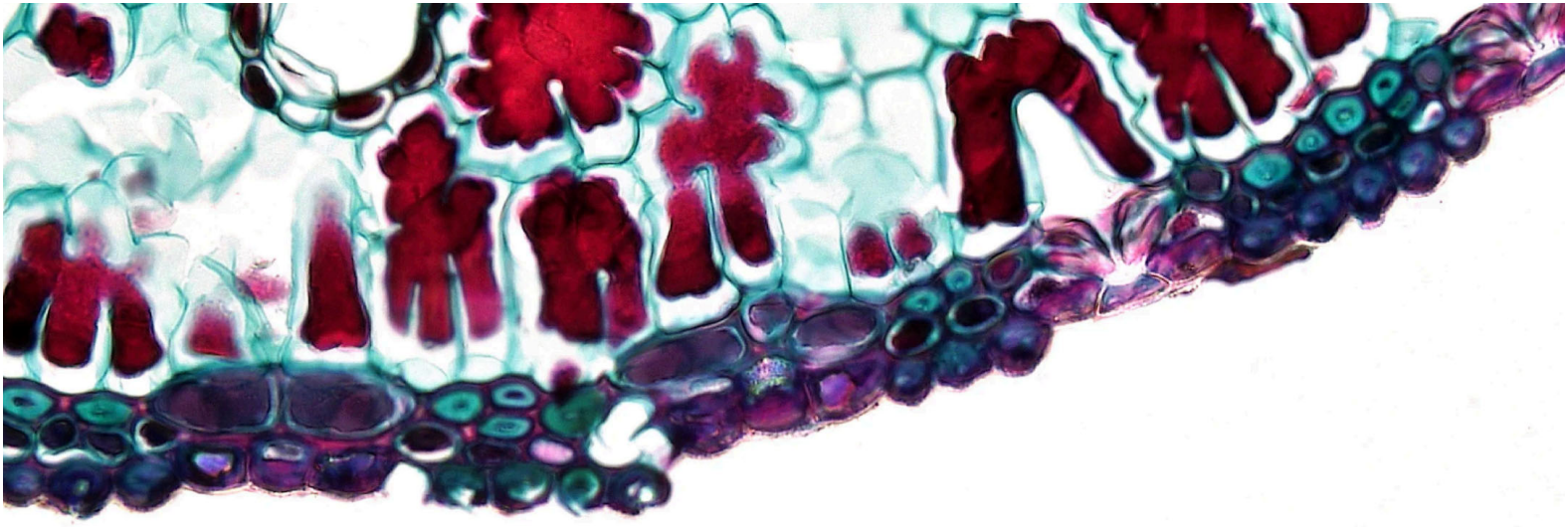

RESULTS: CHAPTER I

1. Background: a common transcriptional program linked to *PPARD* controls EMT induced by metabolic stress and microenvironmental cues in PDAC

The previously described PaCSCs dependency on mitochondrial oxygen phosphorylation (OXPHOS) concomitant to reduced metabolic plasticity render this highly tumorigenic subpopulation very sensitive to mitochondrial inhibition. This scenario opened a new therapeutic window against the subpopulations responsible for chemotherapy failure and tumor relapse. For instance, the antidiabetic drug Metformin, which inhibits the mitochondrial electron transport chain (ETC) complex I (NADH dehydrogenase), has been reported to have antitumoral effects by preferentially targeting PaCSCs[61]. However, further data from our group described certain metabolic plasticity featured by a small portion of PaCSCs with reduced mitochondrial content and increased levels of MYC/PGC1α balance. In consequence, this intermediate PaCSCs population displayed resistance to Metformin[62]. This scenario led the group to interrogate whether this metabolic heterogeneity could be translated into functional heterogeneity. Therefore, the Metformin-resistant cells were characterized by means of morphology and gene expression patterns. Surprisingly, metformin-resistant clones acquired an elongated, mesenchymal-like morphology (**Figure I.1A**) and showed increased expression of the epithelial-to-mesenchymal transition (EMT) genes *ZEB1* and *VIM* (**Figure I.1B**).

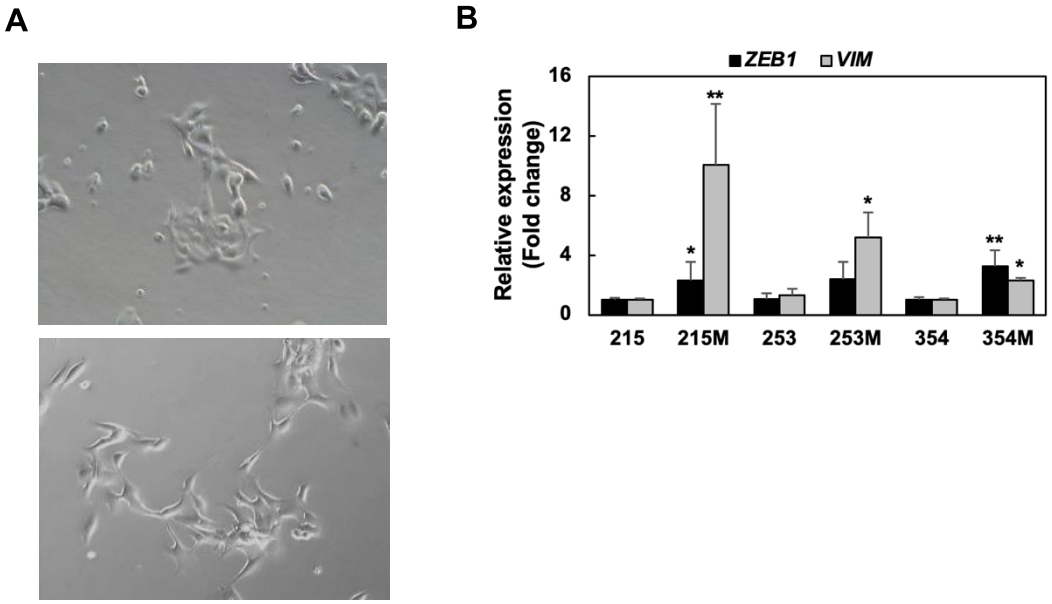

Figure I.1. A) Representative images of parental (top) PDX215 and its Metformin-resistant counterpart (bottom). **B)** RTqPCR for the EMT genes *ZEB1* and *VIM* mRNA levels in different Metformin-resistant PDXs compared to their parental counterparts. M: Metformin-resistant. Data are shown as the fold change to parental cells, depicted as mean ± SEM and analyzed using Mann-Whitney test. * $p<0.05$, ** $p<0.01$.

Metformin causes an energy drop in the cells by inhibiting the ETC complex I, thereby inducing energy crisis[214]. Considering this, in order to discard Metformin off-target effects and confirm that, indeed, EMT-like morphological and gene expression changes are a consequence of metabolic stress, different approaches were pursued. On the one hand, the cells were treated with a panel of partial mitochondrial inhibitors, such as Etomoxir (CPT1a inhibitor), Malonate (complex II inhibitor) and UK5099 (pyruvate carrier inhibitor). On the other hand, the cells were exposed to tumor-like conditions (hypoxia, low pH and low glucose) mimicking the scarcity of the tumor microenvironment (TME). Finally, the cells were incubated with macrophage conditioned medium (MCM) that has been previously described to boost CSC-related properties[99]. These distinct scenarios uncovered the same phenotypic modifications: an elongated morphology (**Figure I.2A**) and enhanced expression of several EMT-related genes (**Figure I.2B**).

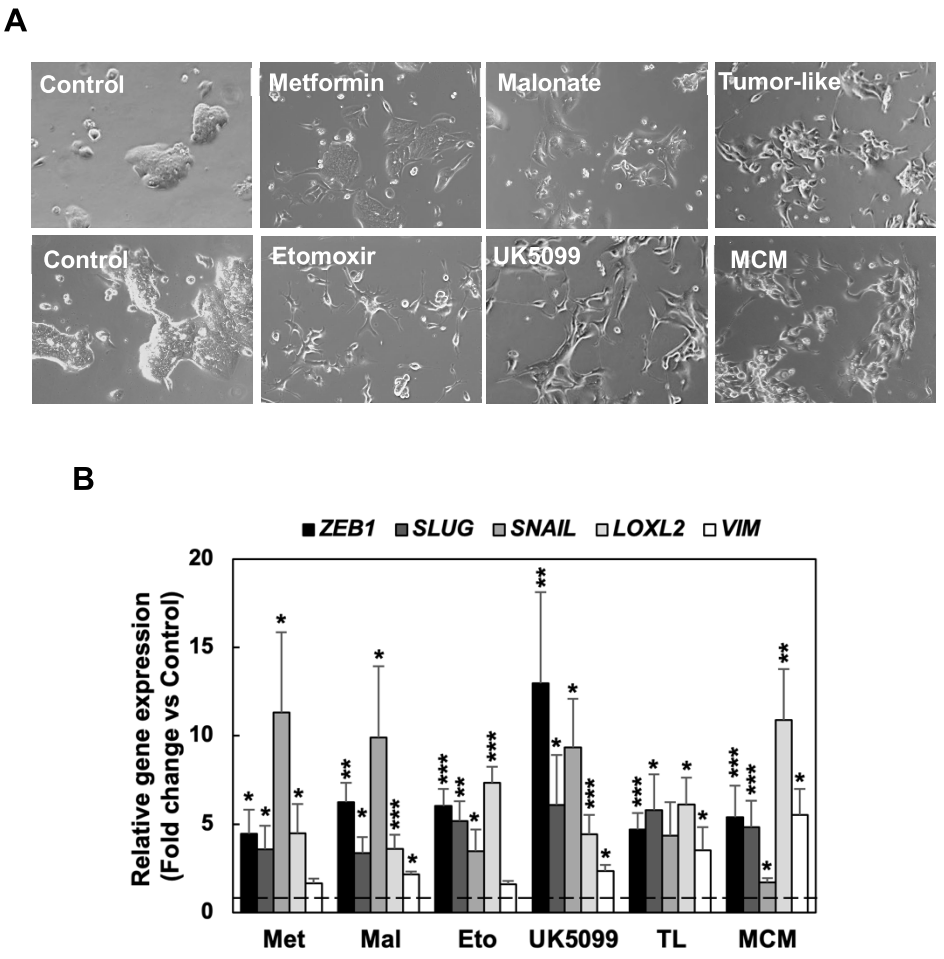

Figure I.2. A) Representative images illustrating morphological changes in PDX354 after 72 hours of treatment with different mitochondrial inhibitors (3 mM Metformin, 5 mM Malonate, 20 µM Etomoxir, 100 µM UK5099), tumor-like conditions (hypoxia (3% O_2), low pH (50 µM HCl) and low glucose (1 mM)) or macrophage-conditioned medium (MCM). **B)** RTqPCR for the EMT genes *ZEB1*, *SLUG*, *SNAIL*, *LOXL2* and *VIM* mRNA levels after treatment as in A (pooled data from PDX185, 215, 253, 354 and A6L). TL: tumor-like conditions. The dashed line represents the value of the control cells. Data are shown as the fold change to control condition, which is represented as the dashed line, depicted as mean ± SEM and analyzed using Mann-Whitney test. * p<0.05, ** p<0.01, *** p<0.005.

These results suggested that the metabolic stress suffered by partial mitochondrial blockade or a starvation situation, as well as microenvironmental cues derived from tumor-associated macrophages (TAMs) are able to exhibit features reminiscent to the EMT program, thereby favoring the acquisition of a more aggressive phenotype. Therefore, in order to find a common metabolic program controlling invasiveness in PDAC, we selected the long chain fatty acid transporter (CPT1a) inhibitor Etomoxir and MCM for further experiments.

A carbohydrate-based PCR array performed on PDX354 revealed common differential expression of several metabolic genes, including the glycolysis-related *MYC*[215] (upregulated) and the OXPHOS-related peroxisome proliferator-activated receptor gamma coactivator 1-alpha[81] (*PPARGC1A* or *PGC1A*, downregulated), in both Etomoxir and MCM conditions (**Figure I.3**). Another gene consistently upregulated in Etomoxir and MCM samples was the peroxisome proliferator-activated receptor delta (*PPARD*, **Figure I.3**).

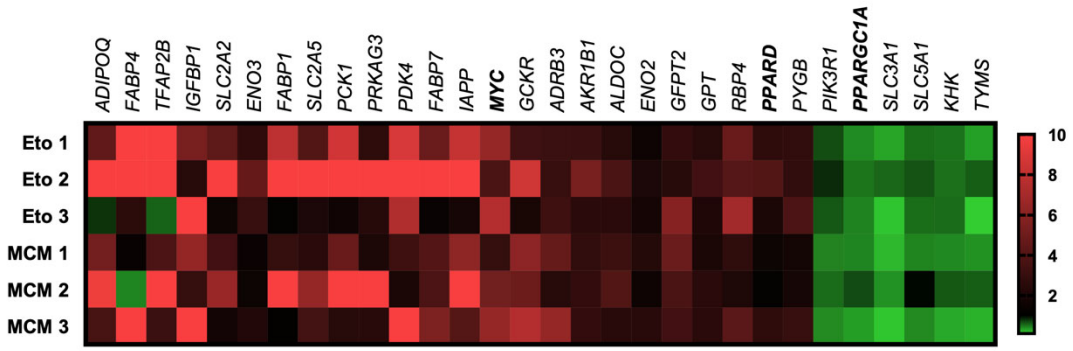

Figure I.3. Carbohydrate PCR array after 48 hours of treatment with 20 μM Etomoxir or MCM in PDX354 (n=3 for each condition).

These results were further validated in collaboration with Christopher Heeschen's lab (Center for single-cell omics and key laboratory of oncogenes and related genes (Shanghai Jia Tong University School of Medicine, China)) by single cell transcriptomic analyses (scRNAseq, **Figure I.4A**) performed on different PDAC circulating tumor cells (CTCs) isolated from patients' blood, which account for a more aggressive phenotype. Both Etomoxir and MCM conditions clustered separately from control condition. Further re-clusterization grouped basically the same way for both treatment approaches, which, in turn, resulted significantly enriched in the Hallmark EMT when compared to control clusters. These results resulted especially relevant since *PPARD* increased expression was mostly confined to cells displaying the highest expression of the Hallmark EMT. (**Figure I.4B**).

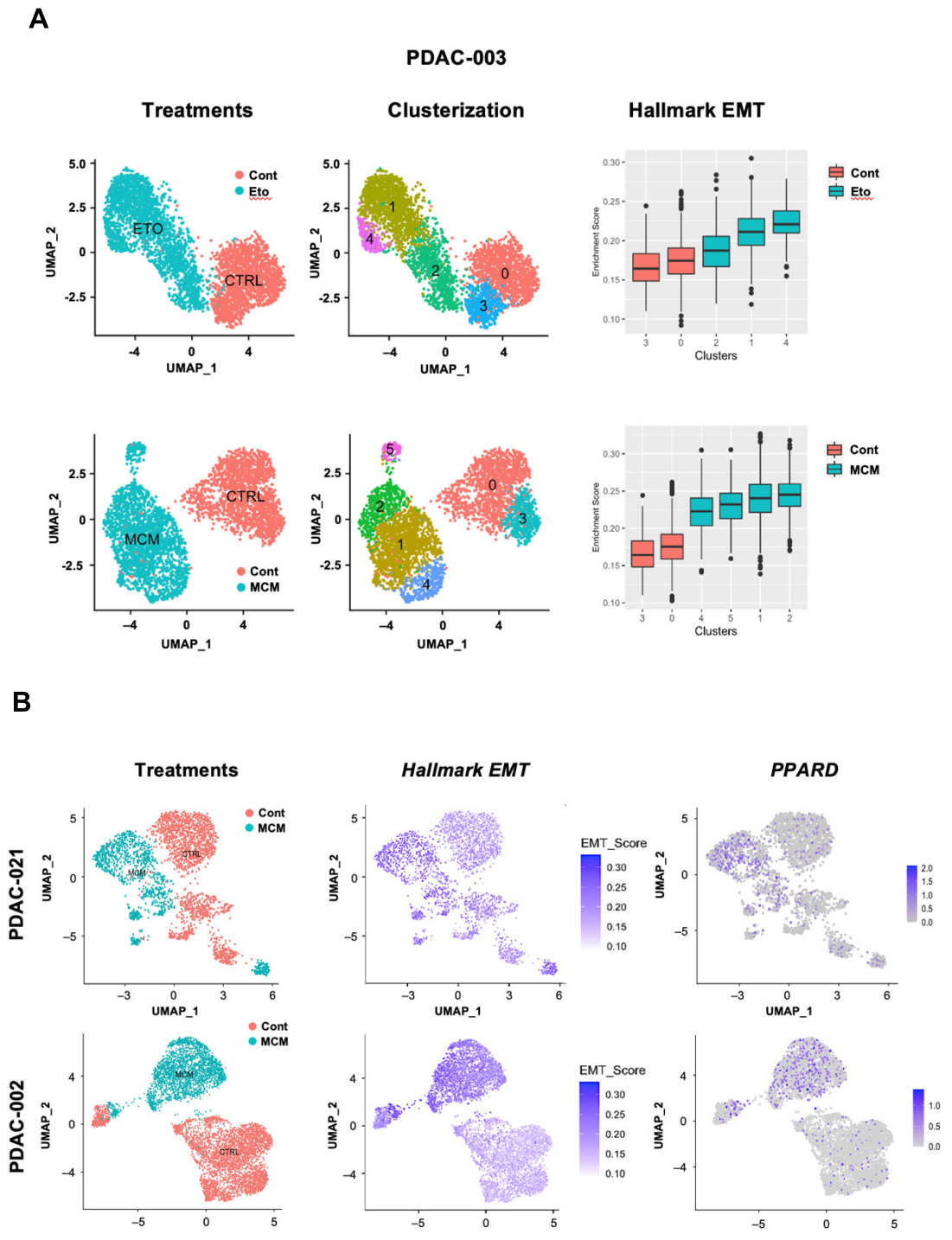

Figure I.4. Single cell transcriptomic analyses of PDAC002, 003 and 021 treated with 20 µM Etomoxir or MCM for 48 hours. Data are represented as UMAP (uniform manifold approximation and projection) plots and showing the different clusters by a color code for Etomoxir (Eto) and MCM conditions and analyzed using Mann-Whitney test (p-value < $2.2e^{-16}$). **A)** Expression of the signature Hallmark EMT in the different clusters from PDAC-003 incubated with 20 µM Etomoxir or MCM for 48 hours. **B)** Simultaneous expression of the signature Hallmark EMT and *PPARD* in MCM-incubated PDAC-002 and 021 cells.

PPAR-δ is a member of the PPAR nuclear hormone receptors that modulates energy homeostasis by controlling the expression of numerous genes implicated in lipid and glucose metabolism[124,127]. Importantly, *PPARD* expression resulted significantly upregulated in human PDAC samples when compared to normal pancreatic tissue from The Cancer Genome Atlas (TCGA, normal and tumoral) and Genotype-Tissue Expression (GTEx, tumoral) datasets (**Figure I.5A**) and predicted disease-free survival (**Figure I.5B**).

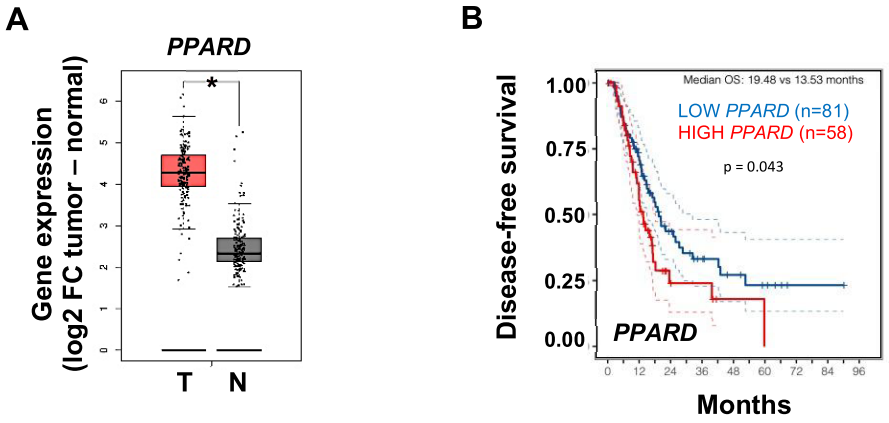

Figure I.5. A) Transcriptomic bioinformatic analyses of *PPARD* comparing normal (N) and PDAC (T) human tissues from TCGA and GTEx datasets. **B)** Kaplan Meier survival curves of disease-free survival form *PPARD*^{HIGH} and *PPARD*^{LOW} PDAC patients.

Further bioinformatic analyses revealed that *PPARD* expression correlated with the expression of an EMT gene signature comprised of *ZEB1*, *SNAIL* and *SLUG* (**Figure I.6A**). Additionally, gene set enrichment analyses (GSEA) in *PPARD*^{HIGH} *versus PPARD*^{LOW} patients revealed a significant enrichment of the Hallmark gene set collection EMT (**Figure I.6B, left panel**), whereas OXPHOS pathway resulted significantly downregulated (**Figure I.6B, right panel**), as we could suspect from the reduced *PGC1A* expression from the carbohydrate PCR array previously performed (**Figure I.3**).

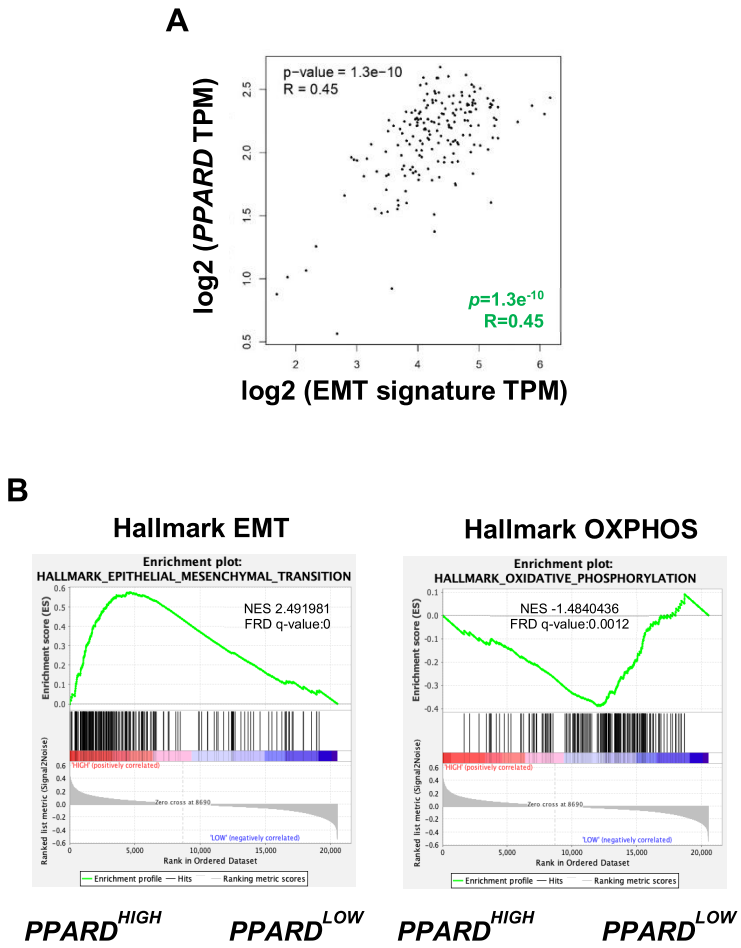

Figure I.6. A) Correlation expression of *PPARD* with an EMT signature composed by *ZEB1*, *SNAIL* and *SLUG* in human tissues from TCGA and GTEx datasets. TPM: transcripts per million. **B)** Gene set enrichment analysis comparing the top 50% *PPARD* expression group (*PPARD*^{HIGH}) with the bottom 50% *PPARD* expression group (*PPARD*^{LOW}) in the TCGA data series. NES (normalized enrichment score) values of the Hallmark gene set EMT (**left panel**) and OXPHOS (**right panel**) meeting the significance criteria: nominal *p*-value of <0.05, FDR <25%.

Taken together, these previous data from the group indicate that PDAC aggressiveness may be modulated by different means resulting in the initiation of the EMT program. Such factors are partial inhibition of the mitochondria and microenvironmental signals derived from TAMs, and both converged in increased *PPARD*, *MYC* and EMT-related genes expression irrespective of the distinct mechanism of action.

Therefore, we hypothesized that PPAR-δ orchestrates the metastatic potential in PDAC in response to metabolic stress and microenvironmental cues by modulating the balance between MYC and PGC1α. Considering this hypothesis and in order to evaluate it, we proposed the following objectives:

1. To assess the functional effects of PPAR-δ activation upon mitochondrial inhibition or environmental signals.
2. To evaluate the potential PPAR-δ downstream effectors through which it orchestrates the invasive phenotype in PDAC.
3. To appraise, *in vitro* and *in vivo*, the consequences of PPAR-δ inhibition on PDAC metastatic potential.

2. PPAR-δ mediates the functional changes associated with invasiveness and metastasis in PDAC

Consistent to the scRNAseq performed in the CTCs-derived primary cultures, we were able to reproduce these results in bulk RNAseq from PDX354. Indeed, the analyses performed in collaboration with Christopher Heeschen's group showed that both treatments grouped in the same gene expression pattern, while control samples displayed quite the opposite result (**Figure I.7A**). Although, no changes in *PPARD*, *MYC* or *PGC1A* individually were found, GSEA analyses revealed enrichment in the glycolytic pathway (**Figure I.7B**). These results confirmed that both partial inhibition of the mitochondria with Etomoxir or secreted factors from TAMs induce a common transcriptional program based on increased glycolysis, as expected by the *MYC* upregulation previously found in the PCR array (**Figure I.3**).

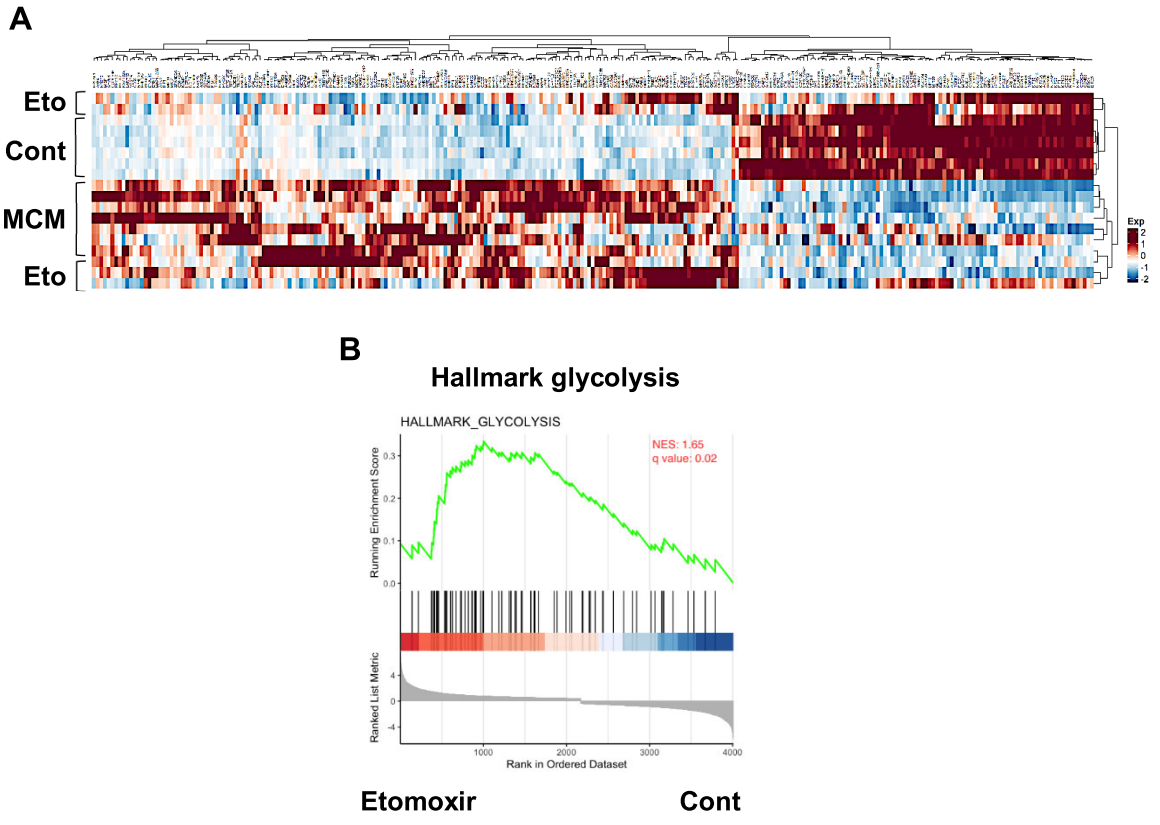

Figure I.7. A) Bulk RNAseq of PDX354 treated with 20 μM Etomoxir or MCM for 48 hours. **B)** GSEA of the Hallmark glycolysis in Etomoxir-treated PDX354 from A. Note that the *in vitro* part of these experiments was done by us while the RNAseq and further analyses were performed in Christopher Heeschen's lab.

Next, we sought to validate the previous RNAseq results by analyzing *PPARD* expression at the mRNA level (**Figure I.8A**). While morphological changes began to be noticeable after 48 hours of treatment, both Etomoxir and MCM increased *PPARD* gene expression at 24 hours, suggesting that the cascade of events starts by PPAR-δ activity. These transcriptional changes in *PPARD* were translated into increased PPAR-δ protein levels (**Figure I.8B**) and activation by direct binding to the PPAR response element (PPRE, **Figure I.8C**). Interestingly, both strategies substantially increased *PPARD*/PPAR-δ gene and protein expression, as well as activity, to levels comparable to the PPAR-δ chemical agonist GW0742 (**Figure I.8A-C**).

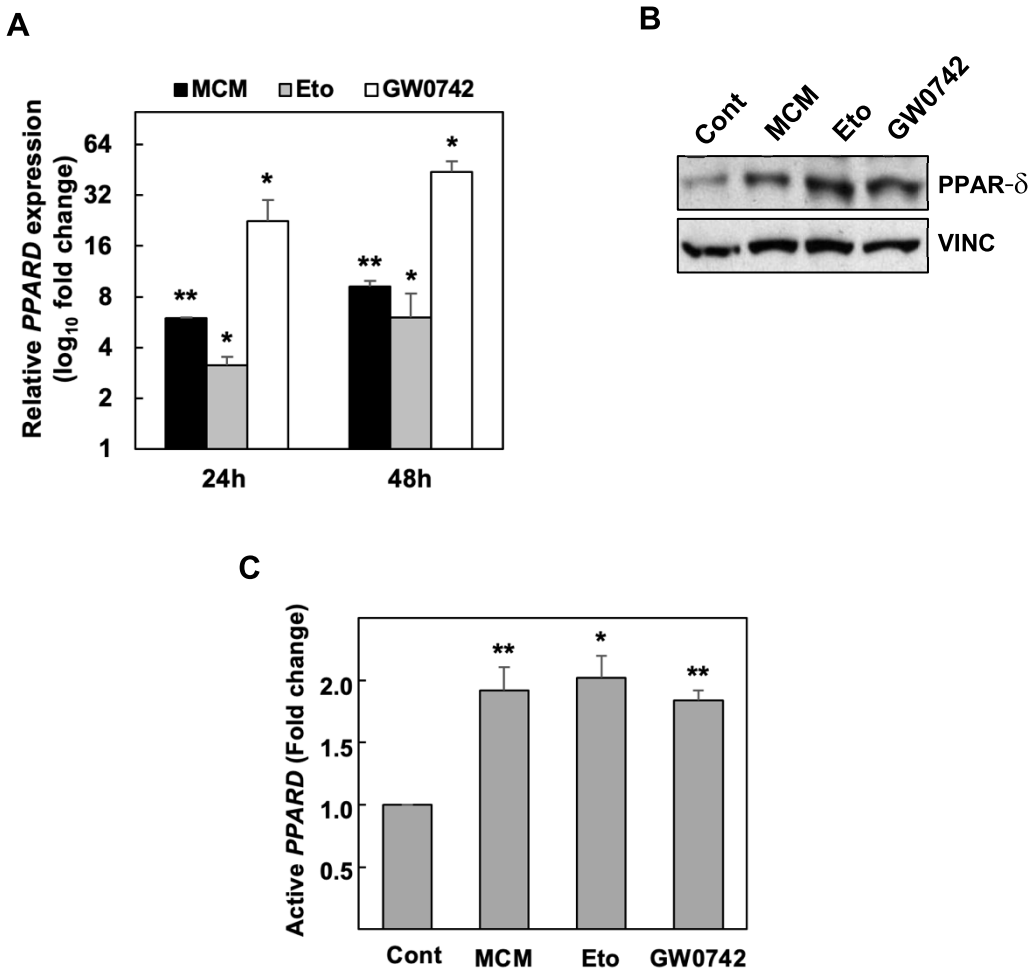

Figure I.8. A) RTqPCR for *PPARD* mRNA levels after 24 and 48 hours of incubation with 20 μM Etomoxir, MCM or 5 μM GW0742 (pooled data from PDX185, 215, 253, 354 and A6L). **B)** Western blot of cell lysates from PDX354 after treatment as in A. Vinculin was used as loading control. **C)** PPAR-δ activity measured as binding to the PPAR response element after incubation with 20 μM Etomoxir, MCM or 5 μM GW0742 for 24 hours in PDX354. In A and C, data are shown as the fold change to control condition, which is represented as the dashed line, depicted as mean ± SEM and analyzed using One-way ANOVA or Kruskal-Wallis test. * $p<0.05$, ** $p<0.01$.

Functionally, the induction of PPAR-δ, either with Etomoxir or MCM, or by its direct activation with the agonists L-165041 (L-165) and GW0742 (GW42), rendered the cells with enhanced invasiveness *in vitro* (**Figure I.9A and I.9B**).

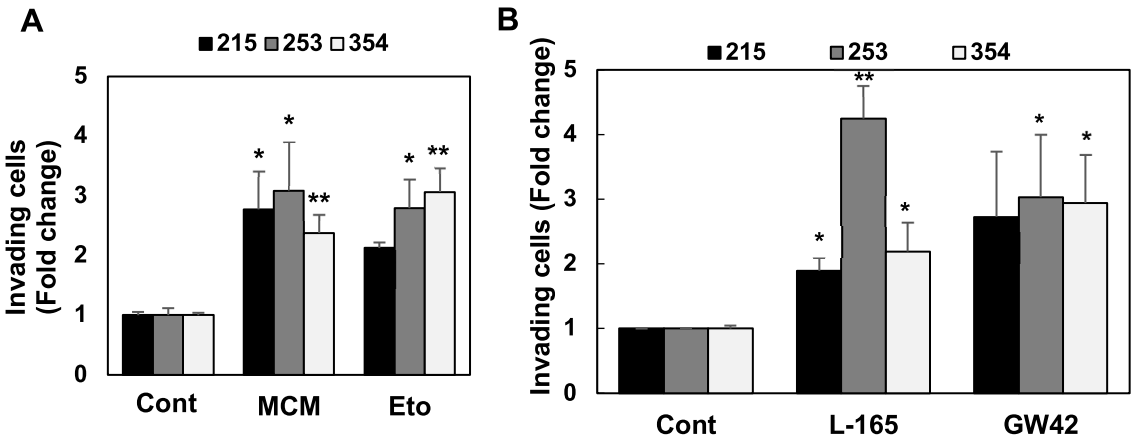

Figure I.9. A) Invasion assay with cells pre-treated with MCM or 20 μM Etomoxir for 48 hours. Cells were seeded in Boyden chambers and, after 16 hours, Diff Quick staining was performed and invading cells were counted. **B)** Invasion assay as in A with cells pre-treated with 5 μM L-165041 (L-165) or GW0742 (GW42) for 48 hours. Data are shown as the fold change to control condition, depicted as mean ± SEM and analyzed using One-way ANOVA or Kruskal-Wallis test. * $p<0.05$, ** $p<0.01$.

The increased *in vitro* invasiveness was confirmed in an *in vivo* experimental metastasis assay by intrasplenic injection of PDX354 stably expressing either a non-targeting shRNA (NT) or a shRNA against *PPARD* (sh#1 *PPARD*) coupled to the expression of the green fluorescence protein (GFP). The cells were pre-treated *in vitro* with doxycycline and/or Etomoxir for 48 hours prior being injected into the spleen of immunodeficient NOD SCID gamma (NSG) mice. Mice were then provided with doxycycline in the drinking water and treated intraperitoneally with Etomoxir for seven days when splenectomies were performed. After nine weeks post surgeries, all mice were euthanized and livers were processed to check GFP expression by RTqPCR (**Figure I.10**).

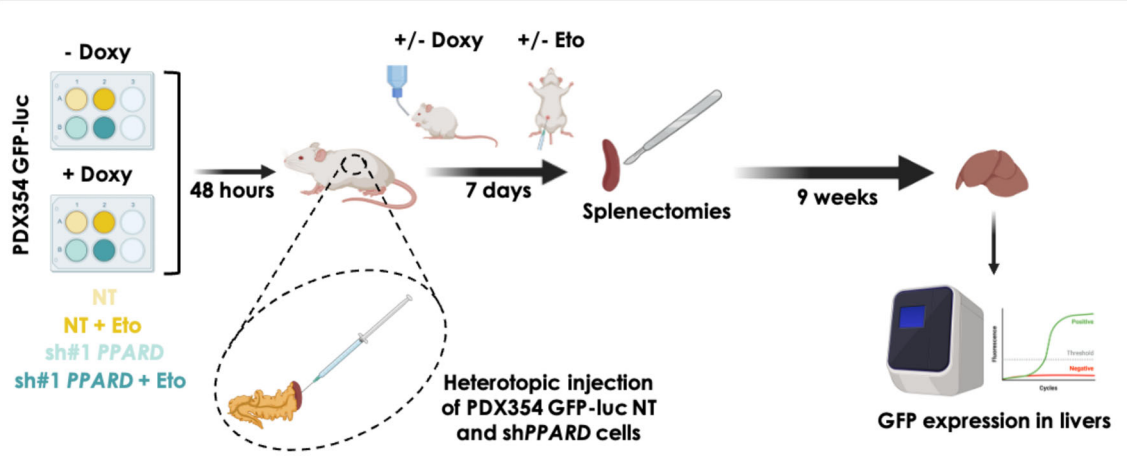

Figure I.10. Schematic overview of the experimental metastasis assay. PDX354 GFP-luc cells transduced with doxycycline-inducible lentiviral vectors stably expressing a non-targeting shRNA (NT) or a shRNA against *PPARD* (sh#1 *PPARD*) were pre-treated *in vitro* with or without 20 µM Etomoxir for 48 hours. Then, cells were heterotopically injected in the spleen of NOD SCID gamma (NSG) immunodeficient mice and, after 7 days, splenectomies were performed. Mice were treated with oral doxycycline (2 mg/mL, drinking water) and/or Etomoxir (15 mg/kg, i.p., daily) post-surgeries and pre-splenectomies. After 9 weeks, all mice were euthanized, livers were collected and GFP expression was analyzed in liver homogenates by RTqPCR.

Livers from Etomoxir-treated mice in which we injected the non-targeting shRNA cells (NT + eto group) showed the highest levels of GFP expression. In contrast, the ones also treated with Etomoxir but in which we injected the sh*PPARD* cells (sh#1 *PPARD* + Eto group) exhibited less GFP signal. Strikingly, livers from vehicle-treated mice in which we injected the sh*PPARD* cells (sh#1 *PPARD* - Eto group) had no GFP expression at all (**Figure I.11A**). Finally, we calculated the percentage of mice with micrometastases (**Figure I.11B**), which reflects the results obtained in Figure I.11A and indicates that PPAR-δ presence is necessary for the metastatic dissemination of PDAC cells.

A

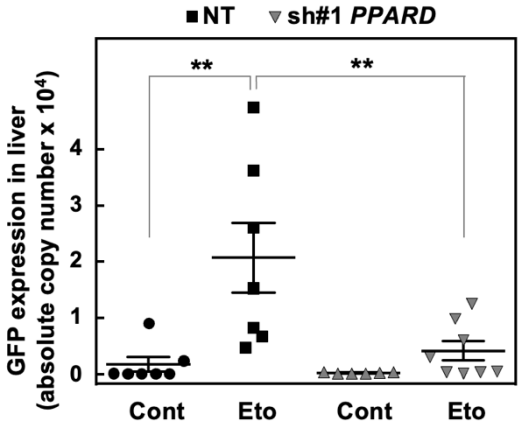

B

Mice w/ micromet	NT	sh#1 *PPARD*
Control	28% (2/7)	0% (0/6)
Etomoxir	100%(7/7)	50% (4/8)

Figure I.11. Experimental metastasis assay of PDX354 GFP-luc cells transduced with doxycycline-inducible lentiviral vectors stably expressing a non-transient shRNA (NT) or a shRNA against *PPARD* (sh#1 *PPARD*). **A)** RTqPCR for GFP in liver homogenates at end point (week nine). **B)** Percentage of micrometastases per group calculated as the number of GFP$^+$ livers divided by the total number of mice per each group and multiplied by 100. Data are shown as the individual absolute *GFP* copy number per mice, depicted as mean ± SEM and analyzed using One-way ANOVA or Kruskal-Wallis test. ** $p<0.01$.

Together, these data demonstrate that the metabolic regulator PPAR-δ is responsible for functional changes concomitant with EMT induction, thereby strongly suggesting an essential role for PPAR-δ in the process of cancer cell invasiveness and metastasis.

3. PPAR-δ modulates the *MYC/PGC1A* balance to promote the invasive phenotype in PDAC

Previous studies from the lab indicated that MYC plays a fundamental role in controlling the metabolic and pluripotent profile of PaCSCs by negatively modulating *PGC1A* expression, a key factor that regulates mitochondrial biogenesis[62]. Notably, we confirmed the PCR array results of increased MYC and reduced PGC1α after MCM and Etomoxir treatment at the protein level (**Figure I.12**). These results are in line with our GSEA analyses that showed a decreased OXPHOS in *PPARD*^{HIGH} patients and increased glycolysis after EMT induction (**Figure I.6B, right panel and I.7B, respectively**), since PGC1α is implicated in mitochondrial metabolism[81], while MYC promotes the expression of several glycolytic genes[215].

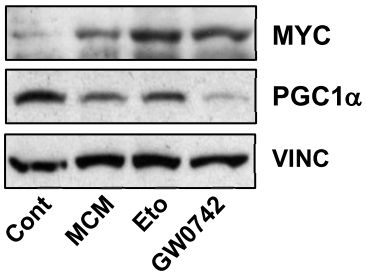

Figure I.12. Western blot of cell lysates from PDX354 after incubation with MCM or treatment with 20 μM Etomoxir or 5 μM GW0742 for 48 hours. Vinculin was used as loading control.

Importantly, the enhanced invasive capability of EMT-induced cells by MCM or Etomoxir was reversed by MYC inhibition (**Figure I.13A**) accompanied by downregulation of the EMT-related genes *VIM* and *ZEB1* (**Figure I.13B**).

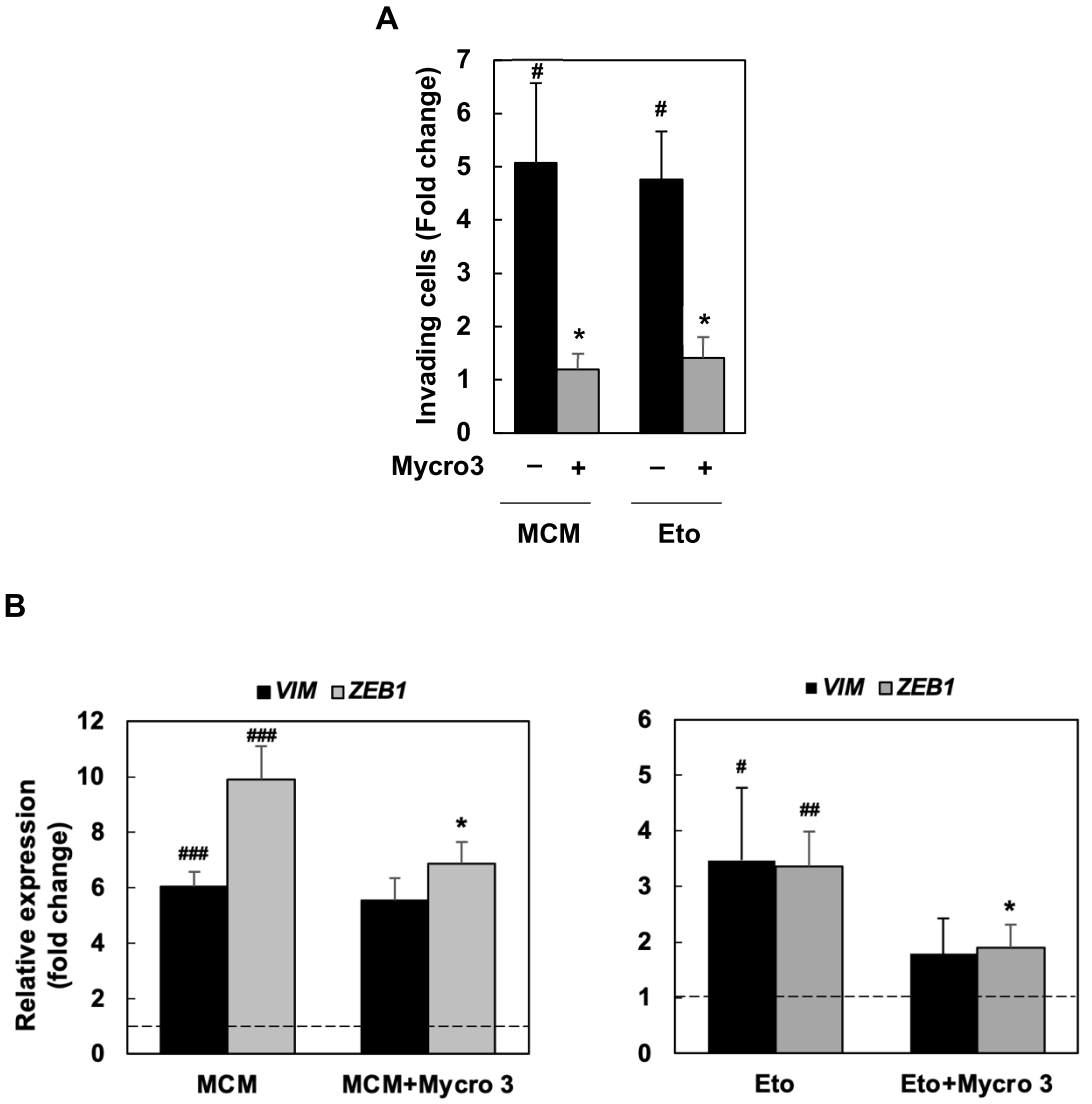

Figure I.13. A) Invasion assay with PDX354 cells pre-treated with MCM or 20 µM Etomoxir for 48 hours in the presence or absence of the MYC/MAX interaction inhibitor Mycro3 (25 µM). Cells were seeded in Boyden chambers and, after 16 hours, Diff Quick staining was performed and invading cells were counted. **B)** RTqPCR for *VIM* and *ZEB1* EMT-related genes mRNA levels after 48 hours of treatment of PDX354 as in A (**left panel:** MCM +/- Mycro3; **right panel:** Etomoxir +/- Mycro3). Data are shown as the fold change to control condition which is represented as the dashed line, depicted as mean ± SEM and analyzed using Students t test. # p<0.05, ## p<0.01, ### <0.005 *versus* control; * p<0.05 *versus* MCM or Etomoxir alone.

Considering the above and the notion that MYC regulates the invasive phenotype in many malignancies[105,106] while it has a crucial role in modulating the metabolic phenotype in PDAC[62], our results suggest a link between PPAR-δ and MYC/PGC1α for two main reasons. On the one hand, at the molecular level, Etomoxir treatment exhibited increased *PPARD* expression (**Figure I.3**), as well as a glycolytic enrichment (**Figure I.7B**), while *PPARD*^{HIGH} patients showed a

decreased in OXPHOS metabolism (**Figure I.6B, right panel**). On the other hand, at the functional level, PPAR-δ-mediated invasiveness and metastasis together with the notion that MYC promotes metastatic spread by directly inducing EMT-related gene expression or indirectly by cooperating with other genes[216,217]. Therefore, in order to elucidate whether and how this regulation is taking place, we performed a *MYC* and *PGC1A* reporter assay on PDAC cells overexpressing *PPARD* (*PPARD* OE) or treated with a PPAR-δ chemical agonist. Importantly, *PPARD* OE or PPAR-δ activation by GW0742 consistently induced *MYC* promoter activity and subsequently reduced *PGC1A* promoter activity (**Figure I.14**). These differences were significantly appreciated from 12 hours onwards in *PPARD* OE, while with PPARD activation the full response took place at 24 hours.

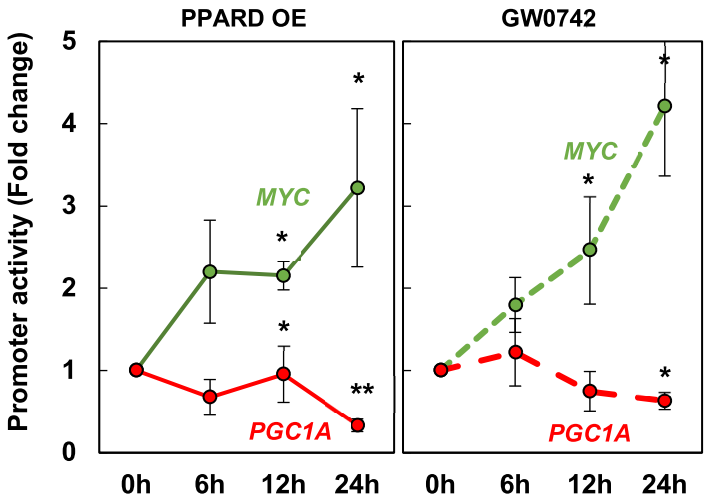

Figure I.14. *MYC* and *PGC1A* reporter assay. Promoter activity was estimated as luciferase bioluminescence at the indicated time points following *PPARD* overexpression (*PPARD* OE, **left panel**) or treatment with 5 μM GW0742 (**right panel**). Data are shown as the fold change to 0 hours, depicted as mean ± SEM and analyzed using Students t test. * $p<0.05$, ** $p<0.01$.

Collectively, these results further reinforce the potential link between the MYC/PGC1α balance and the subsequent induction of invasion/metastasis through PPAR-δ.

4. Therapeutic targeting of PPAR-δ abrogates the invasive and metastatic ability *in vitro* and *in vivo*, respectively

Therapeutic targeting of the oncoprotein MYC has proven to pose real challenge to the extent of being considered a "yet to be drugged" target[218]. For that reason, and considering our previous results demonstrating MYC direct regulation by PPAR-δ and that PPAR-δ mediates invasiveness through MYC, we decided to use either PPAR-δ antagonists or inverse agonists to block invasion and metastasis. First of all, PPAR-δ blockade with either GSK0660 or GSK3787 (antagonists) and DG172 (inverse agonist) decreased the number of invading cells induced by MCM or Etomoxir in our PDXs (**Figure I.15A**) or the basal invasiveness of the metastatic cells (**Figure I.15B**).

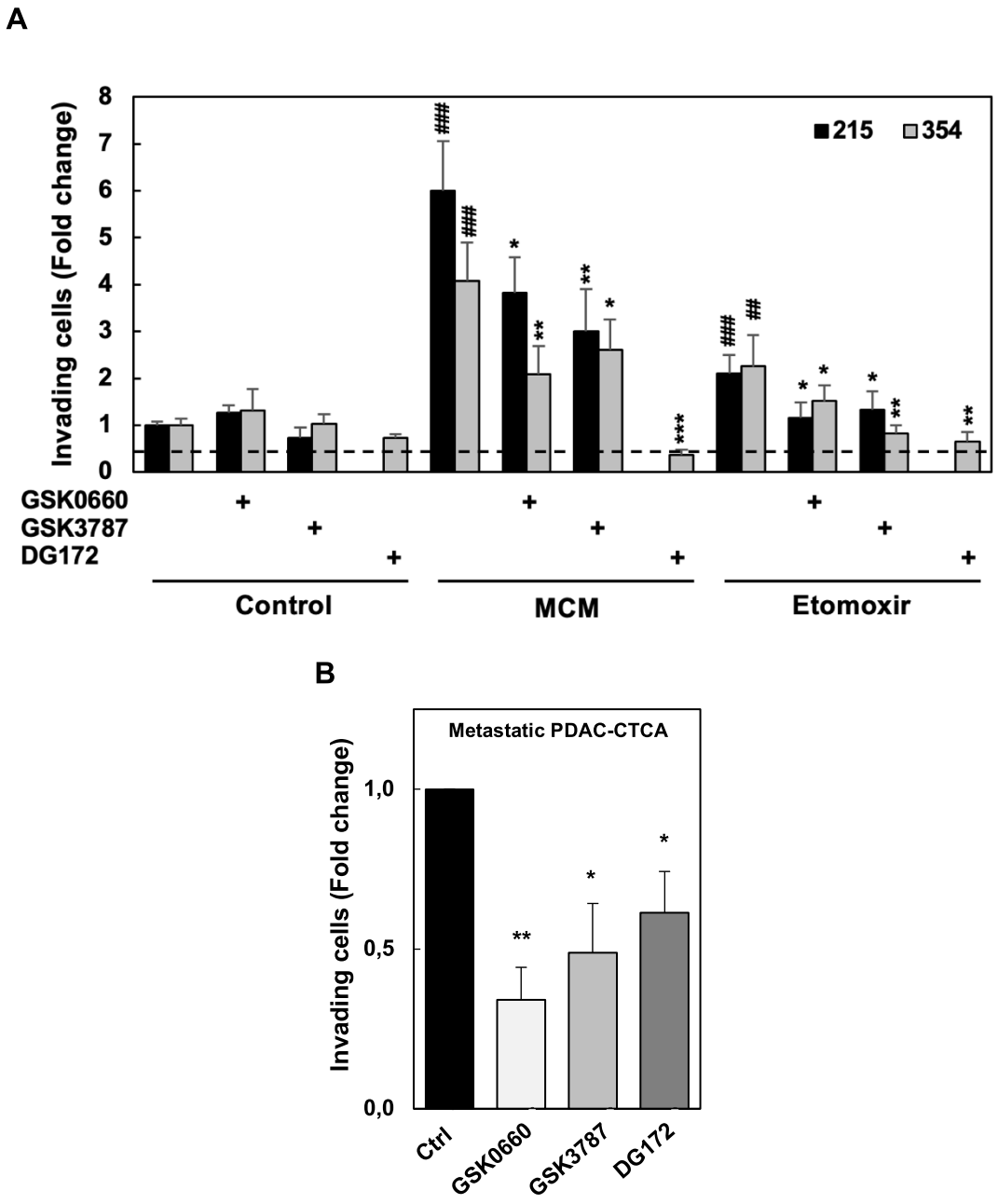

Figure I.15. A) Invasion assay with PDX215 and 354 cells pre-treated with MCM or 40 µM Etomoxir for 24 hours in the presence or absence of the PPAR-δ antagonists GSK0660 and GSK3787 (10 µM) or the inverse agonist DG172 (1 µM). Cells were seeded in Boyden chambers and, after 24 hours, Diff Quick staining was performed and invading cells were counted. **B)** Invasion assay with CTCA cells pre-treated with the PPAR-δ antagonists GSK0660 and GSK3787 (10 µM) or the inverse agonist DG172 (1 µM). Cells were seeded in Boyden chambers and, after 24 hours, Diff Quick staining was performed and invading cells were counted. Data are shown as the fold change to control condition, depicted as mean ± SEM and analyzed using Students t test or Mann-Whitney test. ## p<0.01, ### <0.005 *versus* untreated control; * p<0.05 , ** p<0.01, *** p<0.005 *versus* MCM or Etomoxir alone (A) or control (B).

Afterwards, we sought to validate these *in vitro* results in a hepatic spontaneous metastasis assay in NSG immunocompromised mice. CTCA GFP-luc

cells or the highly invasive PDX265 were pre-treated *in vitro* with a PPAR-δ inducer or antagonist prior being orthotopically injected in the mice pancreas. One week post-surgeries, intraperitoneal treatment with the drugs was started and continued every other day for up to nine weeks, while tumors were followed up

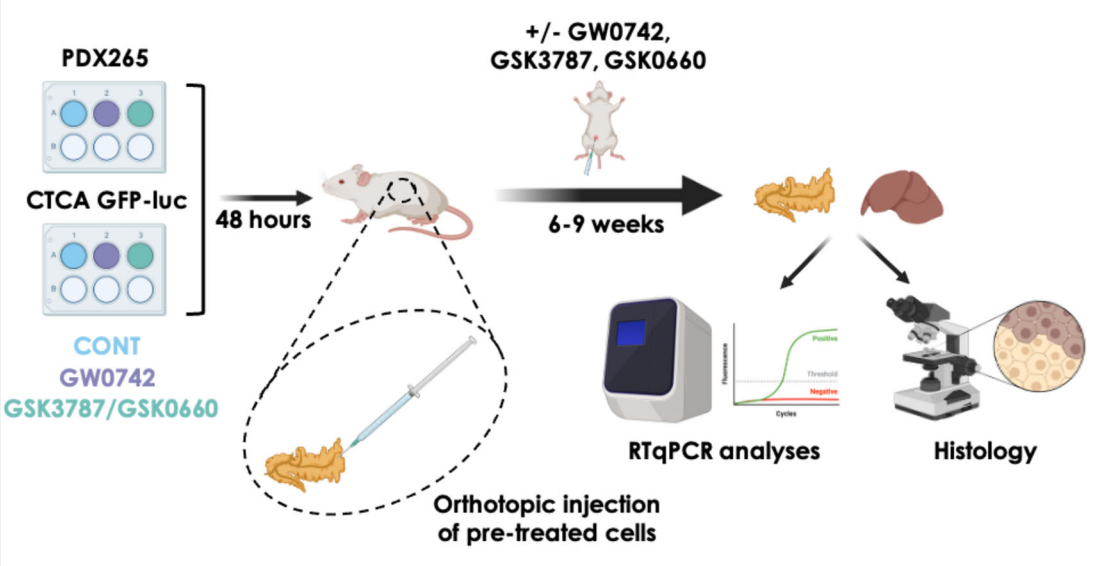

by IVIS® or palpation twice a week. At endpoint, both pancreas and livers were processed for RNA or histology (**Figure I.16**).

Figure I.16. Schematic overview of the spontaneous metastasis assay. PDX265 or CTCA GFP-luc cells were pre-treated *in vitro* with 5 μM GW0742, 10 μM GSK3787 or 10 μM GSK0660 for 48 hours. Then, cells were orthotopically injected in the pancreas of NSG mice and, after seven days, intraperitoneal treatment was started with either PPAR-δ inducer or antagonists every other day. Tumors were followed up by palpation or IVIS® and, after six or nine weeks, mice were euthanized and pancreas and livers processed for RTqPCR analyses or histology.

On the one hand, *PPARD* expression resulted significantly higher in the pancreas of those mice under PPAR-δ activation treatment (i.e., GW0742), while it remained unchanged in those under PPAR-δ blockade (i.e., GSK3787 or GSK0660) (**Figure I.17**).

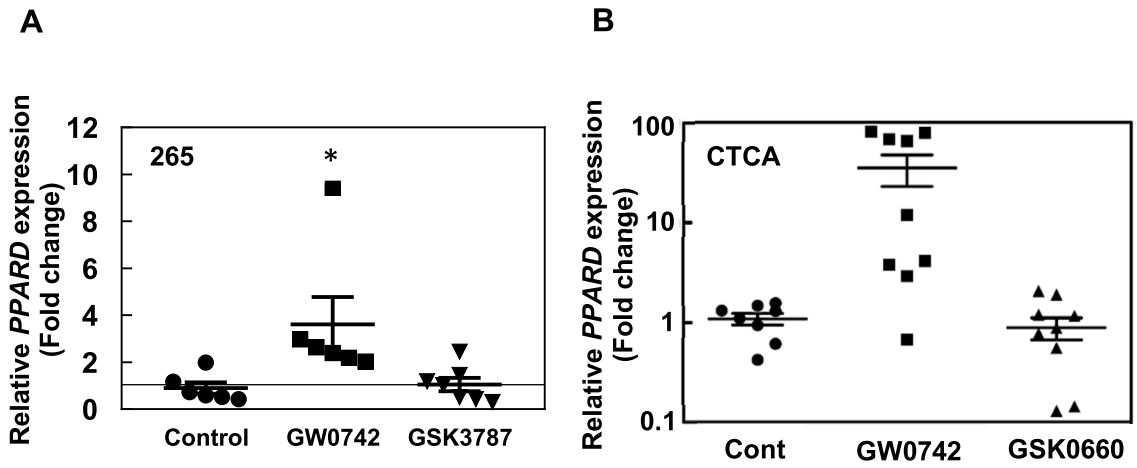

Figure I.17. Spontaneous metastasis assay of PDX265 (**A**) or CTCA GFP-luc (**B**) cells orthotopically injected in the pancreas of NSG mice. **A)** RTqPCR for *PPARD* in pancreas homogenates from PDX265 cells at end point (week six). **B)** RTqPCR for *PPARD* in pancreas homogenates from CTCA GFP-luc cells at end point (week nine). Data are shown as the individual *PPARD* expression per mice relative to control mice, depicted as mean ± SEM and analyzed using One-way ANOVA or Kruskal-Wallis test. * $p<0.05$.

On the other hand, liver homogenates were assessed for metastasis by means of human *GAPDH* (*hGAPDH*) or GFP expression by RTqPCR. In both cases, the signal was increased in the samples derived from PPAR-δ activation and decreased in the ones from PPAR-δ inhibition (**Figure I.18A and I.18B**). Consequently, the metastatic incidence was calculated as the percentage of macrometastases (visually detected) or micrometastases (detected by RTqPCR) and resulted higher with GW0742 treatment and lower with the antagonists' treatment (i.e., GSK3787 or GSK0660), as expected (**Figure I.18C and I.18D, top panels**). Accordingly, hepatic metastatic *foci* extension measured as pancreatic cytokeratin 19 (CK19) detection by immunohistochemistry, despite present in all the conditions, was consistently increased upon PPAR-δ activation and decreased upon PPAR-δ inhibition with the antagonists (**Figure I.18C and I.18D, middle panels**). Most importantly, GW0742 samples had increased levels of MYC and vimentin proteins expressed in the tissue preparations than those of GSK3787 or GSK0660, thus confirming our previous *in vitro* results of PPAR-δ controlling the EMT program through MYC (**Figure I.18C and I.18D, bottom panels**).

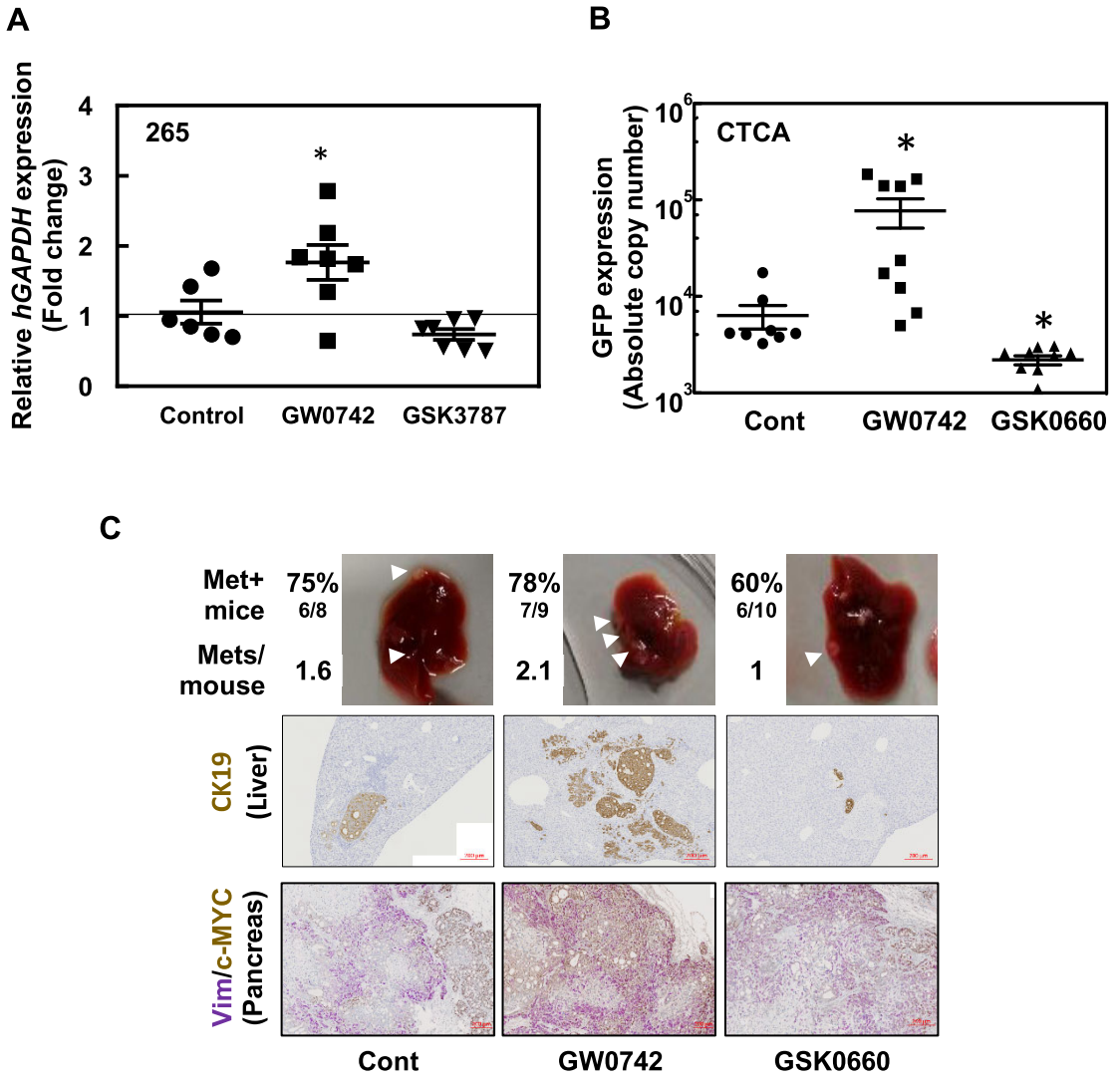

D

	Control	GW0742	GSK3787
Macromet	22%	66%	10%
Micromet	33%	87.5%	10%

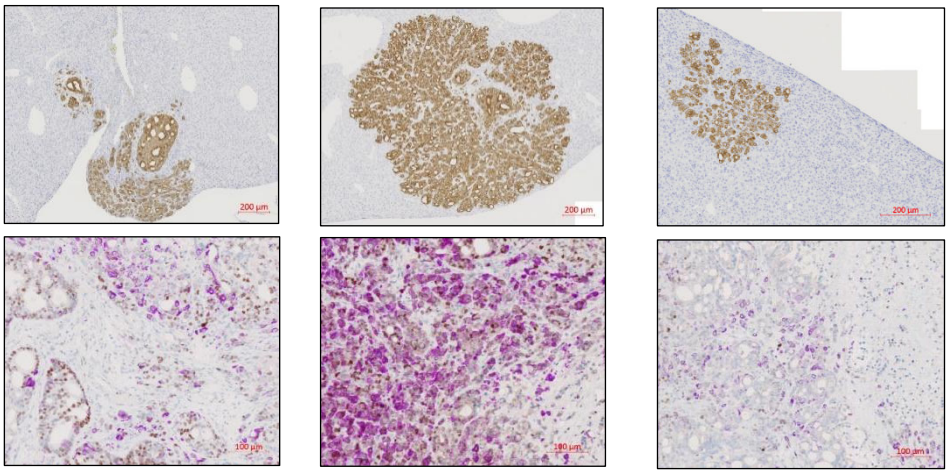

Figure I.18. Spontaneous metastasis assay of PDX265 or CTCA GFP-luc cells orthotopically injected in the pancreas of NSG mice. Arising metastases were evaluated by means of *hGAPDH* or GFP expression by RTqPCR in liver homogenates (**A and B, respectively**), incidence (**C and D, top panels**) and CK19 protein expression in liver preparations (**C and D, middle panels**). MYC and vimentin protein expression was also evaluated in liver preparations (**C and D, bottom panels**).

These data demonstrate that PPAR-δ inhibition reduces the invasive and metastatic potential of PDAC cells *in vitro* and *in vivo*.

Taken together, we have unraveled a previously unknown function of PPAR-δ integrating metabolic stress and stroma-derived stimuli to potentiate the invasive and metastatic ability of PDAC cells through modulation of the MYC/PGC1α ratio. Most importantly, we have proven that small inhibitory compounds targeting PPAR-δ are able to overcome invasiveness by effectively decreasing metastasis onset in pancreatic tumors-bearing mice.

RESULTS: CHAPTER II

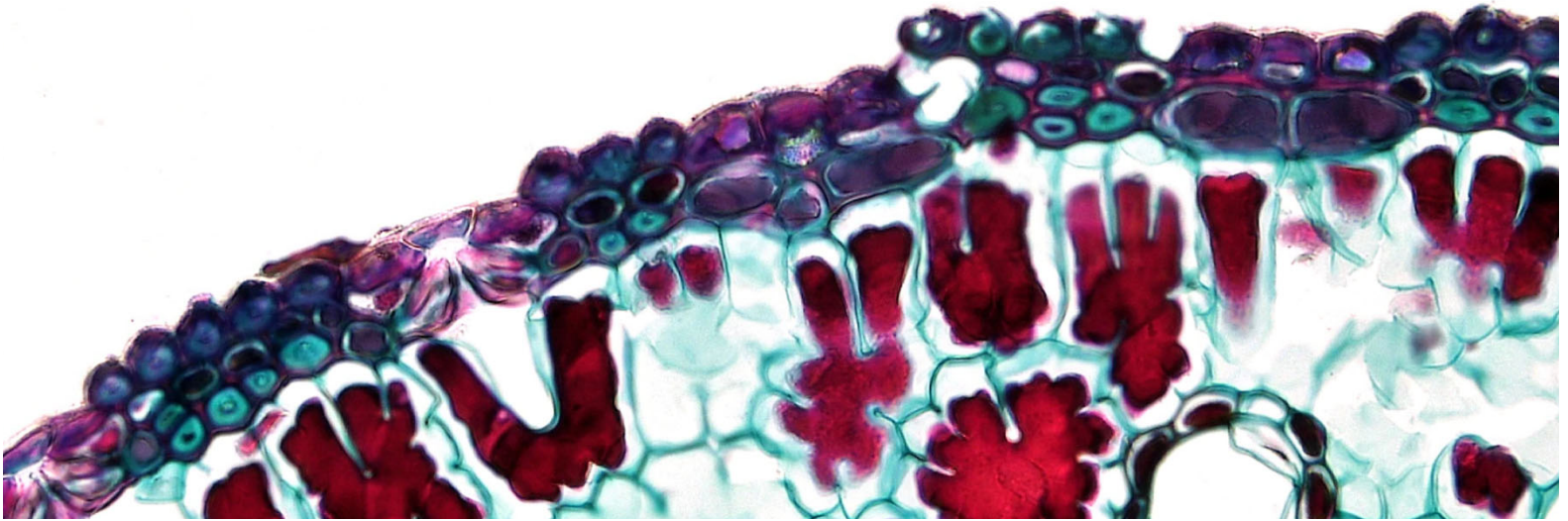

1. Background: PaCSCs have enhanced expression and activation of ALK receptor

Apart from substantial differences in their metabolism, CSCs modulate signaling pathways according to their needs at a given time. In this sense, in order to identify pharmacologically targetable receptor tyrosine kinases (RTKs) specifically activated in PaCSCs, our group ran a RTK array from autofluorescence-sorted CSC-enriching condition –a well-demonstrated CSC biomarker[56]– *versus* differentiated cells (**Figure II.1A**). Among the differentially phosphorylated RTKs, the receptor anaplastic lymphoma kinase (ALK) showed the most prominent upregulation in PaCSCs (i.e., Fluo$^+$ cells, **Figure II.1B**).

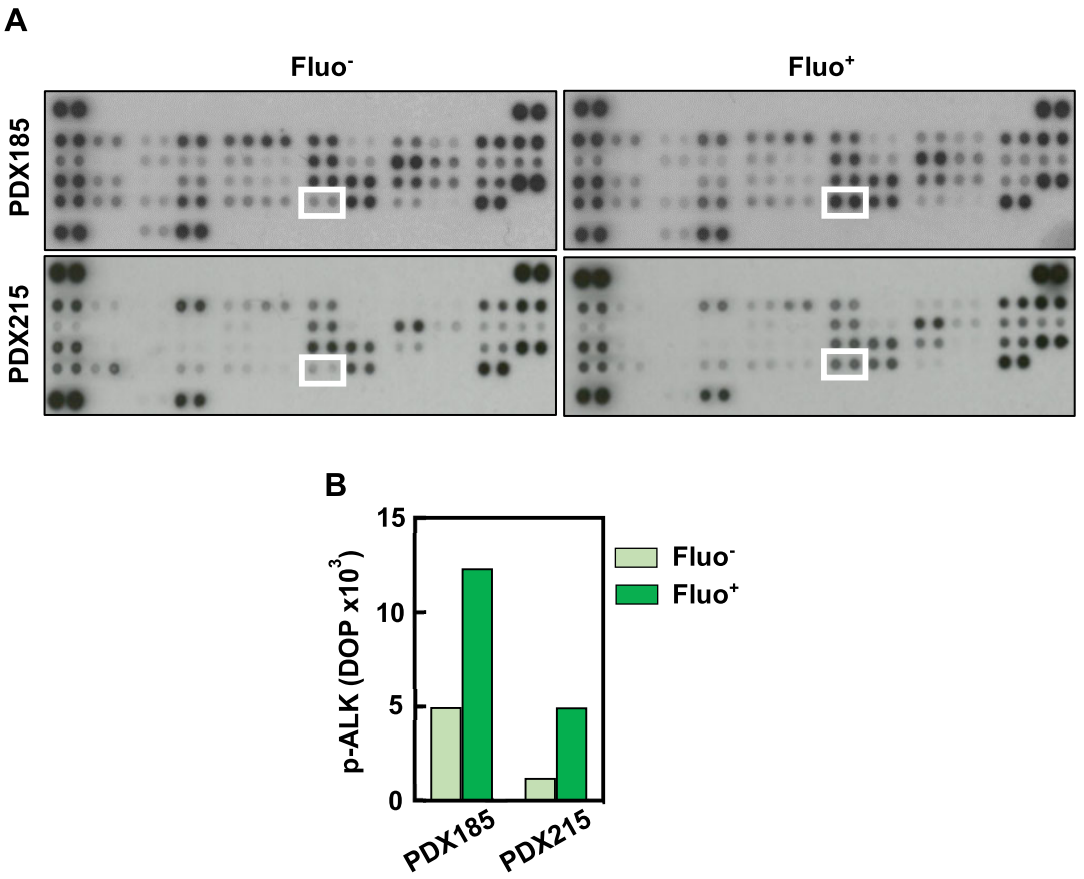

Figure II.1. A) Proteome Profiler Human Phospho-RTK Array in cells sorted by autofluorescence (Fluo$^-$ as non-CSCs, Fluo$^+$ as CSCs) for the indicated PDXs. Dots corresponding to p-ALK are indicated with a white square. **B)** Mean of the quantification of the dots corresponding to p-ALK from A (n=1). DOP: density of pixels.

Notably, ALK total protein expression was also increased in Fluo$^+$ samples and in anchorage-independent cultures (spheres, sph), as another well-known CSC-enriching model for PDAC[20] (**Figure II.2**).

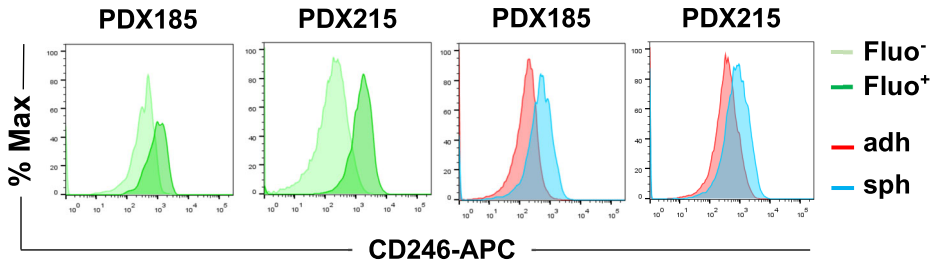

Figure II.2. Representative fluorescence activated cell sorting (FACS) histograms of CD246 (ALK) expression (percentage of maximal fluorescence) in the CSC-enriching conditions autofluorescence (Fluo) and anchorage-independent (spheres, sph) *versus* adherent (adh) cultures in the indicated PDXs (n=1).

These convincing preliminary results opened an exciting new line of research involving a completely previously overlooked RTK in PDAC. Therefore, we hypothesized that ALK signaling pathway regulates PDAC aggressiveness by controlling the self-renewal capacity, tumorigenicity, invasive potential and chemoresistance of PaCSCs. Considering this hypothesis and in order to evaluate it, we proposed the following objectives:

1. To assess ALK pathway in PDAC (stem) cells in terms of gene and protein expression, correlation with stemness and invasiveness, and activation.
2. To evaluate the functional effects of the ALK pathway activation by its ligands *in vitro* and *in vivo* by studying its contribution to the aforementioned PaCSCs features, as well as the immunoevasive properties.
3. To appraise, *in vitro* and *in vivo*, the consequences of the ALK pathway inhibition on viability and the foregoing mentioned PaCSCs characteristics.

2. ALK receptor expression and activation are linked to CSC-related features in PDAC patients

While ALK receptor was shown to be aberrantly expressed and/or activated in several cancer types[169–172], its expression had been previously reported to be very low or even absent in PDAC tissues[189]. For this reason, we decided to verify its expression by western blot in a panel of PDAC patient-derived xenografts (PDXs) and established cell lines. Surprisingly, all of them showed considerable ALK expression and phosphorylation (**Figure II.3**). The previously described different molecular weights of ALK were found in the western blot for all the cell types assessed (220 kDa full-length glycosylated wild type ALK and 180 kDa full-length wild type ALK) (**Figure II.3**).

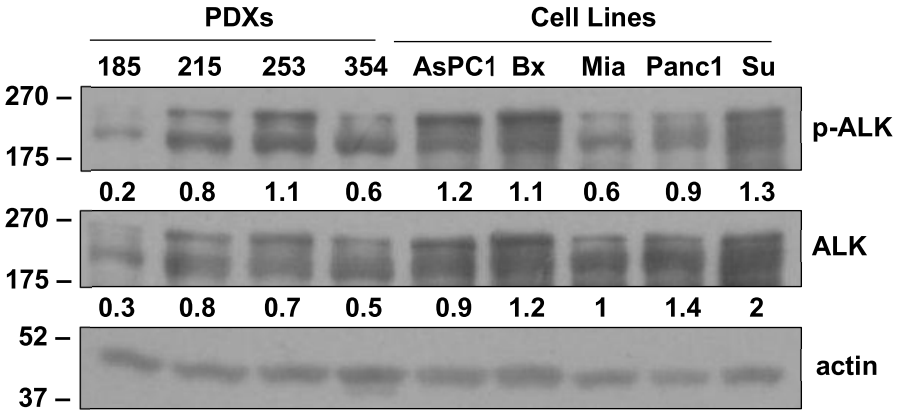

Figure II.3. Western blot of cell lysates comparing PDXs and cell lines to assess p-ALK and ALK protein levels (n=1). Numbers represent the quantification of the band intensity for each protein normalized by actin. Bx: BxPC3; Mia: MiaPaCa2; Su: Su8686.

Apart from autofluorescence and anchorage-independent cultures, there are other feasible models to study PaCSCs and their functionality nowadays. The biomarker CD133 is also commonly used to distinguish stem-like populations to their differentiated counterparts in PDAC[219]. In this work, we focused on the expression of CD133 as a differential surface marker of PaCSCs. Thereby, we sought to validate the previous Fluo/adh-sph results in $CD133^-$ *versus* $CD133^+$ samples. As we expected, the RTK array revealed higher p-ALK levels in the $CD133^+$ population (**Figure II.4A and II.4B**). Notably, $CD133^+$ samples also showed increased ALK protein expression by means of flow cytometry in our PDXs,

including a model of metastatic PDAC established from circulating tumor cells (CTCA, **Figure II.4C**).

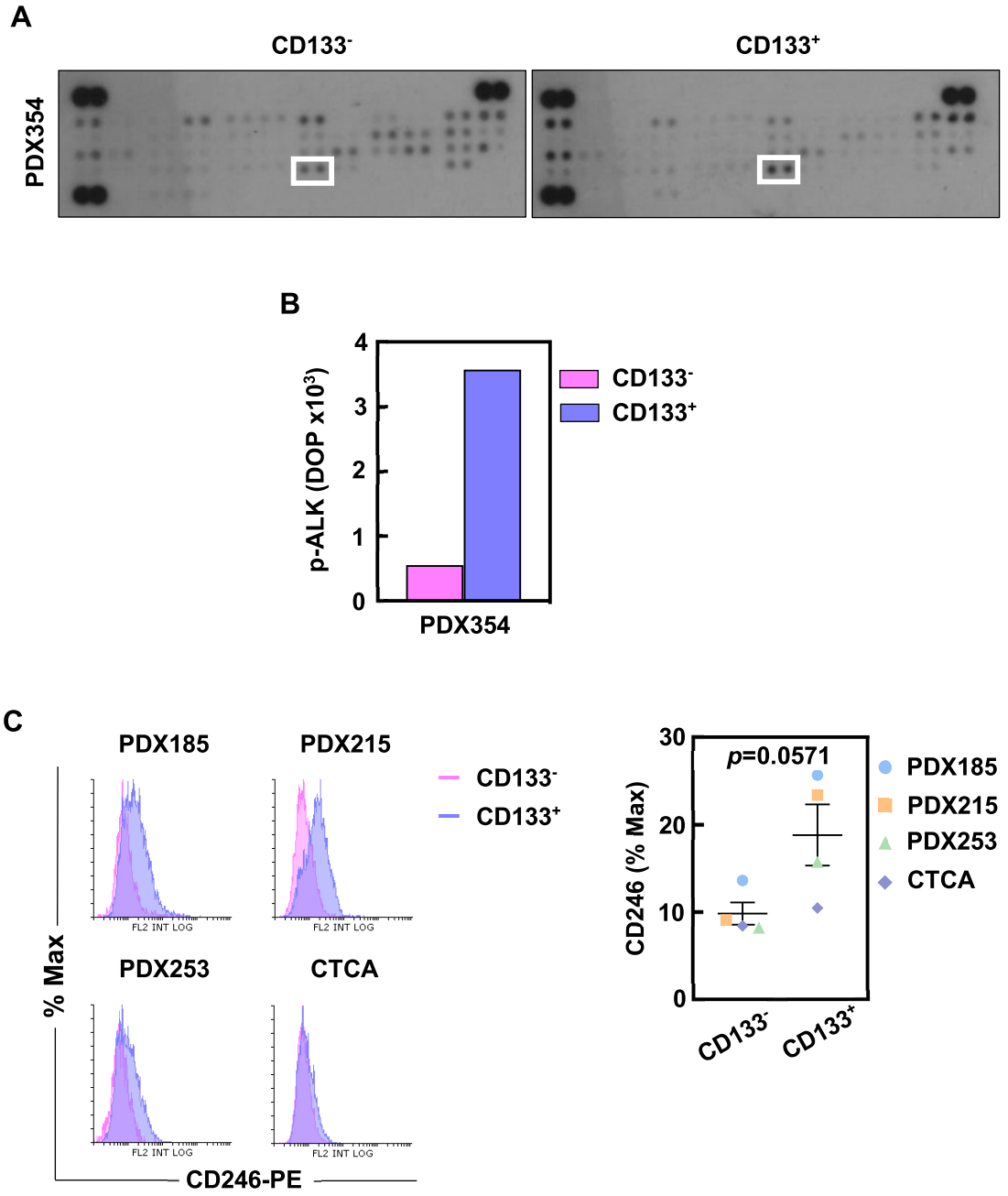

Figure II.4. A) Proteome Profiler Human Phospho-RTK Array in PDX354 cells sorted by CD133 surface marker as CSC-enriching condition. Dots corresponding to p-ALK are indicated with a white square. **B)** Mean of the quantification of the dots corresponding to p-ALK from A (n=1). DOP: density of pixels. **C) Left panel:** flow cytometry histograms of CD246 (ALK) expression (percentage of maximal fluorescence) in CD133$^-$ *versus* CD133$^+$ cell populations; **right panel:** pooled data showing the individual values for the indicated PDXs (n=1 for each PDX). Data are shown as the fold change to CD133$^-$, depicted as mean ± SEM and analyzed using Mann-Whitney test. * p<0.05, ** p<0.01, *** p<0.005.

We additionally validated our findings by western blot in the different models, where CSC-enriching conditions such as Fluo$^+$, CD133$^+$ and spheroids showed increased levels of ALK protein, both total and phosphorylated (**Figure II.5**).

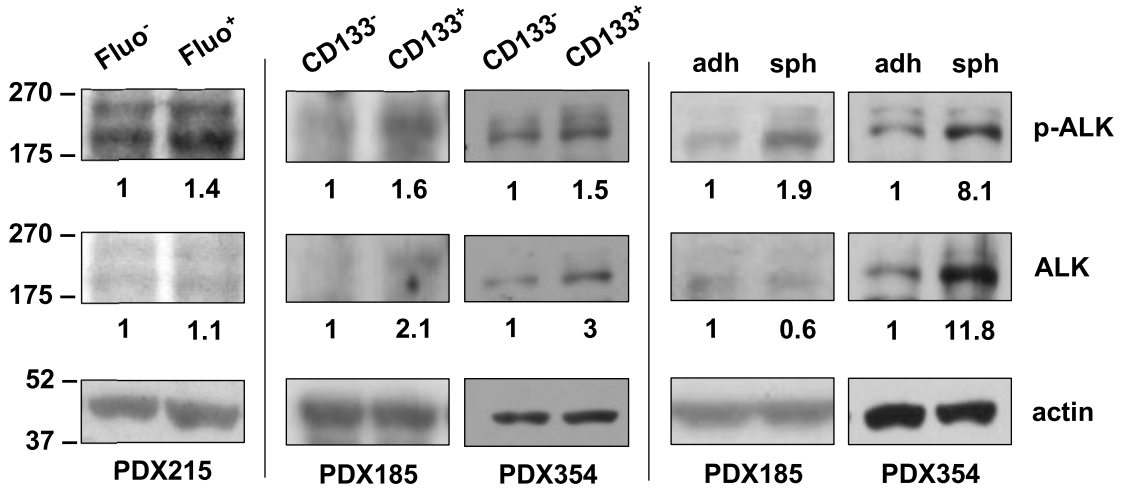

Figure II.5. Western blot of cell lysates from different CSC settings (sorted cells by autofluorescence (Fluo) and CD133 content; cells grown in adherent (adh) *versus* anchorage-independent conditions as spheroids (sph)) in the indicated PDXs to assess p-ALK and ALK protein levels (n=1 for each condition). The numbers represent the quantification of the band intensity of each protein normalized by actin, shown as the fold change to each differentiated cell condition.

Remarkably, CSC-enriching samples also showed increased ALK mRNA (**Figure II.6**). However, these differences were only significant in spheroid samples, probably due to small number of replicates in the other two conditions.

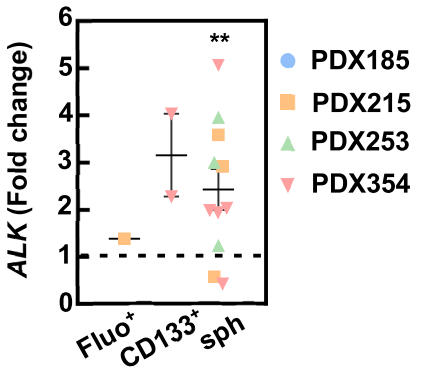

Figure II.6. RTqPCR of *ALK* mRNA levels in the indicated CSC settings: autofluorescence-sorted cells (Fluo), CD133-sorted cells and spheroids (sph). Pooled data showing the individual values for the indicated PDXs (Fluo n=1, CD133 n=2, sph n=11). Data are shown as the fold change to differentiated cells, which is represented as the dashed line, depicted as mean ± SEM and analyzed using Mann-Whitney test. * $p<0.05$, ** $p<0.01$, *** $p<0.005$.

As mentioned above, ALK expression is low in PDAC tissues and chromosomal translocations are very rare[189,190,220]. Indeed, although we detected a positive trend, bioinformatic analyses showed no significant differences in ALK expression in PDAC patients as compared to healthy pancreatic tissue from the Cancer Genome Atlas (TCGA, normal and PDAC) and the Genotype-Tissue Expression (GTEx, normal) datasets (**Figure II.7A**) and revealed a low percentage of genetic alterations in this gene (**Figure II.7B**).

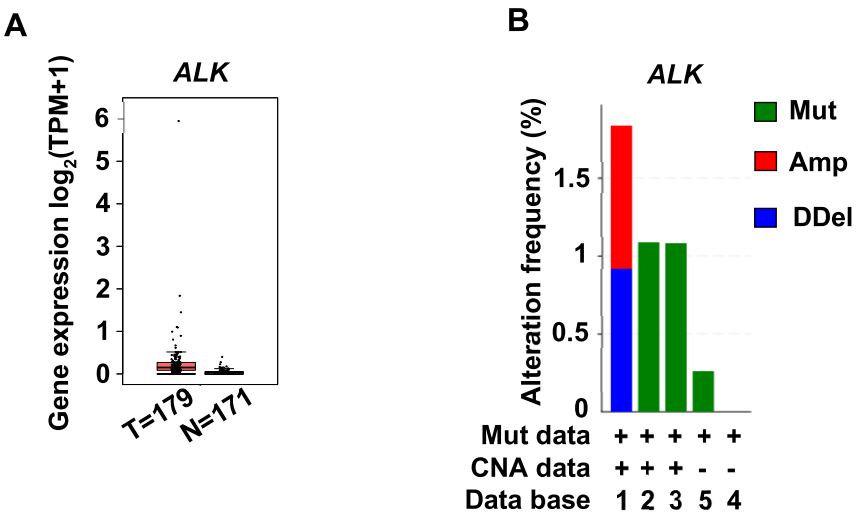

Figure II.7. A) Transcriptomic bioinformatic analyses of *ALK* comparing normal (N) and PDAC (T) human tissues from GTEx and TCGA datasets, respectively (webserver: GEPIA2). **B)** Mutational status of *ALK* from different datasets: 1. Pancreas UTSW, 2. Pancreas TCGA PanCan 2018, 3. Pancreas TCGA, 4. Pancreas ICGC and 5. Pancreas QCMG 2016. Mut: mutation, Amp: amplification, DDel: deep deletion (webserver: cBioPortal).

Additionally, we performed further correlation analyses in the same datasets. As our data points that ALK receptor potentially modulates CSC-related features in PDAC, we first assessed whether its expression correlates with our validated sets of pluripotency (*KLF4*, *NANOG*, *OCT3/4* and *SOX2*)[64] and EMT (*SNAIL*, *SLUG*, *ZEB1* and *LOXL2*)[104,221] genes. According to TGCA and GTEx datasets, *ALK* expression in PDAC patients does not correlate with the expression of either gene signature (**Figure II.8A and II.8B, respectively**), which is not surprising considering *ALK* almost absent expression in PDAC patients[189]. Nonetheless, because bioinformatic analyses based on the sole *ALK* expression in patients resulted inconclusive, we decided to interrogate an *ALK* overexpression (OE) signature composed by 58 genes that was recently described in breast cancer cells[210]. The *ALK* OE signature significantly correlated with both the pluripotency and EMT signatures

(**Figure II.8C and II.6D, respectively**). Notably, this *ALK* OE signature was significantly overexpressed in human PDAC samples (**Figure II.8E**) from the analyzed databases.

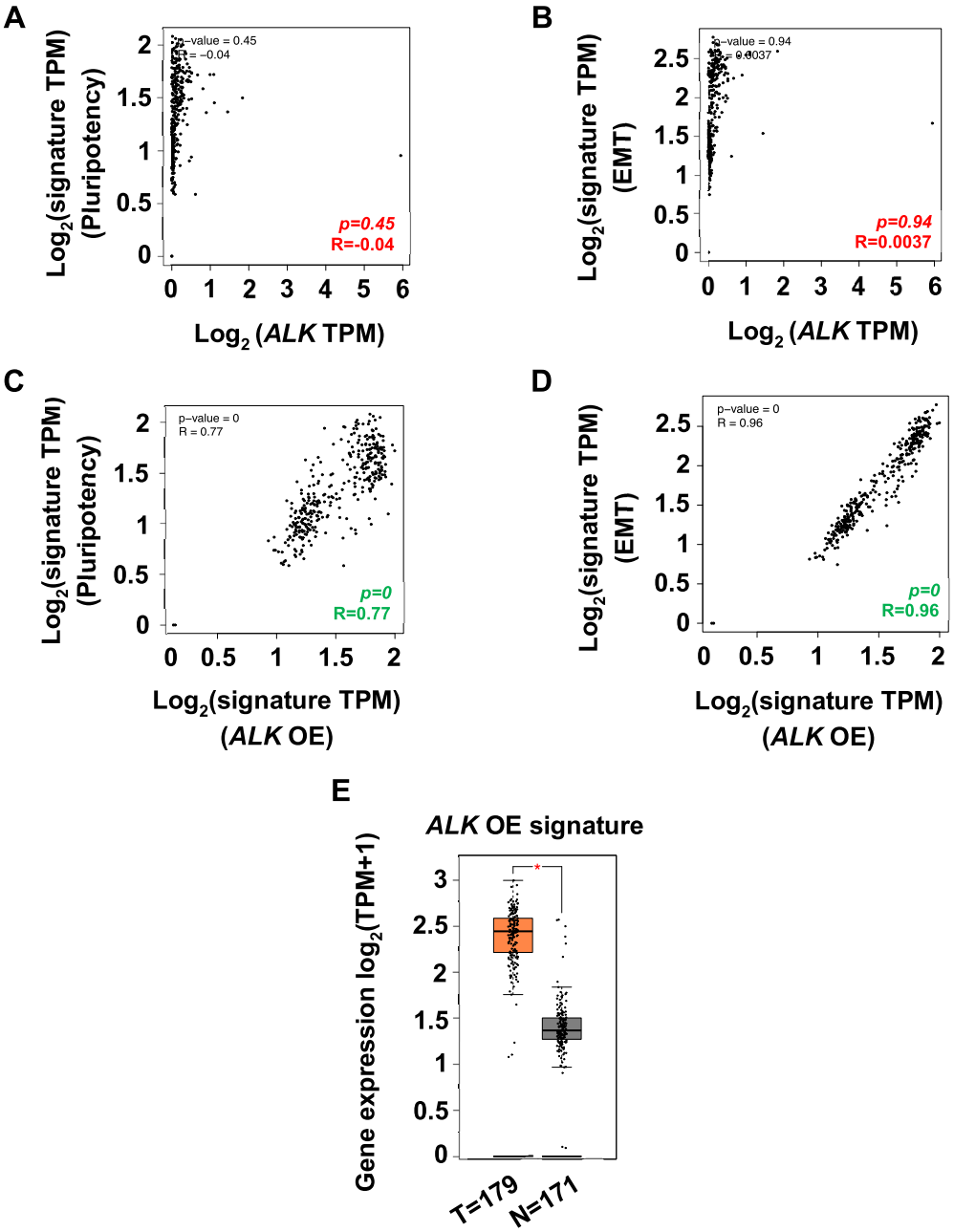

Figure II.8. Transcriptomic bioinformatic analyses comparing normal (N) to PDAC (T) human tissues from GTEx and TCGA datasets, respectively. **A)** Correlation of *ALK* expression with a stemness gene signature composed by *KLF4*, *OCT3/4*, *NANOG* and *SOX2*. **B)** Correlation of *ALK* expression with an EMT gene signature composed by *SNAIL*, *SLUG*, *ZEB1* and *LOXL2*. **C)** Correlation of *ALK* OE signature with the stemness gene signature described in A. **D)** Correlation of *ALK* OE signature with the EMT gene signature described in B. In A-D, the Pearson correlation coefficient (R) is calculated and interpreted as follows together with the *p*-value: the color green represents a *p*-value<0.05 and a R>0.5, while the color red represents either a *p*-value>0.05 or a R<0 (negative correlation). **E)** *ALK* OE signature expression. TPM: transcripts per million.

Despite its low expression, we were able to classify these PDAC patients into high and low *ALK* expression groups for gene set enrichment analysis (GSEA). Interestingly, while *ALK*^{LOW} patients did not show any enrichment, patients with higher *ALK* expression exhibited significant enrichment of pathways related to CSC properties and functionality such as EMT and xenobiotic metabolism (**Figure II.9A**), as well as a stemness signature previously described in PDAC[213] (**Figure II.9B, top panel**). On the other hand, besides pathways related to ALK downstream signaling such as K-Ras or JAK/STAT, *ALK*^{HIGH} samples also showed enrichment of the *ALK* OE gene signature mentioned above (**Figure II.9B, bottom panel**).

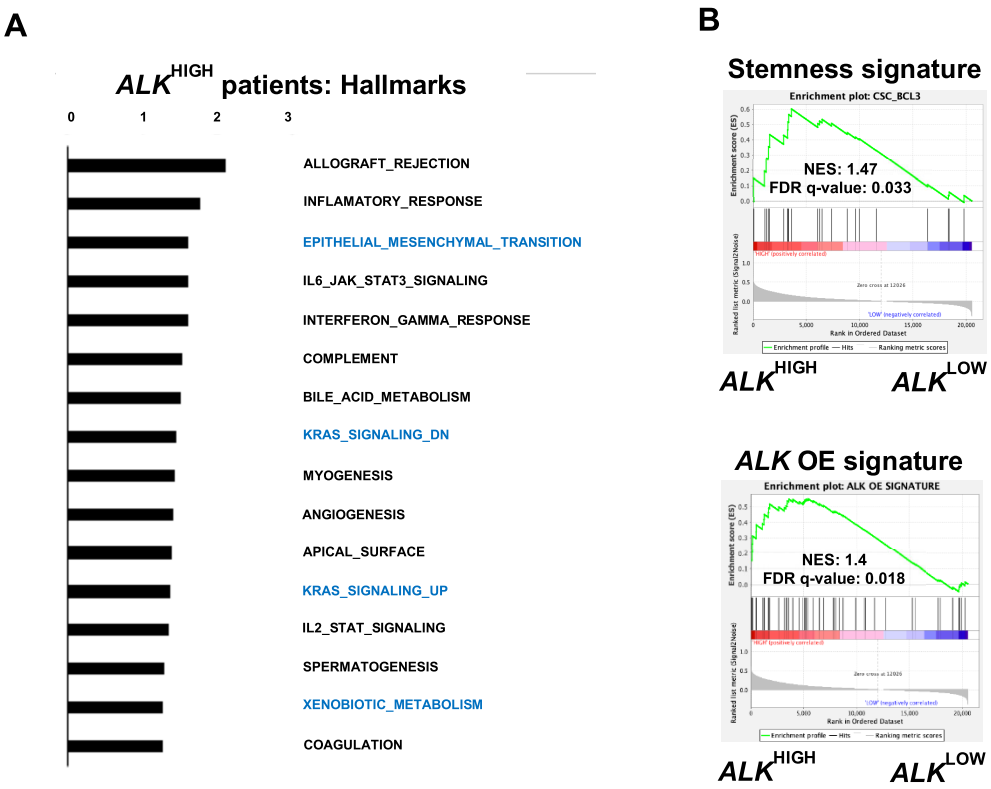

Figure II.9. A) Gene set enrichment analysis comparing the top 50% *ALK* expression group (*ALK*^{HIGH}) with the bottom 50% expression group in the TCGA data series. NES (normalized enrichment score) values of the Hallmark gene sets meeting the significance criteria: nominal *p*-value of <0.05, FDR <25%. **B)** Enrichment plot of stemness (**top panel**) and *ALK* overexpression (OE) (**bottom panel**) signatures in *ALK*^{HIGH} *versus* *ALK*^{LOW}.

In summary, our results indicate that ALK expression and activation is enhanced in PaCSCs from different PDXs, and its function is linked to stemness and CSC-related pathways in human PDAC samples.

3. Ligand-dependent ALK activation contributes to PDAC stemness and invasiveness

Several molecules have been proposed as ALK activators, including midkine (MDK), pleiotrophin (PTN), and family with sequence similarity 150 members A (FAM150A) and B (FAM150B)[170,176]. Interestingly, bioinformatic analyses revealed that *MDK* and *PTN*, but not *FAM150A* nor *FAM150B*, were significantly overexpressed in human PDAC samples when compared to normal pancreas (**Figure II.10A**). Moreover, *MDK* expression showed the most consistent positive correlation with our well-stablished pluripotency and EMT gene sets and the *ALK* OE signature mentioned above (**Figure II.10B**).

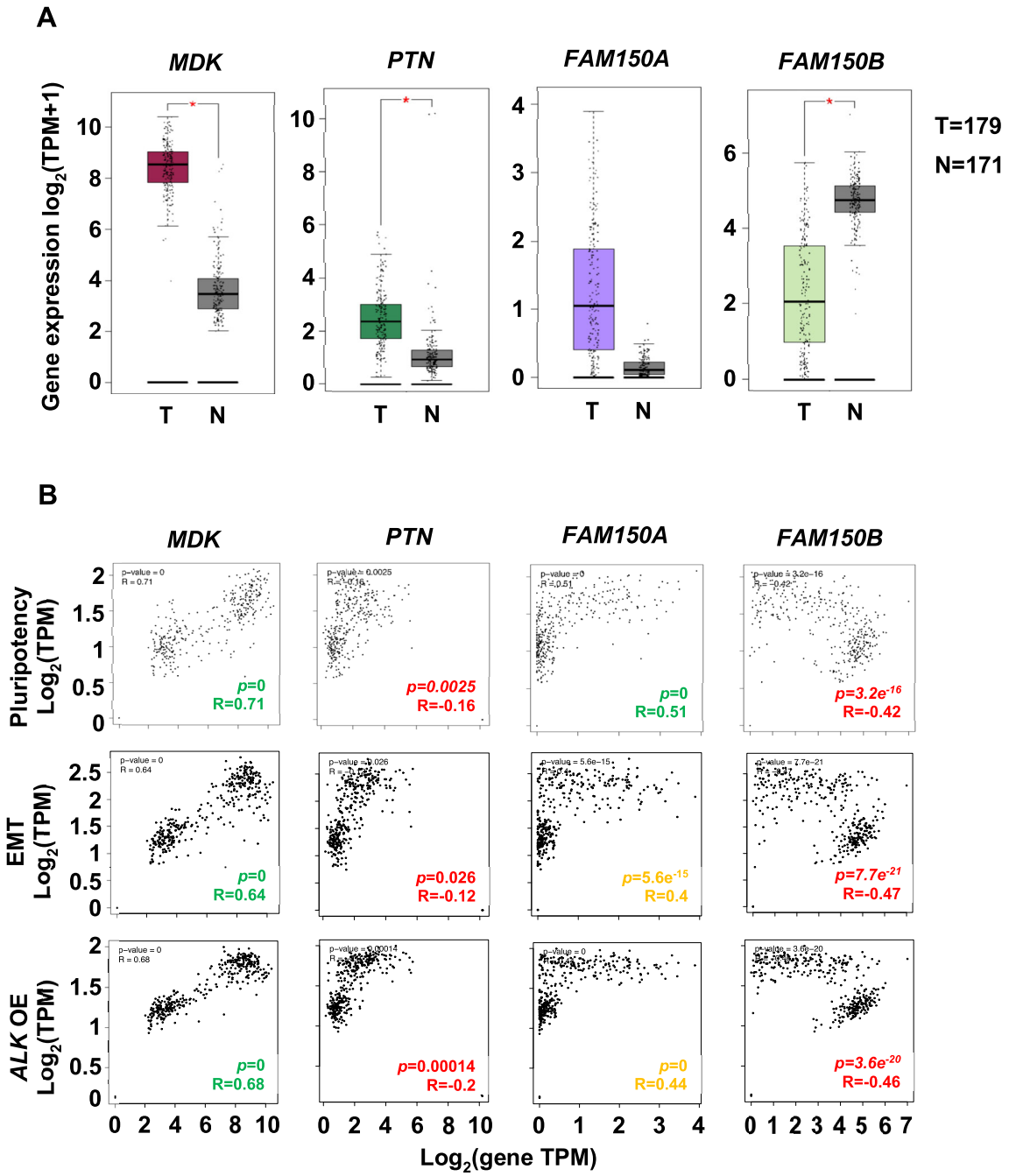

Figure II.10. A) Expression of ALK ligands comparing normal (N) and PDAC (T) human tissues from GTEx and TCGA datasets, respectively. **B)** Correlation expression of ALK ligands with a pluripotency signature composed by *KLF4*, *OCT3/4*, *NANOG* and *SOX2* (**top row**), an EMT signature composed by *ZEB1*, *SNAIL*, *SLUG* and *LOXL2* (**middle row**) or an *ALK* overexpression (OE) signature (**bottom row**) in human tissues from TCGA and GTEx datasets. The Pearson correlation coefficient (R) is calculated and interpreted as follows together with the *p*-value: the color green represents a *p*-value<0.05 and a R>0.5, the color orange represents a *p*-value<0.05 and a R<0.5, while the color red represents either a *p*-value>0.05 or a R<0 (negative correlation). TPM: transcripts per million.

These results obtained in bulk tumor samples were confirmed in collaboration with Álvaro Curiel-García (Columbia University Irving Medical Center, New York,

USA) in a PDAC single-cell transcriptomic dataset[222], where *MDK* showed the strongest positive correlation with three out of the four stemness genes separately (*KLF4*=0.37, *OCT3/4*=0.9, *NANOG*=0.78, *SOX2*=0.81, **Figure II.11A**). Further analyses of this single-cell dataset revealed that *MDK* was expressed by a wide range of cell types, including ductal, acinar and tumor cells as well as fibroblasts (**Figure II.11B**), whereas *PTN* was mainly expressed by stromal cells (**Figure II.11B**). Moreover, these analyses further corroborated the low expression of *ALK* mRNA in PDAC tumors, as it was undetectable at single-cell level in the different PDAC cell populations included in this dataset (**Figure II.11B**).

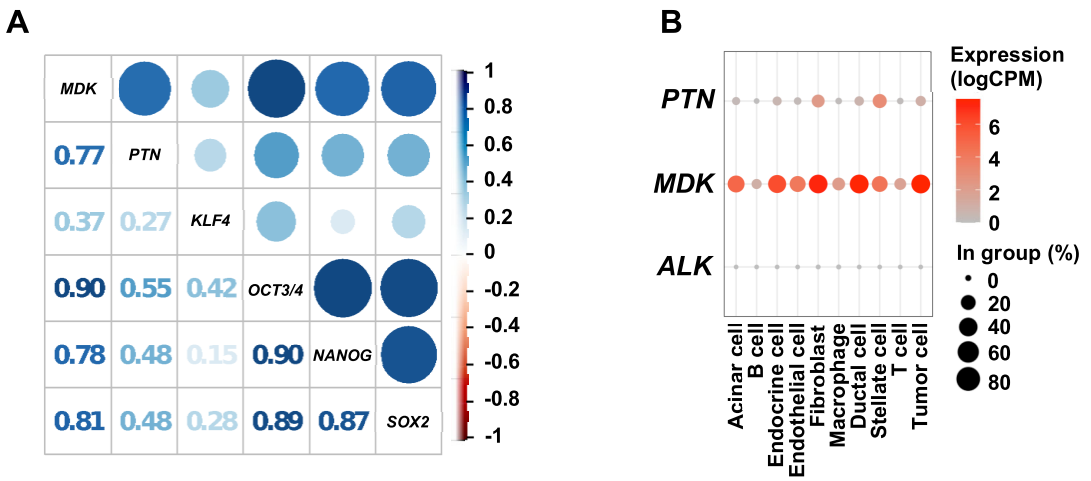

Figure II.11. A) Correlation matrix of the indicated genes in single tumor cells from the Peng scRNAseq dataset[222]. The numbers and dot sizes indicate the R value of each correlation. The blue color indicates a positive correlation, whereas the red color represents a negative correlation. **B)** Single-cell expression analysis of the indicated genes in the different cellular populations included in the Peng scRNAseq dataset. The dot size represents the percentage of cells expressing each gene per population, while the color scale denotes the expression level.

Importantly, we confirmed that MDK was secreted by both subcutaneous and orthotopic PDX tumors *ex vivo* (**Figure II.12A, left and middle panel, respectively**) and *in vivo*, since we detected human MDK in the plasma of mice bearing orthotopic PDXs (**Figure II.12A, right panel**). While only spheroids (sph) showed increased levels of *MDK* expression at the mRNA level (**Figure II.12B**), no significant differences were found in terms of MDK secretion in this CSC-enriching model (**Figure II.12C**).

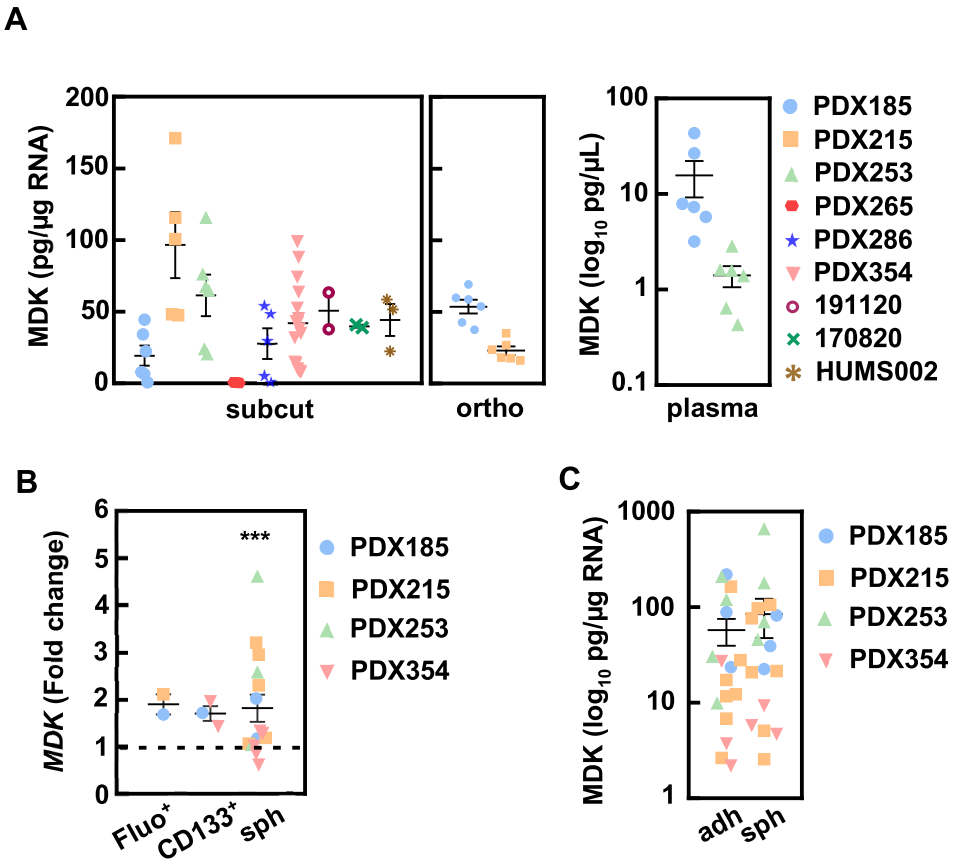

Figure II.12. A) MDK detection in supernatants from subcutaneous (subcut, **left panel**; PDX185 n=6, 215 n=5, 253 n=6, 265 n=4, 286 n=5, 354 n=16, 191120 n=2, 170820 n=2, HUMS002 n=3) and orthotopic (ortho, **middle panel**; n=6 for each PDX) PDX implants *ex vivo* and in plasma (**right panel**; n=6 each PDX) from orthotopic tumor-bearing mice by ELISA. **B)** RTqPCR of *MDK* mRNA levels in the indicated CSC settings: autofluorescence-sorted cells (Fluo), CD133-sorted cells and spheroids (sph). Pooled data showing the individual values for the indicated PDXs (Fluo n=2, CD133 n=3, sph n=15). Data are shown as the fold change to differentiated cells, which is represented as the dashed line, depicted as mean ± SEM and analyzed using Mann-Whitney test. * p<0.05, ** p<0.01, *** p<0.005. **C)** MDK detection in supernants from adherent (adh) and spheroid (sph) cultures by ELISA. Pooled data showing the individual values for the indicated PDXs (185 n=3, 215 n=7, 253 n=4, 354 n=3). Data are shown as the fold change to adherent condition, depicted as mean ± SEM and analyzed using Mann-Whitney test. * p<0.05, ** p<0.01, *** p<0.005.

Treatment with recombinant human MDK induced ALK phosphorylation in the short term (i.e., 1, 2 and 5 minutes; **Figure II.13, left panel**). Later on, phosphorylation was observed in its well-described downstream signaling partner ERK1/2[182] (i.e., 5 and 30 minutes; 1, 2 and 6 hours; **Figure II.13, right**

panel), corroborating ligand-dependent ALK activation with different doses of MDK (i.e., 1, 10 or 100 ng/mL).

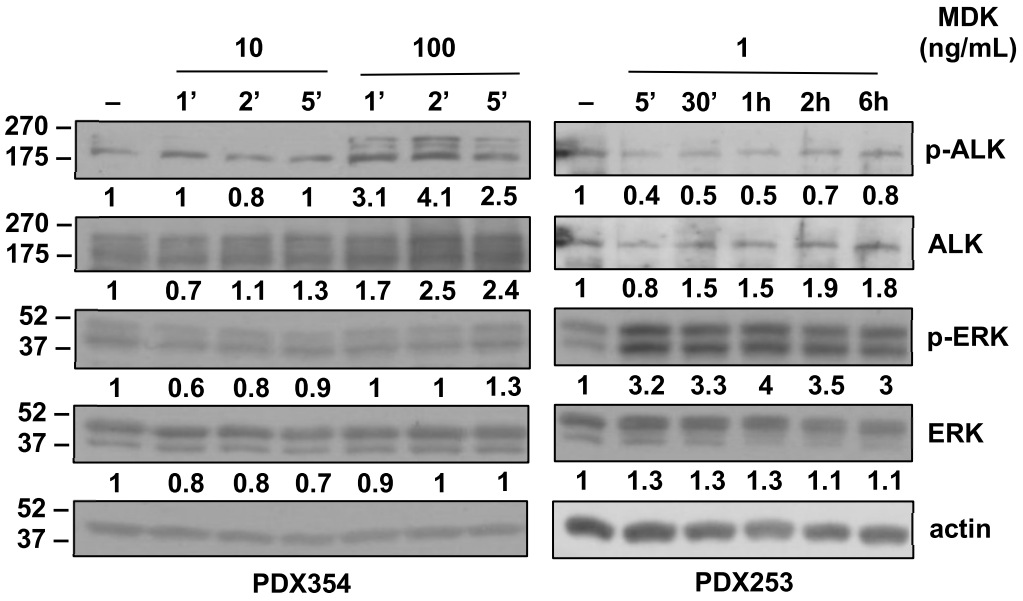

Figure II.13. Kinetics of ALK activation by western blot at the indicated times after treatment with 1, 10 or 100 ng/mL of recombinant MDK. Numbers represent the quantification of the band intensity of each protein normalized by actin, shown as fold change to the control group (n=1 for each PDX).

This activation resulted in improved CSC functionality *in vitro*. First of all, exogenous pre-treatment with MDK strongly enhanced self-renewal irrespective of the dosage by increasing the number of spheroids formed after seven days of assay (**Figure II.14A**). Consequently, the treatment also promoted clonogenicity (**Figure II.14B**). Finally, exogenous MDK increased CSC frequency *in vitro* analyzed by means of an extreme limiting dilution assay (ELDA, **Figure II.14C**). The results from these three experiments together indicate that MDK enhanced self-renewal, and this translated into increased CSC content.

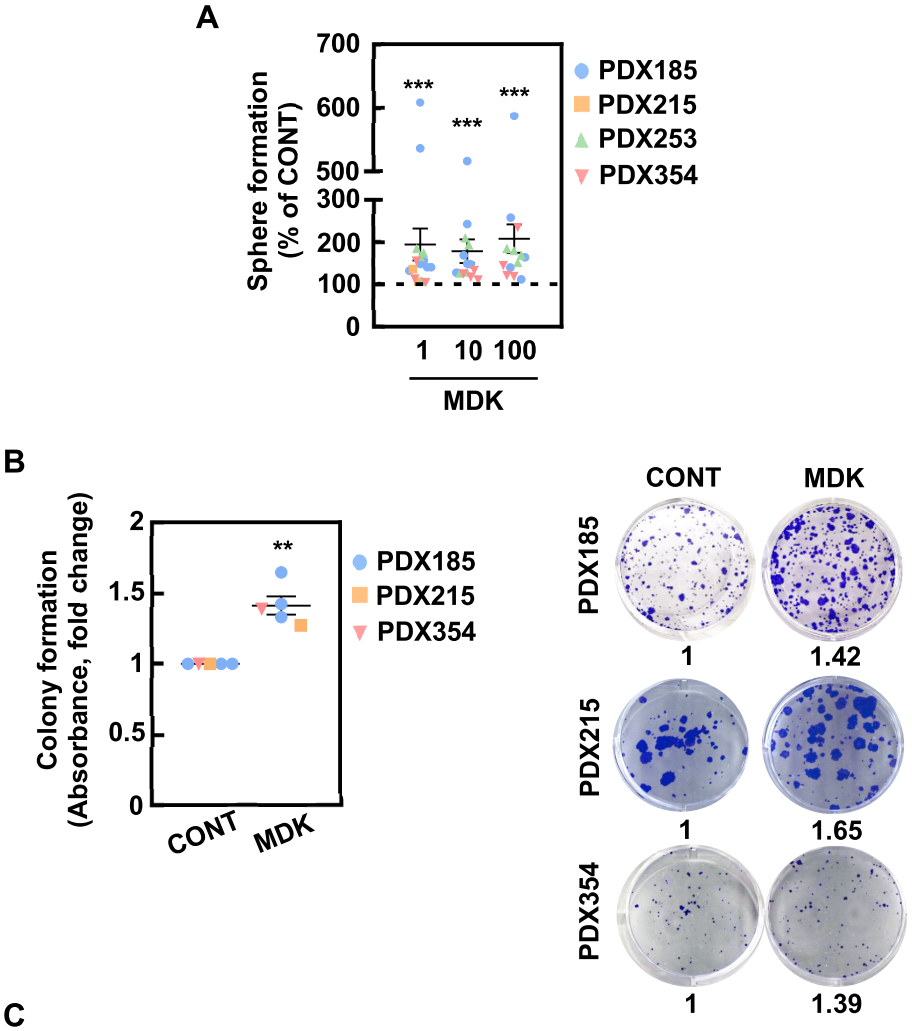

C

		CSC 1/x	*p*-value
PDX185	CONT	28.56	
	MDK 10	15.06	0.0147
	MDK 100	13.23	0.00384
	MDK 500	8.54	$4.25e^{-6}$

Figure II.14. A) Sphere formation assay after pre-treatment with recombinant MDK for 72 hours at the indicated concentrations (ng/mL) in adherent conditions. Pooled data showing the individual values for the indicated PDXs (185 n=7, 215 n=2, 253 n=4, 354 n=4). **B)** Colony formation assay after 21 days of treatment with 10 ng/mL of recombinant MDK. **Left panel:** absorbance of the crystal violet staining. Pooled data showing the individual values for the indicated PDXs (185 n=3, 215 n=1, 354 n=1). **Right panel:** Representative micrographs. The numbers represent the absorbance of crystal violet shown as the fold change to the control group. In A and B, data are shown as the fold change to control condition, which is represented as the dashed line (A), depicted as mean ± SEM and analyzed using Kruskal-Wallis (A) or Mann-Whitney (B) tests. * p<0.05, ** p<0.01, *** p<0.005. **C)** Estimation of the CSC frequency by *in vitro* extreme limiting dilution assay (ELDA) after treatment with the indicated concentrations of recombinant MDK for seven days in PDX185 (n=2). The numbers indicate one CSC every x number of cells. Statistical significance is calculated using a chi-square test.

Next, we sought to validate these results *in vivo* with a tumorigenicity assay (ELDA). Fort that, we pre-treated *in vitro* our cells with MDK and subcutaneously injected them in the flanks of immunocompromised nude mice at decreasing cell densities (**Figure II.15A**). Unfortunately, we were not able to reproduce the results *in vivo* as the CSC frequency did not result in significant differences with MDK pre-treatment (**Figure II.15B**). However, these results suggest that, despite being able to enrich CSC population (**Figure II.14**), the ALK pathway probably need a continuous stimulation *via* MDK in order to maintain its effects on PaCSC functionality in the long term.

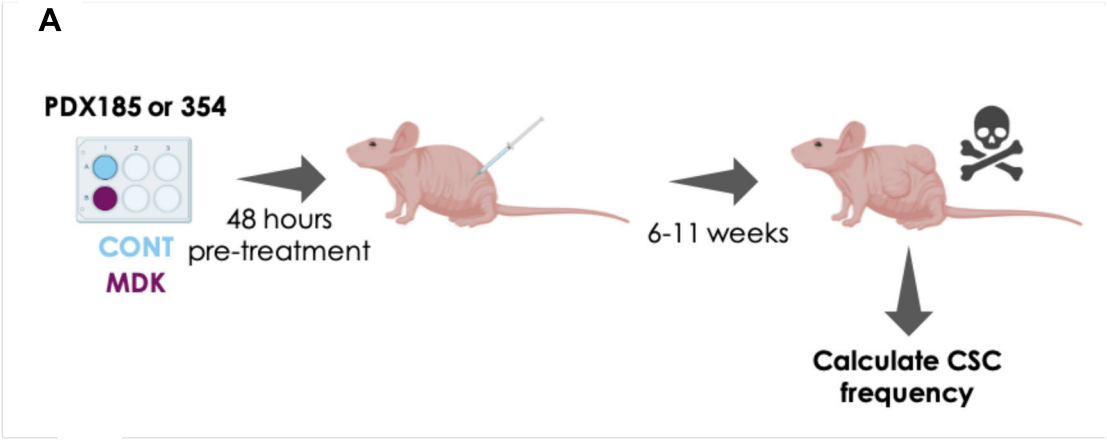

B

		CSC 1/x	*p*-value
PDX185	CONT	1205	
	MDK	3564	0.017

		CSC 1/x	*p*-value
PDX354	CONT	2164	
	MDK	910	0.268

Figure II.15. *In vivo* ELDA with cells of the indicated PDXs (PDX185 n=2, PDX354 n=1) pre-treated *in vitro* with 100 ng/mL MDK for 72 hours and subcutaneously injected into the flanks of nude mice at decreasing cell densities (PDX185 n=8 mice per group, 354 n=6 mice per group). **A)** Schematic overview of the *in vivo* ELDA. **B)** Estimated CSC frequency of PDX185 (**left**) and 354 (**right**). Statistical significance is calculated using a chi-square test.

Despite increased CSC functionality, exogenous MDK treatment did not translated into increased pluripotency genes (**Figure II.16A**) nor stemness surface markers (**Figure II.16B**) expression. These results may indicate that 1. gene and/or protein expression should not be overrated by using it as a single tool, but preferably in combination with functional assays; or 2. the effects on PaCSCs are exclusively at the functional level.

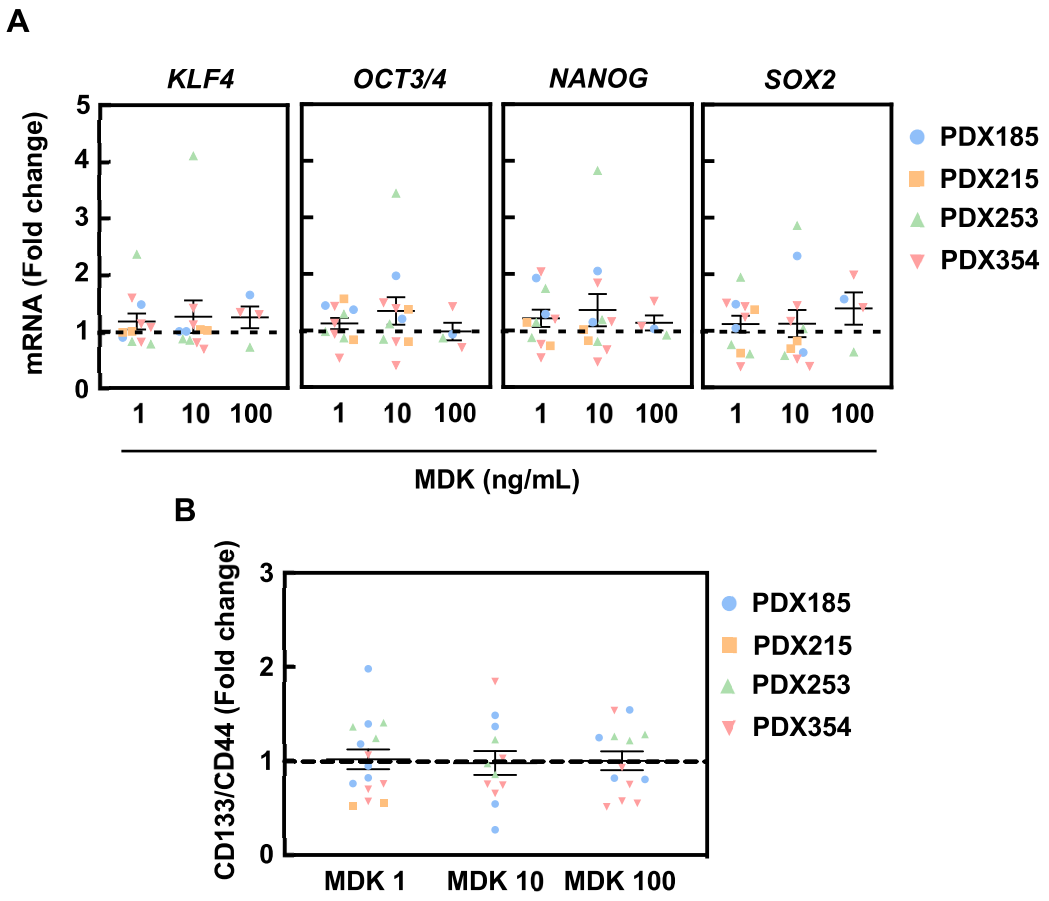

Figure II.16. A) RTqPCR for pluripotency genes mRNA levels after 72 hours of incubation with MDK at the indicated concentrations. Pooled data showing the individual values for the indicated PDXs (185 n=4, 215 n=3, 253 n=4, 354 n=4). **B)** CSC population measured as $CD133^{+}/CD44^{+}$ cells by FACS after 72h of incubation with MDK at the indicated concentrations (ng/mL). Pooled data showing the individual values for the indicated PDXs (185 n=6, 215 n=2, 253 n=3, 354 n=6). Data are shown as the fold change to control condition, which is represented as the dashed line, depicted as mean ± SEM and analyzed using Kruskal-Wallis test.

Additionally, exogenous MDK enhanced migration by increasing wound closure (**Figure II.17**), whose differences were especially visible at 24 and 48 hours.

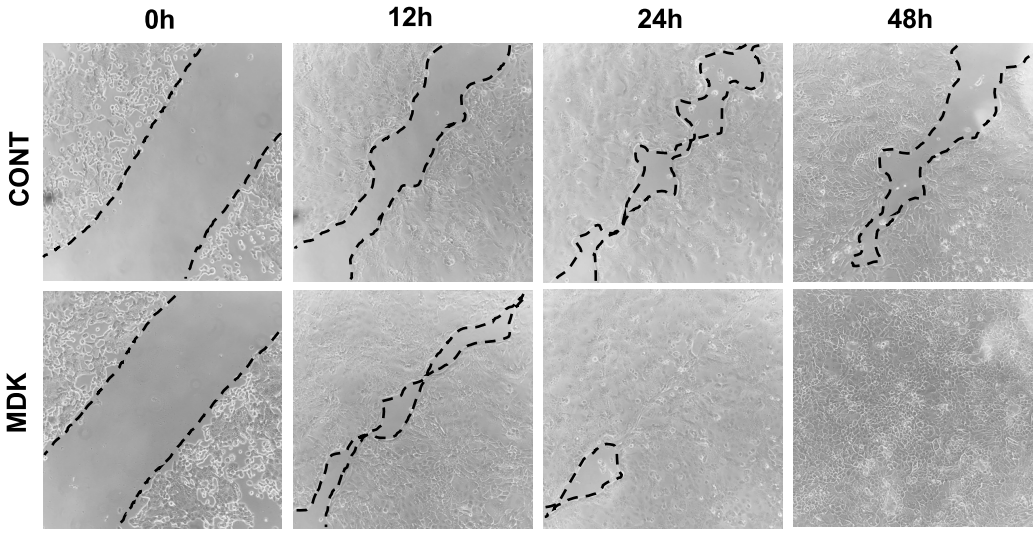

Figure II.17. Scratch wound healing assay of PDX354 treated with 20 ng/mL MDK for 48 hours after performing the scratch. Pictures were taken at the indicated times with an inverted microscope at 10X magnification (n=1).

Similar to pluripotency gene expression, the MDK-induced changes of the EMT genes were minor (**Figure II.18**), thus confirming that MDK acts simply at the functional level.

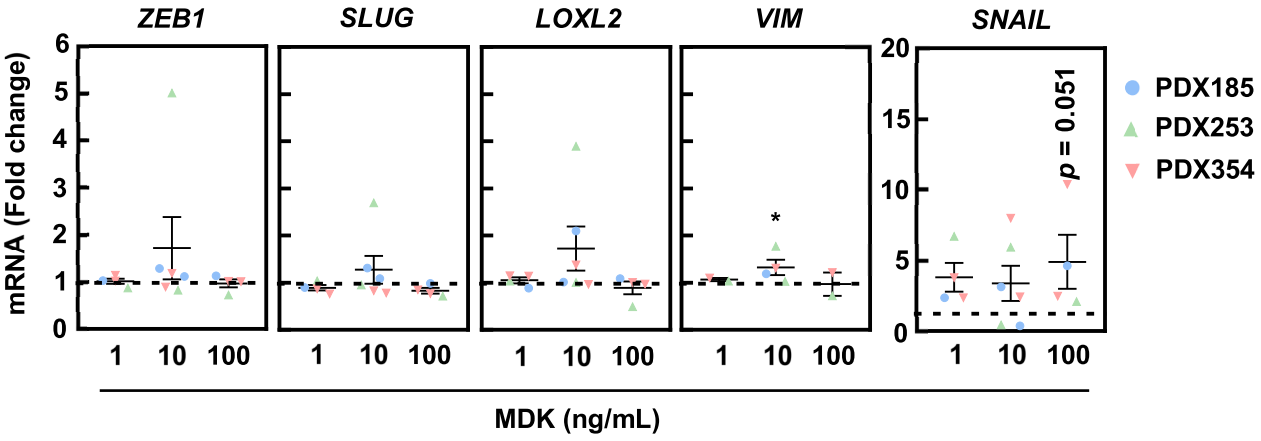

Figure II.18. RTqPCR for EMT genes mRNA levels after 72 hours of incubation with MDK at the indicated concentrations. Pooled data showing the individual values for the indicated PDXs (185 n=2, 253 n=2, 354 n=2). Data are shown as the fold change to control condition, which is represented as the dashed line, depicted as mean ± SEM and analyzed using Kruskal-Wallis test. * p<0.05, ** p<0.01, *** p<0.005.

Comparable results were obtained after treatment with PTN (**Figure II.19-II.22**). Exogenous incubation with PTN activated ALK signaling at short times by inducing ALK and ERK 1/2 phosphorylation (**Figure II.19A**). Likewise, this activation had functional effects on CSCs since both self-renewal and clonogenic capacity were enhanced with the treatment (**Figure II.19B and II.19C, respectively**).

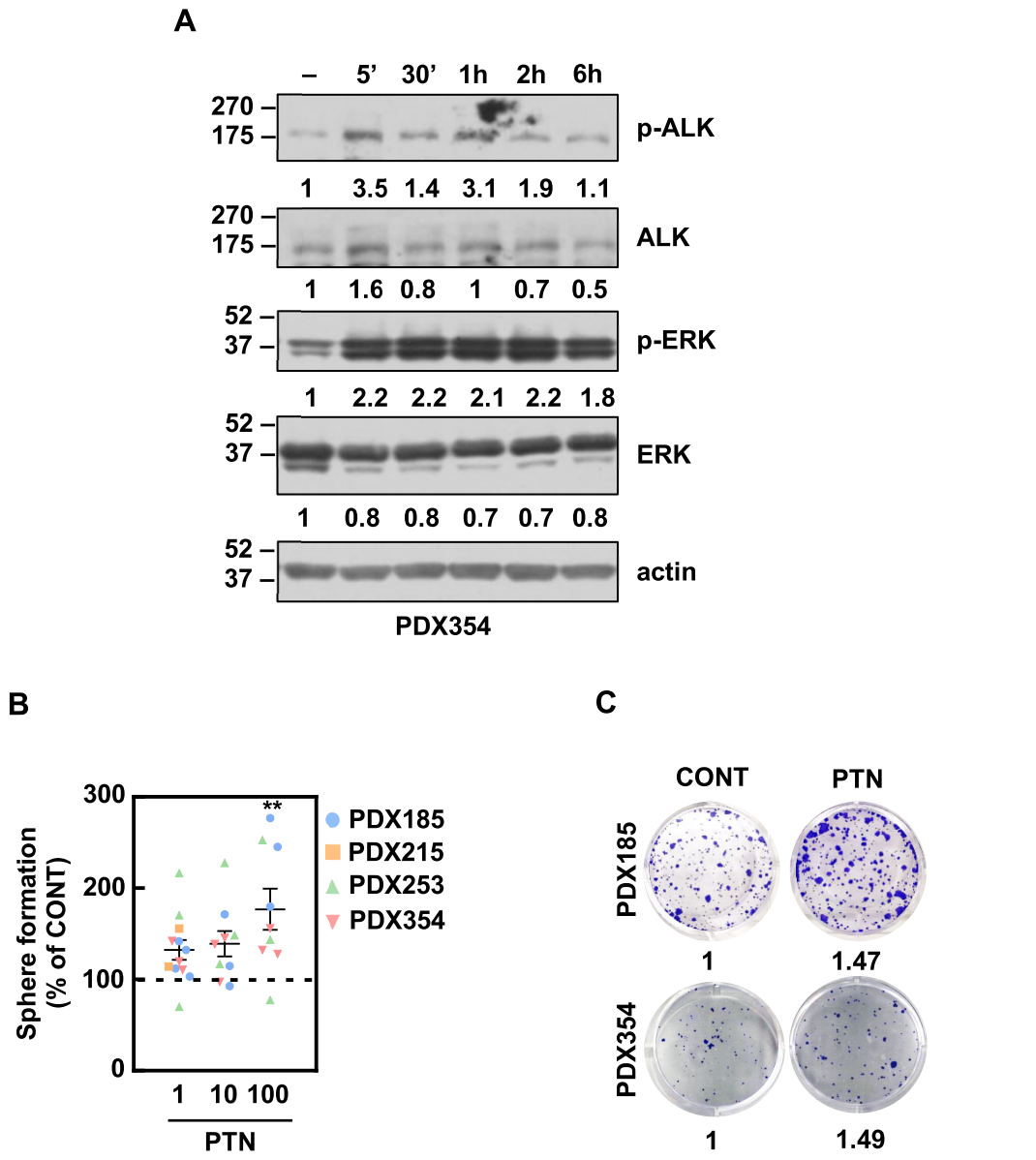

Figure II.19. A) Kinetics of ALK activation after the indicated times of treatment with 1 ng/mL of recombinant PTN measured by Western Blot. Numbers represent the quantification of the band intensity for each protein normalized by actin, shown as the fold change to control condition (n=1). **B)** Sphere formation assay after pre-treatment with recombinant PTN for 72 hours at the indicated concentrations (ng/mL) in adherent conditions. Pooled data showing the individual values for the indicated PDXs (185 n=4, 215 n=2, 253 n=3, 354 n=3). Data are shown as the fold change to control condition, which is represented as the dashed line, depicted as mean ± SEM and analyzed using Kruskal-Wallis test. * $p<0.05$, ** $p<0.01$, *** $p<0.005$. **C)** Representative colony formation assay after 21 days of treatment with 10 ng/mL recombinant PTN (n=1 for each PDX). The numbers represent the crystal violet staining absorbance, shown as the fold change to control condition.

Similar to MDK, PTN did not show increased pluripotency genes (**Figure II. 20A**) nor surface markers (**Figure II.20B**) expression in the cells, but rather significantly decreased the percentage of CD133⁺/CD44⁺ cells (**Figure II.20B**).

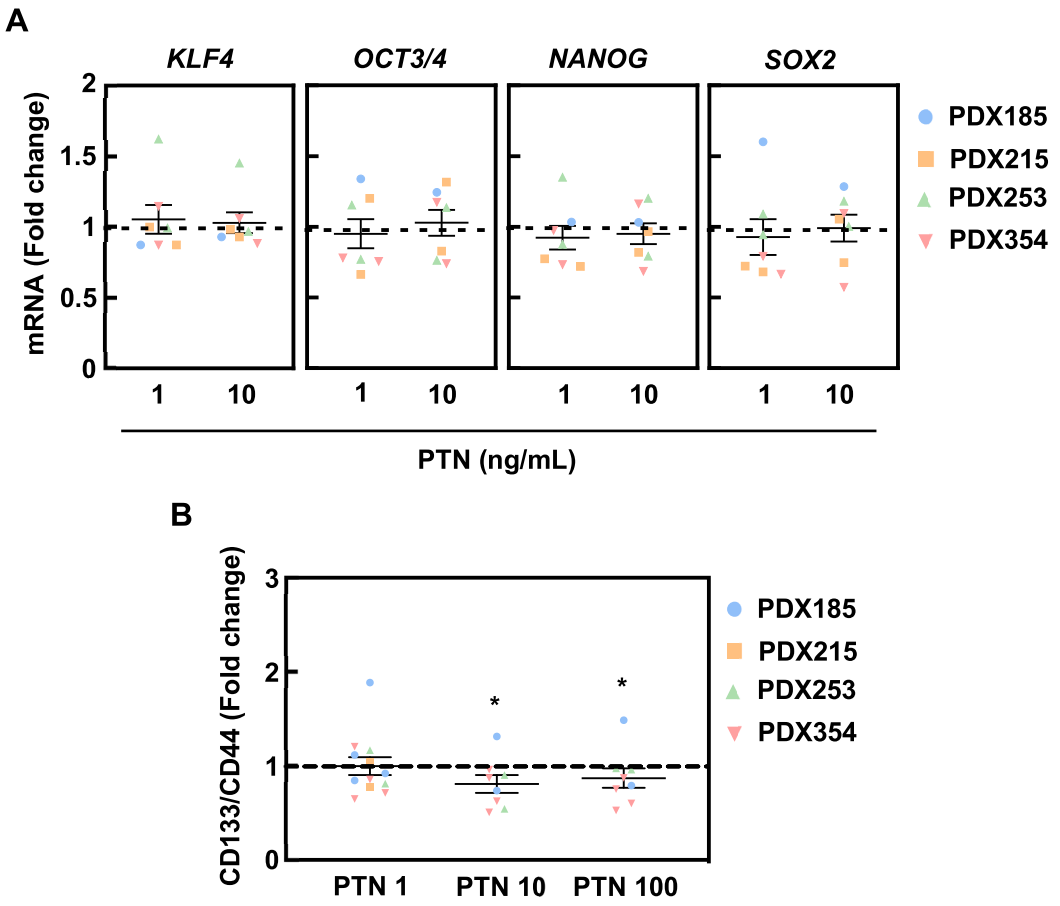

Figure II.20. A) RTqPCR for pluripotency genes mRNA levels after 72 hours of incubation with PTN at the indicated concentrations. Pooled data showing the individual values for the indicated PDXs (185 n=1, 215 n=2, 253 n=2, 354 n=2). **B)** CSC population measured as CD133⁺/CD44⁺ cells by FACS after 72h of incubation with PTN at the indicated concentrations (ng/mL). Pooled data showing the individual values for the indicated PDXs (185 n=4, 215 n=2, 253 n=2, 354 n=4). Data are shown as the fold change to control condition, which is represented as the dashed line, depicted as mean ± SEM and analyzed using Kruskal-Wallis test. * p<0.05, ** p<0.01, *** p<0.005.

Treatment with recombinant PTN increased wound closure (**Figure II.21**). As happened with MDK, the differences were especially visible at 24 and 48 hours.

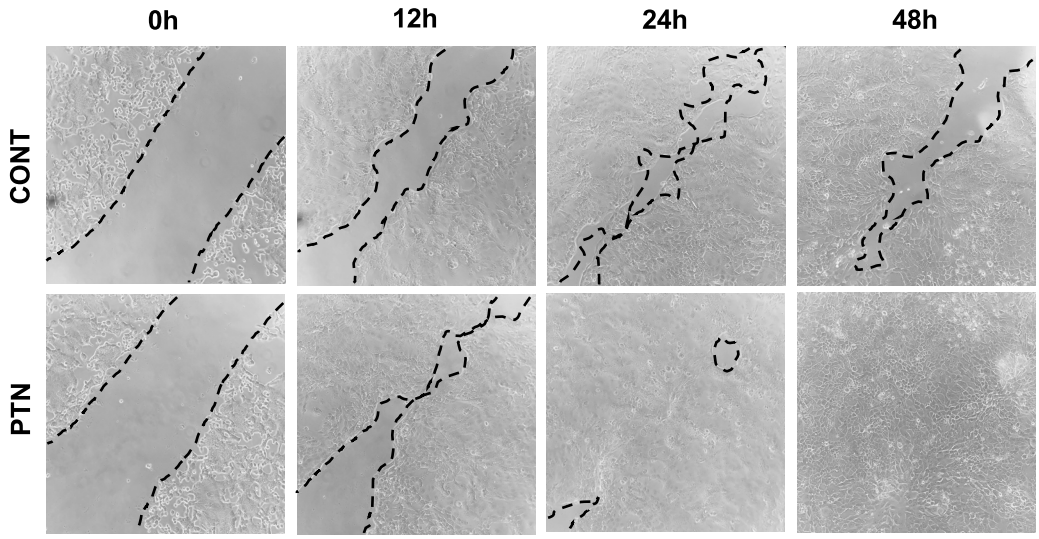

Figure II.21. Scratch wound healing assay of PDX354 treated with 20 ng/mL PTN for 48 hours after performing the scratch. Pictures were taken at the indicated times with an inverted microscope at 10X magnification (n=1).

Finally, comparable to MDK, exogenous PTN barely increased the expression of some of the EMT genes analyzed, although not significantly (**Figure II.22**).

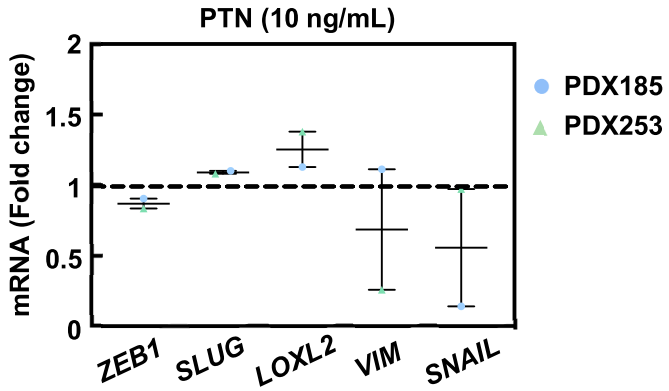

Figure II.22. RTqPCR for EMT genes mRNA levels after 72 hours of incubation with PTN at the indicated concentration. Pooled data showing the individual values of the indicated PDXs (185 n=1, 253 n=1). Data are shown as the fold change to control condition, which is represented as the dashed line, depicted as mean ± SEM and analyzed using Mann-Whitney test. * $p<0.05$, ** $p<0.01$, *** $p<0.005$.

These results confirm that ligand-dependent activation of the ALK pathway enhances PDAC aggressiveness by boosting CSCs properties. Whereas acute treatment with exogenous MDK or PTN did not substantially modify gene expression patterns, their effects on PaCSC properties were completely functional.

4. The crosstalk between TAMs and PaCSCs might be promoting immunoevasion *via* ALK signaling

As demonstrated in PDAC[99] and melanoma[223], cancer cells shape the tumor niche towards a tolerogenic, immunosuppressive microenvironment by inducing macrophage polarization to M2 protumoral macrophages (also called tumor associated macrophages, TAMs). On the one hand, melanoma-secreted MDK has a key role in educating macrophages to favor the immunosuppressive environment through IFN modulation[223]. Likewise, PDAC cells promote monocyte differentiation towards the M2 phenotype to exert their immunosuppressive role. In turn, these TAMs promote aggressiveness of PDAC cells by increasing CSC properties[99]. However, in PDAC, this macrophage polarization has not been linked to MDK.

Considering that MCM enhances PaCSCs properties by increasing self-renewal and tumorigenic capacity and promoting the invasive abilities *via* secreted factors, and that PDAC cells induced *MDK* mRNA levels in TAMs[99], we wondered whether MCM may also trigger ALK pathway signaling. Intriguingly, incubation of PDAC cells with MCM at short times induced a rapid (i.e., 30 minutes and two hours) and potent phosphorylation of ALK receptor in both the PDXs tested while maintaining total ALK levels virtually unchanged (**Figure II.23A**). Conversely, longer exposure times (i.e., 24 hours), while showed different response in p-ALK levels depending on the PDX, probably due to their inherent heterogeneity, both cell types downregulated total ALK protein levels (**Figure II.23B**). These results were further confirmed by RTqPCR as *ALK* mRNA levels were also reduced at longer times of MCM exposure (i.e., 48 hours; **Figure II.23C**).

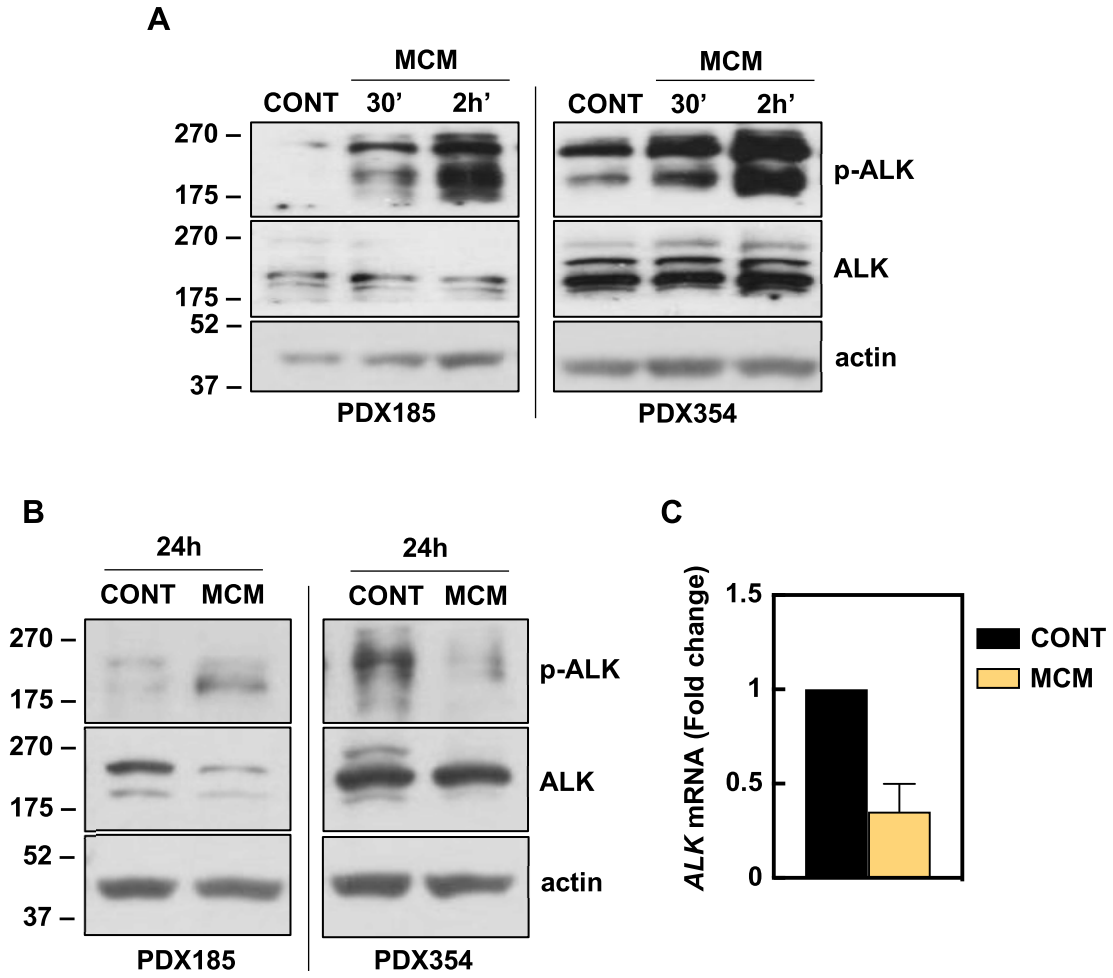

Figure II.23. A, B) Western blot of cell lysates from PDX185 and 354 incubated with M2-polarized macrophages-conditioned medium (MCM) for the indicated times (n=1 for each PDX). Actin was used as loading control. **C)** RTqPCR for *ALK* mRNA levels after 48 hours of incubation with MCM in PDX354 (n=2). Data are shown as the fold change to control condition, depicted as mean ± SEM and analyzed using Mann-Whitney test.

The regulation of PaCSC biology functions on a bidirectional communication between them and all the components of the tumor niche. On the one hand, we know that TAMs significantly upregulate *MDK* mRNA when stimulated by PDAC cells[99]. Despite that, we failed to detect MDK in MCM samples (**Figure II.24A**). On the other hand, incubation of PDAC cells with MCM revealed a trend to increase *MDK* expression in cancer cells (**Figure II.24B**).

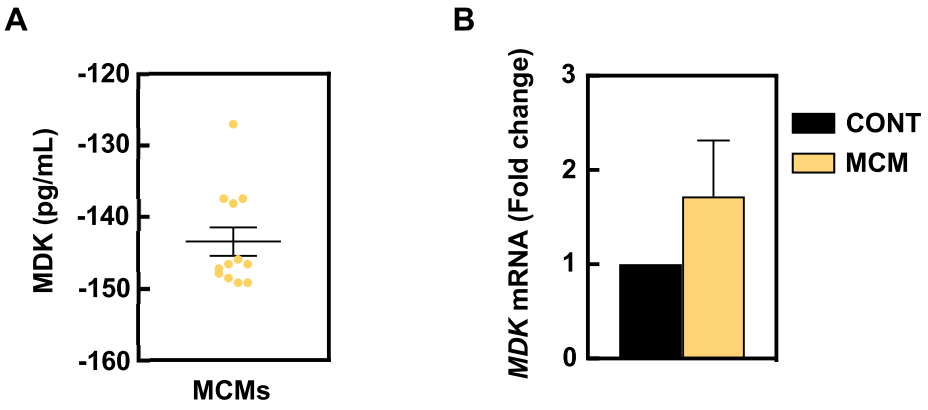

Figure II.24. A) MDK detection in supernants from M2-polarized protumoral macrophages by ELISA. Pooled data showing the individual values of different MCM samples (n=12). Data are depicted as mean ± SEM. **B)** RTqPCR for *MDK* mRNA levels after 48 hours of incubation with MCM in PDX354 (n=2). Data are shown as the fold change to control condition, depicted as mean ± SEM and analyzed using Mann-Whitney test.

Consequently, we decided to perform correlation analyses of our genes of interest with a recently described TAMs infiltration signature comprising 10 upregulated genes in PDAC[211]. Recurrently, neither *ALK* nor *PTN* expression correlated with TAMs infiltration in PDAC (**Figure II.25, left and right panels, respectively**). However, both *ALK* OE signature and *MDK* expression were robustly associated with TAMs infiltration (**Figure II.25, middle-left and middle-right panels, respectively**), especially the *ALK* OE signature.

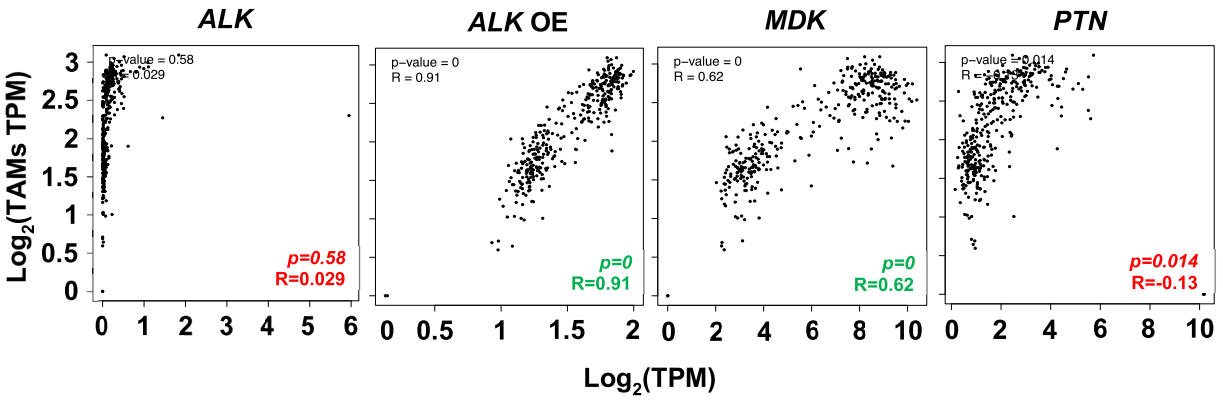

Figure II.25. Correlation expression of a TAMs infiltration signature with *ALK* (**left panel**), *ALK* OE signature (**middle-left panel**), *MDK* (**middle-right panel**) or *PTN* (**right panel**) in human tissues from TCGA and GTEx datasets. The Pearson correlation coefficient (R) is calculated and interpreted as follows together with the *p*-value: the color green represents a *p*-value<0.05 and a R>0.5, while the color red represents either a *p*-value>0.05 or a R<0 (negative correlation). TPM: transcripts per million.

One of the most widely studied mechanisms of immunoevasion in cancer is the one featured by programmed cell death-ligand 1 and programmed cell death-1 (PD-L1 and PD-1, respectively) proteins. The expression of these two proteins promotes self-tolerance by regulating effector T cell activity and viability, as well as avoiding regulatory T cell apoptosis[92]. Because of oncogenic fusion protein NPM/ALK has been linked to increased *PD-L1* expression in T cell lymphoma (ALK$^+$ TCL), we decided to run correlation bioinformatic analyses of *PD-L1* expression with different components of the ALK pathway. While neither *ALK* nor *PTN* expression alone correlated with *PD-L1* expression in PDAC patients (**Figure II.26, left and right panels, respectively**), both the *ALK* OE signature and *MDK* did show a significant positive correlation with *PD-L1* (**Figure II.26, middle-left and middle-right panels, respectively**).

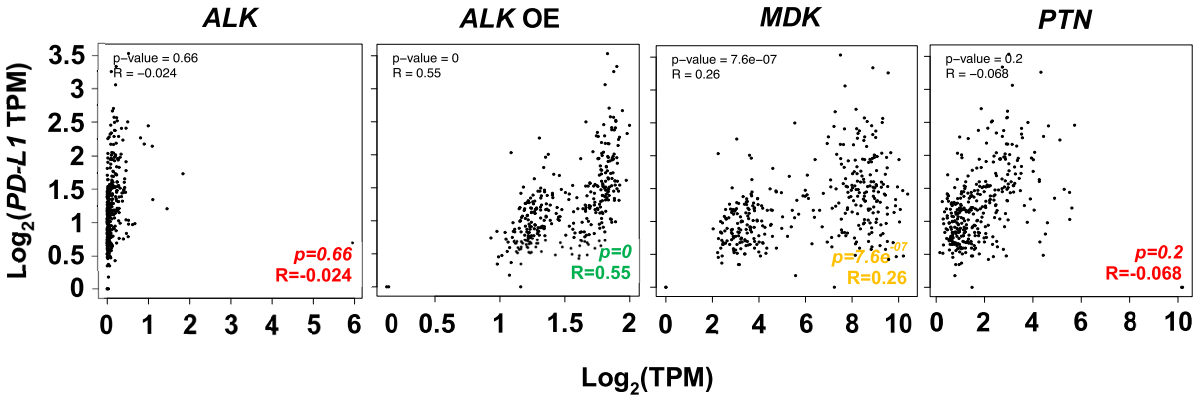

Figure II.26. Correlation expression of *PD-L1* with *ALK* (**left panel**), *ALK* OE signature (**middle-left panel**), *MDK* (**middle-right panel**) or *PTN* (**right panel**) in human tissues from TCGA and GTEx datasets. The Pearson correlation coefficient (R) is calculated and interpreted as follows together with the *p*-value: the color green represents a *p*-value<0.05 and a R>0.5, the color orange represents a *p*-value<0.05 and a R<0.5, while the color red represents either a *p*-value>0.05 or a R<0 (negative correlation). TPM: transcripts per million.

As TAMs are able to induce *PD-L1* expression in PDAC[211], we decided to validate if conditioned medium from TAMs (i.e., MCM) is able to induce *PD-L1* expression in our models. As we thought, MCM induced a significant increase in *PD-L1* mRNA levels (**Figure II.27A**). Although not significant, we detected a slight induction of *PD-L1* expression upon exogenous MDK and PTN treatment in a first attempt with little consistency among the different PDXs tested (**Figure II.27B**).

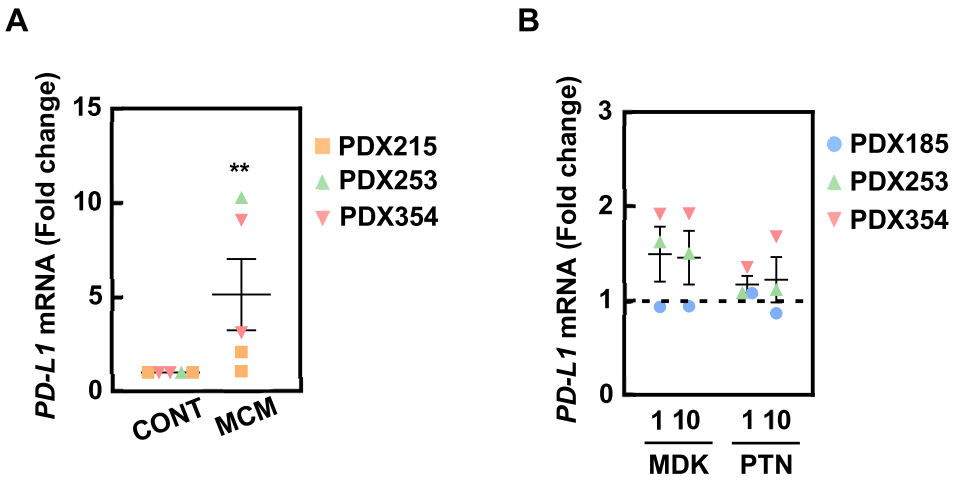

Figure II.27. A) RTqPCR for *PD-L1* mRNA levels after 48 hours of incubation with MCM. Pooled data showing the individual values for the indicated PDXs (215 n=2, 253 n=1, 354 n=2). **B)** RTqPCR for *PD-L1* mRNA levels after 72 hours of incubation with MDK or PTN (ng/mL). Pooled data showing the individual values for the indicated PDXs (185 n=1, 253 n=1, 354 n=1). Data are shown as the fold change to control condition, which is represented as the dashed line, depicted as mean ± SEM and analyzed using Mann-Whitney test. * $p<0.05$, ** $p<0.01$, *** $p<0.005$.

Altogether, these data suggest that the ALK signaling pathway may promote an immunotolerogenic microenvironment involving TAMs *via* secreted factors, although other assays are required in order to support these initial findings.

5. ALK inhibition abrogates CSC functionality *in vitro* and *in vivo*

The use of small compounds, like Crizotinib or Ensartinib, to inhibit ALK signaling is a common approach to treat ALK^+ cancer-related malignancies, such as NSCLC[224]. Considering ALK contribution to stemness in PDAC, we decided to test the effects of these compounds on our PDXs and the metastatic CTCA.

First, both Crizotinib and Ensartinib inhibited cell proliferation, with IC_{50} ranging from 0.7 to 3.8 and 0.4 to 1.8 μM, respectively (**Figure II.28A and II.28B**). Because the IC_{50} calculated is related to inhibition of proliferation in the bulk tumor cells, which is mainly representative of the differentiated cells (95-99% of the total cell density), we decided to use a wider range of the compounds' dosage for further experiments to ensure PaCSCs killing and functional inhibition. As a result, both compounds inhibited ALK phosphorylation and downstream signaling at the selected concentrations (**Figure II.27C**).

A

	Absolute IC_{50} (µM)				
	PDX185	PDX215	PDX253	PDX354	CTCA
CRIZO	3.745	0.809	2.173	1.097	0.681
ENS	1.760	0.3901	1.410	0.7847	1.052

B

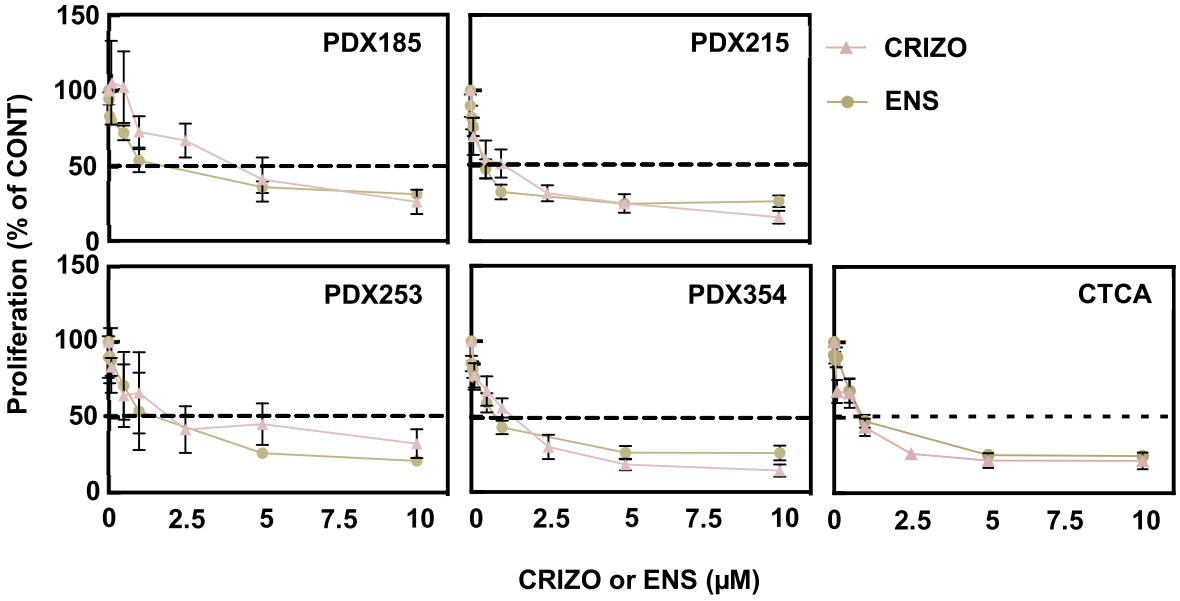

C

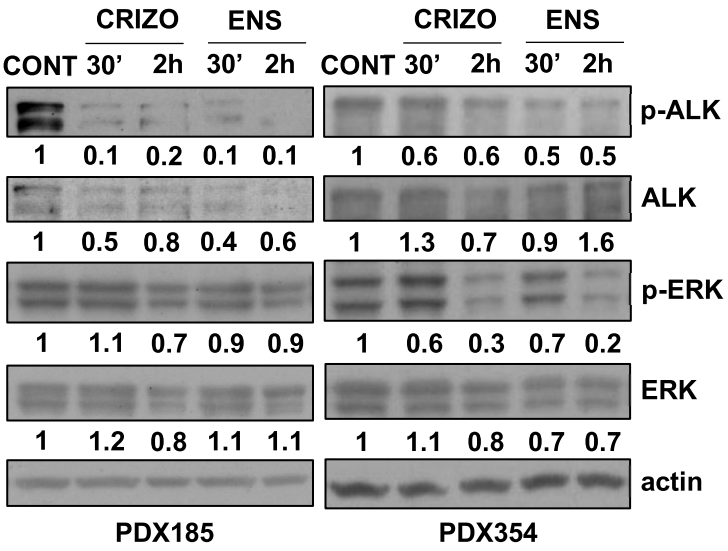

Figure II. 28. A) IC_{50} of Crizotinib and Ensartinib at 72 hours of treatment for each cell type (Crizotinib: PDX185 n=3, 215 n=11, 253 n=3, 354 n=9, CTCA n=17; Ensartinib: PDX185 n=3, 215 n=4, 253 n=2, 354 n=4, CTCA n=6). **B)** Proliferation rate graph of each cell type from which A is derived. Data are shown as the fold change to control condition and depicted as mean ± SEM. The dashed line represents the 50% of cell proliferation inhibition. **C)** Kinetics of ALK inhibition after the indicated times of treatment with 10 µM Crizotinib and 5 µM Ensartinib measured by western blot (n=1 for each PDX). The numbers represent the quantification of the band intensity of each protein normalized by actin, shown as the fold change to the control group.

Consequently, ALK inhibition with Crizotinib induced cell toxicity in most of the cell types assessed and especially at the highest dose tested (**Figure II.29, left panel**). Regardless of the different response of each cell type, toxicity was significantly induced from 0.5 µM in pooled samples (**Figure II.29, right panel**).

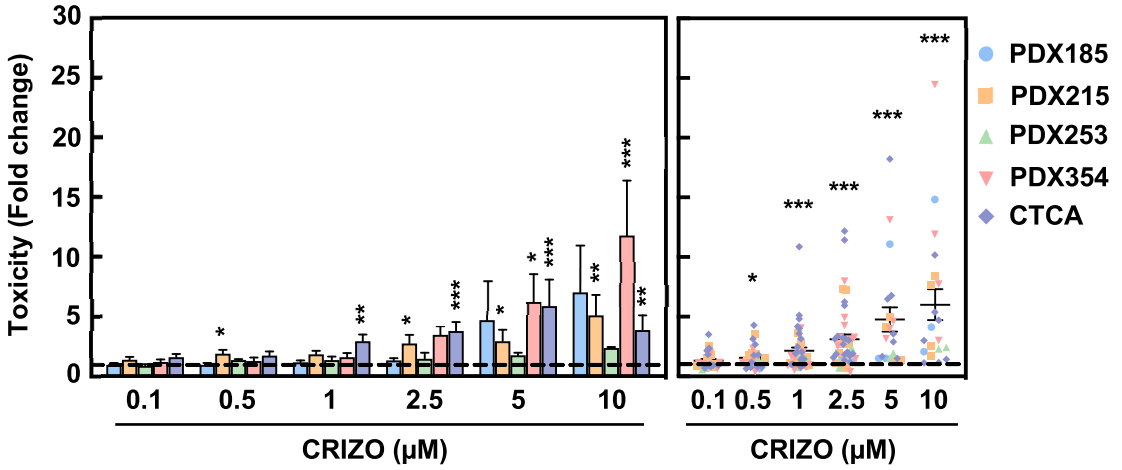

Figure II.29. Toxicity of Crizotinib for each cell type assessed by MultiTox-Fluor Multiplex Cytotoxicity Assay and measured as relative fluorescence units normalized by crystal violet. **Left panel**: mean value for each cell type separately, **right panel**: pooled data showing the individual values for each cell type (PDX185 n=3, 215 n=11, 253 n=3, 354 n=9, CTCA n=18). Data are shown as the fold change to control condition, which is represented as the dashed line, depicted as mean ± SEM and analyzed using Kruskal-Wallis test. * $p<0.05$, ** $p<0.01$, *** $p<0.005$.

We measured next cell death after treatment with both compounds. Treatment with both Crizotinib and Ensartinib efficiently induced cell death in the tumor bulk in all the cell types tested at the highest dosage (**Figure II.30A and II.30B, respectively**).

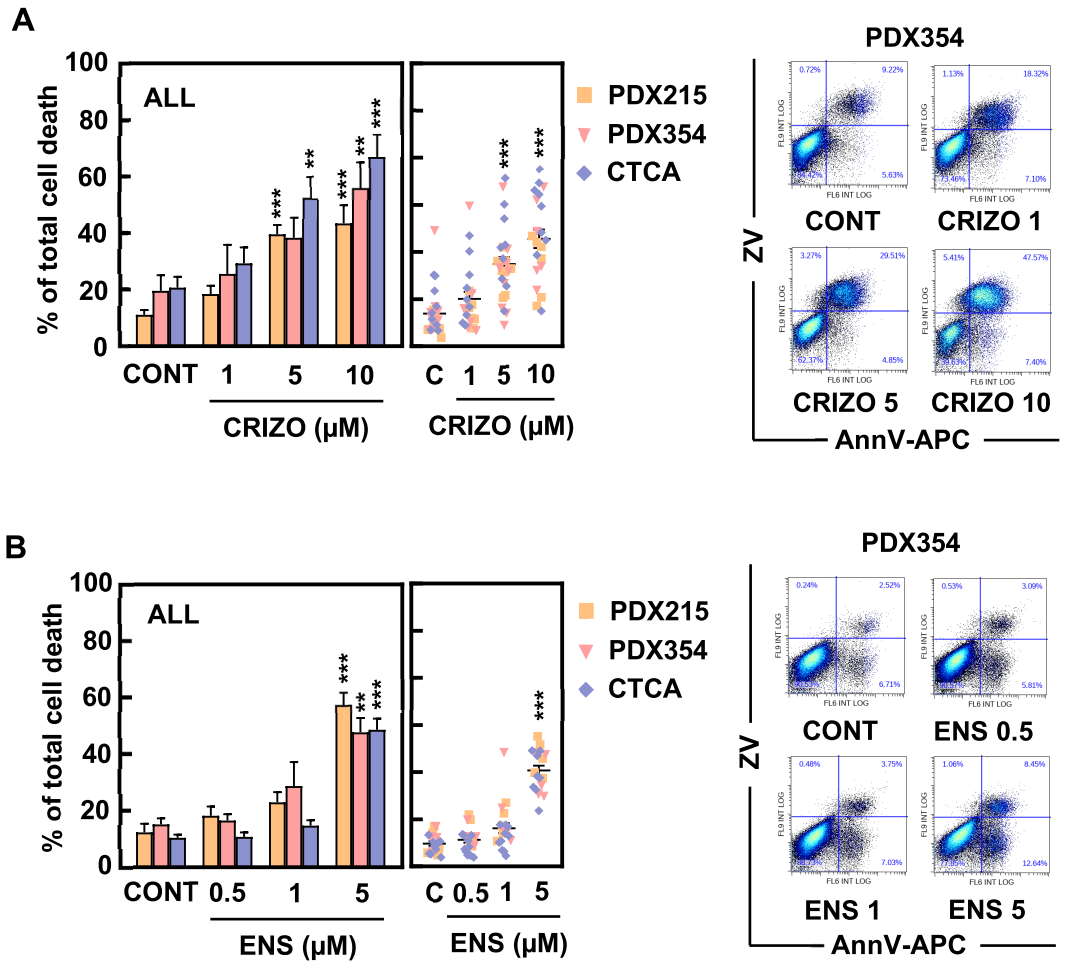

Figure II.30. A, B) Percentage of total cell death measured as the sum of Annexin V⁺, Zombie Violet⁺ and double positive staining by FACS in the whole population after 48 hours of treatment with Crizotinib (**A**; PDX215 n=8, 354 n=9, CTCA n=9) or Ensartinib (**B**; PDX215 n=5, 354 n=5, CTCA n=10). **Left panels:** mean value for each cell type separately (**left**) and pooled data showing the individual values for each cell type (**right**); **right panels:** representative flow cytometry density plots of PDX354. Data are depicted as mean ± SEM and analyzed using Kruskal-Wallis test. * p<0.05, ** p<0.01, *** p<0.005.

Most importantly, both compounds induced cell death in the CD133⁺ population (**Figure II.31A and II.31B**), thus decreasing the CD133 content (**Figure II.31C and II.31D**).

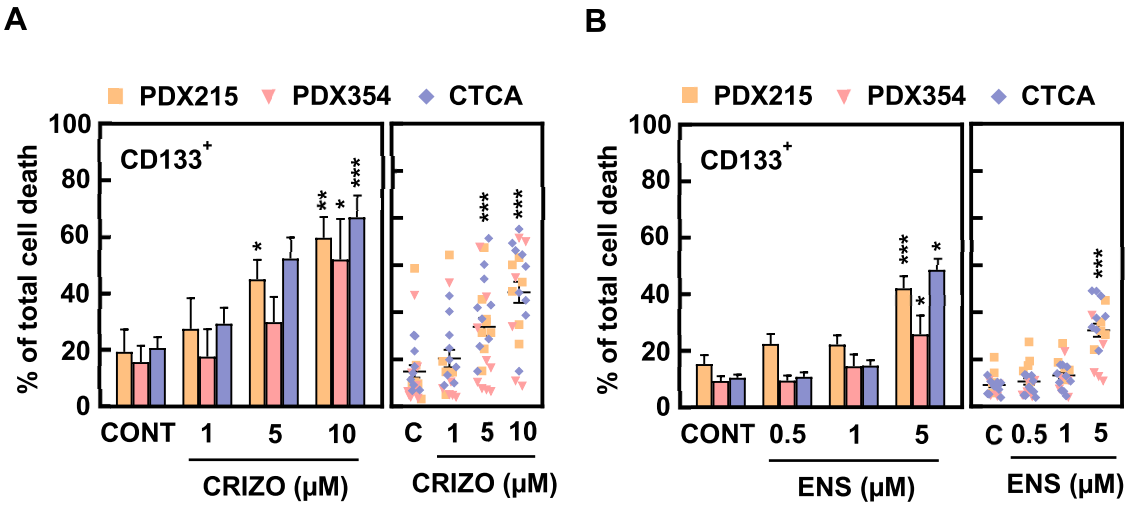
A
B
PDX215
PDX354
CTCA
CD133+
% of total cell death
CONT
CRIZO (μM)
ENS (μM)

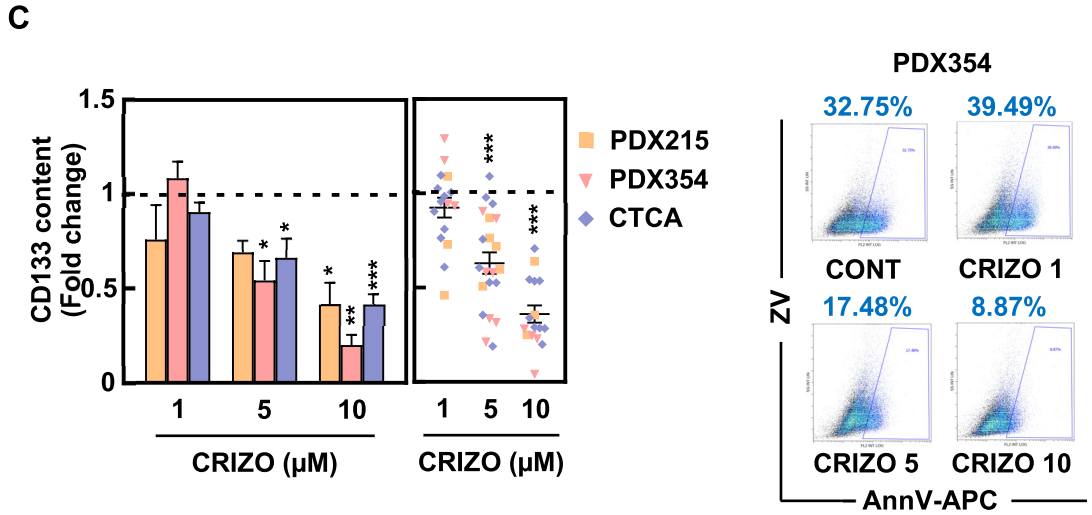
C
CD133 content (Fold change)
PDX215
PDX354
CTCA
CRIZO (μM)
PDX354
32.75%
39.49%
17.48%
8.87%
CONT
CRIZO 1
CRIZO 5
CRIZO 10
ZV
AnnV-APC

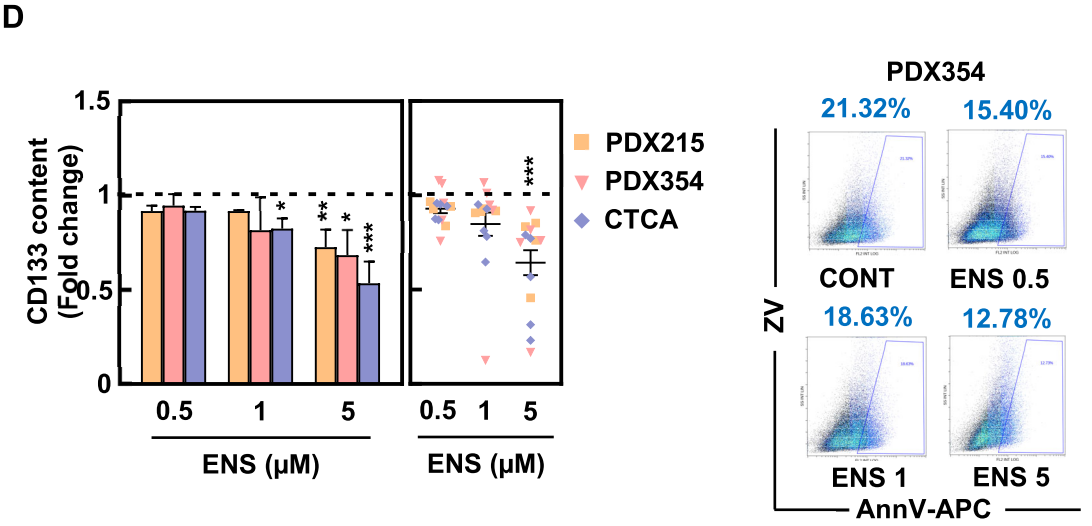
D
CD133 content (Fold change)
PDX215
PDX354
CTCA
ENS (μM)
PDX354
21.32%
15.40%
18.63%
12.78%
CONT
ENS 0.5
ENS 1
ENS 5
ZV
AnnV-APC

Figure II.31. A, B) Percentage of total cell death measured as the sum of Annexin V+, Zombie Violet+ and double positive staining by fACS in CD133+ cells after 48 hours of treatment with Crizotinib (**A**; PDX215 n=8, 354 n=9, CTCA n=9) and Ensartinib (**B**; PDX215 n=5, 354 n=5, CTCA n=10). **Left panels:** mean value of each PDX separately; **right panels:** pooled data showing the individual values of each PDX. **C, D)** CD133 content in samples from A (**C**) and B (**D**). Right panels: mean of the CD133+ content of each PDX separately (left) and pooled data showing the individual values of each PDX (right); right panels: representative flow cytometry density plots of PDX354. In A-D, data are shown as the fold change to control condition, which in C and D is represented as the dashed line, depicted as mean ± SEM and analyzed using Kruskal-Wallis test. * p<0.05, ** p<0.01, *** p<0.005.

As MCM induced EMT and enhanced invasiveness in PDAC cells (**see chapter I**), we assumed that MCM-incubated PDAC cells displayed a more aggressive phenotype that may be comparable to the CTCA metastatic model. This model of induced aggressiveness resulted especially important for us since we observed the activation of the ALK pathway by MCM (**Figure II.23A**). Thus, we decided to evaluate whether MCM-incubated PDAC cells respond as CTCA cells to the treatment with ALK inhibitors. Certainly, both Crizotinib and Ensartinib significantly increased cell death in the three PDXs tested after pre-incubation with MCM (**Figure II.32, left panel**). This resulted especially relevant for Crizotinib in the CD133+ population (**Figure II.32, right panel**).

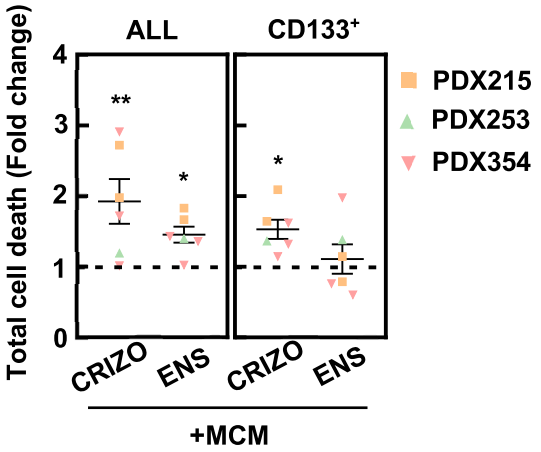

Figure II.32. Percentage of total cell death measured as the sum of Annexin V+, Zombie Violet+ and double positive staining by FACS in the whole population (**left panel**) or in the CD133+ cells (**right panel**) after 48 hours of incubation with MCM prior to 48 hours of treatment with Crizotinib or Ensartinib. Pooled data showing the individual values for the indicated PDXs (215 n=2, 253 n=1, 354 n=3). Data are shown as the fold change to control condition, which is represented as the dashed line, depicted as mean ± SEM and analyzed using Kruskal-Wallis test. * p<0.05, ** p<0.01, *** p<0.005.

Afterwards, since these findings suggested that ALK inhibition particularly targets PaCSCs, we assessed the efficacy of these compounds in impairing stemness-related functionality. Indeed, both Crizotinib and Ensartinib diminished

self-renewal (**Figure II.33A**) and clonogenic capacity (**Figure II.33B**). Likewise, pretreatment with both Crizotinib and Ensartinib decreased CSC frequency *in vitro* (**Figure II. 33C and II.33D**).

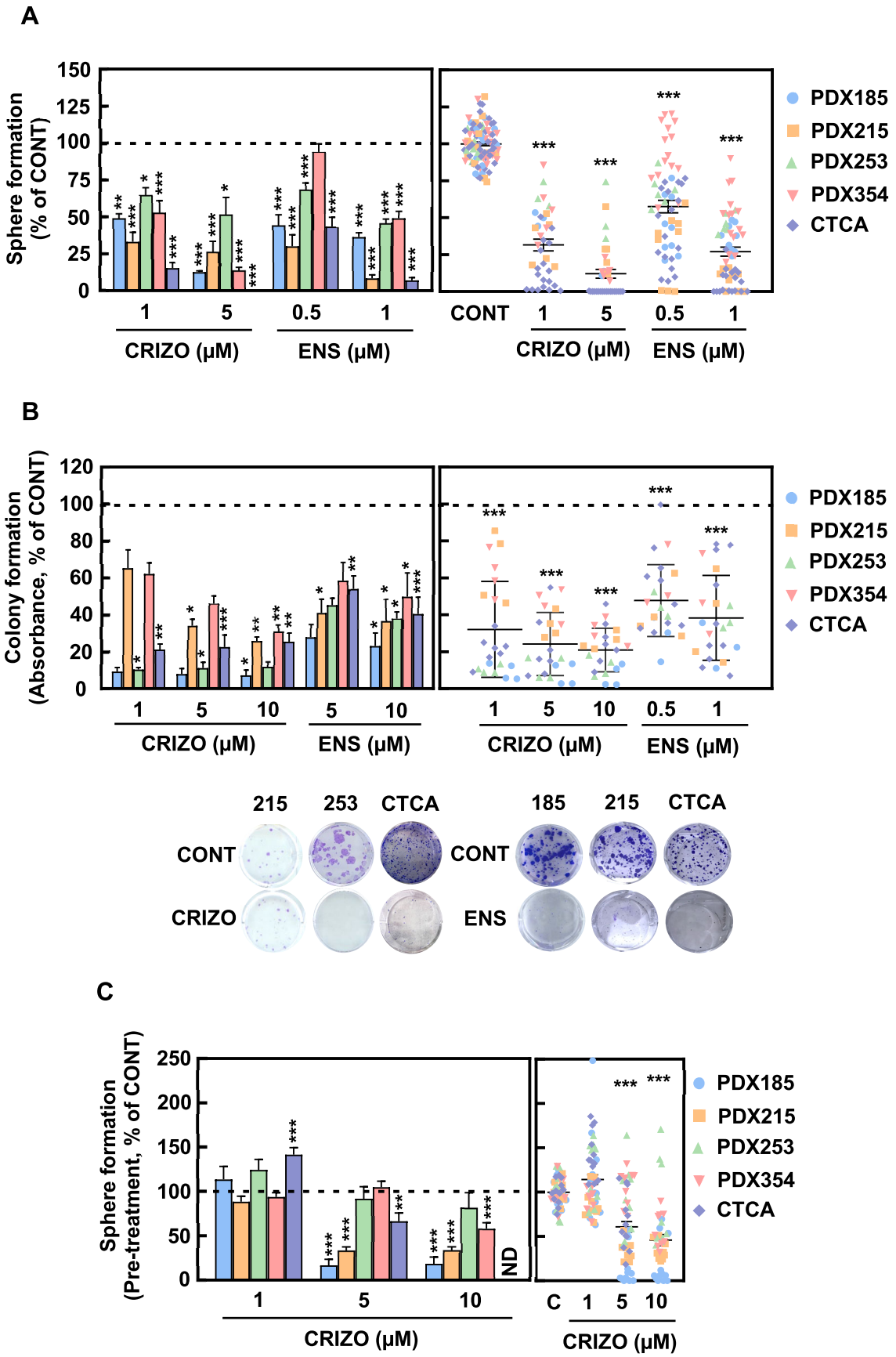

D

	PDX185		CTCA	
	CSC 1/x	*p*-value	CSC 1/x	*p*-value
CONT	28.6		8.39	
CRIZO 1	206.7	$1.69e^{-9}$	6.33	0.474
CRIZO 5	103.2	$1.69e^{-6}$	18.82	0.0455
CRIZO 10	85.6	0.00044	35.34	0.0004
ENS 0.5	75.1	0.0032	18.26	0.0491
ENS 1	315.3	$2.99e^{-13}$	16.55	0.084
ENS 5	183.2	$1.48e^{-8}$	130.51	$3.05e^{-12}$

Figure II.33. A) Sphere formation assay after seven days of treatment with Crizotinib and Ensartinib. Left panel: mean value of each PDX separately. Right panel: pooled data showing the individual values of each cell type (Crizotinib: PDX185 n=3, 215 n=6, 253 n=3, 354 n=6, CTCA n=18; Ensartinib PDX185 n=9, 215 n=9, 253 n=6, 354 n=15, CTCA n=18). **B)** Colony formation assay after 21 days of treatment with Crizotinib and Ensartinib. **Top panels:** absorbance of crystal violet shown as the mean value for each cell type separately (**left**) and pooled data showing the individual values for each cell type (**right**; Crizotinib: PDX185 n=4, 215 n=4, 253 n=4, 354 n=4, CTCA n=8; Ensartinib: PDX185 n=3, 215 n=4, 253 n=3, 354 n=3, CTCA n=10). **Bottom panel:** images of a representative experiment of each cell type treated with either 1 µM Crizotinib or Ensartinib. **C)** Sphere formation assay after pre-treatment with Crizotinib for 48 hours in adherent conditions. **Left panel:** percentage of spheres for each cell type; **right panel:** pooled data showing the individual values for each cell type (PDX185 n=12, 215 n=9, 253 n=9, 354 n=9, CTCA n=12). In A-C, data are shown as the percentage of control condition, which is represented as the dashed line, depicted as mean ± SEM and analyzed using One-way ANOVA or Kruskal-Wallis (CTCA from A, PDX185 from C) tests. * $p<0.05$, ** $p<0.01$, *** $p<0.005$. ND: not determined. **D)** CSC frequency after treatment with Crizotinib and Ensartinib for seven days, estimated by *in vitro* ELDA (n=1). Statistical significance is calculated using a chi-square test.

Then, we moved to assess whether ALK inhibition is capable of reducing invasiveness *in vitro*. Both compounds decreased the number of cells capable of invading the Matrigel™ matrix (**Figure II.34**).

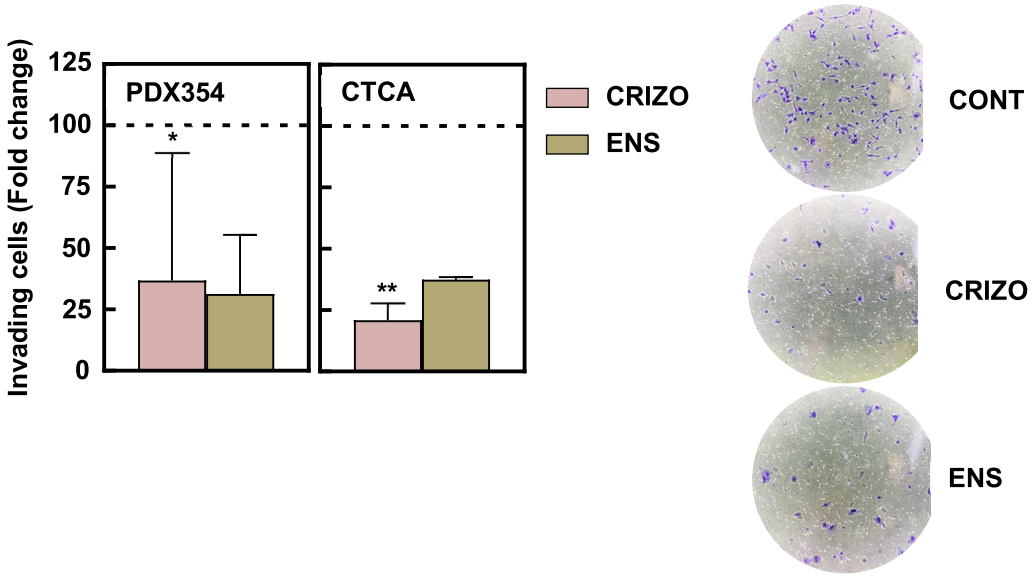

Figure II.34. Invasion assay with the indicated cell type (Crizotinib: PDX354 n=3, CTCA n=5; Ensartinib: PDX354 n=3, CTCA n=2) pre-treated with 2.5 µM Crizotinib or 5 µM Ensartinib for 48 hours. Cells were seeded in Boyden chambers and, after 24 hours, Diff Quick staining was performed and invading cells were counted. **Right panel:** mean of invading cells; **left panel:** pictures of a representative experiment of CTCA taken at 4X with an inverted microscope. Data are shown as the percentage of control condition, which is represented as the dashed line, depicted as mean ± SEM and analyzed using Kruskal-Wallis test. * p<0.05, ** p<0.01, *** p<0.005.

These effects on CSC functionality could be validated *in vivo* by an ELDA (**Figure II.35**).

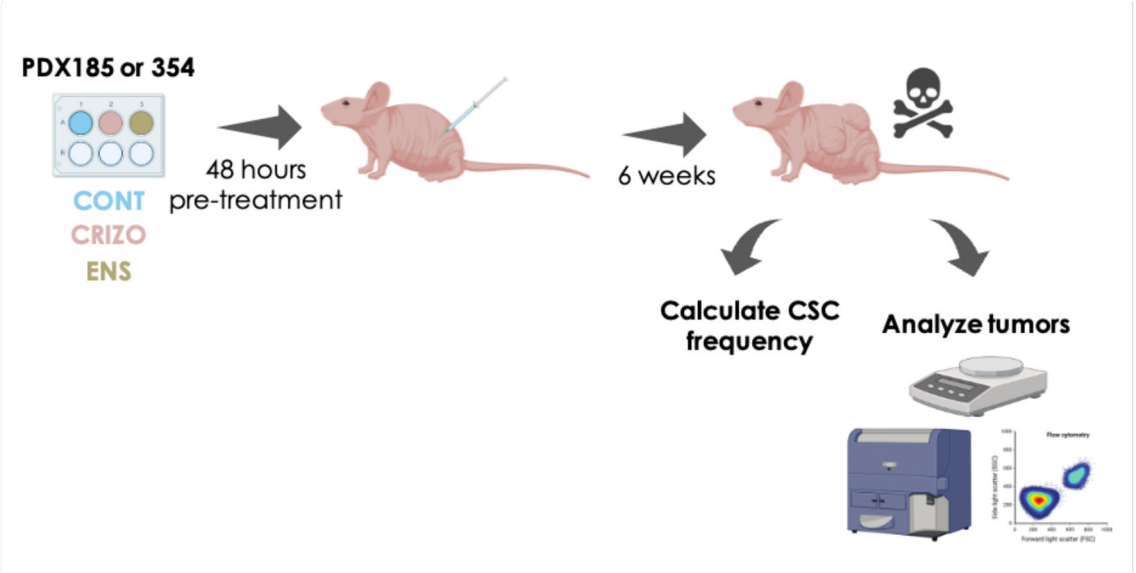

Figure II.35. Schematic overview of the *in vivo* ELDA experiment. Cells pre-treated *in vitro* with 10 µM Crizotinib and 5 µM Ensartinib for 48 hours and subcutaneously injected into the flanks of nude mice at decreasing cell densities. After 6 weeks, mice were euthanized and tumors were harvested for further analyses (PDX185 n=4 mice per group, 354: n=3 per group; all mice beared 2 subcutaneous tumors).

Pretreatment with the compounds efficiently decreased the number and size of tumors (**Figure II.36A**), the percentage of tumorigenicity (**Figure II.36B**) and the CSC frequency (**Figure II.36C**).

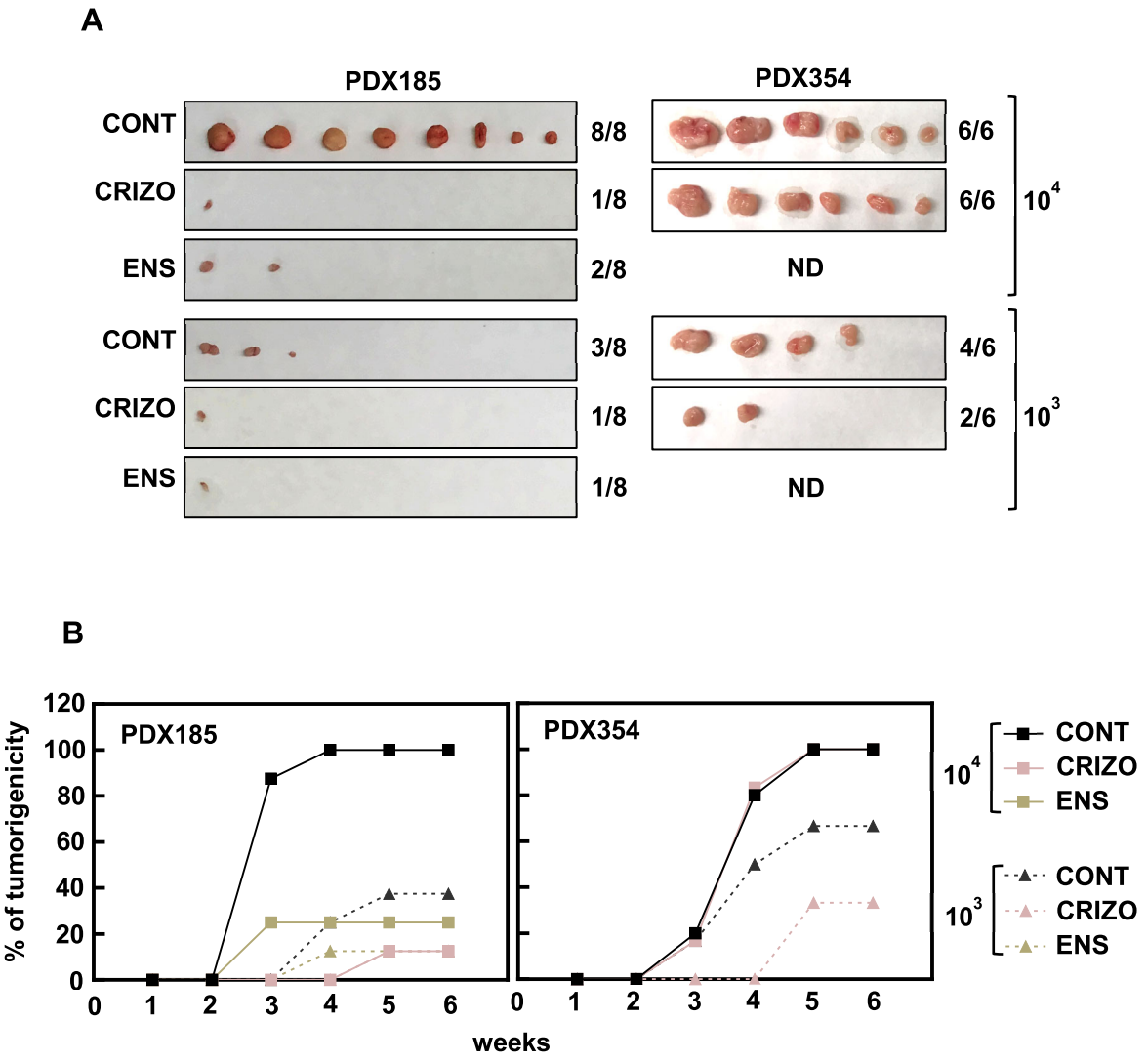

C

		CSC 1/x	*p*-value
PDX185	CONT	1961	
	CRIZO	41148	$1.75e^{-5}$
	ENS	25616	0.0001

		CSC 1/x	*p*-value
PDX354	CONT	910	
	CRIZO	2164	0.268
	ENS	ND	ND

Figure II.36. A) Pictures of tumors at end point (week six). **B)** Percentage of tumorigenicity over time. Note that the curves representing the Crizotinib conditions 10^3 and 10^4 cells overlap in PDX185. **C)** Estimated CSC frequency in PDX185 (**left**) and 354 (**right**). Statistical significance is calculated using a chi-square test. ND: not determined.

Despite no significant differences were found in the CSC frequency in PDX354, we decided to further analyze the tumors corresponding to 10^4 cells injection. Frist, no significant differences were found in tumor volume or weight, regardless of a negative trend with smaller and lighter tumors in Crizotinib condition (**Figure II.37A, left and right panels, respectively**). Importantly, even though the percentage of epithelial tumor cells remained unchanged (**Figure II.37A**), the number of $CD133^+$ cells decreased in the tumors obtained from Crizotinib-pretreated cells when analyzed by FACS (**Figure II.37B**).

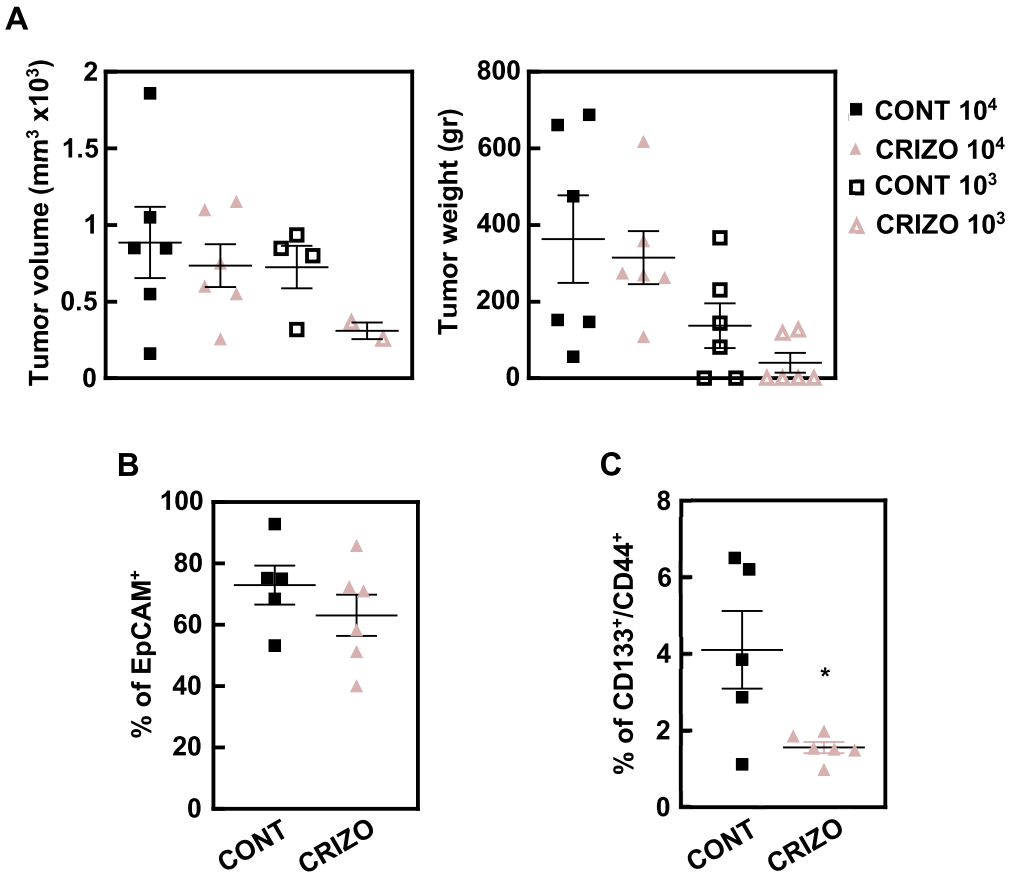

Figure II.37. A) Tumor volume (**left panel**) and weight (**right panel**) of PDX354 tumors from Figure II.36. **B, C)** FACS analyses of PDX354 10^4 tumors from Figure II.36 by which the percentage of $EpCAM^+$ cells (**B**) and the CSC population measured as $CD133^+/CD44^+$ content (**C**) was assessed. In A-C, data are depicted as mean ± SEM and analyzed using Kruskal-Wallis (A) or Mann-Whitney (B and C) tests. * $p<0.05$, ** $p<0.01$, *** $p<0.005$.

These results demonstrate that ALK inhibition targets pancreatic cancer (stem) cells at different levels: 1. by inhibiting cell proliferation and causing toxicity in the bulk tumor cells; 2. by inducing cell death in both differentiated and CSCs; and 3. by effectively impairing PaCSCs functionality *in vitro* and *in vivo*.

6. ALK inhibition prevents chemoresistance *in vitro* and *in* vivo

One of the main contributors to chemotherapy failure in PDAC is its intrinsic chemoresistance[14]. Indeed, conventional chemotherapy usually targets just the tumor bulk, thus enriching the content of chemoresistant CSCs and causing tumor relapse. Considering the toxic effect of ALK inhibitors on PaCSCs, we decided to test if either Crizotinib or Ensartinib were able to sensitize our cells to Gemcitabine treatment *in vitro*. Interestingly, the combination of Gemcitabine with Crizotinib or Ensartinib at low doses decreased considerably the IC_{50} of this chemotherapeutic agent (**Figure II.38A and II.38B**), although in a significant way only in some cases.

A

		Gemcitabine absolute IC_{50} (nM)			
		PDX185		PDX215	
		IC_{50}	*p*-value	IC_{50}	*p*-value
Proliferation	Gem	38.3		246.8	
	+CRIZO	12.4	0.0793	226.6	0.2
	+ENS	3.3	0.0209	38.1	0.049
Viability	Gem	31.3		26.9	
	+CRIZO	9.7	0.0491	8.9	0.4
	+ENS	10.7	0.062	6.0	0.1193

B

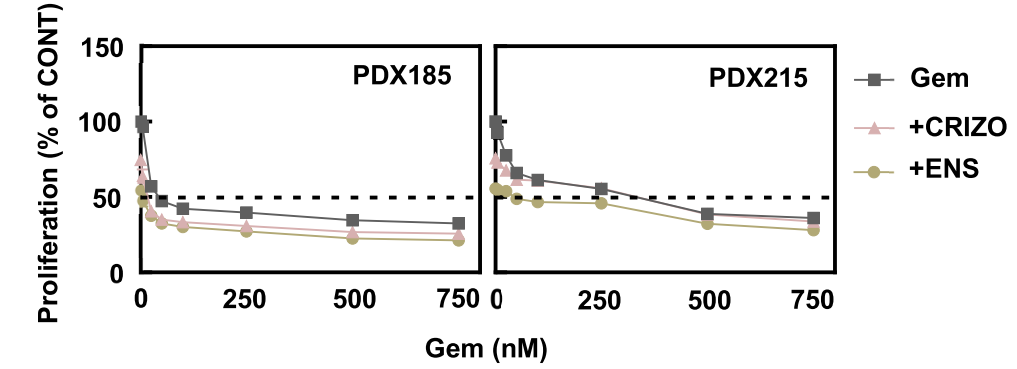

Figure II.38. The combined effect of Gemcitabine and ALK inhibitors was studied using low doses of the compounds (Gem 50 nM unless otherwise specified, Crizotinib 1 μM, Ensartinib 1 μM). **A)** IC_{50} of Gemcitabine at 72 hours of treatment alone and in combination with Crizotinib or Ensartinib for each PDX (185 n=4, 215 n=3). Data are analyzed using One-way ANOVA test. * $p<0.05$, ** $p<0.01$, *** $p<0.005$. **B)** Representative proliferation rate graph of PDX185 and 215 from which A is derived. Data are shown as the fold change to control condition and depicted as mean ± SEM. The dashed line represents the 50% of cell proliferation inhibition.

The diminished IC_{50} resulted in enhanced cell death (**Figure II.39A and II.39B**). Certainly, co-treatment with Ensartinib significantly increased cell death in the $CD133^+$ population (**Figure II.39B**) and decreased CD133 content (**Figure II.39C**) when compared to Gemcitabine alone. These results were especially relevant in the Ensartinib condition (**Figure II.39B and II.39C**).

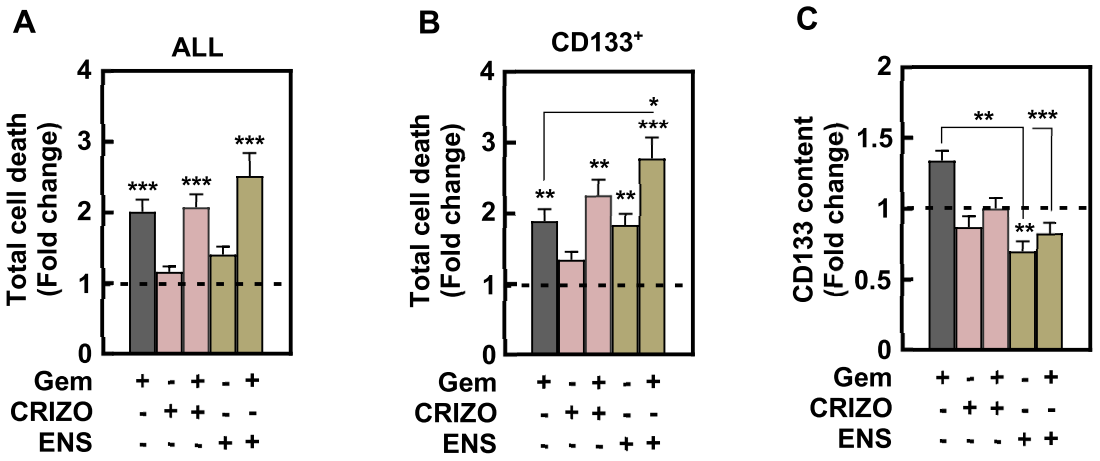

Figure II.39. The combined effect of Gemcitabine and ALK inhibitors was studied using low doses of the compounds (Gem 50 nM unless otherwise specified, Crizotinib 1 μM, Ensartinib 1 μM). Pooled data from PDX185 (n=12), 253 (n=3) and 354 (n=3). **A)** Total cell death measured as the sum of Annexin V^+, Zombie $Violet^+$ and double positive staining in the whole population after 48 hours of treatment as indicated. **B)** Total cell death measured as the sum of Annexin V^+, Zombie $Violet^+$ and double positive staining in $CD133^+$ cells after 48 hours of treatment as indicated. **C)** CD133 content of the samples shown in B. In A-C, data are shown as the fold change to control condition, which is represented as the dashed line, depicted as mean ± SEM and analyzed using Kruskal-Wallis test. * $p<0.05$, ** $p<0.01$, *** $p<0.005$.

Regarding functionality, only Ensartinib inhibited Gemcitabine-induced clonogenicity when the cells were treated at the same time (**Figure II.40A**). However, we failed to see differences in Gemcitabine alone *versus* the combination with ALK inhibitors as for self-renewal capacity (**data not shown**). For this reason, we decided to test a different and more suitable approach by pre-treating the cells in adherent conditions with Gemcitabine for 48 hours followed by seven days of treatment with ALK inhibitors alone in anchorage-independent conditions. This Gemcitabine pre-treatment strategy, while targets highly-proliferative bulk tumor cells (i.e., differentiated cells), allows for a CSC enrichment and further assessment of anti-CSC therapy with ALK inhibitors. Importantly, both Crizotinib and Ensartinib prevented Gemcitabine-induced self-

renewal capacity (**Figure II.40B**), which reflects the enrichment in CSCs induced by Gemcitabine, thus indicating the effectiveness of this combined treatment.

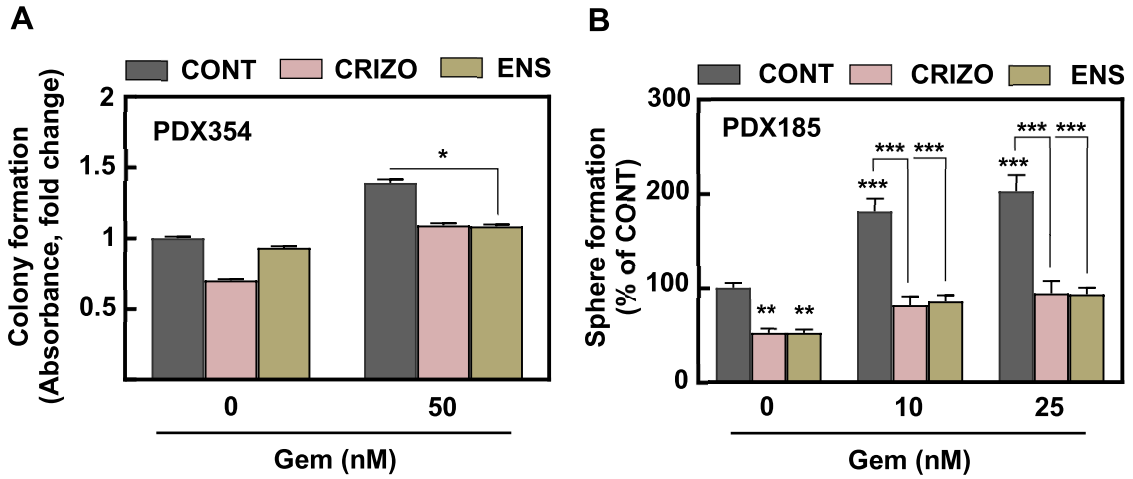

Figure II.40. The combined effect of Gemcitabine and ALK inhibitors was studied using low doses of the compounds (Gem 50 nM unless otherwise specified, Crizotinib 1 μM, Ensartinib 1 μM). **A)** Colony formation assay after 21 days of treatment with Gemcitabine alone or in combination with Crizotinib or Ensartinib at the same time (n=3). **B)** Sphere formation assay after 48 hours of Gemcitabine pre-treatment in adherent conditions prior to seven days of treatment with Crizotinib or Ensartinib in anchorage-independent conditions as indicated (n=9). Data are shown as the fold change to control condition (**A**) or the percentage of control condition (**B**), depicted as mean ± SEM and analyzed using Kruskal-Wallis test. * $p<0.05$, ** $p<0.01$, *** $p<0.005$.

Considering these results, we decided next to transfer this approach into the *in vivo* setting by treating mice bearing subcutaneous PDAC implants with Crizotinib after a chemotherapy cycle with Gemcitabine and Abraxane, the most commonly used chemotherapy combination to treat PDAC nowadays (**Figure II.41**).

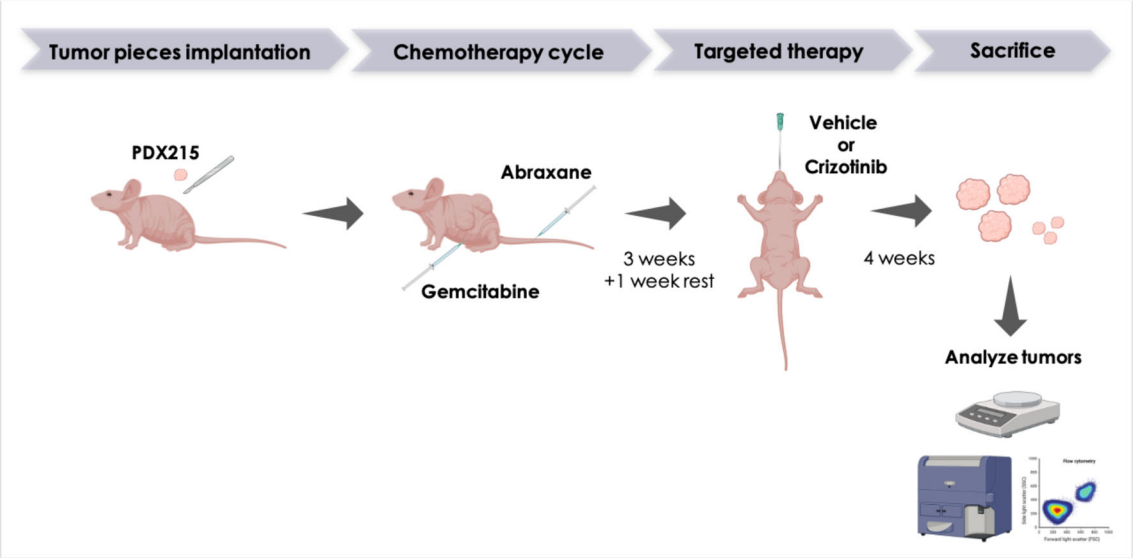

Figure II.41. Schematic overview of the *in vivo* treatment experiment. PDX215 tumor pieces were subcutaneously implanted in the flanks of nude mice. When tumors reached approximately 300 mm^3, one cycle of chemotherapy was given to the animals: 30 mg/kg of Abraxane (i.v., twice a week) in combination with 70 mg/kg of Gemcitabine (i.p., once a week) for 21 days. After seven days of rest, mice were randomized and treated with either vehicle or 25 mg/kg of Crizotinib (oral gavage, twice a day) until end point (n=4 mice per group bearing 2 subcutaneous tumors each).

We first confirmed that treatment with Crizotinib was not toxic to the animals since their body weight remained essentially unchanged (**Figure II.42**).

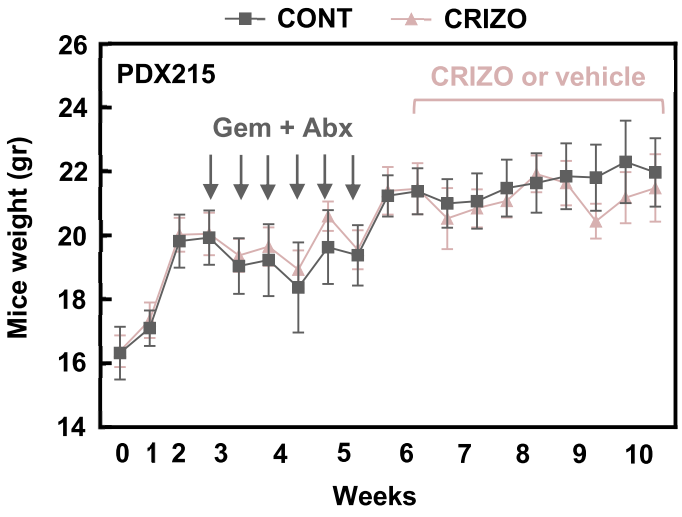

Figure II.42. Mice weight over time.

Strikingly, treatment with Crizotinib significantly delayed tumor growth after chemotherapy (**Figure II.43A**). Crizotinib-treated tumors were significantly smaller (**Figure II.43B and II.43C**) and lighter (**Figure II.43D**) than tumors in the control

group, and in some cases disappeared completely after treatment (**Figure II.43B**).

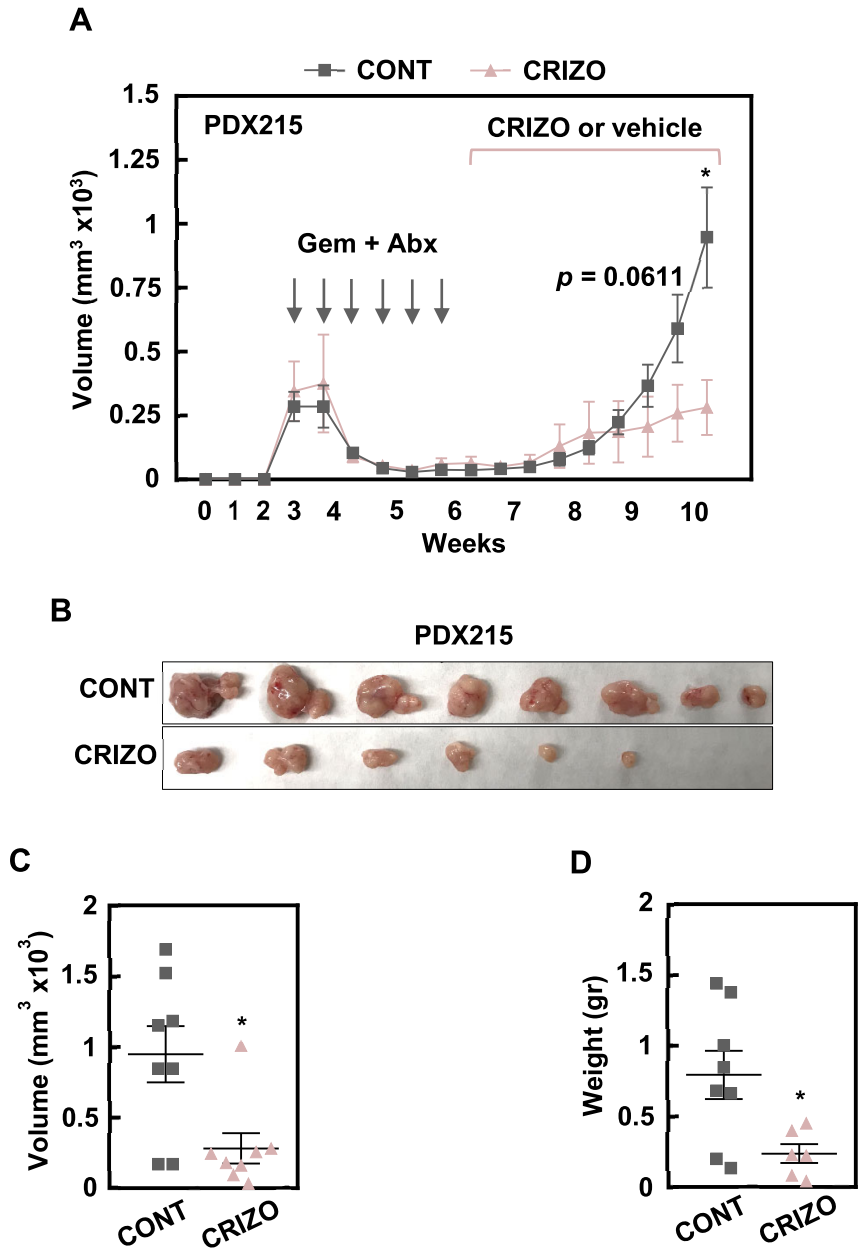

Figure II.43. A) Tumor volume over time. **B)** Pictures of tumors at end point (week 10). **C)** Tumor volume at end point (week 10). **D)** Tumor weight at end point (10 weeks). In A, C and D, data are depicted as mean ± SEM and analyzed using Students t test. * p<0.05, ** p<0.01, *** p<0.005.

Importantly, while no difference was found in the expression of the epithelial marker EpCAM (**Figure II.44A**), Crizotinib-treated tumors showed decreased content of $CD133^+/CD44^+$ cells (**Figure II.44B**) and reduced expression of stemness genes (**Figure II.44C**).

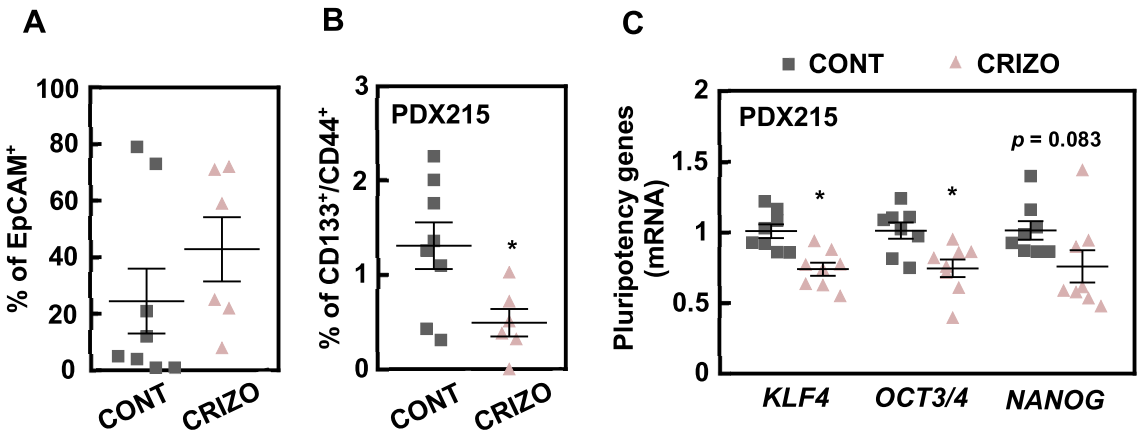

Figure II.44. A) Percentage of EpCAM+ cells of tumours shown in **Figure II.40B**. **B)** Percentage of CD133+/CD44+ cells of tumours shown in Figure II.43B. **C)** Pluripotency gene expression of tumours shown in Figure II.43B. In A-C, data are depicted as mean ± SEM and analyzed using Students t test or One-way ANOVA test. * p<0.05, ** p<0.01, *** p<0.005.

These results confirmed our hypothesis that blocking ALK using small molecule inhibitors delays tumor growth after chemotherapy by targeting PaCSCs.

Taken together, our findings demonstrate an important role of ALK receptor in PaCSCs contributing to PDAC aggressiveness. Importantly, the use of chemotherapeutic agents in combination with ALK inhibitors shows the potential for mitigating the otherwise inevitable tumor relapse after chemotherapy.

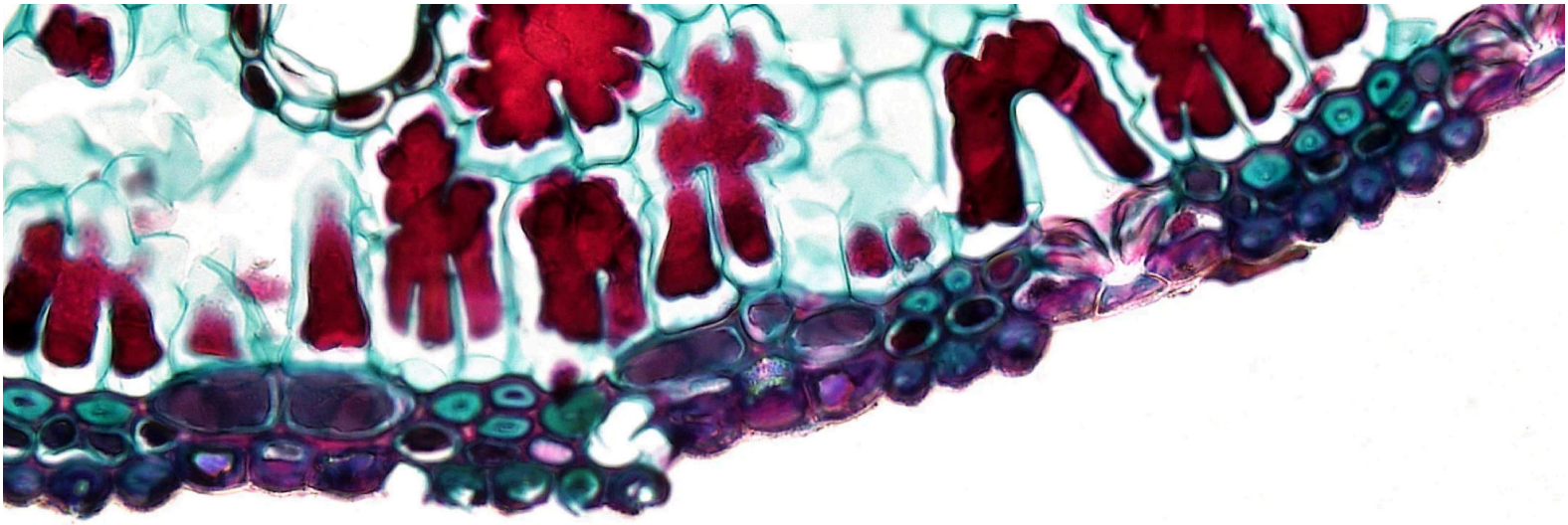

DISCUSSION: CHAPTER I

Therapies targeting the mitochondria have proven to hold promise as anti-CSCs treatment as this cell population is highly dependent on mitochondrial metabolism in many malignancies[74]. Notably, our group have demonstrated that, while differentiated cancer cells feature a glycolytic MYC-dependent metabolism, PaCSCs mainly rely on mitochondrial metabolism with increased expression levels of peroxisome proliferator-activated receptor gamma coactivator 1 alpha (*PPARGC1A* or *PGC1A*). PGC1α modulates metabolism at many levels. On the one hand, it regulates mitochondrial biogenesis, thus promoting OXPHOS[77,80]. On the contrary, it inhibits glycolysis by promoting glycogen anabolism[78,79]. Indeed, our group has demonstrated that, in PDAC, glycolysis inhibition is actually driven by reduced *MYC* expression, since genetic or pharmacologic downregulation of MYC resulted in increased *PGC1A* expression and subsequent mitochondrial oxygen consumption, while reduced glycolytic capacity. Conversely, *MYC* overexpression (OE) induced the opposite results: diminished *PGC1A* expression and oxygen consumption rate to extracellular acidification rate (OCR/ECAR) as a measurement of the metabolic switch from OXPHOS to glycolysis. Therefore, the MYC/PGC1α balance enhances aggressiveness in PDAC by controlling stemness as reduced MYC levels increases *PGC1A* expression in PaCSCs, thereby modulating their metabolism towards OXPHOS[62]. Considering this, mitochondrial targeting seemed a highly promising therapeutic option to eliminate this aggressive subpopulation in PDAC. This is the case, for instance, of the antidiabetic drug metformin, whose specificity targeting PaCSCs was indeed demonstrated by our group. In this study, the group proved that, while metformin induced cell cycle arrest in the differentiated cancer cells, it caused a significant energy crisis on PaCSCs that led to cell death, thus decreasing tumor burden and progression in mouse models[61]. However, further studies from our group on the potential anti-PaCSCs effects of metformin revealed the acquisition of resistance to this compound featured by a plastic population with stemness-related properties but lower mitochondrial load. These cells showed an intermediate metabolism based on mid expression levels of both *MYC* and *PGC1A*, with lower mitochondrial mass but still maintaining its pluripotent state ($CD133^{+}/Mito^{LOW}$)[62]. An increased balance between MYC and PGC1α caused decreased mitochondrial oxygen consumption and increased glucose uptake, lactate release and glycolytic capacity, all indicative of a

metabolic reprogramming. This scenario rendered this PaCSCs $CD133^{+}/Mito^{LOW}$ population resistant to this compound. It was confirmed, then, that the MYC/PGC1α balance determines PDAC aggressiveness by modulating stemness.

Indeed, under such metabolic stress situation induced by metformin, the resistant PaCSC population displayed a gene expression pattern and morphological changes reminiscent of the EMT program (**Figure I.1**). Strikingly, treatment with other mitochondrial partial inhibitors, such as Etomoxir, or exposure to tumor-like conditions (hypoxia, low pH and low glucose) also resulted in the acquisition of an EMT-like phenotype (**Figure I.2**), indicative of a phenotypic adaptation to nutrient shortage. This phenomenon was also further associated to microenvironmental cues derived from tumor-associated macrophages (TAMs), as M2-polarized macrophages-conditioned medium (MCM) displayed identical effects (**Figure I.2**). Importantly, MCM has been reported as a potent inducer of the EMT program in PDAC that potentiates *in vitro* invasiveness[99]. Therefore, regardless of their different mechanism of action, these two approaches (mitochondrial inhibition and MCM) induced a more aggressive phenotype based on an EMT-like gene expression pattern and mesenchymal-like morphological changes (**Figure I.2**). Whether the induction of this phenotype based on metabolic stress potentially primed PDAC cells to invade was addressed later on.

In addition to EMT-related genes, we found other genes differentially expressed in MCM- and Etomoxir-treated cells that are of especial interest for us. Interestingly, the carbohydrate PCR array performed on different primary PDAC patient-derived cells treated with Etomoxir or MCM not only displayed *MYC* upregulation and *PGC1A* downregulation, but also showed a consistent increase in peroxisome proliferator-activated receptor delta (*PPARD*) levels (**Figure I.3**). Indeed, we have now confirmed that PPAR-δ orchestrates PDAC aggressiveness by demonstrating the link between its activity and the acquisition of the EMT phenotype as a prerequisite for invasiveness and metastasis onset. PPAR-δ belongs to the nuclear receptor superfamily of ligand-activated transcription factors[225]. PPAR-δ has been linked to PDAC progression and plays a critical role in promoting metastatic dissemination in different cancers. On the one hand, a comprehensive study interrogated PPAR-δ influence in the metastatic process in

different *in vivo* models across several cancer types, including PDAC: from tail vein experimental metastasis assays with melanoma, lung carcinoma and colon cancer cells, to orthotopic spontaneous metastasis assays with pancreatic and breast cancer cells, as well as an intrasplenic experimental metastasis assay with colon cancer cells. In all these experiments, *PPARD* knockout (KO) cells were used to demonstrate a decrease in metastatic dissemination. Therefore, in these studies, the authors argue contrary to the proposed antitumor effects of PPAR-δ described for many cancers and demonstrated its inherent role in the metastatic process[146]. On the other hand, a mechanistic link between PPAR-δ and invasiveness and metastasis had been proposed in previous studies. In lung adenocarcinoma, fibroblast-derived factor 1 (SDF-1) induced EMT through the CXCR4/β-catenin/PPAR-δ axis, while downregulation of these proteins had the contrary effect. Importantly, they have demonstrated that the final player of this cascade is PPAR-δ, since *CXCR4* knockdown (KD) suppressed both *CTNNB1* (β-catenin) and *PPARD* gene expression, while *CTNNB1* KD inhibited only *PPARD* with no effects on *CXCR4*, and *PPARD* KD did not repress the expression of the other two genes[226]. However, in PDAC no mechanistic link concerning PPAR-δ has been described to date.

Concerning our results, first of all, *PPARD* was significantly overexpressed in PDAC patients from the TCGA and GTEx datasets (**Figure I.5A**), predicted disease-free survival (**Figure I.5B**) and correlated with the expression of our EMT signature (**Figure I.6A**). Additionally, *PPARD*^{HIGH} patients exhibited a significant enrichment of EMT pathways (**Figure I.6B, left panel**). The correlation between EMT and *PPARD* expression was further confirmed by single cell transcriptomic analyses (scRNAseq) performed on different advanced PDAC cells isolated from patients' blood. These analyses exhibited a consistent upregulation of *PPARD* in cells undergoing EMT (**Figure I.4**). Interestingly, MCM and Etomoxir treatment did not only increase *PPARD*/PPAR-δ gene and protein expression to levels comparable to the PPAR-δ chemical agonist GW0742 (**Figure I.8A and I.8B**), but also increased its activation (**Figure I.8C**). Even more important are the functional effects coming from PPAR-δ activation, since different PPAR-δ chemical agonists enhanced *in vitro* invasiveness like both MCM and Etomoxir (**Figure I.9B and I.9A, respectively**). Likewise, Etomoxir enhanced PPAR-δ-mediated metastatic

dissemination *in vivo*, while *PPARD* KD decreased to half the percentage of mice with micrometastases induced by Etomoxir treatment (**Figure I.11**).

MYC is the most common deregulated gene found in human malignancies taking a big part in all hallmarks of cancer, including metastasis. To exert its function, MYC necessarily forms a heterodimer with MAX[227]. There are multiple ways by which MYC regulates invasion and metastasis. For instance, a study in lung cancer demonstrated that MYC cooperates with C-RAF in a C-RAF-driven non-small cell lung cancer (NSCLC) animal model to increase metastasis incidence, although *MYC* OE in low-metastatic NSCLC cells was sufficient to induce metastatic dissemination to the lungs after their subcutaneous inoculation in immunodeficient mice[105]. However, these results may be biased by the inherent tropism of NSCLC cells to their organ-of-origin and not exclusively driven by the metastatic process. Another example is the one found in prostate cancer. In this report, a modified genetically engineered mouse model (GEMM) based on lentiviral targeting of *Pten* and *Tp53* was developed and used to demonstrate *Myc* involvement in prostate cancer metastatic dissemination[106]. While MYC implication in invasiveness and metastasis seems pretty clear, the role of PGC1α remains controversial. In melanoma[228] and prostate cancer[229], PGC1α was shown to act as a tumor suppressor, since its upregulation was proven to be crucial for reducing migration and metastasis in both diseases. Conversely, circulating mammary cancer cells showed increased *PGC1A* expression levels and enhanced mitochondrial biogenesis, while PGC1α inhibition resulted in decreased cytoskeleton remodeling and diminished invasion[230]. However, in PDAC, this link between PGC1α and invasiveness remains elusive. Altogether suggested that the MYC/PGC1α balance determines PDAC aggressiveness not only by modulating stemness, as previously reported by our group[62], but also controlling invasion, and that this could be orchestrated upstream by PPAR-δ.

While it is known that *MYC* promoter carries a PPAR responsive element (PPRE, GeneCards), a correlation between MYC and PPAR-δ to unleash metastatic disease have not been described in any cancer to date. Considering this and our previous results, we hypothesized that the MYC/PGC1α balance may be regulated upstream by PPAR-δ. Importantly, *MYC* appeared overexpressed while *PGC1A* resulted downregulated under the metabolic stress circumstances

studied here (MCM or Etomoxir treatment; **Figure I.3, I.4 and I.12**), as occurred in the previous study of the laboratory[62]. Certainly, we show here that *PPARD* modulates *MYC* promoter activity not only by *PPARD* OE but also with its activation with the chemical agonist GW0742 (**Figure I.14**). Moreover, *PGC1A* promoter activity resulted decreased under the same circumstances, although its late inhibition suggested that this modulation comes from MYC and not directly from PPAR-δ. Importantly, our group have previously confirmed that MYC downregulates *PGC1A* expression by directly binding to its promoter[62], thus posing PGC1α as a downstream target of MYC. Overall, PPAR-δ controls PDAC invasiveness by directly enhancing MYC activity towards an increased glycolytic metabolism which, in turn, downregulates PGC1α and OXPHOS. Additionally, MYC-driven metastatic dissemination may also be motivated by suppression of epithelial genes[231] and induction of mesenchymal ones[232]. Intriguingly, we show here that MYC inhibition further supported the notion that PPAR-δ mediates invasiveness through MYC signaling by significantly decreasing MCM- or Etomoxir-induced EMT-related gene expression and invading cells (**Figure I.13B and I.13A, respectively**).

Previous studies have reported that metabolic stress as a consequence of dysfunctional mitochondrial[233,234] or glutamine deprivation[235] promote invasiveness. In line with these findings, we have shown that the metabolic stress caused by either mitochondrial blockade or a starvation situation (low glucose, low oxygen) promoted the acquisition of a more aggressive phenotype (**Figure I.2**), most likely primed to migrate towards less scarce microenvironments. This phenomenon suggests that metabolic adaptation may occur in cancer cells when they face hostile nutrient shortage, and that this metabolic plasticity is a prerequisite to acquire a more aggressive invading phenotype to increase the probability of surviving. Indeed, this is what takes place in highly tumorigenic pancreatic cancer cells (i.e., PaCSCs) when the tumor progress to metastatic stages since, as mentioned before, different clones of these cells with distinct metabolic phenotypes coexist[62]. In addition to this, the tumor microenvironment (TME) in PDAC is characterized by an extremely abundant and dense stromal compartment with remarkable hypovascularization, which represents one of the hallmarks of PDAC. This situation contributes to the harsh microenvironmental conditions (i.e., nutrient deprivation and lack of oxygen) to which pancreatic

cancer (stem) cells need to adapt in order to thrive[236]. As mentioned earlier in this discussion, further characterization of the metformin-resistant PaCSCs subpopulation suggested that, certainly, metabolic stress or stromal cues unleashed the EMT genetic program through metabolic modulation (**Figure I.2**) although this hypothesis was not confirmed in this PhD work. Overall, this ability of cancer (stem) cells to reprogram their metabolism upon metabolic stress render them highly defiant to the nutrient shortage characteristic of the TME[237,238] and, at least in PDAC, seems to be directly orchestrated by PPAR-δ.

As mentioned before, therapeutic intervention remains challenging in PDAC since diagnosis occur late and common chemotherapeutic agents target differentiated bulk tumor cells while enrich highly aggressive and metastatic cell populations (i.e., PaCSCs). Given our results, different therapeutic possibilities arose to prevent metastatic dissemination in PDAC: to inhibit MYC or to target PPAR-δ. Indeed, several compounds have been tested against MYC with little clinical transcendence, although they have provided important insights about MYC biology[227]. All these unsuccessful attempts are mainly consequence of MYC structure, which lacks traditional binding pockets, and the absence of a resolved crystal structure in its monomer presentation. Therefore, MYC is considered a "yet to be drugged" target, also because its function is completely pleiotropic and not exclusively tumoral[218]. On the other hand, there are some available compounds able to target PPAR-δ, such as GSK0660, GSK3787 and DG172[125]. Indeed, we were able to block MCM- and Etomoxir-induced invasiveness *in vitro* (**Figure I.15**) and, most importantly, reduced metastatic incidence *in vivo* of two highly metastatic PDAC models (**Figure I.18**). Despite none of these compounds are approved in the clinical setting at the moment, we have provided proof of concept that PPAR-δ blockade prevents PDAC cells from disseminating and forming metastatic lesions. However, we are aware that PDAC diagnose occurs when metastatic disease is already present, then, whether PPAR-δ inhibition might represent an efficient approach to be used in this scenario must be further investigated.

In summary, our data demonstrate that PPAR-δ targeting with small compounds decreases metastatic dissemination in PDAC. Therefore, these results provide the rationale for developing novel therapeutic strategies against

aggressive PDAC cells with increased PPAR-δ-mediated metabolic plasticity (**Figure 11**).

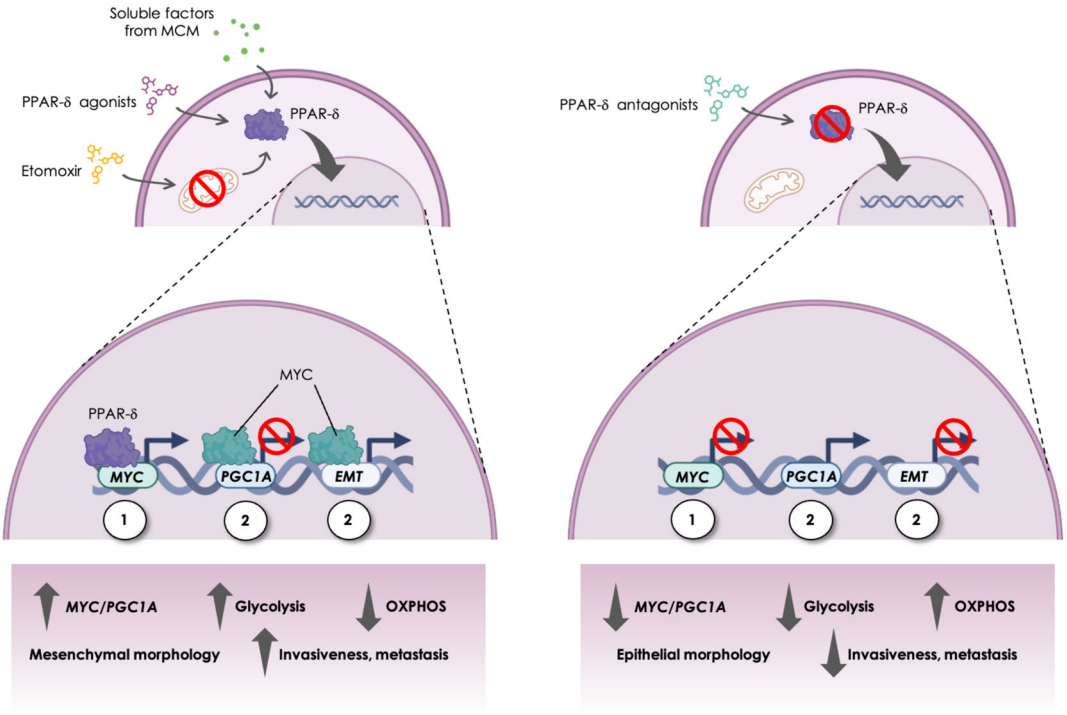

Figure 11. Schematic representation of the main conclusions extracted from chapter I. Mitochondrial inhibition with Etomoxir, soluble factors present in M2-polarized conditioned medium (MCM), or treatment with PPAR-δ agonists activate PPAR-δ to unleash its nuclear function regulating gene expression. On the one hand, it directly binds the *MYC* promoter, thus activating its expression (1). In turn, MYC represses *PGC1A* expression, while activates EMT-related gene expression (2). This scenario fosters a glycolytic, mesenchymal-like phenotype with enhanced invasive capacity (**left panel**). Conversely, pharmacologic targeting of PPAR-δ represses *MYC* (1) to unleash *PGC1A* (2) expression towards an enhanced mitochondrial metabolism with reduced invasiveness (**right panel**).

DISCUSSION: CHAPTER II

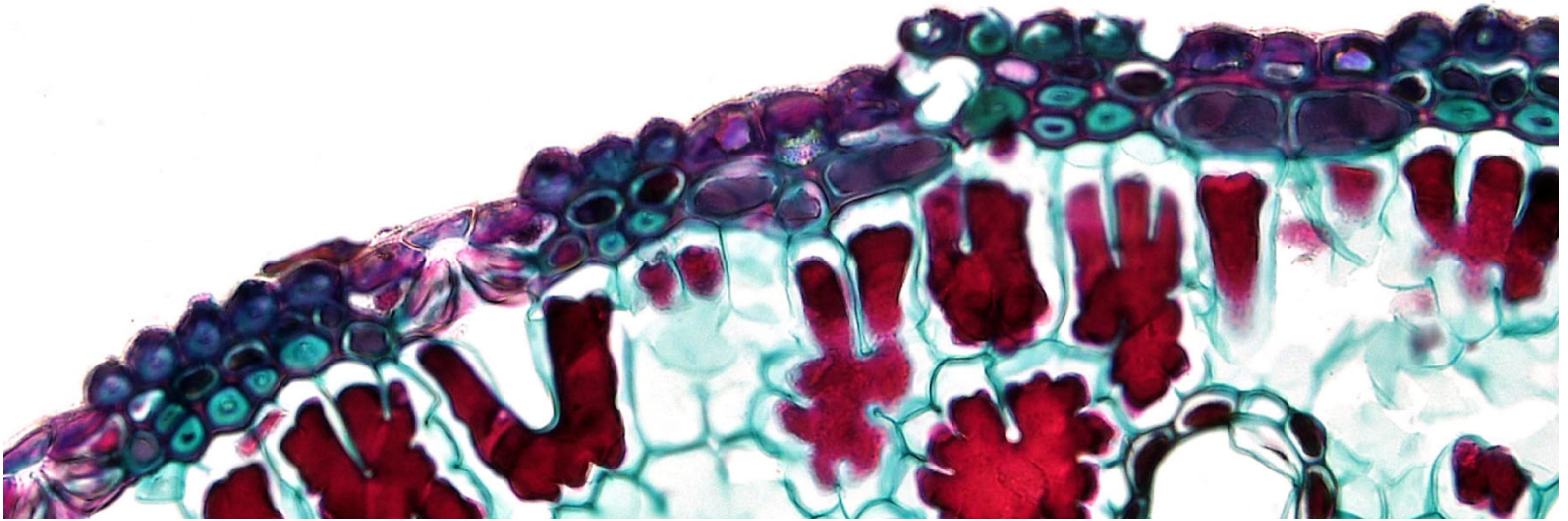

As discussed in the previous chapter, pancreatic ductal adenocarcinoma (PDAC) aggressiveness mostly relies on the presence of aggressive pancreatic cancer stem cells (PaCSCs) that survive after conventional chemotherapy, eventually regrow the tumor and migrate to colonize secondary organs. As pancreatic cancer stem cells (PaCSCs) bear unique features when compared to their most differentiated counterparts, the combination of conventional chemotherapy with anti-PaCSCs therapies may represent a promising alternative to improve long-term survival of PDAC patients. In this sense, receptor and non-receptor tyrosine kinases (RTKs and nRTKs, respectively) represent a much more approachable strategy since they can be targeted by a plethora of specific and clinical-grade compounds. In addition, RTKs and nRTKs control essential cellular mechanisms dysregulated in cancer, such as metabolism, proliferation, survival and, most importantly, stemness[160,161,163,164,239]. Several clinical trials in PDAC are currently exploring the potential benefit of diverse TK inhibitors in PDAC[240].

In order to find novel pharmacologically amenable targets hyperactivated in PaCSCs, we decided to focus on RTKs, since their expression in the cellular membrane allows for targeting by both small molecules and blocking antibodies. Screening of RTKs revealed that the receptor anaplastic lymphoma kinase (ALK) was consistently overexpressed and hyperactivated in PaCSCs, by using different CSC enrichment methods and models to account for intrinsic intra- and intertumoral heterogeneity (**Figures II.1-II.6**). Although the ALK receptor plays an important physiological role in neural development[169,173], it was first discovered in lymphoma as the fusion protein NPL-ALK following chromosomal rearrangement[168]. Subsequently, ALK was shown to be aberrantly expressed and/or activated in several cancer types[169–172]. ALK receptor activation triggers different intracellular signaling pathways involved in proliferation, survival and metabolism, including JAK/STAT and Ras/ERK[182,183]. Importantly, some studies suggested that ALK acts as a regulator of stemness in several cancers[191–194]. However, our results were certainly unexpected, since this receptor has been overlooked in PDAC. The possible cause points to the lack of mRNA overexpression in tumor bulk cells when compared to normal pancreas or the low level of chromosomal rearrangement of the *ALK* gene in PDAC[189] (**Figure II.7**), which is the main pathogenic mechanism associated to ALK in NSCLC and

brain tumors[169–172]. The low *ALK* expression at the mRNA level detected in bulk transcriptomic analysis of The Cancer Genome Atlas (TCGA) and the Genotype-Tissue Expression (GTEx) datasets (**Figure II.7A**) was further evidenced in the single-cell expression analysis (scRNAseq, **Figure II.11B**), where *ALK* was undetectable in the different cell populations of the pancreatic niche, including tumor cells. In fact, detection of *ALK* mRNA levels proved challenging even in our primary cultures (**Figure II.6 and data not shown**). However, we detected considerable ALK expression and phosphorylation in different PDAC PDX models and established cell lines by western blot (**Figures II.3 and II.5**). Our data further reinforces the importance of considering protein post-translational regulation and modifications accompanied with functional assays over purely transcriptomic studies for target discovery screenings.

Nevertheless, further bioinformatic analyses of transcriptomic datasets supported our initial results *in vitro*. Indeed, we were able to link the mRNA expression of both *ALK* and an *ALK* overexpression (OE) signature previously described[210] with pathways related with CSCs in PDAC patients, such as epithelial-to-mesenchymal transition (EMT), drug metabolism and stemness (**Figure II.8A-II.8D and II.9**). In addition, these analyses allowed us to propose the cytokines midkine (MDK) and, to a lesser extent, pleiotrophin (PTN), as the main putative ligands triggering ALK activation in PaCSCs. Indeed, the identification of the actual ALK ligand is a matter of great controversy: while some studies point to MDK and PTN[170,175], others suggest the cytokines FAM150A and B (family with sequence similarity 150 members A and B)[176,241] as main activators of the ALK pathway. While the results obtained for *FAM150A* and *FAM150B* were inconsistent, both *MDK* and *PTN* were overexpressed in PDAC patient samples (**Figure II.10A**), although only *MDK* correlated with the expression of pluripotency and EMT genes in both bulk and scRNAseq data and with the *ALK* OE signature mentioned above (**Figures II.10B and II.11A**). However, we cannot definitely discard the implication of FAM150A nor FAM150B in our system without further experimental analyses.

MDK and PTN are heparin-binding growth factors with multiple regulatory functions in biological processes such as proliferation, differentiation and development through binding to different receptors, including ALK[177,178]. Interestingly, functional assays with recombinant MDK and PTN demonstrated

that ligand-dependent ALK activation increased several CSC-related properties such as self-renewal, clonogenicity and CSC frequency in our PDX models (**Figures II.14, II.19B and II.19C**), indicating that the axis MDK/PTN-ALK enhances stemness in PDAC. Indeed, ALK activation *via* MDK or PTN has been shown to regulate self-renewal and tumorigenicity in glioblastoma[191,192,242], while PTN knockdown favored chemosensitivity and inhibited clonogenic capacity in osteosarcoma[243]. The differences we observed at the functional level, however, were not transferable to the molecular analyses performed by RTqPCR and flow cytometry (**Figures II.16 and II.18**).

Functional assays on the invasive potential were less conclusive due to fewer complementary tests. However, we were able to link the MDK/PTN-ALK axis to invasiveness in PDAC, another key feature of CSCs. Indeed, MDK- and PTN-dependent ALK activation regulated migration/invasion in glioblastoma[242] and glioma[244], respectively. As mentioned above, our bioinformatic analyses correlated *ALK* OE target genes and *MDK* with EMT-related genes, frequently associated with invasiveness (**Figure II.8D and II.10B, middle row, respectively**). Despite the differences found in EMT gene expression after treatment with ALK ligands resulted not significant (**Figures II.18 and II.22**), migration assays suggested a functional link between this pathway and invasiveness (**Figure II.17 and II.21**). These results confirm that ligand-dependent activation of the ALK pathway enhances PDAC aggressiveness by boosting CSCs properties. Whereas acute treatment with exogenous MDK or PTN did not substantially modify gene expression patterns of stemness or EMT programs (**Figures II.16, II.18, II.20 and II.22**), their effects on PaCSC properties were at the functional level, thereby highlighting the importance of performing functional assays with prolonged exposure of the cells to ALK ligands to properly study CSC biology in the long-term.

Our results point to different modes of ALK ligand-dependent activation in PaCSCs. Analysis of the scRNAseq dataset indicated that *MDK* was expressed by a wide range of cells present in the pancreatic niche, including tumor cells (**Figure II.11B**), suggesting that MDK could activate ALK in both an autocrine and paracrine manner. On the one hand, we confirmed the autocrine regulation by the high levels of human MDK present in supernatants of both subcutaneous and orthotopic tumor pieces, plasmas from orthotopic tumor-bearing mice (**Figure II.**

12A) and primary tumor cells in culture regardless of their pluripotency status (**Figure II.12B and II.12C**). On the other hand, regarding the paracrine regulation, PTN was barely expressed in tumor cells according to our analysis of the scRNAseq PDAC dataset (**Figure II.11B**) and was undetectable in PDXs (**data not shown**). In contrast, PTN was expressed by stromal cells, such as fibroblasts and stellate cells (**Figure II.11B**), revealing the potential paracrine regulatory loop in which cells from the tumor microenvironment may sustain PaCSCs through ALK activation *via* PTN. Importantly, regarding MDK-mediated paracrine regulation of ALK, a recently published RNA microarray analysis from tumor-associated macrophages (TAMs) revealed that *MDK* expression is increased in these immune cells after being polarized towards an immunosuppressive phenotype when co-cultured with PDAC cells[99]. Indeed, the incubation of PDAC PDXs with conditioned medium from protumoral macrophages (MCM) –a confirmed inducer of the EMT phenotype in PDAC (**see chapter I**)– further corroborated the link between invasiveness and ALK receptor in PDAC cells, since it appeared strongly phosphorylated (**Figure II.23A**). Additionally, a recently described TAMs infiltration gene expression signature[211] positively correlated with ALK pathway in our bioinformatic analyses (**Figure II.25**). Surprisingly, *MDK* expression positively correlated with this TAMs infiltration signature (**Figure II.25**). However, MDK expression and secretion did not correlate in M2-polarized protumoral macrophages, since it was undetectable in any of the MCM samples assessed (**Figure 24A**), as previously observed in melanoma cells[223,245]. Altogether suggests that a complex crosstalk between CSCs and their niche is taking place. Strikingly, another recent study revealed that melanoma cells secrete MDK to promote an immune-suppressive microenvironment involving TAMs and cytotoxic T cells[223], suggesting that MDK secretion by PaCSCs could also play a role in immunoediting in PDAC. Taken together, we hypothesize that TAMs-PaCSCs crosstalk might modulate PDAC aggressiveness through the ALK signaling pathway *via*: 1. other potential ALK ligands secreted by TAMs; and/or 2. inducing *MDK* expression and secretion in pancreatic cancer (stem) cells (**Figure II.24B**) to exert their function in both paracrine- and autocrine-mediated manners, respectively.

Interferon gamma (IFN-γ) has been described as a classical natural anticancer agent produced by T lymphocytes and natural killer (NK) cells to

stimulate antitumoral macrophages[246–248]. However, it also has been linked to adaptive immune resistance by inducing the expression of immune checkpoints, such as programmed cell death 1 and its ligand (PD-1/PD-L1), in many cancer-related malignancies, including PDAC[93,94]. Strikingly, IFN-γ pathway resulted enriched in *ALK*^{HIGH} patients from our gene set enrichment analyses (GSEA, **Figure II.9A**) and a positive correlation of *ALK* OE signature and MDK with both TAMs infiltration signature and *PD-L1* (**Figure II.25 and II.26, respectively**) was obtained from the bioinformatic analyses performed. In addition to this, we found enhanced *PD-L1* expression after incubation with MCM (**Figure II.27A**) and a positive trend with exogenous MDK or PTN treatment (**Figure II.27B**). On an entirely speculative basis, we hypothesize that the immunosuppressive microenvironment in PDAC could be promoted by an intricate crosstalk between TAMs and cancer (stem) cells through ALK and IFN-γ pathways, as suggested by both the bioinformatic analyses and the *in vitro* results and supported by recent bibliography. Despite PDAC is considered a "cold tumor" with minor, yet not nonexistent, immune infiltration, our hypothesis is that the IFN-γ produced by the limited immune cells in the PDAC TME is sufficient to induce the adaptive immune resistance by which TAMs induce *PD-L1* expression in PaCSCs through MDK- (and/or other ligands)-ALK axis. Likewise, TAMs induce *PD-1* expression in T lymphocytes that will interact with PaCSCs-expressed PD-L1 to exert the immunosuppression (**Figure 12**).

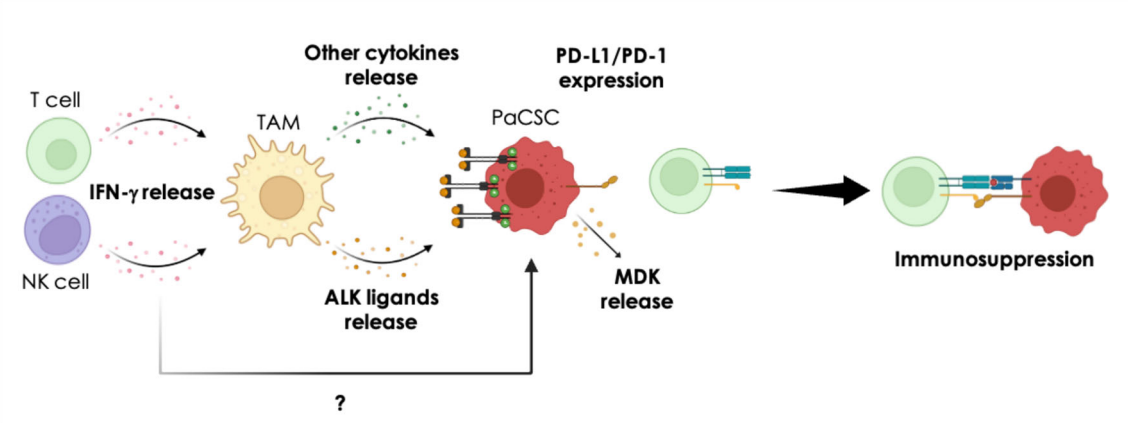

Figure 12. Hypothetical schematic representation of the IFN-γ-mediated adaptive immune resistance through the ALK pathway in PDAC. Immune cells such as T lymphocytes (T cells) and natural killer (NK) cells secrete IFN-γ that will induce the expression of PD-1 on T cells and PD-L1 on PaCSCs through different cytokines and ALK ligands secretion to potentiate the immunosuppressive TME characteristic of pancreatic tumors. Likewise, TAMs-mediated PaCSC stimulation may promote MDK secretion in these cells. Moreover, IFN-γ may act directly on PaCSCs.

Importantly, we have demonstrated the crucial role of ALK for PDAC CSC-related functions not only by exogenous activation of the receptor, but also through pharmacological inhibition strategies using clinically-approved compounds. Crizotinib is a trivalent ALK, c-Met and ROS1 inhibitor approved by the Food and Drug Administration (FDA) to treat cancers expressing oncogenic ALK fusion proteins[198,199] and, later on, those depending on c-Met and/or ROS1 signaling[200]. On the other hand, Ensartinib is a potent and specific next-generation ALK inhibitor currently evaluated in a phase III trial[203], included in our study to discard the off-target effects induced by Crizotinib. Treatment with both Crizotinib and Ensartinib inhibited proliferation (**Figure II.28A and II.28B**), and induced toxicity and cell death *in vitro* (**Figure II.29-II.32**), suggesting that ALK signaling contributes to cell survival. ALK inhibition was effective in our models derived from local (PDXs), metastatic PDAC (CTCA) and EMT-induced PDXs (i.e., with MCM), suggesting this therapeutic approach may be effective in advanced and metastatic patients (**Figure II.30-II.32**). Notably, ALK inhibition drastically decreased the CSC content (**Figure II.31C and II.31D**) and stemness features *in vitro* and *in vivo* (**Figure II.33, II.36 and II.37**). Finally, ALK inhibition also reduced the migratory and invasive abilities in our models (**Figure II.34**). Altogether, these results demonstrate that ALK is functionally necessary for PaCSC maintenance during tumor progression.

Therapy failure and recurrence remain a major issue in PDAC management due to its intrinsic chemoresistance. In addition, conventional treatments target the tumor bulk and enriches the CSC content, responsible for tumor relapse. Our GSEA revealed that PDAC patients with higher levels of *ALK* expression have enhanced xenobiotic metabolism (**Figure II.9A**), a process by which tumor cells reduce drugs' bioavailability, thus increasing cytoprotection. Some studies on MDK and PTN also support the implication of the ALK pathway in chemoresistance. In osteosarcoma, PTN reduced chemosensitivity through enhancing ALK/GSK3β/β-catenin signaling by increasing multidrug resistance protein 1 (*ABCB1*, *P-glycoprotein* or *MDR1*) expression[121]. Likewise, MDK derived from cancer-associated fibroblasts (CAFs) of different malignancies reduced chemotherapy-induced cell death *via* expression of the long non coding RNA (lncRNA) *ANRIL* by increasing the expression of the multidrug resistance-associated protein 1 and 2 (*ABCC1* and *ABCC2*, respectively)[119]. Interestingly,

an early study demonstrated that MDK depletion sensitizes PDAC cells to Gemicitabine[120]. Although mediated through Notch-2 receptor in this case, the implication of MDK with chemoresistance was evidenced in PDAC for the first time in this study.

Here, we demonstrate that both Crizotinib and Ensartinib decreased the IC_{50} of Gemcitabine more than half (**Figure II.38**), with stronger effects by Ensartinib treatment. Importantly, both ALK inhibitors in combination with Gemcitabine decreased PaCSC content by inducing cell death (**Figure II.39**) and abrogated Gemcitabine-induced clonogenicity (**Figure II.40A**) and self-renewal (**Figure II.40B**). Importantly, Crizotinib treatment significantly delayed tumor relapse *in vivo* (**Figure II.43A**) and some tumors even disappeared after treatment (**Figure II.43B**). Moreover, tumors from Crizotinib-treated mice showed reduced stemness markers (**Figure II.44B and II.44C**), indicating a successful PaCSC targeting *in vivo*. Since development of resistance to Crizotinib has been reported already[249], further *in vivo* experiments would be needed in order to test Ensartinib, a compound still in the process of approval by the FDA. Besides its improved specificity, this inhibitor was more potent than Crizotinib either alone or in combination with Gemcitabine *in vitro*. Considering our results, we would expect a reduction of the required dosage *in vivo* to obtain a positive response, further translated into minimal side effects when applied as combinatory treatment.

In summary, our results demonstrate that PaCSCs sustain their stemness program through MDK (and PTN)-dependent activation of the ALK signaling pathway. Importantly, this pathway can be pharmacologically targeted with small molecule inhibitors that, combined with conventional chemotherapy, showed promising effects for an effective long-term treatment of PDAC (**Figure 13**).

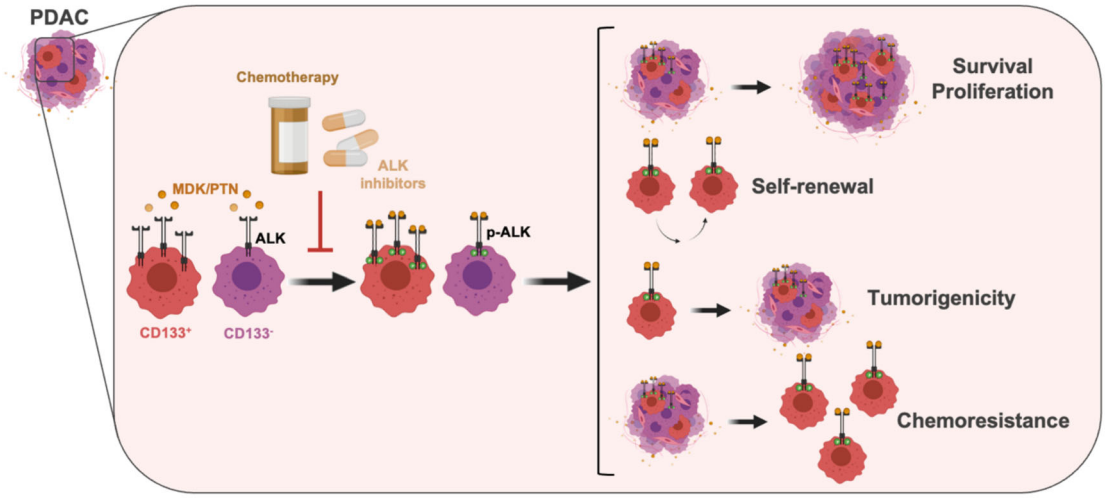

Figure 13. Schematic representation of the main conclusions extracted from chapter II. PaCSCs express higher levels of the ALK receptor, leading to an hyperactivated pathway with consequences on survival, proliferation, self-renewal, tumorigenicity and chemoresistance. Targeting the MDK/PTN-ALK axis with clinically-approved inhibitors impairs *in vivo* tumorigenicity and chemoresistance in PDAC, suggesting a new treatment approach to improve the long-term survival of these patients. *Parejo-Alonso et al., 2023.*

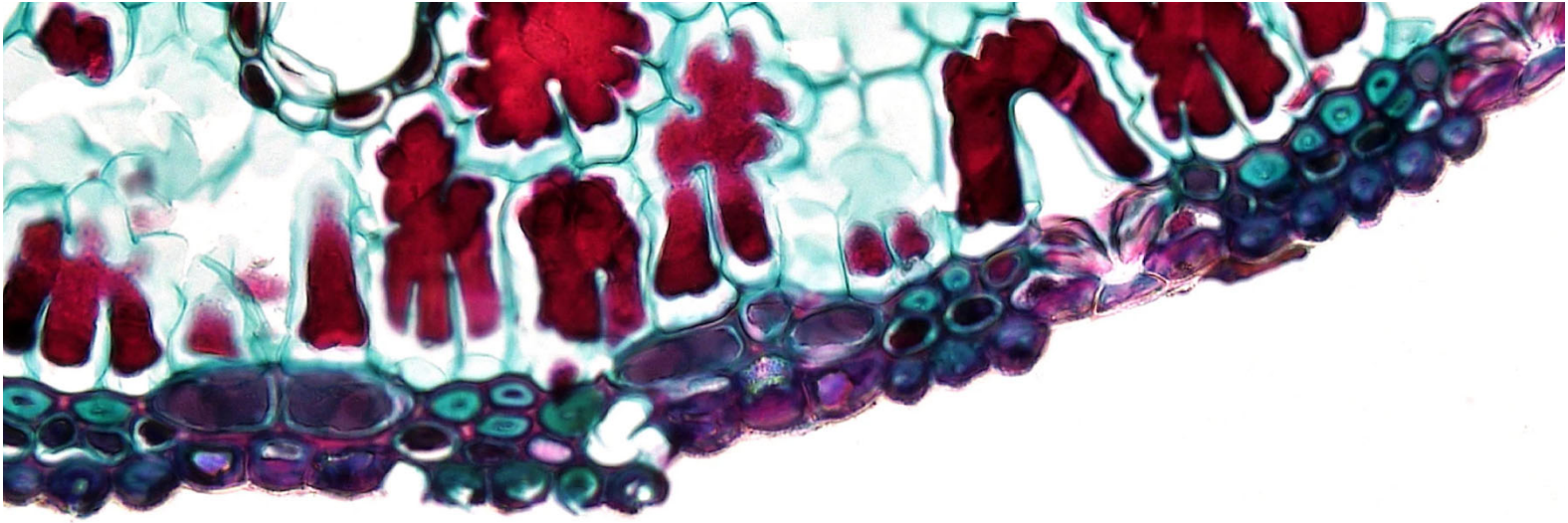

GENERAL DISCUSSION

Pancreatic ductal adenocarcinoma (PDAC) aggressiveness mainly relies on two key factors: delayed detection, since symptoms are mild and/or unspecific even at advanced disease stages, and its intrinsic resistance to current treatment regiments[10], thus making PDAC progression to metastatic disease a silent process. Unfortunately, current therapeutic strategies for PDAC disease translate into dismal curative opportunities since most of these patients eventually develop resistance to chemotherapy and tumor relapse[14] featured by a small but unique subpopulation of cancer cells known as pancreatic cancer stem cells (PaCSCs)[20,219]. Therefore, it seems likely that either early detection or combining chemotherapy with drugs targeting CSCs –directly eliminating them and/or indirectly inhibiting their functionality– may be the only way to ensure long-term survival of PDAC patients. However, there is not a reliable biomarker for PDAC early detection nowadays, which aggravates the difficulties in the already challenging PDAC management. In our group, we are focused on the differential features that render PaCSCs unique *versus* the most differentiated progenies in order to find targetable vulnerabilities against them. In this PhD work, two different approaches were investigated to counteract PDAC aggressiveness by targeting important elements for CSCs biology and functionality: metabolic reprograming and extracellular signal transduction, both considered hallmarks of cancer[73,250].

On the one hand, the distinct metabolic phenotype between differentiated cancer cells and CSCs represents an appropriate candidate for the development of specific anti-CSCs therapeutic strategies. While the preferred metabolic pathway used by CSCs differ in different cancer types[42], it has been well-demonstrated that PaCSCs are exclusively dependent on mitochondrial oxygen phosphorylation (OXPHOS)[61]. However, our group set to modify the adjective "exclusive" to "highly" by further proving the presence of metabolic plasticity within this previously described "metabolically static" subpopulation. The balance between MYC and PGC1α regulates the metabolic phenotype seen in PaCSCs, impacting their pluripotency status[62] and modifying their invasive abilities. Here, we demonstrate that PPAR-δ orchestrates PaCSCs metabolic plasticity by controlling MYC/PGC1α balance towards increased invasiveness, thereby constituting an accurate candidate to avoid the metastatic dissemination in PDAC. However, this approach may represent a

double-edged sword. While this strategy seems a suitable therapeutic opportunity for metastatic PDAC, the metabolic modulation that takes place when inhibiting PPAR-δ towards increased PGC1α may enhance other stemness properties in these cells, such as tumorigenicity and chemoresistance. In any case, further studies would be needed in order to prove whether this scenario may be happening upon PPAR-δ/MYC/PGC1α-dependent metabolic rewiring. However, we may anticipate that a combinatory therapeutic approach with mitochondrial inhibitors would be needed to counteract the potential arising metabolic plasticity-mediated resistance towards the opposite OXPHOS-dependent phenotype.

On the other hand, receptor and non-receptor tyrosine kinases (RTKs and nRTKs, respectively) represent an equally suitable strategy since they can be targeted by a plethora of specific and clinical-grade compounds. Besides this, RTKs and nRTKs control essential cellular mechanisms dysregulated in cancer, such as metabolism, proliferation, survival and, most importantly, stemness[154,155,251]. Several clinical trials in PDAC are currently exploring the potential benefit of diverse TK inhibitors in PDAC[15]. Here, we define an important role of anaplastic lymphoma kinase (ALK) receptor in PaCSCs functionality by demonstrating its direct implication in enhancing self-renewal, tumorigenicity and chemoresistance. Indeed, this strategy represents a huge therapeutic opportunity with high chances of success since ALK receptor can be blocked by numerous compounds already approved for their clinical use. In addition to this, the fact that this receptor is barely expressed in healthy adult tissues reduces the potential adverse effects coming from a possible prolonged systemic treatment.

In summary, despite a more in-depth investigation may be required, both strategies showed promising results and bear the potential to benefit PDAC patients in the future.

CONCLUSIONS

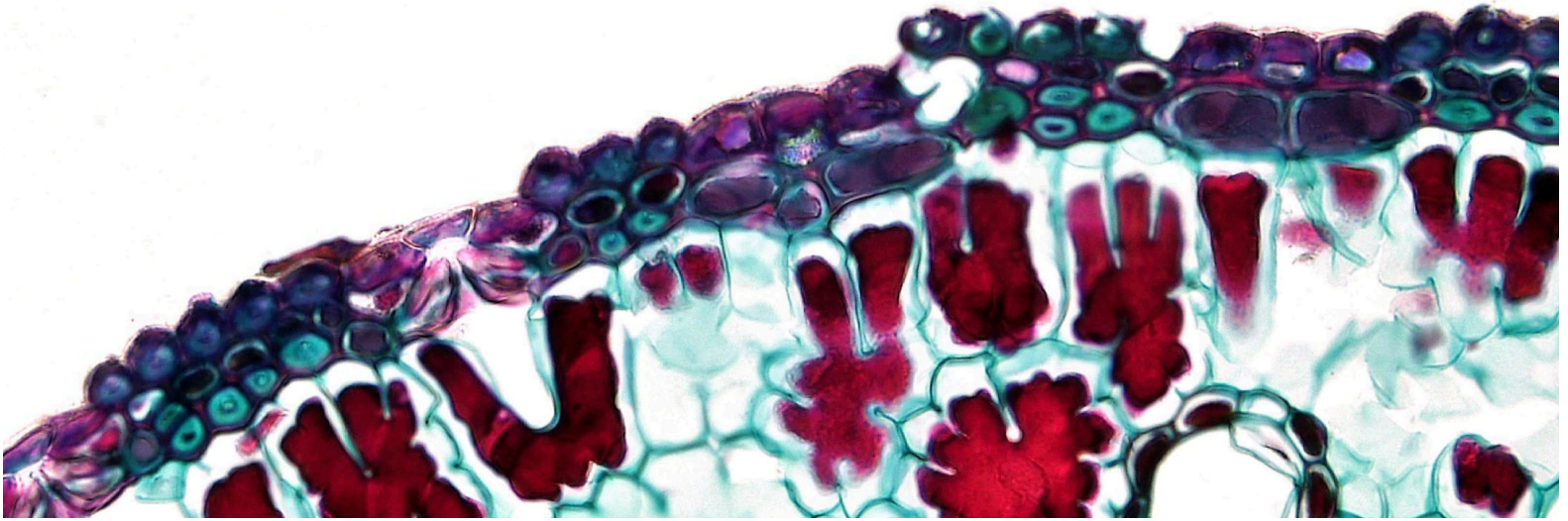

The following conclusions can be drawn from the results presented in this doctoral thesis:

CHAPTER I:

1. A common transcriptional program integrates metabolic stress (mitochondrial inhibition with Etomoxir) and microenvironmental cues derived from TAMs (incubation with MCM) characterized by increased glycolytic metabolism.

2. Both Etomoxir and MCM induce *PPARD*/PPAR-δ gene and protein expression, as well as activation of PPAR-δ.

3. Functionally, PPAR-δ activation by Etomoxir and MCM enhances the invasive and metastatic potential of PDAC PDXs *in vitro* and *in vivo*.

4. MYC is a direct downstream effector of the PPAR-δ signaling pathway.

5. PPAR-δ blockade reduces the *in vitro* basal and Etomoxir- and MCM-induces invasive abilities of PDAC metastatic and local PDXs, respectively, as well as the *in vivo* metastatic incidence of PDAC orthotopic-bearing mice.

CHAPTER II:

1. ALK receptor is expressed in different PDXs and stablished cell lines from PDAC.

2. ALK receptor is overexpressed and preferentially phosphorylated in PaCSCs.

3. MDK and PTN activate ALK, thus enhancing self-renewal, clonogenicity and CSC frequency *in vitro*.

4. Pharmacological targeting of ALK induces cell death in $CD133^+$ PaCSCs and impairs stem functionality *in vitro* and *in vivo*.

5. Combination of clinically-approved ALK inhibitors with chemotherapy targets PaCSCs *in vitro* and delays tumor relapse *in vivo*.

De los resultados presentados en esta tesis doctoral pueden extraerse las siguientes conclusiones:

CAPÍTULO I:

1. Un programa transcripcional común integra el estrés metabólico (inhibición mitocondrial con Etomoxir) y señales microambientales derivadas de los TAMs (incubación con MCM) caracterizado por un augmento del metabolismo glicolítico.

2. Tanto Etomoxir como MCM inducen la expresión génica y proteica de *PPARD*/PPAR-δ, así como la activación de PPAR-δ.

3. A nivel funcional, la activación de PPAR-δ mediante Etomoxir y MCM aumenta el potencial invasivo y metastático de los PDXs de PDAC *in vitro* e *in vivo*.

4. MYC es un efector directo de la vía de señalización de PPAR-δ.

5. El bloqueo de PPAR-δ reduce, *in vitro*, la capacidad invasiva basal e inducida por Etomoxir y MCM de los PDXs de PDAC metastáticos y locales, respectivamente, así como la incidencia metastática *in vivo* de ratones con tumores ortotópicos de páncreas.

CAPÍTULO II:

1. El receptor ALK se expresa en diferentes PDXs y líneas células establecidas de PDAC.

2. El receptor ALK se encuentra más expresado y fosforilado de forma preferente en PaCSCs.

3. MDK and PTN activan ALK, aumentando, así, la capacidad de auto-renovación, clonogenicidad, y frecuencia *in vitro* de CSC.

4. La inhibición farmacológica de ALK induce muerte celular en las PaCSCs $CD133^+$ y afecta la funcionalidad de las células madre *in vitro* e *in vivo*.

5. La combinación de inhibidores de ALK clínicamente aprobados con quimioterapia ataca a las PaCSCs *in vitro* y retrasa la recidiva *in vivo*.

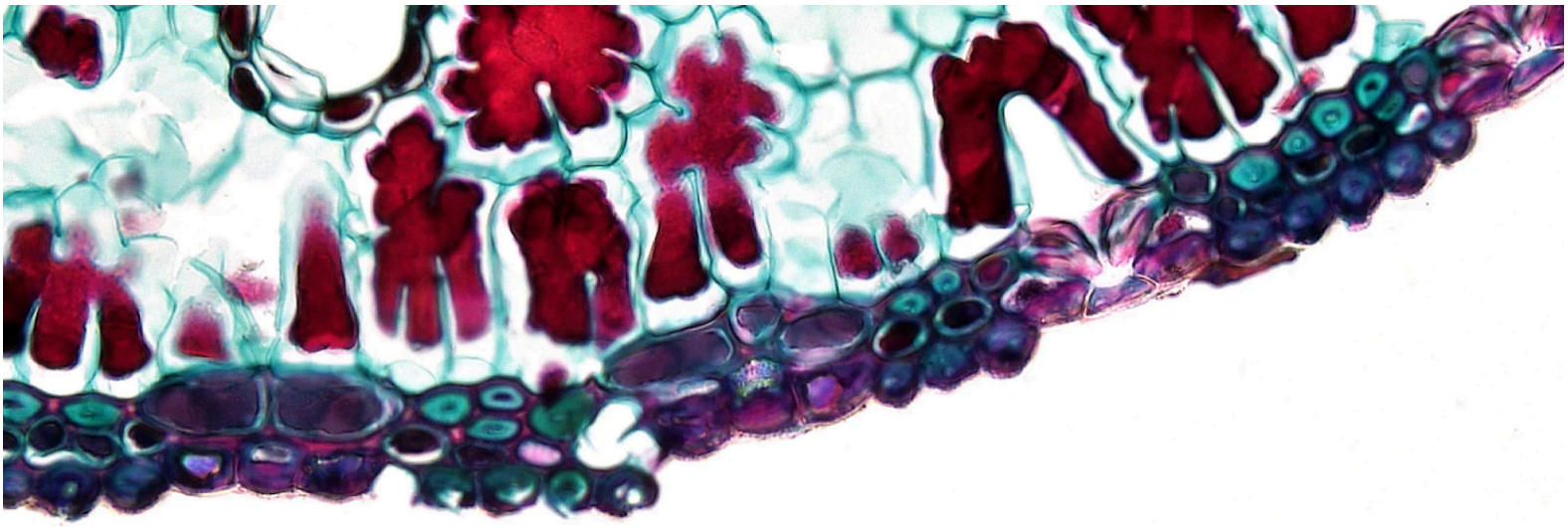

REFERENCES

1 Atkinson MA, Campbell-Thompson M, Kusmartseva I, Kaestner KH. Organisation of the human pancreas in health and in diabetes. *Diabetologia* 2020; **63**: 1966–1973. [DOI: 10.1007/s00125-020-05203-7]

2 Las_cifras_del_Cancer_en_Espana_2023.pdf. Available from: https://seom.org/images/Las_cifras_del_Cancer_en_Espana_2023.pdf

3 Bray F, Ferlay J, Soerjomataram I, Siegel RL, Torre LA, Jemal A. Global cancer statistics 2018: GLOBOCAN estimates of incidence and mortality worldwide for 36 cancers in 185 countries. *CA: A Cancer Journal for Clinicians* 2018; **68**: 394–424. [DOI: 10.3322/caac.21492]

4 Rawla P, Sunkara T, Gaduputi V. Epidemiology of Pancreatic Cancer: Global Trends, Etiology and Risk Factors. *World J Oncol* 2019; **10**: 10–27. [PMID: 30834048 DOI: 10.14740/wjon1166]

5 Ferreira RMM, Sancho R, Messal HA, Nye E, Spencer-Dene B, Stone RK, Stamp G, Rosewell I, Quaglia A, Behrens A. Duct- and Acinar-Derived Pancreatic Ductal Adenocarcinomas Show Distinct Tumor Progression and Marker Expression. *Cell Reports* 2017; **21**: 966–978. [DOI: 10.1016/j.celrep.2017.09.093]

6 Kopp JL, von Figura G, Mayes E, Liu F-F, Dubois CL, Morris JP, Pan FC, Akiyama H, Wright CVE, Jensen K, Hebrok M, Sander M. Identification of Sox9-Dependent Acinar-to-Ductal Reprogramming as the Principal Mechanism for Initiation of Pancreatic Ductal Adenocarcinoma. *Cancer Cell* 2012; **22**: 737–750. [DOI: 10.1016/j.ccr.2012.10.025]

7 Bardeesy N, DePinho RA. Pancreatic cancer biology and genetics. *Nat Rev Cancer* 2002; **2**: 897–909. [DOI: 10.1038/nrc949]

8 Dunne RF, Hezel AF. Genetics and Biology of Pancreatic Ductal Adenocarcinoma. *Hematology/Oncology Clinics of North America* 2015; **29**: 595–608. [DOI: 10.1016/j.hoc.2015.04.003]

9 Espiau-Romera P, Courtois S, Parejo-Alonso B, Sancho P. Molecular and Metabolic Subtypes Correspondence for Pancreatic Ductal Adenocarcinoma Classification. *JCM* 2020; **9**: 4128. [PMID: 24784121 DOI: 10.3390/jcm9124128]

10 De la Cruz, Maria Syl D., Young, Alisa P., Ruffin, Mack T. Diagnosis and Management of Pancreatic Cancer. *Pancreatic Cancer* 2014; **89**: 7.

11 Hidalgo M. Pancreatic Cancer. *N Engl J Med* 2010; **362**: 1605–1617. [DOI: 10.1056/NEJMra0901557]

12 Neoptolemos JP, Kleeff J, Michl P, Costello E, Greenhalf W, Palmer DH. Therapeutic developments in pancreatic cancer: current and future perspectives. *Nat Rev Gastroenterol Hepatol* 2018; **15**: 333–348. [DOI: 10.1038/s41575-018-0005-x]

13 Pancreatic Cancer Europe. Pancreatic Cancer Europe. Available from: https://pancreaticcancereurope.eu/

14 Zeng S, Pöttler M, Lan B, Grützmann R, Pilarsky C, Yang H. Chemoresistance in Pancreatic Cancer. *Int J Mol Sci* 2019; **20**: 4504. [PMID: 31514451 DOI: 10.3390/ijms20184504]

15 Katayama ES, Hue JJ, Bajor DL, Ocuin LM, Ammori JB, Hardacre JM, Winter JM. A comprehensive analysis of clinical trials in pancreatic cancer: what is coming down the pike? *Oncotarget* 2020; **11**: 3489–3501. [PMID: 33014285 DOI: 10.18632/oncotarget.27727]

16 Rosenzweig A, Moravek C, Matrisian LM. More efficient clinical trials in pancreatic cancer: develop better treatment options, faster. *Journal of Cancer Metastasis and Treatment* 2022; **8**: 46. [DOI: 10.20517/2394-4722.2022.58]

17 Moore MJ, Goldstein D, Hamm J, Figer A, Hecht JR, Gallinger S, Au HJ, Murawa P, Walde D, Wolff RA, Campos D, Lim R, Ding K, Clark G, Voskoglou-Nomikos T, Ptasynski M, Parulekar W. Erlotinib Plus Gemcitabine Compared With Gemcitabine Alone in Patients With Advanced Pancreatic Cancer: A Phase III Trial of the National Cancer Institute of Canada Clinical Trials Group. *JCO* 2007; **25**: 1960–1966. [DOI: 10.1200/JCO.2006.07.9525]

18 Golan T, Hammel P, Reni M, Van Cutsem E, Macarulla T, Hall MJ, Park J-O, Hochhauser D, Arnold D, Oh D-Y, Reinacher-Schick A, Tortora G, Algül H, O'Reilly EM, McGuinness D, Cui KY, Schlienger K, Locker GY, Kindler HL. Maintenance Olaparib for Germline *BRCA* -Mutated Metastatic Pancreatic Cancer. *N Engl J Med* 2019; **381**: 317–327. [DOI: 10.1056/NEJMoa1903387]

19 Hermann PC, Huber SL, Herrler T, Aicher A, Ellwart JW, Guba M, Bruns CJ, Heeschen C. Distinct Populations of Cancer Stem Cells Determine Tumor Growth and Metastatic Activity in Human Pancreatic Cancer. *Cell Stem Cell* 2007; **1**: 313–323. [DOI: 10.1016/j.stem.2007.06.002]

20 Li C, Heidt DG, Dalerba P, Burant CF, Zhang L, Adsay V, Wicha M, Clarke MF, Simeone DM. Identification of Pancreatic Cancer Stem Cells. *Cancer Res* 2007; **67**: 1030–1037. [PMID: 17283135 DOI: 10.1158/0008-5472.CAN-06-2030]

21 Johnson BE, Mazor T, Hong C, Barnes M, Aihara K, McLean CY, Fouse SD, Yamamoto S, Ueda H, Tatsuno K, Asthana S, Jalbert LE, Nelson SJ, Bollen AW, Gustafson WC, Charron E, Weiss WA, Smirnov IV, Song JS, Olshen AB, Cha S, Zhao Y, Moore RA, Mungall AJ, Jones SJM, Hirst M, Marra MA, Saito N, Aburatani H, Mukasa A, Berger MS, Chang SM, Taylor BS, Costello JF. Mutational Analysis Reveals the Origin and Therapy-Driven Evolution of Recurrent Glioma. *Science* 2014; **343**: 189–193. [DOI: 10.1126/science.1239947]

22 Eleveld TF, Oldridge DA, Bernard V, Koster J, Daage LC, Diskin SJ, Schild L, Bentahar NB, Bellini A, Chicard M, Lapouble E, Combaret V, Legoix-Né P, Michon J, Pugh TJ, Hart LS, Rader J, Attiyeh EF, Wei JS, Zhang S, Naranjo A, Gastier-Foster JM, Hogarty MD, Asgharzadeh S, Smith MA, Guidry Auvil JM, Watkins TBK, Zwijnenburg DA, Ebus ME, van Sluis P, Hakkert A, van Wezel E, van der Schoot CE, Westerhout EM, Schulte JH, Tytgat GA, Dolman MEM, Janoueix-Lerosey I, Gerhard

DS, Caron HN, Delattre O, Khan J, Versteeg R, Schleiermacher G, Molenaar JJ, Maris JM. Relapsed neuroblastomas show frequent RAS-MAPK pathway mutations. *Nat Genet* 2015; **47**: 864–871. [DOI: 10.1038/ng.3333]

23 Nikbakht H, Panditharatna E, Mikael LG, Li R, Gayden T, Osmond M, Ho C-Y, Kambhampati M, Hwang EI, Faury D, Siu A, Papillon-Cavanagh S, Bechet D, Ligon KL, Ellezam B, Ingram WJ, Stinson C, Moore AS, Warren KE, Karamchandani J, Packer RJ, Jabado N, Majewski J, Nazarian J. Spatial and temporal homogeneity of driver mutations in diffuse intrinsic pontine glioma. *Nat Commun* 2016; **7**: 11185. [DOI: 10.1038/ncomms11185]

24 Eckert MA, Pan S, Hernandez KM, Loth RM, Andrade J, Volchenboum SL, Faber P, Montag A, Lastra R, Peter ME, Yamada SD, Lengyel E. Genomics of Ovarian Cancer Progression Reveals Diverse Metastatic Trajectories Including Intraepithelial Metastasis to the Fallopian Tube. *Cancer Discovery* 2016; **6**: 1342–1351. [DOI: 10.1158/2159-8290.CD-16-0607]

25 Kreso A, Dick JE. Evolution of the Cancer Stem Cell Model. *Cell Stem Cell* 2014; **14**: 275–291. [DOI: 10.1016/j.stem.2014.02.006]

26 Nowell PC. The Clonal Evolution of Tumor Cell Populations: Acquired genetic lability permits stepwise selection of variant sublines and underlies tumor progression. *Science* 1976; **194**: 23–28. [DOI: 10.1126/science.959840]

27 McGranahan N, Swanton C. Clonal Heterogeneity and Tumor Evolution: Past, Present, and the Future. *Cell* 2017; **168**: 613–628. [DOI: 10.1016/j.cell.2017.01.018]

28 Greaves M, Maley CC. Clonal evolution in cancer. *Nature* 2012; **481**: 306–313. [DOI: 10.1038/nature10762]

29 Dagogo-Jack I, Shaw AT. Tumour heterogeneity and resistance to cancer therapies. *Nat Rev Clin Oncol* 2018; **15**: 81–94. [DOI: 10.1038/nrclinonc.2017.166]

30 Lapidot T, Sirard C, Vormoor J, Murdoch B, Hoang T, Caceres-Cortes J, Minden M, Paterson B, Caligiuri MA, Dick JE. A cell initiating human acute myeloid leukaemia after transplantation into SCID mice. *Nature* 1994; **367**: 645–648. [DOI: 10.1038/367645a0]

31 Shackleton M, Quintana E, Fearon ER, Morrison SJ. Heterogeneity in Cancer: Cancer Stem Cells versus Clonal Evolution. *Cell* 2009; **138**: 822–829. [DOI: 10.1016/j.cell.2009.08.017]

32 Al-Hajj M, Wicha MS, Benito-Hernandez A, Morrison SJ, Clarke MF. Prospective identification of tumorigenic breast cancer cells. *Proceedings of the National Academy of Sciences* 2003; **100**: 3983–3988. [DOI: 10.1073/pnas.0530291100]

33 Singh SK, Hawkins C, Clarke ID, Squire JA, Bayani J, Hide T, Henkelman RM, Cusimano MD, Dirks PB. Identification of human brain tumour initiating cells. *Nature* 2004; **432**: 396–401. [DOI: 10.1038/nature03128]

34 Prince ME, Sivanandan R, Kaczorowski A, Wolf GT, Kaplan MJ, Dalerba P, Weissman IL, Clarke MF, Ailles LE. Identification of a subpopulation of cells with cancer stem cell properties in head and neck squamous cell carcinoma. *Proc Natl Acad Sci USA* 2007; 104: 973–978. [DOI: 10.1073/pnas.0610117104]

35 Eramo A, Lotti F, Sette G, Pilozzi E, Biffoni M, Di Virgilio A, Conticello C, Ruco L, Peschle C, De Maria R. Identification and expansion of the tumorigenic lung cancer stem cell population. *Cell Death Differ* 2008; **15**: 504–514. [DOI: 10.1038/sj.cdd.4402283]

36 Collins AT, Berry PA, Hyde C, Stower MJ, Maitland NJ. Prospective Identification of Tumorigenic Prostate Cancer Stem Cells. *Cancer Research* 2005; **65**: 10946–10951. [DOI: 10.1158/0008-5472.CAN-05-2018]

37 Patrawala L, Calhoun T, Schneider-Broussard R, Li H, Bhatia B, Tang S, Reilly JG, Chandra D, Zhou J, Claypool K, Coghlan L, Tang DG. Highly purified CD44+ prostate cancer cells from xenograft human tumors are enriched in tumorigenic and metastatic progenitor cells. *Oncogene* 2006; **25**: 1696–1708. [DOI: 10.1038/sj.onc.1209327]

38 O'Brien CA, Pollett A, Gallinger S, Dick JE. A human colon cancer cell capable of initiating tumour growth in immunodeficient mice. *Nature* 2007; **445**: 106–110. [DOI: 10.1038/nature05372]

39 Ricci-Vitiani L, Lombardi DG, Pilozzi E, Biffoni M, Todaro M, Peschle C, De Maria R. Identification and expansion of human colon-cancer-initiating cells. *Nature* 2007; **445**: 111–115. [DOI: 10.1038/nature05384]

40 Wu C, Wei Q, Utomo V, Nadesan P, Whetstone H, Kandel R, Wunder JS, Alman BA. Side population cells isolated from mesenchymal neoplasms have tumor initiating potential. *Cancer Res* 2007; **67**: 8216–8222. [PMID: 17804735 DOI: 10.1158/0008-5472.CAN-07-0999]

41 O'Brien-Ball C, Biddle A. Reprogramming to developmental plasticity in cancer stem cells. *Developmental Biology* 2017; **430**: 266–274. [DOI: 10.1016/j.ydbio.2017.07.025]

42 Sancho P, Barneda D, Heeschen C. Hallmarks of cancer stem cell metabolism. *Br J Cancer* 2016; **114**: 1305–1312. [PMID: 27219018 DOI: 10.1038/bjc.2016.152]

43 Dunn GP, Bruce AT, Ikeda H, Old LJ, Schreiber RD. Cancer immunoediting: from immunosurveillance to tumor escape. *Nat Immunol* 2002; **3**: 991–998. [DOI: 10.1038/ni1102-991]

44 Walcher L, Kistenmacher A-K, Suo H, Kitte R, Dluczek S, Strauß A, Blaudszun A-R, Yevsa T, Fricke S, Kossatz-Boehlert U. Cancer Stem Cells—Origins and Biomarkers: Perspectives for Targeted Personalized Therapies. *Front Immunol* 2020; **11**: 1280. [DOI: 10.3389/fimmu.2020.01280]

45 Mani SA, Guo W, Liao M-J, Eaton ENg, Ayyanan A, Zhou AY, Brooks M, Reinhard F, Zhang CC, Shipitsin M, Campbell LL, Polyak K, Brisken C, Yang J, Weinberg RA. The Epithelial-Mesenchymal Transition Generates Cells with Properties of Stem Cells. *Cell* 2008; **133**: 704–715. [DOI: 10.1016/j.cell.2008.03.027]

46 Cazet AS, Hui MN, Elsworth BL, Wu SZ, Roden D, Chan C-L, Skhinas JN, Collot R, Yang J, Harvey K, Johan MZ, Cooper C, Nair R, Herrmann D, McFarland A, Deng N, Ruiz-Borrego M, Rojo F, Trigo JM, Bezares S, Caballero R, Lim E, Timpson P, O'Toole S, Watkins DN, Cox TR, Samuel MS, Martín M, Swarbrick A. Targeting stromal remodeling and cancer stem cell plasticity overcomes chemoresistance in triple negative breast cancer. *Nat Commun* 2018; **9**: 2897. [DOI: 10.1038/s41467-018-05220-6]

47 Vermeulen L, De Sousa E Melo F, van der Heijden M, Cameron K, de Jong JH, Borovski T, Tuynman JB, Todaro M, Merz C, Rodermond H, Sprick MR, Kemper K, Richel DJ, Stassi G, Medema JP. Wnt activity defines colon cancer stem cells and is regulated by the microenvironment. *Nat Cell Biol* 2010; **12**: 468–476. [DOI: 10.1038/ncb2048]

48 Wang Z, Li Y, Kong D, Banerjee S, Ahmad A, Azmi AS, Ali S, Abbruzzese JL, Gallick GE, Sarkar FH. Acquisition of Epithelial-Mesenchymal Transition Phenotype of Gemcitabine-Resistant Pancreatic Cancer Cells Is Linked with Activation of the Notch Signaling Pathway. *Cancer Res* 2009; **69**: 2400–2407. [DOI: 10.1158/0008-5472.CAN-08-4312]

49 Xie M, Zhang L, He C, Xu F, Liu J, Hu Z, Zhao L, Tian Y. Activation of Notch-1 enhances epithelial-mesenchymal transition in gefitinib-acquired resistant lung cancer cells. *J Cell Biochem* 2012; **113**: 1501–1513. [PMID: 22173954 DOI: 10.1002/jcb.24019]

50 Virchow R. An Address on the Value of Pathological Experiments. *Br Med J* 1881; **2**: 198–203. [PMID: 20749954 DOI: 10-1136/bmj.2.1075.198]

51 Singh SK, Clarke ID, Terasaki M, Bonn VE, Hawkins C, Squire J, Dirks PB. Identification of a cancer stem cell in human brain tumors. *Cancer Res* 2003; **63**: 5821–5828. [PMID: 14522905]

52 Suetsugu A, Nagaki M, Aoki H, Motohashi T, Kunisada T, Moriwaki H. Characterization of CD133+ hepatocellular carcinoma cells as cancer stem/progenitor cells. *Biochemical and Biophysical Research Communications* 2006; **351**: 820–824. [DOI: 10.1016/j.bbrc.2006.10.128]

53 Shepherd CJ, Rizzo S, Ledaki I, Davies M, Brewer D, Attard G, De Bono J, Hudson DL. Expression profiling of CD133 $^{+}$ and CD133 $^{-}$ epithelial cells from human prostate. *Prostate* 2008; **68**: 1007–1024. [DOI: 10.1002/pros.20765]

54 Wright MH, Calcagno AM, Salcido CD, Carlson MD, Ambudkar SV, Varticovski L. Brca1 breast tumors contain distinct CD44+/CD24- and CD133+cells with cancer stem cell characteristics. *Breast Cancer Res* 2008; **10**: R10. [DOI: 10.1186/bcr1855]

55 Shmelkov SV, St.Clair R, Lyden D, Rafii S. AC133/CD133/Prominin-1. *The International Journal of Biochemistry & Cell Biology* 2005; **37**: 715–719. [DOI: 10.1016/j.biocel.2004.08.010]

56 Miranda-Lorenzo I, Dorado J, Lonardo E, Alcala S, Serrano AG, Clausell-Tormos J, Cioffi M, Megias D, Zagorac S, Balic A, Hidalgo M, Erkan M, Kleeff J, Scarpa A, Sainz B, Heeschen C. Intracellular autofluorescence: a biomarker for epithelial cancer stem cells. *Nat Methods* 2014; **11**: 1161–1169. [DOI: 10.1038/nmeth.3112]

57 Rasheed ZA, Yang J, Wang Q, Kowalski J, Freed I, Murter C, Hong S-M, Koorstra J-B, Rajeshkumar NV, He X, Goggins M, Iacobuzio-Donahue C, Berman DM, Laheru D, Jimeno A, Hidalgo M, Maitra A, Matsui W. Prognostic Significance of Tumorigenic Cells With Mesenchymal Features in Pancreatic Adenocarcinoma. *JNCI: Journal of the National Cancer Institute* 2010; **102**: 340–351. [DOI: 10.1093/jnci/djp535]

58 Alcalá S, Martinelli P, Hermann PC, Heeschen C, Sainz B. The Anthrax Toxin Receptor 1 (ANTXR1) Is Enriched in Pancreatic Cancer Stem Cells Derived from Primary Tumor Cultures. *Stem Cells International* 2019; **2019**: 1–13. [DOI: 10.1155/2019/1378639]

59 Wang VM-Y, Ferreira RMM, Almagro J, Evan T, Legrave N, Zaw Thin M, Frith D, Carvalho J, Barry DJ, Snijders AP, Herbert E, Nye EL, MacRae JI, Behrens A. CD9 identifies pancreatic cancer stem cells and modulates glutamine metabolism to fuel tumour growth. *Nat Cell Biol* 2019; **21**: 1425–1435. [DOI: 10.1038/s41556-019-0407-1]

60 Li C, Wu J, Hynes M, Dosch J, Sarkar B, Welling TH, Pasca Di Magliano M, Simeone DM. c-Met Is a Marker of Pancreatic Cancer Stem Cells and Therapeutic Target. *Gastroenterology* 2011; **141**: 2218-2227.e5. [DOI: 10.1053/j.gastro.2011.08.009]

61 Lonardo E, Cioffi M, Sancho P, Sanchez-Ripoll Y, Trabulo SM, Dorado J, Balic A, Hidalgo M, Heeschen C. Metformin Targets the Metabolic Achilles Heel of Human Pancreatic Cancer Stem Cells. *PLoS One* 2013; **8**. [PMID: 24204632 DOI: 10.1371/journal.pone.0076518]

62 Sancho P, Burgos-Ramos E, Tavera A, Bou Kheir T, Jagust P, Schoenhals M, Barneda D, Sellers K, Campos-Olivas R, Graña O, Viera CR, Yuneva M, Sainz B, Heeschen C. MYC/PGC-1α Balance Determines the Metabolic Phenotype and Plasticity of Pancreatic Cancer Stem Cells. *Cell Metabolism* 2015; **22**: 590–605. [DOI: 10.1016/j.cmet.2015.08.015]

63 Valle S, Alcalá S, Martin-Hijano L, Cabezas-Sáinz P, Navarro D, Muñoz ER, Yuste L, Tiwary K, Walter K, Ruiz-Cañas L, Alonso-Nocelo M, Rubiolo JA, González-Arnay E, Heeschen C, Garcia-Bermejo L, Hermann PC, Sánchez L, Sancho P, Fernández-Moreno MÁ, Sainz B. Exploiting oxidative phosphorylation to promote the stem and immunoevasive properties of pancreatic cancer stem cells. *Nat Commun* 2020; **11**: 5265. [DOI: 10.1038/s41467-020-18954-z]

64 Courtois S, de Luxán-Delgado B, Penin-Peyta L, Royo-García A, Parejo-Alonso B, Jagust P, Alcalá S, Rubiolo JA, Sánchez L, Sainz B, Heeschen C, Sancho P. Inhibition of Mitochondrial Dynamics Preferentially Targets Pancreatic Cancer Cells with Enhanced Tumorigenic and Invasive Potential. *Cancers* 2021; **13**: 698. [DOI: 10.3390/cancers13040698]

65 Tang F, Barbacioru C, Bao S, Lee C, Nordman E, Wang X, Lao K, Surani MA. Tracing the Derivation of Embryonic Stem Cells from the Inner Cell Mass by Single-Cell RNA-Seq Analysis. *Cell Stem Cell* 2010; **6**: 468–478. [PMID: 20452321 DOI: 10.1016/j.stem.2010.03.015]

66 Herreros-Villanueva M. Embryonic stem cell factors and pancreatic cancer. *WJG* 2014; **20**: 2247. [DOI: 10.3748/wjg.v20.i9.2247]

67 Takahashi K, Tanabe K, Ohnuki M, Narita M, Ichisaka T, Tomoda K, Yamanaka S. Induction of Pluripotent Stem Cells from Adult Human Fibroblasts by Defined Factors. *Cell* 2007; **131**: 861–872. [DOI: 10.1016/j.cell.2007.11.019]

68 Maddipati R, Katz JP. KLF4 Initiates Acinar Cell Reprogramming and Is Essential for the Early Stages of Pancreatic Carcinogenesis. *Cancer Cell* 2016; **29**: 247–248. [DOI: 10.1016/j.ccell.2016.02.019]

69 Wei D, Wang L, Yan Y, Jia Z, Gagea M, Li Z, Zuo X, Kong X, Huang S, Xie K. KLF4 Is Essential for Induction of Cellular Identity Change and Acinar-to-Ductal Reprogramming during Early Pancreatic Carcinogenesis. *Cancer Cell* 2016; **29**: 324–338. [DOI: 10.1016/j.ccell.2016.02.005]

70 Warburg O. THE METABOLISM OF TUMORS IN THE BODY. *The Journal of General Physiology* 1927; **8**: 519–530. [DOI: 10.1085/jgp.8.6.519]

71 Potter M, Newport E, Morten KJ. The Warburg effect: 80 years on. *Biochem Soc Trans* 2016; **44**: 1499–1505. [PMID: 27911732 DOI: 10.1042/BST20160094]

72 Jia D, Park JH, Jung KH, Levine H, Kaipparettu BA. Elucidating the Metabolic Plasticity of Cancer: Mitochondrial Reprogramming and Hybrid Metabolic States. *Cells* 2018; **7**: 21. [DOI: 10.3390/cells7030021]

73 Hanahan D, Weinberg RA. Hallmarks of Cancer: The Next Generation. *Cell* 2011; **144**: 646–674. [DOI: 10.1016/j.cell.2011.02.013]

74 Jagust P, de Luxán-Delgado B, Parejo-Alonso B, Sancho P. Metabolism-Based Therapeutic Strategies Targeting Cancer Stem Cells. *Front Pharmacol* 2019; **10**. [PMID: 30967773 DOI: 10.3389/fphar.2019.00203]

75 Hermann PC, Sancho P, Cañamero M, Martinelli P, Madriles F, Michl P, Gress T, de Pascual R, Gandia L, Guerra C, Barbacid M, Wagner M, Vieira CR, Aicher A, Real FX, Sainz B, Heeschen C. Nicotine Promotes Initiation and Progression of KRAS-Induced Pancreatic Cancer via Gata6-Dependent Dedifferentiation of Acinar Cells in Mice. *Gastroenterology* 2014; **147**: 1119-1133.e4. [DOI: 10.1053/j.gastro.2014.08.002]

76 Jagust P, Alcalá S, Jr BS, Heeschen C, Sancho P. Glutathione metabolism is essential for self-renewal and chemoresistance of pancreatic cancer stem cells. *WJSC* 2020; **12**: 1410–1428. [DOI: 10.4252/wjsc.v12.i11.1410]

77 Kelly DP, Scarpulla RC. Transcriptional regulatory circuits controlling mitochondrial biogenesis and function. *Genes Dev* 2004; **18**: 357–368. [DOI: 10.1101/gad.1177604]

78 Michael LF, Wu Z, Cheatham RB, Puigserver P, Adelmant G, Lehman JJ, Kelly DP, Spiegelman BM. Restoration of insulin-sensitive glucose transporter (GLUT4) gene expression in muscle cells by the transcriptional coactivator PGC-1. *Proc Natl Acad Sci USA* 2001; **98**: 3820–3825. [DOI: 10.1073/pnas.061035098]

79 Wende AR, Schaeffer PJ, Parker GJ, Zechner C, Han D-H, Chen MM, Hancock CR, Lehman JJ, Huss JM, McClain DA, Holloszy JO, Kelly DP. A Role for the Transcriptional Coactivator PGC-1α in Muscle Refueling. *Journal of Biological Chemistry* 2007; **282**: 36642–36651. [DOI: 10.1074/jbc.M707006200]

80 Leone TC, Lehman JJ, Finck BN, Schaeffer PJ, Wende AR, Boudina S, Courtois M, Wozniak DF, Sambandam N, Bernal-Mizrachi C, Chen Z, O. Holloszy J, Medeiros DM, Schmidt RE, Saffitz JE, Abel ED, Semenkovich CF, Kelly DP. PGC-1α Deficiency Causes Multi-System Energy Metabolic Derangements: Muscle Dysfunction, Abnormal Weight Control and Hepatic Steatosis. *PLoS Biol* 2005; **3**: e101. [DOI: 10.1371/journal.pbio.0030101]

81 Wu Z, Puigserver P, Andersson U, Zhang C, Adelmant G, Mootha V, Troy A, Cinti S, Lowell B, Scarpulla RC, Spiegelman BM. Mechanisms Controlling Mitochondrial Biogenesis and Respiration through the Thermogenic Coactivator PGC-1. *Cell* 1999; **98**: 115–124. [DOI: 10.1016/S0092-8674(00)80611-X]

82 Haemmerle G, Moustafa T, Woelkart G, Büttner S, Schmidt A, van de Weijer T, Hesselink M, Jaeger D, Kienesberger PC, Zierler K, Schreiber R, Eichmann T, Kolb D, Kotzbeck P, Schweiger M, Kumari M, Eder S, Schoiswohl G, Wongsiriroj N, Pollak NM, Radner FPW, Preiss-Landl K, Kolbe T, Rülicke T, Pieske B, Trauner M, Lass A, Zimmermann R, Hoefler G, Cinti S, Kershaw EE, Schrauwen P, Madeo F, Mayer B, Zechner R. ATGL-mediated fat catabolism regulates cardiac mitochondrial function via PPAR-α and PGC-1. *Nat Med* 2011; **17**: 1076–1085. [DOI: 10.1038/nm.2439]

83 Hondares E, Pineda-Torra I, Iglesias R, Staels B, Villarroya F, Giralt M. PPARδ, but not PPARα, activates PGC-1α gene transcription in muscle. *Biochemical and Biophysical Research Communications* 2007; **354**: 1021–1027. [DOI: 10.1016/j.bbrc.2007.01.092]

84 Chen C-L, Uthaya Kumar DB, Punj V, Xu J, Sher L, Tahara SM, Hess S, Machida K. NANOG Metabolically Reprograms Tumor-Initiating Stem-like Cells through Tumorigenic Changes in Oxidative Phosphorylation and Fatty Acid Metabolism. *Cell Metabolism* 2016; **23**: 206–219. [DOI: 10.1016/j.cmet.2015.12.004]

85 Hershey BJ, Vazzana R, Joppi DL, Havas KM. Lipid Droplets Define a Sub-Population of Breast Cancer Stem Cells. *JCM* 2019; **9**: 87. [DOI: 10.3390/jcm9010087]

86 Tirinato L, Pagliari F, Di Franco S, Sogne E, Marafioti MG, Jansen J, Falqui A, Todaro M, Candeloro P, Liberale C, Seco J, Stassi G, Di Fabrizio E. ROS and Lipid Droplet accumulation induced by high glucose exposure in healthy colon and Colorectal Cancer Stem Cells. *Genes & Diseases* 2020; **7**: 620–635. [DOI: 10.1016/j.gendis.2019.09.010]

87 Brandi J, Dando I, Pozza ED, Biondani G, Jenkins R, Elliott V, Park K, Fanelli G, Zolla L, Costello E, Scarpa A, Cecconi D, Palmieri M. Proteomic analysis of pancreatic cancer stem cells: Functional role of fatty acid synthesis and mevalonate pathways. *Journal of Proteomics* 2017; **150**: 310–322. [DOI: 10.1016/j.jprot.2016.10.002]

88 Sunami Y, Rebelo A, Kleeff J. Lipid Metabolism and Lipid Droplets in Pancreatic Cancer and Stellate Cells. *Cancers* 2017; **10**: 3. [DOI: 10.3390/cancers10010003]

89 Royo-García A, Courtois S, Parejo-Alonso B, Espiau-Romera P, Sancho P. Lipid droplets as metabolic determinants for stemness and chemoresistance in cancer. *WJSC* 2021; **13**: 1307–1317. [DOI: 10.4252/wjsc.v13.i9.1307]

90 Muller M, Haghnejad V, Schaefer M, Gauchotte G, Caron B, Peyrin-Biroulet L, Bronowicki J-P, Neuzillet C, Lopez A. The Immune Landscape of Human Pancreatic Ductal Carcinoma: Key Players, Clinical Implications, and Challenges. *Cancers* 2022; **14**: 995. [DOI: 10.3390/cancers14040995]

91 Bellone G, Turletti A, Artusio E, Mareschi K, Carbone A, Tibaudi D, Robecchi A, Emanuelli G, Rodeck U. Tumor-Associated Transforming Growth Factor-$^{N}_{L}$ and Interleukin-10 Contribute to a Systemic Th2 Immune Phenotype in Pancreatic Carcinoma Patients. 1999; **155**. [PMID: 10433946 DOI: 10.1016/s0002-9440(10)65149-8]

92 Han Y, Liu D, Li L. PD-1/PD-L1 pathway: current researches in cancer. 2020; : 16. [PMID: 32266087]

93 Ribas A. Adaptive Immune Resistance: How Cancer Protects from Immune Attack. *Cancer Discovery* 2015; **5**: 915–919. [DOI: 10.1158/2159-8290.CD-15-0563]

94 Qian J, Wang C, Wang B, Yang J, Wang Y, Luo F, Xu J, Zhao C, Liu R, Chu Y. The IFN-γ/PD-L1 axis between T cells and tumor microenvironment: hints for glioma anti-PD-1/PD-L1 therapy. *J Neuroinflammation* 2018; **15**: 290. [PMID: 30333036 DOI: 10.1186/s12974-018-1330-2]

95 Romano S, Tufano M, D'Arrigo P, Vigorito V, Russo S, Romano MF. Cell stemness, epithelial-to-mesenchymal transition, and immunoevasion: Intertwined aspects in cancer metastasis. *Seminars in Cancer Biology* 2020; **60**: 181–190. [DOI: 10.1016/j.semcancer.2019.08.015]

96 Tsuchiya H, Shiota G. Immune evasion by cancer stem cells. *Regenerative Therapy* 2021; **17**: 20–33. [DOI: 10.1016/j.reth.2021.02.006]

97 Hou Y-C, Chao Y-J, Hsieh M-H, Tung H-L, Wang H-C, Shan Y-S. Low CD8+ T Cell Infiltration and High PD-L1 Expression Are Associated with Level of CD44+/CD133+

Cancer Stem Cells and Predict an Unfavorable Prognosis in Pancreatic Cancer. *Cancers* 2019; **11**: 541. [DOI: 10.3390/cancers11040541]

98 Zhu Y, Karakhanova S, Huang X, Deng SP, Werner J, Bazhin AV. Influence of interferon-α on the expression of the cancer stem cell markers in pancreatic carcinoma cells. *Experimental Cell Research* 2014; **324**: 146–156. [DOI: 10.1016/j.yexcr.2014.03.020]

99 Sainz B, Martín B, Tatari M, Heeschen C, Guerra S. ISG15 Is a Critical Microenvironmental Factor for Pancreatic Cancer Stem Cells. *Cancer Research* 2014; **74**: 7309–7320. [DOI: 10.1158/0008-5472.CAN-14-1354]

100 Friedl P, Wolf K. Tumour-cell invasion and migration: diversity and escape mechanisms. *Nat Rev Cancer* 2003; **3**: 362–374. [DOI: 10.1038/nrc1075]

101 Palamaris K, Felekouras E, Sakellariou S. Epithelial to Mesenchymal Transition: Key Regulator of Pancreatic Ductal Adenocarcinoma Progression and Chemoresistance. *Cancers* 2021; **13**: 5532. [DOI: 10.3390/cancers13215532]

102 Jolly MK. Implications of the Hybrid Epithelial/Mesenchymal Phenotype in Metastasis. *Front Oncol* 2015; **5**. [DOI: 10.3389/fonc.2015.00155]

103 Sainz B, Alcala S, Garcia E, Sanchez-Ripoll Y, Azevedo MM, Cioffi M, Tatari M, Miranda-Lorenzo I, Hidalgo M, Gomez-Lopez G, Cañamero M, Erkan M, Kleeff J, García-Silva S, Sancho P, Hermann PC, Heeschen C. Microenvironmental hCAP-18/LL-37 promotes pancreatic ductal adenocarcinoma by activating its cancer stem cell compartment. *Gut* 2015; **64**: 1921–1935. [DOI: 10.1136/gutjnl-2014-308935]

104 Alonso-Nocelo M, Ruiz-Cañas L, Sancho P, Görgülü K, Alcalá S, Pedrero C, Vallespinos M, López-Gil JC, Ochando M, García-García E, David Trabulo SM, Martinelli P, Sánchez-Tomero P, Sánchez-Palomo C, Gonzalez-Santamaría P, Yuste L, Wörmann SM, Kabacaoğlu D, Earl J, Martin A, Salvador F, Valle S, Martin-Hijano L, Carrato A, Erkan M, García-Bermejo L, Hermann PC, Algül H, Moreno-Bueno G, Heeschen C, Portillo F, Cano A, Sainz, Jr B. Macrophages direct cancer cells through a LOXL2-mediated metastatic cascade in pancreatic ductal adenocarcinoma. *Gut* 2022; : gutjnl-2021-325564. [DOI: 10.1136/gutjnl-2021-325564]

105 Rapp UR, Korn C, Ceteci F, Karreman C, Luetkenhaus K, Serafin V, Zanucco E, Castro I, Potapenko T. Myc Is a Metastasis Gene for Non-Small-Cell Lung Cancer. *PLoS ONE* 2009; **4**: e6029. [DOI: 10.1371/journal.pone.0006029]

106 Cho H, Herzka T, Zheng W, Qi J, Wilkinson JE, Bradner JE, Robinson BD, Castillo-Martin M, Cordon-Cardo C, Trotman LC. RapidCaP, a Novel GEM Model for Metastatic Prostate Cancer Analysis and Therapy, Reveals Myc as a Driver of *Pten* -Mutant Metastasis. *Cancer Discovery* 2014; **4**: 318–333. [DOI: 10.1158/2159-8290.CD-13-0346]

107 Kalluri R, Weinberg RA. The basics of epithelial-mesenchymal transition. *J Clin Invest* 2009; **119**: 1420–1428. [DOI: 10.1172/JCI39104]

108 Dimitrov-Markov S, Perales-Patón J, Bockorny B, Dopazo A, Muñoz M, Baños N, Bonilla V, Menendez C, Duran Y, Huang L, Perea S, Muthuswamy SK, Al-Shahrour F, Lopez-Casas PP, Hidalgo M. Discovery of New Targets to Control Metastasis in Pancreatic Cancer by Single-cell Transcriptomics Analysis of Circulating Tumor Cells. *Molecular Cancer Therapeutics* 2020; **19**: 1751–1760. [DOI: 10.1158/1535-7163.MCT-19-1166]

109 Carstens JL, Yang S, Correa de Sampaio P, Zheng X, Barua S, McAndrews KM, Rao A, Burks JK, Rhim AD, Kalluri R. Stabilized epithelial phenotype of cancer cells in primary tumors leads to increased colonization of liver metastasis in pancreatic cancer. *Cell Reports* 2021; **35**: 108990. [DOI: 10.1016/j.celrep.2021.108990]

110 Rhim AD, Mirek ET, Aiello NM, Maitra A, Bailey JM, McCallister F, Reichert M, Beatty GL, Rustgi AK, Vonderheide RobertH, Leach SD, Stanger BZ. EMT and dissemination precede pancreatic tumor formation. *Cell* 2012; **148**: 349–361. [PMID: 22265420 DOI: 10.1016/j.cell.2011.11.025]

111 Poruk KE, Blackford AL, Weiss MJ, Cameron JL, He J, Goggins M, Rasheed ZA, Wolfgang CL, Wood LD. Circulating Tumor Cells Expressing Markers of Tumor-Initiating Cells Predict Poor Survival and Cancer Recurrence in Patients with Pancreatic Ductal Adenocarcinoma. *Clinical Cancer Research* 2017; **23**: 2681–2690. [DOI: 10.1158/1078-0432.CCR-16-1467]

112 Liu Y, Cao X. Characteristics and Significance of the Pre-metastatic Niche. *Cancer Cell* 2016; **30**: 668–681. [DOI: 10.1016/j.ccell.2016.09.011]

113 Penny HL, Sieow JL, Adriani G, Yeap WH, See Chi Ee P, San Luis B, Lee B, Lee T, Mak SY, Ho YS, Lam KP, Ong CK, Huang RYJ, Ginhoux F, Rotzschke O, Kamm RD, Wong SC. Warburg metabolism in tumor-conditioned macrophages promotes metastasis in human pancreatic ductal adenocarcinoma. *OncoImmunology* 2016; **5**: e1191731. [DOI: 10.1080/2162402X.2016.1191731]

114 Abdullah LN, Chow EK. Mechanisms of chemoresistance in cancer stem cells. *Clinical and Translational Medicine* 2013; **2**. [DOI: 10.1186/2001-1326-2-3]

115 Begicevic R-R, Falasca M. ABC Transporters in Cancer Stem Cells: Beyond Chemoresistance. *IJMS* 2017; **18**: 2362. [DOI: 10.3390/ijms18112362]

116 Li H, Jiang W, Liu X-N, Yuan L-Y, Li T-J, Li S, Xu S-S, Zhang W-H, Gao H-L, Han X, Wang W-Q, Wu C-T, Yu X-J, Xu H-X, Liu L. TET1 downregulates epithelial-mesenchymal transition and chemoresistance in PDAC by demethylating CHL1 to inhibit the Hedgehog signaling pathway. *Oncogene* 2020; **39**: 5825–5838. [DOI: 10.1038/s41388-020-01407-8]

117 Okuno K, Xu C, Pascual-Sabater S, Tokunaga M, Han H, Fillat C, Kinugasa Y, Goel A. Berberine Overcomes Gemcitabine-Associated Chemoresistance through Regulation of Rap1/PI3K-Akt Signaling in Pancreatic Ductal Adenocarcinoma. *Pharmaceuticals* 2022; **15**: 1199. [DOI: 10.3390/ph15101199]

118 Cao F, Li J, Sun H, Liu S, Cui Y, Li F. HES 1 is essential for chemoresistance induced by stellate cells and is associated with poor prognosis in pancreatic cancer. *Oncology Reports* 2015; **33**: 1883–1889. [DOI: 10.3892/or.2015.3789]

119 Zhang D, Ding L, Li Y, Ren J, Shi G, Wang Y, Zhao S, Ni Y, Hou Y. Midkine derived from cancer-associated fibroblasts promotes cisplatin-resistance via up-regulation of the expression of lncRNA ANRIL in tumour cells. *Sci Rep* 2017; **7**: 1–11. [DOI: 10.1038/s41598-017-13431-y]

120 Gungor C, Zander H, Effenberger KE, Vashist YK, Kalinina T, Izbicki JR, Yekebas E, Bockhorn M. Notch Signaling Activated by Replication Stress-Induced Expression of Midkine Drives Epithelial-Mesenchymal Transition and Chemoresistance in Pancreatic Cancer. *Cancer Research* 2011; **71**: 5009–5019. [DOI: 10.1158/0008-5472.CAN-11-0036]

121 Wu D, Liu L, Yan X, Wang C, Wang Y, Han K, Lin S, Gan Z, Min D. Pleiotrophin promotes chemoresistance to doxorubicin in osteosarcoma by upregulating P-glycoprotein. *Oncotarget* 2017; **8**: 63857–63870. [DOI: 10.18632/oncotarget.19148]

122 Ganguly K, Bhatia R, Rauth S, Kisling A, Atri P, Thompson C, Vengoji R, Ram Krishn S, Shinde D, Thomas V, Kaur S, Mallya K, Cox JL, Kumar S, Batra SK. Mucin 5AC Serves as the Nexus for β-Catenin/c-Myc Interplay to Promote Glutamine Dependency During Pancreatic Cancer Chemoresistance. *Gastroenterology* 2022; **162**: 253-268.e13. [DOI: 10.1053/j.gastro.2021.09.017]

123 Parasido E, Avetian GS, Naeem A, Graham G, Pishvaian M, Glasgow E, Mudambi S, Lee Y, Ihemelandu C, Choudhry M, Peran I, Banerjee PP, Avantaggiati ML, Bryant K, Baldelli E, Pierobon M, Liotta L, Petricoin E, Fricke ST, Sebastian A, Cozzitorto J, Loots GG, Kumar D, Byers S, Londin E, DiFeo A, Narla G, Winter J, Brody JR, Rodriguez O, Albanese C. The Sustained Induction of c-MYC Drives Nab-Paclitaxel Resistance in Primary Pancreatic Ductal Carcinoma Cells. *Molecular Cancer Research* 2019; **17**: 1815–1827. [DOI: 10.1158/1541-7786.MCR-19-0191]

124 Michalik L, Auwerx J, Berger JP, Chatterjee VK, Glass CK, Gonzalez FJ, Grimaldi PA, Kadowaki T, Lazar MA, O'Rahilly S, Palmer CNA, Plutzky J, Reddy JK, Spiegelman BM, Staels B, Wahli W. International Union of Pharmacology. LXI. Peroxisome Proliferator-Activated Receptors. *Pharmacol Rev* 2006; **58**: 726–741. [DOI: 10.1124/pr.58.4.5]

125 Attianese GMG, Desvergne B. Integrative and Systemic Approaches for Evaluating PPARβ/δ (PPARD) Function. *Nucl Recept Signal* 2015; **13**: nrs.13001. [DOI: 10.1621/nrs.13001]

126 Gearing KL, Göttlicher M, Teboul M, Widmark E, Gustafsson JA. Interaction of the peroxisome-proliferator-activated receptor and retinoid X receptor. *Proc Natl Acad Sci USA* 1993; **90**: 1440–1444. [DOI: 10.1073/pnas.90.4.1440]

127 Kota B, Huang T, Roufogalis B. An overview on biological mechanisms of PPARs. *Pharmacological Research* 2005; **51**: 85–94. [DOI: 10.1016/j.phrs.2004.07.012]

128 Krey G, Keller H, Mahfoudi A, Medin J, Ozato K, Dreyer C, Wahli W. Xenopus peroxisome proliferator activated receptors: Genomic organization, response element recognition, heterodimer formation with retinoid X receptor and activation by fatty acids. *The Journal of Steroid Biochemistry and Molecular Biology* 1993; **47**: 65–73. [DOI: 10.1016/0960-0760(93)90058-5]

129 Kliewer SA, Forman BM, Blumberg B, Ong ES, Borgmeyer U, Mangelsdorf DJ, Umesono K, Evans RM. Differential expression and activation of a family of murine peroxisome proliferator-activated receptors. *Proc Natl Acad Sci USA* 1994; **91**: 7355–7359. [DOI: 10.1073/pnas.91.15.7355]

130 Shureiqi I, Jiang W, Zuo X, Wu Y, Stimmel JB, Leesnitzer LM, Morris JS, Fan H-Z, Fischer SM, Lippman SM. The 15-lipoxygenase-1 product 13-S-hydroxyocta-decadienoic acid down-regulates PPAR-delta to induce apoptosis in colorectal cancer cells. *Proc Natl Acad Sci USA* 2003; **100**: 9968-73. [PMID: 12909723 DOI: 10.1073/pnas.1631086100]

131 Coleman JD, Prabhu KS, Thompson JT, Reddy PS, Peters JM, Peterson BR, Reddy CC, Vanden Heuvel JP. The oxidative stress mediator 4-hydroxynonenal is an intracellular agonist of the nuclear receptor peroxisome proliferator-activated receptor-β/δ (PPARβ/δ). *Free Radical Biology and Medicine* 2007; **42**: 1155–1164. [DOI: 10.1016/j.freeradbiomed.2007.01.003]

132 Malek MA, Hoang M-H, Jia Y, Lee JH, Jun HJ, Lee D-H, Lee HJ, Lee C, Lee MK, Hwang BY, Lee S-J. Ombuin-3-O-β-d-glucopyranoside from Gynostemma pentaphyllum is a dual agonistic ligand of peroxisome proliferator-activated receptors α and δ/β. *Biochemical and Biophysical Research Communications* 2013; **430**: 1322–1328. [DOI: 10.1016/j.bbrc.2012.12.020]

133 Burns K, Vandenheuvel J. Modulation of PPAR activity via phosphorylation. *Biochimica et Biophysica Acta (BBA) - Molecular and Cell Biology of Lipids* 2007; **1771**: 952–960. [DOI: 10.1016/j.bbalip.2007.04.018]

134 Tanaka T, Yamamoto J, Iwasaki S, Asaba H, Hamura H, Ikeda Y, Watanabe M, Magoori K, Ioka RX, Tachibana K, Watanabe Y, Uchiyama Y, Sumi K, Iguchi H, Ito S, Doi T, Hamakubo T, Naito M, Auwerx J, Yanagisawa M, Kodama T, Sakai J. Activation of peroxisome proliferator-activated receptor delta induces fatty acid beta-oxidation in skeletal muscle and attenuates metabolic syndrome. *Proc Natl Acad Sci USA* 2003; **100**: 15924-9. [PMID: 14676330 DOI: 10.1073/pnas.0306981100]

135 Winzell MS, Wulff EM, Olsen GS, Sauerberg P, Gotfredsen CF, Ahrén B. Improved insulin sensitivity and islet function after PPARδ activation in diabetic db/db mice. *European Journal of Pharmacology* 2010; **626**: 297–305. [DOI: 10.1016/j.ejphar.2009.09.053]

136 Lee C-H, Olson P, Hevener A, Mehl I, Chong L-W, Olefsky JM, Gonzalez FJ, Ham J, Kang H, Peters JM, Evans RM. PPARdelta regulates glucose metabolism and insulin

sensitivity. *Proc Natl Acad Sci USA* 2006; **103**: 3444-9. [PMID: 16492734 DOI: 10.1073/pnas.0511253103]

137 Peters JM, Shah YM, Gonzalez FJ. The role of peroxisome proliferator-activated receptors in carcinogenesis and chemoprevention. *Nat Rev Cancer* 2012; **12**: 181–195. [DOI: 10.1038/nrc3214]

138 Yang L, Zhou J, Ma Q, Wang C, Chen K, Meng W, Yu Y, Zhou Z, Sun X. Knockdown of PPAR δ Gene Promotes the Growth of Colon Cancer and Reduces the Sensitivity to Bevacizumab in Nude Mice Model. *PLoS ONE* 2013; **8**: e60715. [DOI: 10.1371/journal.pone.0060715]

139 Beyaz S, Mana MD, Roper J, Kedrin D, Saadatpour A, Hong S-J, Bauer-Rowe KE, Xifaras ME, Akkad A, Arias E, Pinello L, Katz Y, Shinagare S, Abu-Remaileh M, Mihaylova MM, Lamming DW, Dogum R, Guo G, Bell GW, Selig M, Nielsen GP, Gupta N, Ferrone CR, Deshpande V, Yuan G-C, Orkin SH, Sabatini DM, Yilmaz ÖH. High-fat diet enhances stemness and tumorigenicity of intestinal progenitors. *Nature* 2016; **531**: 53–58. [DOI: 10.1038/nature17173]

140 Shen B, Li A, Wan Y-JY, Shen G, Zhu J, Nie Y. Lack of PPAR β / δ -Inactivated SGK-1 Is Implicated in Liver Carcinogenesis. *BioMed Research International* 2020; **2020**: 1–11. [DOI: 10.1155/2020/9563851]

141 Kim M-J, Choi Y-K, Park SY, Jang SY, Lee JY, Ham HJ, Kim B-G, Jeon H-J, Kim J-H, Kim J-G, Lee I-K, Park K-G. PPARδ Reprograms Glutamine Metabolism in Sorafenib-Resistant HCC. *Molecular Cancer Research* 2017; **15**: 1230–1242. [DOI: 10.1158/1541-7786.MCR-17-0061]

142 Yao P-L, Morales JL, Zhu B, Kang B-H, Gonzalez FJ, Peters JM. Activation of Peroxisome Proliferator-Activated Receptor-β/δ (PPAR-β/δ) Inhibits Human Breast Cancer Cell Line Tumorigenicity. *Molecular Cancer Therapeutics* 2014; **13**: 1008–1017. [DOI: 10.1158/1535-7163.MCT-13-0836]

143 Wang X, Wang G, Shi Y, Sun L, Gorczynski R, Li Y-J, Xu Z, Spaner DE. PPAR-delta promotes survival of breast cancer cells in harsh metabolic conditions. *Oncogenesis* 2016; **5**: e232–e232. [DOI: 10.1038/oncsis.2016.41]

144 Coleman JD, Thompson JT, Smith RW, Prokopczyk B, Vanden Heuvel JP. Role of Peroxisome Proliferator-Activated Receptor β / δ and B-Cell Lymphoma-6 in Regulation of Genes Involved in Metastasis and Migration in Pancreatic Cancer Cells. *PPAR Research* 2013; **2013**: 1–11. [DOI: 10.1155/2013/121956]

145 Smith RW, Coleman JD, Thompson JT, Vanden Heuvel JP. Therapeutic potential of GW501516 and the role of Peroxisome proliferator-activated receptor β/δ and B-cell lymphoma 6 in inflammatory signaling in human pancreatic cancer cells. *Biochemistry and Biophysics Reports* 2016; **8**: 395-402. [PMID: 28955982 DOI: 10.1016/bbrep.2016.10.014]

146 Zuo X, Xu W, Xu M, Tian R, Moussalli MJ, Mao F, Zheng X, Wang J, Morris JS, Gagea M, Eng C, Kopetz S, Maru DM, Rashid A, Broaddus R, Wei D, Hung M-C,

Sood AK, Shureiqi I. Metastasis regulation by PPARD expression in cancer cells. *JCI Insight* 2017; **2**. [DOI: 10.1172/jci.insight.91419]

147 Liu Y, Deguchi Y, Wei D, Liu F, Moussalli MJ, Deguchi E, Li D, Wang H, Valentin LA, Colby JK, Wang J, Zheng X, Ying H, Gagea M, Ji B, Shi J, Yao JC, Zuo X, Shureiqi I. Rapid acceleration of KRAS-mutant pancreatic carcinogenesis via remodeling of tumor immune microenvironment by PPARδ. *Nat Commun* 2022; **13**: 2665. [DOI: 10.1038/s41467-022-30392-7]

148 Abrego J, Sanford-Crane H, Oon C, Xiao X, Betts CB, Sun D, Nagarajan S, Diaz L, Sandborg H, Bhattacharyya S, Xia Z, Coussens LM, Tontonoz P, Sherman MH. A Cancer Cell–Intrinsic GOT2–PPARδ Axis Suppresses Antitumor Immunity. *Cancer Discovery* 2022; **12**: 2414–2433. [DOI: 10.1158/2159-8290.CD-22-0661]

149 Odegaard JI, Ricardo-Gonzalez RR, Red Eagle A, Vats D, Morel CR, Goforth MH, Subramanian V, Mukundan L, Ferrante AW, Chawla A. Alternative M2 Activation of Kupffer Cells by PPARδ Ameliorates Obesity-Induced Insulin Resistance. *Cell Metabolism* 2008; **7**: 496–507. [DOI: 10.1016/j.cmet.2008.04.003]

150 Krebs EG, Fischer EH. PHOSPHORYLASE ACTIVITY OF SKELETAL MUSCLE EXTRACTS. *Journal of Biological Chemistry* 1955; **216**: 113–120. [DOI: 10.1016/S0021-9258(19)52288-8]

151 Fischer EH, Krebs EG. CONVERSION OF PHOSPHORYLASE b TO PHOSPHORYLASE a IN MUSCLE EXTRACTS. *Journal of Biological Chemistry* 1955; **216**: 121–132. [DOI: 10.1016/S0021-9258(19)52289-X]

152 Manning G, Whyte DB, Martinez R, Hunter T, Sudarsanam S. The Protein Kinase Complement of the Human Genome. *Science* 2002; **298**: 1912–1934. [DOI: 10.1126/science.1075762]

153 Robinson DR, Wu Y-M, Lin S-F. The protein tyrosine kinase family of the human genome. *Oncogene* 2000; **19**: 5548–5557. [DOI: 10.1038/sj.onc.1203957]

154 Sever R, Brugge JS. Signal Transduction in Cancer. *Cold Spring Harb Perspect Med* 2015; **5**. [PMID: 25833940 DOI: 10.1101/cshperspect.a006098]

155 Du Z, Lovly CM. Mechanisms of receptor tyrosine kinase activation in cancer. *Mol Cancer* 2018; **17**: 58. [DOI: 10.1186/s12943-018-0782-4]

156 Katoh M. Antibody-drug conjugate targeting protein tyrosine kinase 7, a receptor tyrosine kinase-like molecule involved in WNT and vascular endothelial growth factor signaling: effects on cancer stem cells, tumor microenvironment and whole-body homeostasis. *Ann Transl Med* 2017; **5**: 462. [PMID: 29285495 DOI: 10.21037/atm.2017.09.11]

157 Kawana S, Saito R, Miki Y, Kimura Y, Abe J, Sato I, Endo M, Sugawara S, Sasano H. Suppression of tumor immune microenvironment via microRNA-1 after epidermal growth factor receptor-tyrosine kinase inhibitor resistance acquirement in lung

adenocarcinoma. *Cancer Med* 2020; **10**: 718–727. [PMID: 33305905 DOI: 10.1002/cam4.3639]

158 Pulkkinen HH, Kiema M, Lappalainen JP, Toropainen A, Beter M, Tirronen A, Holappa L, Niskanen H, Kaikkonen MU, Ylä-Herttuala S, Laakkonen JP. BMP6/TAZ-Hippo signaling modulates angiogenesis and endothelial cell response to VEGF. *Angiogenesis* 2021; **24**: 129–144. [PMID: 33021694 DOI: 10.1007/s10456-020-09748-4]

159 Choi YJ, Kim JH, Rho JK, Kim JS, Choi C-M, Kim WS, Son J, Lee JC. AXL and MET receptor tyrosine kinases are essential for lung cancer metastasis. *Oncology Reports* 2017; **37**: 2201–2208. [DOI: 10.3892/or.2017.5482]

160 Zheng Z, Shao N, Weng H, Li W, Zhang J, Zhang L, Yang L, Ye S. Correlation between epidermal growth factor receptor and tumor stem cell markers CD44/CD24 and their relationship with prognosis in breast invasive ductal carcinoma. *Med Oncol* 2015; **32**: 275. [PMID: 25429827 DOI: 10.1007/s12032-014-0275-2]

161 Wang X, Reyes ME, Zhang D, Funakoshi Y, Trape AP, Gong Y, Kogawa T, Eckhardt BL, Masuda H, Pirman DA, Yang P, Reuben JM, Woodward WA, Bartholomeusz C, Hortobagyi GN, Tripathy D, Ueno NT. EGFR signaling promotes inflammation and cancer stem-like activity in inflammatory breast cancer. *Oncotarget* 2017; **8**: 67904–67917. [PMID: 28978083 DOI: 10.18632/oncotarget.18958]

162 Ko J, Meyer AN, Haas M, Donoghue DJ. Characterization of FGFR signaling in prostate cancer stem cells and inhibition via TKI treatment. *Oncotarget* 2021; **12**: 22–36. [PMID: 33456711 DOI: 10.18632/oncotarget.27859]

163 Binda E, Visioli A, Giani F, Lamorte G, Copetti M, Pitter KL, Huse JT, Cajola L, Zanetti N, DiMeco F, De Filippis L, Mangiola A, Maira G, Anile C, De Bonis P, Reynolds BA, Pasquale EB, Vescovi AL. The EphA2 Receptor Drives Self-Renewal and Tumorigenicity in Stem-Like Tumor-Propagating Cells from Human Glioblastomas. *Cancer Cell* 2012; **22**: 765–780. [PMID: 23238013 DOI: 10.1016/j.ccr.2012.11.005]

164 Day BW, Stringer BW, Al-Ejeh F, Ting MJ, Wilson J, Ensbey KS, Jamieson PR, Bruce ZC, Lim YC, Offenhäuser C, Charmsaz S, Cooper LT, Ellacott JK, Harding A, Leveque L, Inglis P, Allan S, Walker DG, Lackmann M, Osborne G, Khanna KK, Reynolds BA, Lickliter JD, Boyd AW. EphA3 Maintains Tumorigenicity and Is a Therapeutic Target in Glioblastoma Multiforme. *Cancer Cell* 2013; **23**: 238–248. [DOI: 10.1016/j.ccr.2013.01.007]

165 Taddei ML, Giannoni E, Morandi A, Ippolito L, Ramazzotti M, Callari M, Gandellini P, Chiarugi P. Mesenchymal to amoeboid transition is associated with stem-like features of melanoma cells. *Cell Commun Signal* 2014; **12**: 24. [PMID: 24690323 DOI: 10.1186/1478-811X-12-24]

166 Song W, Ma Y, Wang J, Brantley-Sieders D, Chen J. JNK signaling mediates EPHA2-dependent tumor cell proliferation, motility, and cancer stem cell-like properties in

non-small cell lung cancer. *Cancer Res* 2014; **74**: 2444–2454. [PMID: 24607842 DOI: 10.1158/0008-5472.CAN-13-2136]

167 Alcalá S, Mayoral-Varo V, Ruiz-Cañas L, López-Gil JC, Heeschen C, Martín-Pérez J, Sainz B. Targeting SRC Kinase Signaling in Pancreatic Cancer Stem Cells. *IJMS* 2020; **21**: 7437. [DOI: 10.3390/ijms21207437]

168 Morris SW, Kirstein MN, Valentine MB, Dittmer KG, Shapiro DN, Saltman DL, Look AT. Fusion of a Kinase Gene, *ALK*, to a Nucleolar Protein Gene, *NPM* , in Non-Hodgkin's Lymphoma. *Science* 1994; **263**: 1281–1284. [DOI: 10.1126/science.8122112]

169 Palmer RH, Vernersson E, Grabbe C, Hallberg B. Anaplastic lymphoma kinase: signalling in development and disease. *Biochem J* 2009; **420**: 345–361. [PMID: 19459784 DOI: 10.1042/BJ20090387]

170 Wellstein A. ALK receptor activation, ligands and therapeutic targeting in glioblastoma and in other cancers. *Front Oncol* 2012; **2**. [PMID: 23267434 DOI: 10.3389/fonc.2012.00192]

171 García-Regalado A, González-De la Rosa CH. The Role of Anaplastic Lymphoma Kinase in Human Cancers. *Oncology & Hematology Review (US)* 2013; **09**: 149. [DOI: 10.17925/OHR.2013.09.2.149]

172 Huang H. Anaplastic Lymphoma Kinase (ALK) Receptor Tyrosine Kinase: A Catalytic Receptor with Many Faces. *Int J Mol Sci* 2018; **19**. [PMID: 30400214 DOI: 10.3390/ijms19113448]

173 Iwahara T, Fujimoto J, Wen D, Cupples R, Bucay N, Arakawa T, Mori S, Ratzkin B, Yamamoto T. Molecular characterization of ALK, a receptor tyrosine kinase expressed specifically in the nervous system. *Oncogene* 1997; **14**: 439–449. [DOI: 10.1038/sj.onc.1200849]

174 Morris SW, Naeve C, Mathew P, James PL, Kirstein MN, Cui X, Witte DP. ALK, the chromosome 2 gene locus altered by the t(2;5) in non-Hodgkin's lymphoma, encodes a novel neural receptor tyrosine kinase that is highly related to leukocyte tyrosine kinase (LTK). *Oncogene* 1997; **14**: 2175–2188. [DOI: 10.1038/sj.onc.1201062]

175 Stoica GE, Kuo A, Powers C, Bowden ET, Sale EB, Riegel AT, Wellstein A. Midkine Binds to Anaplastic Lymphoma Kinase (ALK) and Acts as a Growth Factor for Different Cell Types. *J Biol Chem* 2002; **277**: 35990–35998. [PMID: 12122009 DOI: 10.1074/jbc.M205749200]

176 Guan J, Umapathy G, Yamazaki Y, Wolfstetter G, Mendoza P, Pfeifer K, Mohammed A, Hugosson F, Zhang H, Hsu AW, Halenbeck R, Hallberg B, Palmer RH. FAM150A and FAM150B are activating ligands for anaplastic lymphoma kinase. *eLife* 2015; **4**: e09811. [DOI: 10.7554/eLife.09811]

177 Muramatsu T. Midkine, a heparin-binding cytokine with multiple roles in development, repair and diseases. *Proc Jpn Acad Ser B Phys Biol Sci* 2010; **86**: 410–425. [PMID: 20431264 DOI: 10.2183/pjab.86.410]

178 Wang X. Pleiotrophin: Activity and mechanism. *Adv Clin Chem* 2020; **98**: 51–89. [PMID: 32564788 DOI: 10.1016/bs.acc.2020.02.003]

179 Murray PB, Lax I, Reshetnyak A, Ligon GF, Lillquist JS, Natoli EJ, Shi X, Folta-Stogniew E, Gunel M, Alvarado D, Schlessinger J. Heparin is an activating ligand of the orphan receptor tyrosine kinase ALK. *Sci Signal* 2015; **8**: ra6. [PMID: 25605972 DOI: 10.1126/scisignal.2005916]

180 Zhang H, Pao LI, Zhou A, Brace AD, Halenbeck R, Hsu AW, Bray TL, Hestir K, Bosch E, Lee E, Wang G, Liu H, Wong BR, Kavanaugh WM, Williams LT. Deorphanization of the human leukocyte tyrosine kinase (LTK) receptor by a signaling screen of the extracellular proteome. *Proc Natl Acad Sci USA* 2014; **111**: 15741–15745. [DOI: 10.1073/pnas.1412009111]

181 Fadeev A, Mendoza-Garcia P, Irion U, Guan J, Pfeifer K, Wiessner S, Serluca F, Singh AP, Nüsslein-Volhard C, Palmer RH. ALKALs are in vivo ligands for ALK family receptor tyrosine kinases in the neural crest and derived cells. *Proc Natl Acad Sci USA* 2018; **115**. [DOI: 10.1073/pnas.1719137115]

182 Hallberg B, Palmer RH. The role of the ALK receptor in cancer biology. *Ann Oncol* 2016; **27**: iii4–iii15. [DOI: 10.1093/annonc/mdw301]

183 Hallberg B, Palmer RH. Mechanistic insight into ALK receptor tyrosine kinase in human cancer biology. *Nat Rev Cancer* 2013; **13**: 685–700. [DOI: 10.1038/nrc3580]

184 Soda M, Choi YL, Enomoto M, Takada S, Yamashita Y, Ishikawa S, Fujiwara S, Watanabe H, Kurashina K, Hatanaka H, Bando M, Ohno S, Ishikawa Y, Aburatani H, Niki T, Sohara Y, Sugiyama Y, Mano H. Identification of the transforming EML4-ALK fusion gene in non-small-cell lung cancer. *Nature* 2007; **448**: 561–566. [DOI: 10.1038/nature05945]

185 Ducray SP, Natarajan K, Garland GD, Turner SD, Egger G. The Transcriptional Roles of ALK Fusion Proteins in Tumorigenesis. *Cancers* 2019; **11**: 1074. [DOI: 10.3390/cancers11081074]

186 Stylianou DC, Auf der Maur A, Kodack DP, Henke RT, Hohn S, Toretsky JA, Riegel AT, Wellstein A. Effect of single-chain antibody targeting of the ligand-binding domain in the anaplastic lymphoma kinase receptor. *Oncogene* 2009; **28**: 3296–3306. [DOI: 10.1038/onc.2009.184]

187 Chen Y, Takita J, Choi YL, Kato M, Ohira M, Sanada M, Wang L, Soda M, Kikuchi A, Igarashi T, Nakagawara A, Hayashi Y, Mano H, Ogawa S. Oncogenic mutations of ALK kinase in neuroblastoma. *Nature* 2008; **455**: 971–974. [DOI: 10.1038/nature07399]

188 El Demellawy D, McGowan-Jordan J, De Nanassy J, Chernetsova E, Nasr A. Update on molecular findings in rhabdomyosarcoma. *Pathology* 2017; **49**: 238–246. [DOI: 10.1016/j.pathol.2016.12.345]

189 Ormanns S, Assmann G, Reu S, Gallmeier E, Bader DC, Kleespies A, Haas M, Kruger S, Heinemann V, Kirchner T, Boeck S. ALK expression is absent in pancreatic ductal adenocarcinoma. *J Cancer Res Clin Oncol* 2014; **140**: 1625–1628. [PMID: 25017418 DOI: 10.1007/s00432-014-1774-4]

190 Shimada Y, Kohno T, Ueno H, Ino Y, Hayashi H, Nakaoku T, Sakamoto Y, Kondo S, Morizane C, Shimada K, Okusaka T, Hiraoka N. An Oncogenic ALK Fusion and an RRAS Mutation in KRAS Mutation-Negative Pancreatic Ductal Adenocarcinoma. *Oncologist* 2017; **22**: 158–164. [PMID: 28167572 DOI: 10.1634/theoncologist.2016-0194]

191 Koyama-Nasu R, Haruta R, Nasu-Nishimura Y, Taniue K, Katou Y, Shirahige K, Todo T, Ino Y, Mukasa A, Saito N, Matsui M, Takahashi R, Hoshino-Okubo A, Sugano H, Manabe E, Funato K, Akiyama T. The pleiotrophin-ALK axis is required for tumorigenicity of glioblastoma stem cells. *Oncogene* 2014; **33**: 2236–2244. [DOI: 10.1038/onc.2013.168]

192 López-Valero I, Dávila D, González-Martínez J, Salvador-Tormo N, Lorente M, Saiz-Ladera C, Torres S, Gabicagogeascoa E, Hernández-Tiedra S, García-Taboada E, Mendiburu-Eliçabe M, Rodríguez-Fornés F, Sánchez-Domínguez R, Segovia JC, Sánchez-Gómez P, Matheu A, Sepúlveda JM, Velasco G. Midkine signaling maintains the self-renewal and tumorigenic capacity of glioma initiating cells. *Theranostics* 2020; **10**: 5120–5136. [DOI: 10.7150/thno.41450]

193 Xu B-S, Chen H-Y, Que Y, Xiao W, Zeng M-S, Zhang X. ALK ATI interacts with c-Myc and promotes cancer stem cell-like properties in sarcoma. *Oncogene* 2020; **39**: 151–163. [DOI: 10.1038/s41388-019-0973-5]

194 Matsumoto T, Oda Y, Hasegawa Y, Hashimura M, Oguri Y, Inoue H, Yokoi A, Tochimoto M, Nakagawa M, Jiang Z, Saegusa M. Anaplastic Lymphoma Kinase Overexpression Is Associated with Aggressive Phenotypic Characteristics of Ovarian High-Grade Serous Carcinoma. *The American Journal of Pathology* 2021; **191**: 1837–1850. [DOI: 10.1016/j.ajpath.2021.06.009]

195 Hasan MdK, Nafady A, Takatori A, Kishida S, Ohira M, Suenaga Y, Hossain S, Akter J, Ogura A, Nakamura Y, Kadomatsu K, Nakagawara A. ALK is a MYCN target gene and regulates cell migration and invasion in neuroblastoma. *Sci Rep* 2013; **3**: 3450. [DOI: 10.1038/srep03450]

196 Ueda T, Nakata Y, Yamasaki N, Oda H, Sentani K, Kanai A, Onishi N, Ikeda K, Sera Y, Honda Z, Tanaka K, Sata M, Ogawa S, Yasui W, Saya H, Takita J, Honda H. ALKR1275Q perturbs extracellular matrix, enhances cell invasion and leads to the development of neuroblastoma in cooperation with MYCN. *Oncogene* 2016; **35**: 4447–4458. [DOI: 10.1038/onc.2015.519]

197 Peng L, Zhu L, Sun Y, Stebbing J, Selvaggi G, Zhang Y, Yu Z. Targeting ALK Rearrangements in NSCLC: Current State of the Art. *Front Oncol* 2022; **12**: 863461. [DOI: 10.3389/fonc.2022.863461]

198 Kwak EL, Bang Y-J, Camidge DR, Shaw AT, Solomon B, Maki RG, Ou S-HI, Dezube BJ, Jänne PA, Costa DB, Varella-Garcia M, Kim W-H, Lynch TJ, Fidias P, Stubbs H, Engelman JA, Sequist LV, Tan W, Gandhi L, Mino-Kenudson M, Wei GC, Shreeve SM, Ratain MJ, Settleman J, Christensen JG, Haber DA, Wilner K, Salgia R, Shapiro GI, Clark JW, Iafrate AJ. Anaplastic Lymphoma Kinase Inhibition in Non–Small-Cell Lung Cancer. *N Engl J Med* 2010; **363**: 1693–1703. [DOI: 10.1056/NEJMoa1006448]

199 Gerber DE, Minna JD. ALK Inhibition for Non-Small Cell Lung Cancer: From Discovery to Therapy in Record Time. *Cancer Cell* 2010; **18**: 548–551. [DOI: 10.1016/j.ccr.2010.11.033]

200 Puccini A, Marín-Ramos NI, Bergamo F, Schirripa M, Lonardi S, Lenz H-J, Loupakis F, Battaglin F. Safety and Tolerability of c-MET Inhibitors in Cancer. *Drug Saf* 2019; **42**: 211–233. [DOI: 10.1007/s40264-018-0780-x]

201 Costa DB, Kobayashi S, Pandya SS, Yeo W-L, Shen Z, Tan W, Wilner KD. CSF Concentration of the Anaplastic Lymphoma Kinase Inhibitor Crizotinib. *JCO* 2011; **29**: e443–e445. [DOI: 10.1200/JCO.2010.34.1313]

202 Choi YL, Soda M, Yamashita Y, Ueno T, Takashima J, Nakajima T, Yatabe Y, Takeuchi K, Hamada T, Haruta H, Ishikawa Y, Kimura H, Mitsudomi T, Tanio Y, Mano H. EML4-ALK Mutations in Lung Cancer That Confer Resistance to ALK Inhibitors. *N Engl J Med* 2010; **363**: 1734–1739. [DOI: 10.1056/NEJMoa1007478]

203 Horn L, Wang Z, Wu G, Poddubskaya E, Mok T, Reck M, Wakelee H, Chiappori AA, Lee DH, Breder V, Orlov S, Cicin I, Cheng Y, Liu Y, Fan Y, Whisenant JG, Zhou Y, Oertel V, Harrow K, Liang C, Mao L, Selvaggi G, Wu Y-L. Ensartinib vs Crizotinib for Patients With Anaplastic Lymphoma Kinase–Positive Non–Small Cell Lung Cancer. *JAMA Oncol* 2021; **7**: 1–9. [PMID: 34473194 DOI: 10.1001/jamaoncol.2021.3523]

204 Fukuda K, Takeuchi S, Arai S, Katayama R, Nanjo S, Tanimoto A, Nishiyama A, Nakagawa T, Taniguchi H, Suzuki T, Yamada T, Nishihara H, Ninomiya H, Ishikawa Y, Baba S, Takeuchi K, Horiike A, Yanagitani N, Nishio M, Yano S. Epithelial-to-Mesenchymal Transition Is a Mechanism of ALK Inhibitor Resistance in Lung Cancer Independent of *ALK* Mutation Status. *Cancer Research* 2019; **79**: 1658–1670. [DOI: 10.1158/0008-5472.CAN-18-2052]

205 Shen J, Meng Y, Wang K, Gao M, Du J, Wang J, Li Z, Zuo D, Wu Y. EML4-ALK G1202R mutation induces EMT and confers resistance to ceritinib in NSCLC cells via activation of STAT3/Slug signaling. *Cell Signal* 2022; **92**: 110264. [PMID: 35085771 DOI: 10.1016/j.cellsig.2022.110264]

206 Verdura S, Encinar JA, Teixidor E, Segura-Carretero A, Micol V, Cuyàs E, Bosch-Barrera J, Menendez JA. Silibinin Overcomes EMT-Driven Lung Cancer Resistance

to New-Generation ALK Inhibitors. *Cancers* 2022; **14**: 6101. [DOI: 10.3390/cancers14246101]

207 Mueller M, Hermann PC, Witthauer J, Rubio-Viqueira B, Leicht SF, Huber S, Ellwart JW, Mustafa M, Bartenstein P, D'Haese JG, Schoenberg MH, Berger F, Jauch K, Hidalgo M, Heeschen C. Combined Targeted Treatment to Eliminate Tumorigenic Cancer Stem Cells in Human Pancreatic Cancer. *Gastroenterology* 2009; **137**: 1102-1113. [DOI: 10.1053/j.gastro.2009.05.053]

208 Hu Y, Smyth GK. ELDA: Extreme limiting dilution analysis for comparing depleted and enriched populations in stem cell and other assays. *Journal of Immunological Methods* 2009; **347**: 70-78. [DOI: 10.1016/j.jim.2009.06.008]

209 Tang Z, Kang B, Li C, Chen T, Zhang Z. GEPIA2: an enhanced web server for large-scale expression profiling and interactive analysis. *Nucleic acids Res* 2019; **47**: W556-W560. [PMID: 31114875 DOI: 10.1093/nar/gkz430]

210 Mazzeschi M, Sgarzi M, Romaniello D, Gelfo V, Cavallo C, Ambrosi F, Morselli A, Miano C, Laprovitera N, Girone C, Ferracin M, Santi S, Rihawi K, Ardizzoni A, Fiorentino M, D'Uva G, Győrffy B, Palmer R, Lauriola M. The autocrine loop of ALK receptor and ALKAL2 ligand is an actionable target in consensus molecular subtype 1 colon cancer. *J Exp Clin Cancer Res* 2022; **41**: 113. [DOI: 10.1186/s13046-022-02309-1]

211 Xia Q, Jia J, Hu C, Lu J, Li J, Xu H, Fang J, Feng D, Wang L, Chen Y. Tumor-associated macrophages promote PD-L1 expression in tumor cells by regulating PKM2 nuclear translocation in pancreatic ductal adenocarcinoma. *Oncogene* 2022; **41**: 865-877. [DOI: 10.1038/s41388-021-02133-5]

212 Gao J, Aksoy BA, Dogrusoz U, Dresdner G, Sumer SO, Sun Y, Jacobsen A, Sinha R, Larsson E, Cerami E, Sander C, Schultz N. Integrative Analysis of Complex Cancer Genomics and Clinical Profiles Using the cBioPortal. *Sci Signal* 2013; **6**: pl1. [PMID: 23550210 DOI: 10.1126/scisignal.2004088]

213 Ai J, Wörmann SM, Görgülü K, Vallespinos M, Zagorac S, Alcala S, Wu N, Kabacaoglu D, Berninger A, Navarro D, Kaya-Aksoy E, Ruess DA, Ciecielski KJ, Kowalska M, Demir IE, Ceyhan GO, Heid I, Braren R, Riemann M, Schreiner S, Hofmann S, Kutschke M, Jastroch M, Slotta-Huspenina J, Muckenhuber A, Schlitter AM, Schmid RM, Steiger K, Diakopoulos KN, Lesina M, Sainz B, Algül H. Bcl3 Couples Cancer Stem Cell Enrichment With Pancreatic Cancer Molecular Subtypes. *Gastroenterology* 2021; **161**: 318-332.e9. [PMID: 33819482 DOI: 10.1053/j.gastro.2021.03.051]

214 Foretz M, Guigas B, Bertrand L, Pollak M, Viollet B. Metformin: From Mechanisms of Action to Therapies. *Cell Metabolism* 2014; **20**: 953-966. [DOI: 10.1016/j.cmet.2014.09.018]

215 Goetzman ES, Prochownik EV. The Role for Myc in Coordinating Glycolysis, Oxidative Phosphorylation, Glutaminolysis, and Fatty Acid Metabolism in Normal

and Neoplastic Tissues. *Front Endocrinol* 2018; **9**: 129. [DOI: 10.3389/fendo.2018.00129]

216 Wolfer A, Ramaswamy S. MYC and Metastasis. *Cancer Research* 2011; **71**: 2034–2037. [DOI: 10.1158/0008-5472.CAN-10-3776]

217 Meškytė EM, Keskas S, Ciribilli Y. MYC as a Multifaceted Regulator of Tumor Microenvironment Leading to Metastasis. *IJMS* 2020; **21**: 7710. [DOI: 10.3390/ijms21207710]

218 Dang CV, Reddy EP, Shokat KM, Soucek L. Drugging the 'undruggable' cancer targets. *Nat Rev Cancer* 2017; **17**: 502–508. [DOI: 10.1038/nrc.2017.36]

219 Hermann PC, Huber SL, Herrler T, Aicher A, Ellwart JW, Guba M, Bruns CJ, Heeschen C. Distinct Populations of Cancer Stem Cells Determine Tumor Growth and Metastatic Activity in Human Pancreatic Cancer. *Cell Stem Cell* 2007; **1**: 313–323. [DOI: 10.1016/j.stem.2007.06.002]

220 Singhi AD, Ali SM, Lacy J, Hendifar A, Nguyen K, Koo J, Chung JH, Greenbowe J, Ross JS, Nikiforova MN, Zeh HJ, Sarkaria IS, Dasyam A, Bahary N. Identification of Targetable *ALK* Rearrangements in Pancreatic Ductal Adenocarcinoma. *J Natl Compr Canc Netw* 2017; **15**: 555–562. [DOI: 10.6004/jnccn.2017.0058]

221 Parejo-Alonso B, Barneda D, Trabulo S, Courtois S, Compte-Sancerni S, Ruiz-Cañas L, Zheng Q, Tang J, Chen M, Guo Z, Schmitz U, Irún P, Penin-Peyta L, Crusz SM, Cano-Galiano A, Lopez-Escalona S, Jagust P, Espiau-Romera P, Yuneva M, Lin M-L, Lanas A, Sainz B, Heeschen C, Sancho P. PPAR-delta acts as a metabolic master checkpoint for metastasis in pancreatic cancer. Cancer Biology [DOI:10.1101/2021.11.15.468579]

222 Peng J, Sun B-F, Chen C-Y, Zhou J-Y, Chen Y-S, Chen H, Liu L, Huang D, Jiang J, Cui G-S, Yang Y, Wang W, Guo D, Dai M, Guo J, Zhang T, Liao Q, Liu Y, Zhao Y-L, Han D-L, Zhao Y, Yang Y-G, Wu W. Single-cell RNA-seq highlights intra-tumoral heterogeneity and malignant progression in pancreatic ductal adenocarcinoma. *Cell Res* 2019; **29**: 725–738. [DOI: 10.1038/s41422-019-0195-y]

223 Cerezo-Wallis D, Contreras-Alcalde M, Troulé K, Catena X, Mucientes C, Calvo TG, Cañón E, Tejedo C, Pennacchi PC, Hogan S, Kölblinger P, Tejero H, Chen AX, Ibarz N, Graña-Castro O, Martinez L, Muñoz J, Ortiz-Romero P, Rodriguez-Peralto JL, Gómez-López G, Al-Shahrour F, Rabadán R, Levesque MP, Olmeda D, Soengas MS. Midkine rewires the melanoma microenvironment toward a tolerogenic and immune-resistant state. *Nat Med* 2020; **26**: 1865–1877. [DOI: 10.1038/s41591-020-1073-3]

224 Shaw AT, Kim D-W, Nakagawa K, Seto T, Crinó L, Ahn M-J, De Pas T, Besse B, Solomon BJ, Blackhall F, Wu Y-L, Thomas M, O'Byrne KJ, Moro-Sibilot D, Camidge DR, Mok T, Hirsh V, Riely GJ, Iyer S, Tassell V, Polli A, Wilner KD, Jänne PA. Crizotinib versus Chemotherapy in Advanced *ALK* -Positive Lung Cancer. *N Engl J Med* 2013; **368**: 2385–2394. [DOI: 10.1056/NEJMoa1214886]

225 Lemberger T, Desvergne B, Wahli W. PEROXISOME PROLIFERATOR-ACTIVATED RECEPTORS: A Nuclear Receptor Signaling Pathway in Lipid Physiology. *Annu Rev Cell Dev Biol* 1996; **12**: 335–363. [DOI: 10.1146/annurev.cellbio.12.1.335]

226 Wang Y, Lan W, Xu M, Song J, Mao J, Li C, Du X, Jiang Y, Li E, Zhang R, Wang Q. Cancer-associated fibroblast-derived SDF-1 induces epithelial-mesenchymal transition of lung adenocarcinoma via CXCR4/β-catenin/PPARδ signalling. *Cell Death Dis* 2021; **12**: 214. [DOI: 10.1038/s41419-021-03509-x]

227 Truica MI, Burns MC, Han H, Abdulkadir SA. Turning Up the Heat on MYC: Progress in Small-Molecule Inhibitors. *Cancer Research* 2021; **81**: 248–253. [DOI: 10.1158/0008-5472.CAN-20-2959]

228 Luo C, Lim J-H, Lee Y, Granter SR, Thomas A, Vazquez F, Widlund HR, Puigserver P. A PGC1α-mediated transcriptional axis suppresses melanoma metastasis. *Nature* 2016; **537**: 422–426. [DOI: 10.1038/nature19347]

229 Torrano V, Valcarcel-Jimenez L, Cortazar AR, Liu X, Urosevic J, Castillo-Martin M, Fernández-Ruiz S, Morciano G, Caro-Maldonado A, Guiu M, Zúñiga-García P, Graupera M, Bellmunt A, Pandya P, Lorente M, Martín-Martín N, Sutherland JD, Sanchez-Mosquera P, Bozal-Basterra L, Zabala-Letona A, Arruabarrena-Aristorena A, Berenguer A, Embade N, Ugalde-Olano A, Lacasa-Viscasillas I, Loizaga-Iriarte A, Unda-Urzaiz M, Schultz N, Aransay AM, Sanz-Moreno V, Barrio R, Velasco G, Pinton P, Cordon-Cardo C, Locasale JW, Gomis RR, Carracedo A. The metabolic co-regulator PGC1α suppresses prostate cancer metastasis. *Nat Cell Biol* 2016; **18**: 645–656. [DOI: 10.1038/ncb3357]

230 LeBleu VS, O'Connell JT, Gonzalez Herrera KN, Wikman H, Pantel K, Haigis MC, de Carvalho FM, Damascena A, Domingos Chinen LT, Rocha RM, Asara JM, Kalluri R. PGC-1α mediates mitochondrial biogenesis and oxidative phosphorylation in cancer cells to promote metastasis. *Nat Cell Biol* 2014; **16**: 992–1003. [DOI: 10.1038/ncb3039]

231 Ma L, Young J, Prabhala H, Pan E, Mestdagh P, Muth D, Teruya-Feldstein J, Reinhardt F, Onder TT, Valastyan S, Westermann F, Speleman F, Vandesompele J, Weinberg RA. miR-9, a MYC/MYCN-activated microRNA, regulates E-cadherin and cancer metastasis. *Nat Cell Biol* 2010; **12**: 247–256. [DOI: 10.1038/ncb2024]

232 Smith AP, Verrecchia A, Fagà G, Doni M, Perna D, Martinato F, Guccione E, Amati B. A positive role for Myc in TGFβ-induced Snail transcription and epithelial-to-mesenchymal transition. *Oncogene* 2009; **28**: 422–430. [DOI: 10.1038/onc.2008.395]

233 Porporato PE, Payen VL, Pérez-Escuredo J, De Saedeleer CJ, Danhier P, Copetti T, Dhup S, Tardy M, Vazeille T, Bouzin C, Feron O, Michiels C, Gallez B, Sonveaux P. A Mitochondrial Switch Promotes Tumor Metastasis. *Cell Reports* 2014; **8**: 754–766. [DOI: 10.1016/j.celrep.2014.06.043]

234 Han S, Jeong Y, Choi Y, Hwang S, Bae Y, Chang Y. Mitochondrial dysfunction induces the invasive phenotype, and cell migration and invasion, through the

induction of AKT and AMPK pathways in lung cancer cells. *Int J Mol Med* 2018; **42**: 1644-1652. [PMID: 29916527 DOI: 10.3892/ijmm.2018.3733]

235 Recouvreux MV, Moldenhauer MR, Galenkamp KMO, Jung M, James B, Zhang Y, Lowy A, Bagchi A, Commisso C. Glutamine depletion regulates Slug to promote EMT and metastasis in pancreatic cancer. *Journal of Experimental Medicine* 2020; **217**: e20200388. [DOI: 10.1084/jem.20200388]

236 Vaziri-Gohar A, Zarei M, Brody JR, Winter JM. Metabolic Dependencies in Pancreatic Cancer. *Front Oncol* 2018; **8**: 617. [DOI: 10.3389/fonc.2018.00617]

237 Danhier P, Copetti T, De Preter G, Leveque P, Feron O, Jordan BF, Sonveaux P, Gallez B. Influence of Cell Detachment on the Respiration Rate of Tumor and Endothelial Cells. *PLoS ONE* 2013; **8**: e53324. [DOI: 10.1371/journal.pone.0053324]

238 Daniel Y, Lelou E, Aninat C, Corlu A, Cabillic F. Interplay between Metabolism Reprogramming and Epithelial-to-Mesenchymal Transition in Cancer Stem Cells. *Cancers* 2021; **13**: 1973. [DOI: 10.3390/cancers13081973]

239 Huang J, Chen P, Liu K, Liu J, Zhou B, Wu R, Peng Q, Liu Z-X, Li C, Kroemer G, Lotze M, Zeh H, Kang R, Tang D. CDK1/2/5 inhibition overcomes IFNG-mediated adaptive immune resistance in pancreatic cancer. *Gut* 2021; **70**: 890–899. [DOI: 10.1136/gutjnl-2019-320441]

240 Lakkakula BVKS, Farran B, Lakkakula S, Peela S, Yarla NS, Bramhachari PV, Kamal MA, Saddala MS, Nagaraju GP. Small molecule tyrosine kinase inhibitors and pancreatic cancer—Trials and troubles. *Seminars in Cancer Biology* 2019; **56**: 149–167. [DOI: 10.1016/j.semcancer.2018.09.011]

241 Moog-Lutz C, Degoutin J, Gouzi JY, Frobert Y, Carvalho NB, Bureau J, Créminon C, Vigny M. Activation and Inhibition of Anaplastic Lymphoma Kinase Receptor Tyrosine Kinase by Monoclonal Antibodies and Absence of Agonist Activity of Pleiotrophin. *J Biol Chem* 2005; **280**: 26039–26048. [DOI: 10.1074/jbc.M501972200]

242 Hu B, Qin C, Li L, Wei L, Mo X, Fan H, Lei Y, Wei F, Zou D. Midkine promotes glioblastoma progression via PI3K-Akt signaling. *Cancer Cell Int* 2021; **21**: 509. [DOI: 10.1186/s12935-021-02212-3]

243 Wu D, Liu L, Yan X, Wang C, Wang Y, Han K, Lin S, Gan Z, Min D. Pleiotrophin promotes chemoresistance to doxorubicin in osteosarcoma by upregulating P-glycoprotein. *Oncotarget* 2017; **8**: 63857–63870. [PMID: 28969035 DOI: 10.18632/oncotarget.19148]

244 Qin EY, Cooper DD, Abbott KL, Lennon J, Nagaraja S, Mackay A, Jones C, Vogel H, Jackson PK, Monje M. Neural Precursor-Derived Pleiotrophin Mediates Subventricular Zone Invasion by Glioma. *Cell* 2017; **170**: 845-859.e19. [DOI: 10.1016/j.cell.2017.07.016]

245 Olmeda D, Cerezo-Wallis D, Riveiro-Falkenbach E, Pennacchi PC, Contreras-Alcalde M, Ibarz N, Cifdaloz M, Catena X, Calvo TG, Cañón E, Alonso-Curbelo D, Suarez J, Osterloh L, Graña O, Mulero F, Megías D, Cañamero M, Martínez-Torrecuadrada JL, Mondal C, Di Martino J, Lora D, Martinez-Corral I, Bravo-Cordero JJ, Muñoz J, Puig S, Ortiz-Romero P, Rodriguez-Peralto JL, Ortega S, Soengas MS. Whole-body imaging of lymphovascular niches identifies pre-metastatic roles of midkine. *Nature* 2017; **546**: 676–680. [DOI: 10.1038/nature22977]

246 Fang C, Weng T, Hu S, Yuan Z, Xiong H, Huang B, Cai Y, Li L, Fu X. IFN-γ-induced ER stress impairs autophagy and triggers apoptosis in lung cancer cells. *Oncoimmunology* 2021; **10**: 1962591. [PMID: 34408924 DOI: 10.1080/2162402X.2021.1962591]

247 Sun L, Kees T, Almeida AS, Liu B, He X-Y, Ng D, Han X, Spector DL, McNeish IA, Gimotty P, Adams S, Egeblad M. Activating a collaborative innate-adaptive immune response to control metastasis. *Cancer Cell* 2021; **39**: 1361-1374.e9. [PMID: 34478639 DOI: 10.1016/j.ccell.2021.08.005]

248 Garris CS, Arlauckas SP, Kohler RH, Trefny MP, Garren S, Piot C, Engblom C, Pfirschke C, Siwicki M, Gungabeesoon J, Freeman GJ, Warren SE, Ong S, Browning E, Twitty CG, Pierce RH, Le MH, Algazi AP, Daud AI, Pai SI, Zippelius A, Weissleder R, Pittet MJ. Successful anti-PD-1 cancer immunotherapy requires T cell-dendritic cell crosstalk involving the cytokines IFN-γ and IL-12. *Immunity* 2018; **49**: 1148-1161.e7. [PMID: 30552023 DOI: 10.1016/j.immuni.2018.09.024]

249 Dagogo-Jack I, Shaw AT. Crizotinib resistance: implications for therapeutic strategies. *Ann Oncol* 2016; **27**: iii42–iii50. [PMID: 27573756 DOI: 10.1093/annonc/mdw305]

250 Douglas H. Hallmarks of Cancer: New Dimensions. *Cancer Discov* 2022; **12**: 31-46. [PMID: 35022204 DOI: 10.1158/2159-8290.CD-21-1059]

ANNEX I

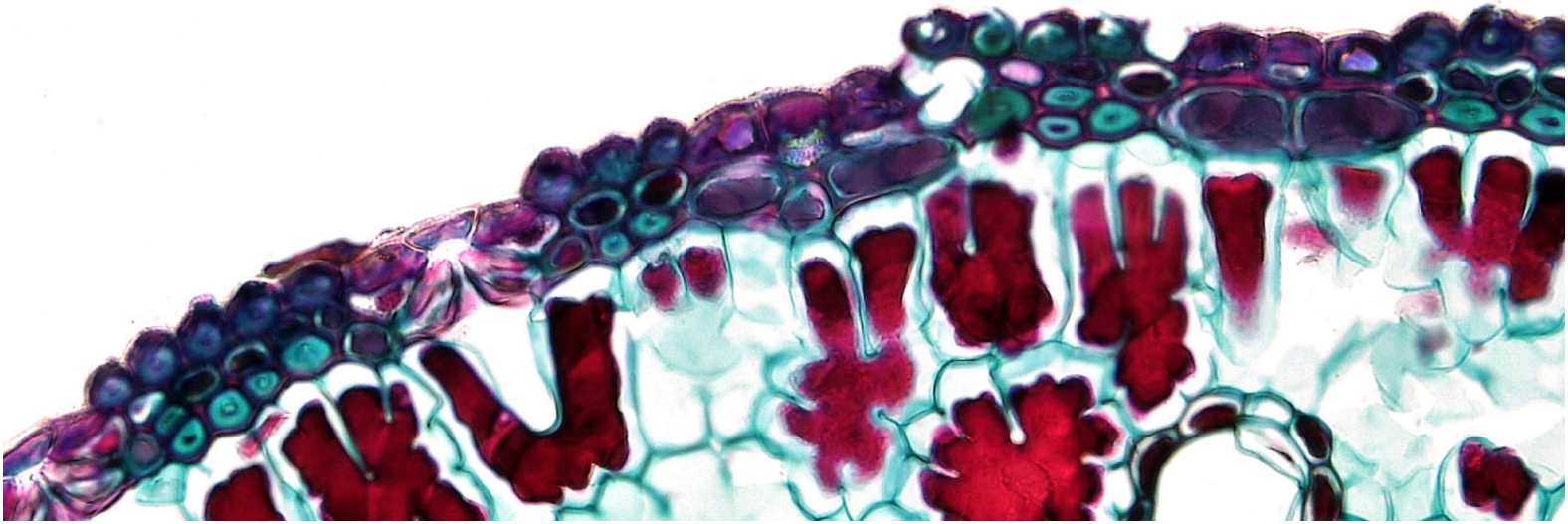

PPAR-delta acts as a metabolic master checkpoint for metastasis in pancreatic cancer

Beatriz Parejo-Alonso[1], David Barneda[2], Sara Trabulo[2], Sarah Courtois[1], Sara Compte-Sancerni[2], Laura Ruiz-Cañas[3,4], Quan Zheng[5], Jiajia Tang[5], Minchun Chen[5], Zhenyang Guo[5], Ulf Schmitz[6], Pilar Irún[1,7], Laure Penin-Peyta[2], Shanthini M. Crusz[2], Andres Cano-Galiano[2], Sergio Lopez-Escalona[2], Petra Jagust[2], Pilar Espiau-Romera[1], Mariia Yuneva[8], Meng-Lay Lin[2], Angel Lanas[1,7,9], Bruno Sainz Jr[3,4], Christopher Heeschen[5,10] and Patricia Sancho[1,2]

[1] IIS Aragón, Zaragoza 50009, Spain;

[2] Barts Cancer Institute, Queen Mary University of London, United Kingdom;

[3] Department of Biochemistry, Autónoma University of Madrid (UAM), School of Medicine, Instituto de Investigaciones Biomédicas (IIBm) "Alberto Sols" CSIC-UAM, 28029 Madrid, Spain;

[4] Chronic Diseases and Cancer, Area 3, Instituto Ramón y Cajal de Investigación Sanitaria (IRYCIS), Madrid, Spain;

[5] Center for Single-Cell Omics and Key Laboratory of Oncogenes and Related Genes, Shanghai Jiao Tong University School of Medicine, China;

[6] Department of Molecular & Cell Biology, College of Public Health, Medical and Veterinary Sciences, James Cook University, Australia

[7] Centro de Investigación Biomédica en Red de Enfermedades Hepáticas y Digestivas (CIBEREHD), Instituto de Salud Carlos III (ISCIII), Zaragoza, Spain;

[8] Oncogenes and Tumour Metabolism Laboratory, Francis Crick Institute, 1 Midland Rd, Kings Cross, London NW1 1AT, United Kingdom;

[9] Department of Gastroenterology, Hospital Universitario Lozano Blesa. IIS Aragón, Zaragoza 50009, Spain;

[10] Pancreatic Cancer Heterogeneity, Candiolo Cancer Institute, FPO-IRCCS, Candiolo, Turin, Italy.

Correspondence: Dr. Patricia Sancho, PhD, IIS Aragón, Hospital Universitario Miguel Servet, Zaragoza, Spain, Email: psancho@iisaragon.es; Dr. Christopher Heeschen, MD, PhD, (Center for Single-Cell Omics, Shanghai Jiao Tong University School of Medicine, China, Email: christopher.heeschen@icloud.com

Text: 58,755 characters (*including spaces, references, and figure legends)*; Summary: 166 words

SUMMARY

In pancreatic cancer, emerging evidence suggests that PPAR-δ overexpression is associated with tumor progression and metastasis, but a mechanistic link is still missing. Here we now show that PPAR-δ acts as the integrating upstream regulator for the metabolic rewiring, which is preceding the subsequent initiation of an invasive/metastatic program. Specifically, paracrine and metabolic cues regularly found in the metastasis-promoting tumor stroma consistently enhance, via induction of PPAR-δ activity, the glycolytic capacity and reserve of pancreatic cancer cells, respectively, accompanied by decreased mitochondrial oxygen consumption. Consequently, genetic or pharmacological inhibition of PPAR-δ results in reduced invasiveness and metastasis. Mechanistically, PPAR-δ acts by shifting the *MYC*/*PGC1A* balance towards *MYC*, enhancing metabolic plasticity. Targeting *MYC* similarly prevents the metabolic switch and subsequent initiation of invasiveness. Therefore, our data demonstrate that PPAR-δ is a key initiator for the metabolic reprogramming in pancreatic cancer, thereby acting as a checkpoint for the phenotypic change towards invasiveness. These findings provide compelling evidence for a novel treatment strategy to combat pancreatic cancer progression.

Keywords: Pancreatic ductal adenocarcinoma, Epithelial-to-mesenchymal transition, Metastasis, Cancer stem cells, Metabolism, MYC, PGC1A, PPAR, PPARD

INTRODUCTION

Pancreatic Ductal Adenocarcinoma (PDAC), the most frequent form of pancreatic cancer is an extremely lethal disease with high metastatic potential (Hidalgo, 2010). At the time of diagnosis, 80-90% of the patients are already at an advanced/metastatic disease stage, with very limited therapeutic options and a particularly poor long-term outcome (Siegel et al., 2017). This can, at least in part, be attributed to the hierarchical organization of PDAC, containing cells with tumor-initiating properties or cancer stem cells (CSCs), which constitute the driving force for disease progression, metastasis, and chemo-resistance (Hermann et al., 2007; Li et al., 2007).

CSCs are capable of unlimited self-renewal, thereby maintaining the CSC pool and also giving rise to the more differentiated progenies (non-CSCs) with a high proliferative capacity. Although both CSCs and non-CSCs can acquire mobility by processes such as epithelial-to-mesenchymal transition (EMT), the arising metastatic CSCs would predominantly be able to initiate secondary lesions due to their strong tumor-initiating capacity. Thus, complementing current chemotherapies with strategies that efficiently target CSCs, bears the potential to eventually improve patients' long-term survival (Gallmeier et al., 2011; Lonardo et al., 2011; Mueller et al., 2009; Zhang et al., 2016).

We recently reported that *c-MYC* (hereinafter referred to as *MYC*) plays an essential role in defining the metabolic phenotype and stemness of PDAC cells, by negatively controlling the expression of the mitochondrial biogenesis factor *PGC1A* (Peroxisome proliferator-activated receptor gamma coactivator 1-alpha) (Sancho et al., 2015). Reduced *MYC* expression in CSCs was required to unleash *PGC1A* and promoted an OXPHOS-dependent metabolic phenotype, thereby enhancing their self-renewal capacity. This rendered CSCs particularly sensitive to mitochondrial targeting (i.e. Metformin), whereas differentiated cancer cells, characterized by increased *MYC* expression and a glycolytic phenotype, were not sensitive to Metformin.

Intriguingly, however, a subpopulation of CSCs turned out to be resistant to mitochondrial inhibition due to an increased *MYC*/*PGC1A* ratio and metabolic plasticity, allowing them to modulate their metabolism in response to exogenous environmental cues. This subset of Metformin-resistant CSCs displayed a highly invasive phenotype, suggesting a potential link between metabolism and

invasiveness. Indeed, here we now conclusively show that metabolic reprogramming induced by PPAR-δ (Peroxisome Proliferator-Activated Receptor delta) via enhancing *MYC*/*PGC1A* ratio, which precedes and facilitates the acquisition of an invasive, EMT-like phenotype in PDAC cancer (stem) cells. This phenotype was induced either through partial inhibition of mitochondrial activity and nutrient stress, respectively, or via stromal cues. Single-cell RNAseq identified PPAR-δ as a directly druggable upstream target, which integrates both nutrient-sensing and stromal signals to modulate cellular metabolism and subsequently invasiveness and metastasis via increasing the *MYC*/*PGC1A* ratio. Therefore, targeting PPAR-δ represents a novel and translatable approach to counteract PDAC progression and metastasis.

RESULTS

Induction of an EMT-like phenotype in PDAC cells. We have previously shown while prolonged treatment of PDAC cultures with the mitochondrial complex I inhibitor Metformin eliminated a large fraction of CSCs, outgrowth of pre-existing resistant CSC clones occurred (Sancho et al., 2015; Lonardo et al., 2013). These prevalent Metformin-resistant cells were morphologically distinct with an elongated shape and diminished cell-to-cell contact and showed upregulation of EMT-related genes, e.g. *VIM* and *ZEB1* (**Figure S1A**).

To determine if the acquisition of an EMT-like phenotype could be a general downstream consequence of diminished mitochondrial activity, we next treated various primary PDAC cultures using distinct means to inhibit their mitochondrial functions, e.g. reducing mitochondrial uptake of different carbon sources or diminishing the activity of the electron transport chain (ETC). Indeed, short-term treatment with Malonate (complex II inhibitor), Etomoxir (mitochondrial long-chain fatty acid transporter blocker) and UK5099 (mitochondrial pyruvate carrier blocker) resulted in morphological and gene expression changes in the cells that are consistent with the induction of EMT (**Figure 1A, S1B**). Interestingly, mimicking conditions frequently found in the tumor microenvironment (low pH, nutrient deprivation, hypoxia) induced similar alterations in morphology and gene expression (**Figure 1A, S1B**). Even glucose or glutamine deprivation alone induced

expression of EMT genes (**Figure S1C**). Thus, decreased mitochondrial activity, either directly induced by inhibitors or indirectly by diminishing metabolic substrates, consistently led to the induction of an EMT-like phenotype.

We previously identified microenvironmental signals from tumor-associated macrophages (TAMs) and pancreatic stellate cells (PSCs) that strongly induce invasion and metastasis in PDAC (Lonardo et al., 2012; Sainz et al., 2014, 2015). Co-culturing PDAC cells with primary human TAMs or PSCs resulted in up-regulation of *VIM* and *ZEB1* (**Figure S1D**). The observed changes in gene expression induced by TAMs could be mimicked by macrophage-conditioned medium (MCM) (**Figure 1B),** and were comparable to the changes induced by Etomoxir **(Figure 1C)**. Treatment with MCM or Etomoxir consistently upregulated *ZEB1* in both $CD133^+$ CSCs and $CD133^-$ non-CSCs, independent of their mitochondrial content (**Figure S1E**), but did not significantly alter their self-renewal capacity (**Figure S1F**). In line with the outlined morphological and transcriptional changes, the cells in both models showed a consistent and strong induction of *in vitro* invasiveness and *in vivo* metastasis, respectively (**Figure 1D, 1E**).

From this diverse panel of invasion/metastasis-inducers, we selected MCM and Etomoxir as the most suitable and relevant stimuli for our subsequent studies. This selection was based on their distinct mechanism of EMT induction: 1) microenvironmental signals from TAMs (MCM) and 2) partial impairment of mitochondrial activity by Etomoxir-mediated inhibition of fatty acid uptake, which resulted in a comparable and reproducible increase of cell invasiveness *in vitro* and metastasis *in vivo* (**Figure 1D, 1E**).

A common transcriptional program linked to PPARD controls invasiveness and metastasis induced by microenvironmental signals. In order to detect common global transcriptional changes induced by both MCM and Etomoxir, we next performed single-cell RNAseq (scRNAseq) analyses for three different PDAC models. Notably, scRNAseq showed that the majority of cells underwent a strong induction of the Hallmark EMT signature, whereas a smaller subset of cells did not respond to the EMT cues (e.g. Cluster 2, **Figure 2A**). As expected from their distinct mechanism of action, distinct transcriptional profiles in response to EMT induction were noted for MCM and Etomoxir

(**Figure 2SA**). These findings were consistent with the diverse morphological changes upon induction of EMT where a subset of cancer cells maintained their epithelial morphology (**Figure S2B**).

Intriguingly, while MCM and Etomoxir induced a distinct transcriptional profile compared to untreated control cells (**Figure S2A**), Gene Set Enrichment Analysis (GSEA) analysis revealed that both treatments consistently activated metabolic pathways such as glycolysis and hypoxia, an effect that again was mostly confined to cells responding to EMT induction (**Figure 2A, S2C**). Bulk transcriptional analysis showed a similar trend, although differences were less pronounced, most likely due to contained cells that did not respond to EMT induction (**Figure S2C, S2D**). Together, these data demonstrate that the majority of PDAC cells undergo similar metabolic changes in response to EMT induction.

We then further analyzed the scRNAseq data sets to identify specific metabolism-related genes and regulators. Most intriguingly, upon induction of EMT we noted a consistent upregulation of the nuclear Peroxisome Proliferator-activated Receptor-δ (*PPARD*) across the different clusters (**Figure 2B**). While *PPARD* upregulation was heterogeneous, it was mostly confined to cells displaying the Hallmark EMT signature. *PPARD* is a member of the *PPAR* subfamily of nuclear hormone receptors, together with *PPARA* and *PPARG*. This subfamily modulates energy homeostasis by controlling the expression of numerous genes involved in lipid and glucose metabolism (Dubois et al., 2017). Notable, we only found *PPARD* to be consistently upregulated in EMT cells, whereas the expression of other family members, e.g. *PPARA* and *PPARG*, was not altered (**Figure 2B**).

We next performed a series of bioinformatic analyses of publicly accessible human datasets, to further interrogate a possible association of these nuclear receptors with human PDAC aggressiveness and metastasis. First, analysis of TCGA and GTEx datasets (http://gepia.cancer-pku.cn/index.html) showed significantly increased expression levels for the *PPAR* family members *PPARD* and *PPARG* for tumor tissue versus normal tissue (**Figure 3A**), which also correlated with poor outcome (**Figure 3B**). Interestingly, only *PPARD* expression positively correlated with an EMT-related gene signature formed by *ZEB1, SNAIL* and *SLUG* in the tumor (**Figure 3C**). We performed GSEA of the TCGA dataset and compared samples belonging to the top and bottom quartiles of *PPARD* expression.

Applying the Hallmark gene set collection, we found that the EMT pathway was one of the most significantly enriched pathways in patients with high *PPARD* expression, together with metabolism-related pathways glycolysis and hypoxia (**Figure 3D, 3E**). Consistently, the OXPHOS pathway was significantly downregulated in the high *PPARD* expression quartile (**Figure 3D, 3E**). Together, these results mirror the transcriptional expression pattern induced by our *in vitro* EMT conditions, further corroborating how hypothesis that *PPARD* acts as a key regulator for the metastatic program in PDAC.

PPAR-δ controls invasiveness and metastasis in PDAC. Using our panel of five inducers of EMT, we were able to confirm a consistent upregulation of *PPARD*, irrespective of the trigger (**Figure 4A**). Although MCM and Etomoxir also upregulated other members of the *PPAR* family, i.e. *PPARA* and *PPARG* (**Figure S3A, S3B**), we found that only *PPARD* was significantly up-regulated during the first 24h, when changes of cellular morphology and *ZEB1* expression were still minor or even undetectable (**Figure S3A, S3B**). The exclusive and rapid PPAR-δ activation within 24h could be further corroborated by demonstrating direct binding to its consensus sequence (**Figure 4B**) and preferential up-regulation of PPAR-δ target genes (**Figure S3C**).

Importantly, treatment of PDAC cells with PPAR-δ chemical agonists (GW0742, GW501516, and L-165), but not PPAR-α or PPAR-γ agonists (e.g. WY14643 and rosiglitazone), resulted in a dose-dependent induction of EMT-related genes and typical morphological changes (**Figure S4A, S4B**). Conversely, knockdown of *PPARD* (**Figure S4C**) virtually abrogated the transcriptional changes induced by MCM, Etomoxir and the PPAR-δ agonist L-165 (**Figure S4D**). Functionally, PPAR-δ activation by agonists resulted in enhanced invasiveness *in vitro* (**Figure 4C**) and metastasis *in vivo* (**Figure 4D**). Moreover, knockdown of *PPARD* reversed MCM, Etomoxir, or PPAR-δ agonist-induced invasiveness (**Figure 4E**) as well as Etomoxir-induced metastasis *in vivo* (**Figure 4F**). Together, these data demonstrate that PPAR-δ, but not other PPARs, is responsible for transcriptional and functional changes concomitant with EMT induction, thereby strongly suggesting an essential role for PPAR-δ in the process of cancer cell invasiveness and metastasis.

PPAR-δ controls a metabolic program linked to invasiveness and metastasis in PDAC. As shown above, EMT induction by microenvironmental signals was strongly linked to a metabolic transcriptional program characterized by glycolysis and hypoxia signaling induction and OXPHOS inhibition (**Figure 2**); features also observed in patients expressing high *PPARD* levels (**Figure 3D, 3E**). Interestingly, using a carbohydrate metabolism PCR array, we found genes implicated in uptake and intermediary metabolism of alternative sugars such as fructose, TCA substrates, amino acids and lipids to be commonly upregulated following EMT induction with MCM, Etomoxir, or the pyruvate carrier inhibitor UK5099 (**Figure 5A**).

Moreover, the PCR array confirmed a significant increase of *PPARD* and a switch in the *MYC*/*PGC1A* balance towards increased *MYC* expression (**Figure 5A**). We had previously described a similar switch in Metformin-resistant primary PDAC cells (Sancho et al., 2015), favoring glucose metabolism via glycolysis versus OXPHOS. As predicted by the above transcriptional profiling, metabolic parameters associated with enhanced glycolytic activity (glycolysis, glycolytic capacity and reserve) were increased upon induction of EMT with MCM or Etomoxir in CSCs and non-CSCs (**Figure 5B, 5C**). Conversely, mitochondrial oxygen consumption rate (OCR) was reduced upon pretreatment with MCM or Etomoxir. Both maximal and ATP-linked OCR were inhibited by 40-50% upon the indicated treatments, with similar changes in CSCs and non-CSCs (**Figure 5B, 5C**), despite their different baseline levels (Sancho et al., 2015). These effects on OCR could be mimicked by co-culture of the cancer cells with primary human TAMs or PSCs (**Figure S5A-C**).

Of note, metabolic changes related to glycolysis were less evident (**Figure 5C**), corroborated by a slight enhancement of glucose uptake and release of lactate and alanine upon treatment (**Figure S5D-F**). However, both glycolytic capacity and reserve, which measure metabolic plasticity as the ability to switch to alternative pathways upon complete inhibition of mitochondrial ATP, were increased upon EMT induction (**Figure 5C**). We therefore hypothesized that EMT induction favors the combined metabolism of glucose by glycolysis together with the use of alternative carbon sources in mitochondria, as suggested by the PCR array data. This would be particularly relevant for CSC

functionality as most of these cells in the native state lack metabolic plasticity and are unable to compensate mitochondrial impairment by switching to glycolysis (Sancho et al., 2015).

To further test this hypothesis, we performed a series of experiments manipulating *PPARD* expression and function by genetic and pharmacological means. Functionally, when PPAR-δ induction was prevented by inducible knockdown, the metabolic changes associated with EMT, e.g. increased glycolytic capacity and diminished mitochondrial respiration, were abrogated (**Figure 6A**). Conversely, treatment of PDAC cells with the chemical agonists GW0742 and L-165, which specifically activated and upregulated *PPARD* (**Figure 4B, S3D**), recapitulated the metabolic switch induced by induction of EMT (**Figure 6B**). Consistent with PPARs stimulation of lipid metabolism and, specifically, fatty acid oxidation (FAO), decreased glucose-dependent respiration was completely rescued by the addition of palmitate and carnitine to the culture medium (**Figure 6C**). This suggests that PPAR-δ promoted glucose diversion to glycolysis while upregulating the FAO machinery to provide an alternative carbon source for TCA cycle when substrates are available.

Downstream signaling cascade initiating the metabolic switch and promoting invasiveness. *MYC* plays an essential role in defining the metabolic phenotype and stemness of PDAC cells by negatively controlling the expression of the mitochondrial biogenesis factor PGC-1α (Sancho et al., 2015). On the other hand, decreased PGC-1α expression was shown to be essential for inducing migration and metastasis in melanoma and prostate cancer (Luo et al., 2016; Torrano et al., 2016). Here, in addition to the changes in *MYC* and *PGC1A* expression upon treatment with MCM, Etomoxir, and UK5099 (**Figure 5A**), we found that direct overexpression of *MYC* induced an EMT-like phenotype (**Figure S6A**). Together, these data suggest an intricate link between the altered *MYC*/*PGC1A* balance and the subsequent induction of invasiveness/metastasis. This metabolic reprogramming could be either cause or consequence of acquiring a migratory/metastatic phenotype.

We hypothesized that the PPAR-δ-mediated induction of metastatic activity was related to changes in the *MYC*/*PGC1A* ratio. To test this hypothesis, we first analyzed the *MYC*/*PGC1A* ratio in our diverse EMT/metastasis models. Indeed, induction of metastatic activity by diminishing mitochondrial activity due to ETC inhibition or lack of fuel resulted in a consistent increase of the

MYC/*PGC1A* ratio (**Figure 7A, S6B**). Notably, the absolute changes in the expression of either MYC or PGC1A individually did not always correlate with the induction of the EMT-like phenotype. For some models, the increase in *MYC* expression was rather modest or absent, whereas *PGC1A* was still greatly reduced and *vice versa*. Instead, we found that, at the mRNA level, an increased *MYC*/*PGC1A* ratio was most consistently linked to an EMT phenotypic induction. At the protein level, however, MCM, Etomoxir, and the PPAR-δ agonist GW0742 reproducibly increased MYC expression and diminished PGC-1α expression (**Figure 7B**). Moreover, *PPARD* knockdown, which inhibited invasion and metastasis (**Figure 4E-4F**), diminished the increase in the *MYC*/*PGC1A* ratio induced by MCM, Etomoxir, and PPAR-δ agonist L-165, respectively (**Figure S6C**). Finally, *PPARD* overexpression or PPAR-δ agonist treatment consistently induced *MYC* promoter activity and subsequently reduced *PGC1A* promoter activity (**Figure 7C**), indicating a direct link between *PPARD* expression and the *MYC*/*PGC1A* ratio. Indeed, the enhanced invasiveness of the cancer cells following treatment with the PPAR-δ agonist could be reversed by either *MYC* knockdown or *PGC1A* overexpression (**Figure 7D**), essentially attributing PPAR-δ's pro-metastatic effects to its ability to increase the *MYC*/*PGC1A* ratio.

To further corroborate our finding that the *MYC*/*PGC1A* ratio is crucially implicated in the metastatic process, we next analyzed different models with functional and/or physiological relevance. Specifically, we found that 1) the *MYC*/*PGC1A* ratio most closely correlated with patients' survival (**Figure S6D**), 2) migrating cells showed both increased levels of EMT-associated genes and *MYC*/*PGC1A* ratio compared to non-migrating cells (**Figure S6E**); 3) the *MYC*/*PGC1A* ratio of disseminated cells from patients with advanced PDAC was 1,000–8,000x higher compared to the ratio observed for cells derived from primary tumors (**Figure S6F**), and 4) circulating tumor cells (CTC) in xenograft models showed increased *MYC* expression compared to the corresponding primary tumors (**Figure S6G**).

The latter finding was most pronounced in cells with increased expression of stemness genes as a putative pool of circulating CSCs (**Figure S6H**). Notably, *PGC1A* expression was very low to undetectable in most circulating single cancer cells and therefore the *MYC*/*PGC1A* ratio could not be

calculated in this instance (data not shown). Interestingly, once the pro-metastatic PDX cells had formed actual liver metastases, they showed very low *MYC*/*PGC1A* ratios, with reduced *MYC* expression and *PGC1A* levels exceeding those found in primary tumors (**Figure S6I**). These changes in gene expression were associated with a reversion to their original mitochondria-driven metabolic state (**Figure S6J**).

To further validate the crucial functional role of the altered *MYC*/*PGC1A* ratio for inducing the EMT program, we next used an inducible *MYC* knockdown system to prevent *MYC* upregulation upon EMT induction. *MYC* knockdown was induced 48 hours before exposing the cells to EMT-inducing conditions. As expected, *MYC* knockdown essentially prevented the downregulation of *PGC1A* upon treatment with MCM or Etomoxir (**Figure S6K)** and the subsequent switch in the metabolic phenotype associated with EMT (**Figure 7E, 7F**). *MYC* knockdown also prevented *ZEB1* upregulation and induction of invasiveness (**Figure 7G, 7H**).

As blocking the *MYC*/*PGC1A*-governed metabolic program prevented the pro-metastatic phenotype induced by microenvironmental cues or fuel deprivation, we next aimed to pharmacologically inhibit *MYC* expression using the MYC/MAX interaction inhibitor Mycro3 in order to mimic the effects of *MYC* knockdown. Pretreating the cells with Mycro3 efficiently reduced the upregulation of *VIM* and *ZEB1* in response to EMT induction by MCM and Etomoxir (**Figure S6L**) and prevented induction of invasiveness (**Figure 7I**). These data could be further corroborated by overexpression of *PGC1A* prior to EMT induction, which prevented the metabolic changes induced by MCM and Etomoxir, respectively (**Figure S6M, left panel**) and consequently the cells did not acquire an invasive phenotype (**Figure S6M, right panel**).

Together, these data support our hypothesis that, upon PPAR-δ activation, *MYC* (through inhibition of *PGC1A*) not only governs the metabolic changes related to EMT, but also initiates and mediates the EMT/invasive program as a whole.

Therapeutic targeting of PPAR-δ abrogates metastatic activity. Finally, we tested if PPAR-δ could be blocked pharmacologically to inhibit invasion and metastasis *in vitro* and *in vivo*. Indeed, pre-treatment with the PPAR-δ antagonists GSK0660 and GSK3787 or the inverse agonist DG172

inhibited the invasive capacity conferred by MCM or Etomoxir treatment (**Figure 8A**), or the basal invasive capacity of highly metastatic PDAC-265 cells (**Figure 8B**). Importantly, these *in vitro* results could be corroborated *in vivo* using a model of spontaneous metastasis following orthotopic injection of PDAC-265 cells. *PPARD* expression was significantly increased in PPAR-δ agonist GW0742-treated mice (**Figure 8C**), which translated into higher metastatic spread in GW0742-treated mice, whereas the PPAR-δ antagonist GSK3787 significantly reduced metastatic dissemination (**Figure 8D, 8E**). Of note, MYC and Vimentin protein expression were significantly increased in tumors treated with GW0742 (**Figure 8E, lower panel**).

In summary, PPAR-δ integrates nutrient-sensing and stromal signals to reprogram PDAC cell metabolism via *MYC/PGC1A,* promoting cancer cell invasiveness and *in vivo* metastasis in PDAC. Importantly, this process can be pharmacologically reversed using existing small molecule inhibitors, thus providing a potential new avenue for the treatment of advanced PDAC.

DISCUSSION

PPAR-δ is a member of the nuclear receptor superfamily of ligand-activated transcription factors. It regulates a variety of biological functions, in a cell and context-dependent manner, including cellular metabolism, proliferation, differentiation and survival, as well as inflammation (Giordano Attianese and Desvergne, 2015). Probably due to strong cell context-dependency and utilization of diverse model systems, the role of PPAR-δ in cancer has remained controversial (Wagner and Wagner, 2020). Although occasionally related to tumor suppression (Martín-Martín et al., 2018), increased *PPARD* expression has mostly been linked to enhanced metastasis in several *in vivo* models (Zuo et al., 2017). Even more importantly, poor patient outcome, including reduced metastasis-free survival correlated with *PPARD* expression in various cancer types (Abdollahi et al., 2007; Zuo et al., 2017). However, while accumulating evidence suggest that PPAR-δ also promotes tumor progression and metastasis in PDAC (Liu et al., 2020; Sanford-Crane et al., 2020; Zuo et al., 2017), other reports have questioned these finding (Coleman et al., 2013; Smith et al., 2016).

Our data now clearly support the notion that PPARD promotes progression and metastasis in PDAC. First, using single-cell analysis of various PDAC primary cultures, we found that *PPARD* was exclusively upregulated in cells actually undergoing EMT (**Figure 2A&B**). We also found PPARD to be overexpressed in the PAAD TCGA dataset (**Figure 3A**) and correlated with disease-free survival (**Figure 3B**). Interestingly, *PPARD*-high patients also showed enrichment for pathways related to cellular metabolism, inflammation, cell cycle, and EMT (**Figure 3D, 3E**), in line with our *in vitro* findings using single-cell analysis (**Figure 2 & S2**). Such broad transcriptional program controlled by PPAR-δ suggested to us that it represents a strong candidate for integrating the multiple pathways regulating tumor progression and metastasis in PDAC. Indeed, our present data now suggest that the implication of PPAR-δ in the interplay between tumor cells and TAMs may be bidirectional, since we found *PPARD* upregulation and activation in response to microenvironmental signals from TAMs (**Figure 2, 4A, 4B**). This could create a positive feedback loop *in vivo*, further promoting tumor progression via induction of EMT in cancer cells.

EMT can also be induced by metabolic stress resulting from impaired mitochondrial metabolism (**Figure 1**), which could be related to either genomic or transcriptional defects, e.g. lack of mitochondrial DNA (Guha et al., 2014), mutations in TCA cycle enzymes (Grassian et al., 2012; Loriot et al., 2012; Sciacovelli et al., 2016), or downregulation of components of the OXPHOS system (Gaude and Frezza, 2016). Our data now demonstrate that not only (epi-) genetic inhibition of mitochondrial function, but also functional inhibition of mitochondria, e.g. via pharmacological inhibition of the ETC, is sufficient to induce a metastatic program in PDAC, in line with findings for other cancer types (Han et al., 2018; Porporato et al., 2014).

Even more strikingly, we found that nutrient stress was similarly effective at inducing EMT and invasiveness of cancer cells (**Figure 1, S1**). Indeed, although glutamine deprivation has recently been described as an inducer of EMT via *Slug* upregulation in KPC-derived murine PDAC cells (Recouvreux et al., 2020), we here describe a wider phenomenon: inhibition of mitochondrial uptake of diverse carbon substrates (glutamine, pyruvate, fatty acids) and/or lack of oxygen, thereby mimicking the hypoxic and acidic tumor microenvironment, consistently induced EMT. Notably,

mitochondrial activity was also repressed by microenvironmental signals such as TAM-derived factors, indicating a common metabolic route in the context of EMT (**Figure 5B, 5C**).

As PPAR-δ was the only PPAR family member activated by stromal signals or in response to metabolic stress conditions (**Figure 4B**), we hypothesized that PPAR-δ acts as an integrating sensor of diverse signals from the tumor microenvironment, and subsequently activates the EMT program to 1) gain metabolic plasticity and thereby adapt and survive in challenging environmental conditions and 2) acquire mobility, evade the primary tumor and search for more permissive environments elsewhere. Interestingly, it was recently proposed that inflammatory signals can trigger a pseudo-starvation response driving invasiveness, independent of nutrient abundance (García-Jiménez and Goding, 2019), suggesting that PPAR-δ controls such starvation/pseudo-starvation responses as a prerequisite for induction of EMT and subsequent metastasis in PDAC.

To our knowledge, this is the first report associating PPAR-δ with tumor progression and metastasis via metabolic rewiring. PPAR-δ initiates a global pro-metastatic metabolic program via increasing the *MYC*/*PGC1A* ratio. Notably, changes in the ratio predicted the aggressiveness of PDAC cells and overall patient survival more accurately than each of the two genes individually. Indeed, the pro-invasive effects of enhanced PPAR-δ activation could be reversed by either *MYC* knockdown/pharmacological inhibition or *PGC1A* overexpression (**Figures 7, S7**). Pharmacological or genetic induction of *PPARD* resulted in a rapid upregulation of *MYC* (24h), suggesting a direct interaction as the *MYC* promoter carries a PPAR responsive element (PPRE; Genecard), although *MYC* upregulation may occur indirectly via the microRNA Let-7c (Shah et al., 2007). But our promoter activity assays confirmed that *PPARD* stimulation directly induced *MYC* promoter activity and subsequently reduced *PGC1A* promoter activity (**Figure 7C**). The resulting pro-invasive effects could be reversed by knockdown of *MYC* or overexpression of *PGC1A* (**Figure 7D**).

MYC and PGC-1α have been connected to metabolic switch and tumor progression/metastasis. Specifically, *MYC* expression promotes cellular de-differentiation, EMT, and increased metastatic potential (Bian et al., 2017; Ischenko et al., 2015; Soucek et al., 2013). Indeed, the molecular signature of aggressive squamous/mesenchymal PDAC includes *MYC*-activated signaling pathways

(Bailey et al., 2016). Moreover, analysis of PDAC models revealed that *MYC* overexpression is associated with less differentiated tumors and a glycolysis-related gene signature (Bian et al., 2017). Indeed, we found that *MYC* upregulation suppressed *PGC1A* resulting in an altered metabolism with enhanced global glycolytic/plastic capacity (conferred by *MYC*), accompanied by inhibition of mitochondrial oxygen consumption and activity (as a result of *PGC1A* downregulation via *MYC*).

Our data show that metabolic plasticity is crucial to support the increased energetic needs during invasion and the subsequent metastatic process. As metastatic cells decrease their mitochondrial function (Danhier et al., 2013; Schafer et al., 2009), they need to rely on alternative sources to maintain their energy balance, and activation of glycolysis seems to be the most plausible option. However, our results demonstrate that the increase in glycolytic activity upon EMT induction is rather modest (**Figure 5B, 5C and S5**). Instead, we found that glycolytic reserve was more profoundly enhanced in EMT cells, rather suggesting increased metabolic plasticity and diversification of metabolic substrates, e.g. alternative sugars or fatty acids (**Figure 5A, S6**).

Although CSCs and non-CSCs are similarly capable of undergoing EMT, regardless of their basal metabolic phenotype (**Figure S1E**), CSCs are the most capable and aggressive cells for establishing new metastatic sites due to their inherent self-renewal and tumor-initiating capacities (Hermann et al., 2007). Previously we also reported that most CSCs in the primary tumor are strictly dependent on OXPHOS activity and that these harbor the highest tumorigenic potential. Here we now expand on these findings by showing that in CSCs undergoing EMT the self-renewal capacity remained essentially unchanged (**Figure S1F**). While these results were rather unexpected they do suggest an intricate interplay between stemness, EMT and cellular metabolism (Daniel et al., 2021). Considering the importance of maintaining stemness in cancer (Wang et al., 2019; Zhang et al., 2017), we hypothesize that during the EMT process PPAR-δ becomes a key driver of stemness, rendering CSCs less dependent on mitochondrial metabolism. Future studies should further dissect this potential mechanistic duality in CSCs.

Finally, we found that genetic or pharmacological targeting of PPAR-δ inhibited tumor aggressiveness and metastasis *in vitro* and *in vivo* (**Figure 8**). These data are in line with previous

reports for murine PDAC models showing that *Ppard* knock-down strongly decreased tumorigenesis mouse melanoma cells (Zuo et al., 2017), and *Ppard* knockout inhibited tumor progression in KC mice on a high-fat diet (Liu et al., 2020). Taken together, accumulating data now strongly support the concept that PPAR-δ inhibition reduces the *MYC*/*PGC1A* ratio and thereby diminishes PDAC progression and metastasis. These data provide the rational for developing novel PPAR-δ-targeting treatment strategies to combat advanced pancreatic cancer.

AUTHOR CONTRIBUTIONS

B.P-A, D.B. and S.T. acquired, analyzed, interpreted data and assisted in the development of the study concept; S.C., S.C.-S., Q.Z., J. T., M.C., Z.G., P.I., L.P.-P., S.M.C., S.L.-E. and P.E. acquired and analyzed *in vitro* data; A.C-G, Q.Z., J. T., M.C., Z.G., performed single-cell RNA extraction and ddPCR and 10x RNA-seq, respectively; L.R.-C., S.C., P.J., and B.S. Jr performed *in vivo* experiments; U.L. and M-L.L. performed bioinformatics analyses; M.Y. analyzed GC-MS data; A.L. contributed with funds and critical advice; C.H. and P.S. developed the study concept, obtained funding, interpreted the data, and wrote the manuscript.

ACKNOWLEDGEMENTS

Authors would like to acknowledge the use of the BCI Flow Cytometry and Pathology Facilities, as well as the CIBA Flow Cytometry, Pathology and Microscopy Facilities (Servicios Científico-Técnicos, IACS-Universidad de Zaragoza). We would like to thank Arkaitz Carracedo, Veronica Torrano, and Natalia Martin-Martin for constructive data discussion and providing us with the *PGC1A* and *PPARD* overexpression lentiviral vectors.

The research was supported by the ERC Advanced Investigator Grant (Pa-CSC 233460, to C.H.), the European Community's Seventh Framework Programme (FP7/2007-2013) under grant agreement n° 602783 (CAM-PaC, to C.H.), the Fondazione del Piemonte per l'Oncologia – IRCCS (PTCRC-Intra 2021, to C.H.), the Pancreatic Cancer Research Fund (2015 Award round, to P.S.), the Instituto de Salud Carlos III through the Miguel Servet Program (CP16/00121 to P.S.) and Fondo de

Investigaciones Sanitarias (PI17/00082 to P.S.) (both co-financed by European funds (FSE: "el FSE invierte en tu futuro" and FEDER: "una manera de hacer Europa," respectively), the Worldwide Cancer Research Charity together with Asociación Española contra el Cáncer (AECC) (19-0250, to P.S.), the Fero Foundation (to B.S.,Jr.), a Coordinated grant (GC16173694BARB) from the AECC (to B.S., Jr.), an Investigator Grant (NHMRC #1196405, to U.S.) and a Cancer Council NSW project grant (RG20-12, to U.S).

DISCLOSURE OF POTENTIAL CONFLICT OF INTEREST

S.M.C. reports a travel grant from Tesaro and honoraria for educational events from BMS and GSK. The remaining authors have no conflict of interest to disclose.

References

Abdollahi, A., Schwager, C., Kleeff, J., Esposito, I., Domhan, S., Peschke, P., Hauser, K., Hahnfeldt, P., Hlatky, L., Debus, J., et al. (2007). Transcriptional network governing the angiogenic switch in human pancreatic cancer. Proc. Natl. Acad. Sci. *104*, 12890–12895.

Agerbæk, M.Ø., Bang-Christensen, S.R., Yang, M.-H., Clausen, T.M., Pereira, M.A., Sharma, S., Ditlev, S.B., Nielsen, M.A., Choudhary, S., Gustavsson, T., et al. (2018). The VAR2CSA malaria protein efficiently retrieves circulating tumor cells in an EpCAM-independent manner. Nat. Commun. *9*, 3279.

Bailey, P., Chang, D.K., Nones, K., Johns, A.L., Patch, A.M., Gingras, M.C., Miller, D.K., Christ, A.N., Bruxner, T.J.C., Quinn, M.C., et al. (2016). Genomic analyses identify molecular subtypes of pancreatic cancer. Nature *531*, 47–52.

Bian, B., Bigonnet, M., Gayet, O., Loncle, C., Maignan, A., Gilabert, M., Moutardier, V., Garcia, S., Turrini, O., Delpero, J., et al. (2017). Gene expression profiling of patient□derived pancreatic cancer xenografts predicts sensitivity to the BET bromodomain inhibitor JQ1: implications for individualized medicine efforts. EMBO Mol. Med. e201606975.

Butler, A., Hoffman, P., Smibert, P., Papalexi, E., and Satija, R. (2018). Integrating single-cell transcriptomic data across different conditions, technologies, and species. Nat. Biotechnol. 2018 365 *36*, 411–420.

Coleman, J.D., Thompson, J.T., Smith, R.W., Prokopczyk, B., and Vanden Heuvel, J.P. (2013). Role of Peroxisome Proliferator-Activated Receptor β/δ and B-Cell Lymphoma-6 in Regulation of Genes Involved in Metastasis and Migration in Pancreatic Cancer Cells. PPAR Res. *2013*, 121956.

Danhier, P., Copetti, T., De Preter, G., Leveque, P., Feron, O., Jordan, B.F., Sonveaux, P., and Gallez, B. (2013). Influence of Cell Detachment on the Respiration Rate of Tumor and Endothelial Cells. PLoS One *8*, e53324.

Daniel, Y., Lelou, E., Aninat, C., Corlu, A., and Cabillic, F. (2021). Interplay between Metabolism Reprogramming and Epithelial-to-Mesenchymal Transition in Cancer Stem Cells. Cancers (Basel). *13*, 1973.

Dubois, V., Eeckhoute, J., Lefebvre, P., and Staels, B. (2017). Distinct but complementary contributions of PPAR isotypes to energy homeostasis. J. Clin. Invest. *127*, 1202–1214.

Gallmeier, E., Hermann, P.C., Mueller, M.-T., Machado, J.G., Ziesch, A., De Toni, E.N., Palagyi, A., Eisen, C., Ellwart, J.W., Rivera, J., et al. (2011). Inhibition of Ataxia Telangiectasia- and Rad3 -Related Function

Abrogates the In Vitro and In Vivo Tumorigenicity of Human Colon Cancer Cells Through Depletion of the CD133+ Tumor-Initiating Cell Fraction. Stem Cells *29*, 418–429.

García-Jiménez, C., and Goding, C.R. (2019). Starvation and Pseudo-Starvation as Drivers of Cancer Metastasis through Translation Reprogramming. Cell Metab. *29*, 254–267.

Gaude, E., and Frezza, C. (2016). Tissue-specific and convergent metabolic transformation of cancer correlates with metastatic potential and patient survival. Nat. Commun. *7*, 13041.

Giordano Attianese, G.M.P., and Desvergne, B. (2015). Integrative and systemic approaches for evaluating PPARβ/δ (PPARD) function. Nucl. Recept. Signal. *13*, e001.

Grassian, A.R., Lin, F., Barrett, R., Liu, Y., Jiang, W., Korpal, M., Astley, H., Gitterman, D., Henley, T., Howes, R., et al. (2012). Isocitrate Dehydrogenase (IDH) Mutations Promote a Reversible ZEB1/MicroRNA (miR)-200-dependent Epithelial-Mesenchymal Transition (EMT). J. Biol. Chem. *287*, 42180–42194.

Guha, M., Srinivasan, S., Ruthel, G., Kashina, A.K., Carstens, R.P., Mendoza, A., Khanna, C., Van Winkle, T., and Avadhani, N.G. (2014). Mitochondrial retrograde signaling induces epithelial-mesenchymal transition and generates breast cancer stem cells. Oncogene *33*, 5238–5250.

Han, S.Y., Jeong, Y.J., Choi, Y., Hwang, S.K., Bae, Y.S., and Chang, Y.C. (2018). Mitochondrial dysfunction induces the invasive phenotype, and cell migration and invasion, through the induction of AKT and AMPK pathways in lung cancer cells. Int. J. Mol. Med. *42*, 1644–1652.

Hermann, P.C., Huber, S.L., Herrler, T., Aicher, A., Ellwart, J.W., Guba, M., Bruns, C.J., and Heeschen, C. (2007). Distinct Populations of Cancer Stem Cells Determine Tumor Growth and Metastatic Activity in Human Pancreatic Cancer. Cell Stem Cell *1*, 313–323.

Hidalgo, M. (2010). Pancreatic Cancer. N. Engl. J. Med. *362*, 1605–1617.

Ischenko, I., Petrenko, O., and Hayman, M.J. (2015). A MEK/PI3K/HDAC inhibitor combination therapy for KRAS mutant pancreatic cancer cells. Oncotarget *6*, 15814–15827.

Li, C., Heidt, D.G., Dalerba, P., Burant, C.F., Zhang, L., Adsay, V., Wicha, M., Clarke, M.F., and Simeone, D.M. (2007). Identification of pancreatic cancer stem cells. Cancer Res. *67*, 1030–1037.

Liu, Y., Deguchi, Y., Wei, D., Moussalli, M.J., Li, D., Wang, H., Valentin, L.A., Colby, J.K., Liu, F., Wang, J., et al. (2020). Ppard Is Essential in Acceleration of Pancreatic Ductal Adenocarcinoma Development by High-

Fat Diet in Mutant Kras Mice. BioRxiv 10.1101/2020.12.04.412320.

Lonardo, E., Hermann, P.C., Mueller, M.-T., Huber, S., Balic, A., Miranda-Lorenzo, I., Zagorac, S., Alcala, S., Rodriguez-Arabaolaza, I., Ramirez, J.C., et al. (2011). Nodal/Activin Signaling Drives Self-Renewal and Tumorigenicity of Pancreatic Cancer Stem Cells and Provides a Target for Combined Drug Therapy. Cell Stem Cell *9*, 433–446.

Lonardo, E., Frias-Aldeguer, J., Hermann, P.C., and Heeschen, C. (2012). Pancreatic stellate cells form a niche for cancer stem cells and promote their self-renewal and invasiveness. Cell Cycle *11*, 1282–1290.

Loriot, C., Burnichon, N., Gadessaud, N., Vescovo, L., Amar, L., Libé, R., Bertherat, J., Plouin, P.-F., Jeunemaitre, X., Gimenez-Roqueplo, A.-P., et al. (2012). Epithelial to Mesenchymal Transition Is Activated in Metastatic Pheochromocytomas and Paragangliomas Caused by *SDHB* Gene Mutations. J. Clin. Endocrinol. Metab. *97*, E954–E962.

Luo, C., Lim, J.-H.H., Lee, Y., Granter, S.R., Thomas, A., Vazquez, F., Widlund, H.R., and Puigserver, P. (2016). A PGC1α-mediated transcriptional axis suppresses melanoma metastasis. Nature *537*, 422–426.

Martín-Martín, N., Zabala-Letona, A., Fernández-Ruiz, S., Arreal, L., Camacho, L., Castillo-Martin, M., Cortazar, A.R., Torrano, V., Astobiza, I., Zúñiga-García, P., et al. (2018). PPARδ Elicits Ligand-Independent Repression of Trefoil Factor Family to Limit Prostate Cancer Growth. Cancer Res. *78*, 399 LP – 409.

McGinnis, C.S., Murrow, L.M., and Gartner, Z.J. (2019). DoubletFinder: Doublet Detection in Single-Cell RNA Sequencing Data Using Artificial Nearest Neighbors. Cell Syst. *8*, 329-337.e4.

Mueller, M., Hermann, P.C., Witthauer, J., Rubio–Viqueira, B., Leicht, S.F., Huber, S., Ellwart, J.W., Mustafa, M., Bartenstein, P., D'Haese, J.G., et al. (2009). Combined Targeted Treatment to Eliminate Tumorigenic Cancer Stem Cells in Human Pancreatic Cancer. Gastroenterology *137*, 1102–1113.

Porporato, P.E., Payen, V.L., Pérez-Escuredo, J., De Saedeleer, C.J., Danhier, P., Copetti, T., Dhup, S., Tardy, M., Vazeille, T., Bouzin, C., et al. (2014). A Mitochondrial Switch Promotes Tumor Metastasis. Cell Rep. *8*, 754–766.

Recouvreux, M.V., Moldenhauer, M.R., Galenkamp, K.M.O., Jung, M., James, B., Zhang, Y., Lowy, A., Bagchi, A., and Commisso, C. (2020). Glutamine depletion regulates Slug to promote EMT and metastasis in pancreatic cancer. J. Exp. Med. *217*, e20200388.

Sainz, B., Martín, B., Tatari, M., Heeschen, C., and Guerra, S. (2014). ISG15 Is a Critical Microenvironmental

Factor for Pancreatic Cancer Stem Cells. Cancer Res. *74*, 7309–7320.

Sainz, B., Alcala, S., Garcia, E., Sanchez-Ripoll, Y., Azevedo, M.M., Cioffi, M., Tatari, M., Miranda-Lorenzo, I., Hidalgo, M., Gomez-Lopez, G., et al. (2015). Microenvironmental hCAP-18/LL-37 promotes pancreatic ductal adenocarcinoma by activating its cancer stem cell compartment. Gut *64*, 1921–1935.

Sancho, P., Burgos-Ramos, E., Tavera, A., Bou Kheir, T., Jagust, P., Schoenhals, M., Barneda, D., Sellers, K., Campos-Olivas, R., Graña, O., et al. (2015). MYC/PGC-1α Balance Determines the Metabolic Phenotype and Plasticity of Pancreatic Cancer Stem Cells. Cell Metab. *22*, 590–605.

Sanford-Crane, H., Abrego, J., Oon, C., Xiao, X., Nagarajan, S., Tontonoz, P., and Sherman, M.H. (2020). A cancer cell-intrinsic GOT2-PPARd axis suppresses antitumor immunity. BioRxv 10.1101/2020.12.25.424393.

Schafer, Z.T., Grassian, A.R., Song, L., Jiang, Z., Gerhart-Hines, Z., Irie, H.Y., Gao, S., Puigserver, P., and Brugge, J.S. (2009). Antioxidant and oncogene rescue of metabolic defects caused by loss of matrix attachment. Nature *461*, 109–113.

Sciacovelli, M., Gonçalves, E., Johnson, T.I., Zecchini, V.R., da Costa, A.S.H., Gaude, E., Drubbel, A.V., Theobald, S.J., Abbo, S.R., Tran, M.G.B., et al. (2016). Fumarate is an epigenetic modifier that elicits epithelial-to-mesenchymal transition. Nature *537*, 544–547.

Shah, Y.M., Morimura, K., Yang, Q., Tanabe, T., Takagi, M., and Gonzalez, F.J. (2007). Peroxisome Proliferator-Activated Receptor α Regulates a MicroRNA-Mediated Signaling Cascade Responsible for Hepatocellular Proliferation. Mol. Cell. Biol. *27*, 4238–4247.

Siegel, R.L., Miller, K.D., and Jemal, A. (2017). Cancer statistics, 2017. CA. Cancer J. Clin. *67*, 7–30.

Smith, R.W., Coleman, J.D., Thompson, J.T., and Vanden Heuvel, J.P. (2016). Therapeutic potential of GW501516 and the role of Peroxisome proliferator-activated receptor β/δ and B-cell lymphoma 6 in inflammatory signaling in human pancreatic cancer cells. Biochem. Biophys. Reports *8*, 395–402.

Soucek, L., Whitfield, J.R., Sodir, N.M., Massó-Vallés, D., Serrano, E., Karnezis, A.N., Swigart, L.B., and Evan, G.I. (2013). Inhibition of Myc family proteins eradicates KRas-driven lung cancer in mice. Genes Dev. *27*, 504–513.

Torrano, V., Valcarcel-Jimenez, L., Cortazar, A.R., Liu, X., Urosevic, J., Castillo-Martin, M., Fernández-Ruiz, S., Morciano, G., Caro-Maldonado, A., Guiu, M., et al. (2016). The metabolic co-regulator PGC1α suppresses prostate cancer metastasis. Nat. Cell Biol. *18*, 645–656.

Wagner, N., and Wagner, K.D. (2020). PPAR Beta/Delta and the Hallmarks of Cancer. Cells *9*.

Wang, D., Fu, L., Wei, J., Xiong, Y., and DuBois, R.N. (2019). PPARD mediates the effect of dietary fat in promoting colorectal cancer metastasis. Cancer Res. *79*, 4480–4490.

Zhang, Z., Duan, Q., Zhao, H., Liu, T., Wu, H., Shen, Q., Wang, C., and Yin, T. (2016). Gemcitabine treatment promotes pancreatic cancer stemness through the Nox/ROS/NF-κB/STAT3 signaling cascade. Cancer Lett. *382*, 53–63.

Zhang, Z., Duan, Y., Wu, Z., Zhang, H., Ren, J., and Huang, L. (2017). Ppard is an inhibitor of cartilage growth in external ears. Int. J. Biol. Sci. *13*, 669–681.

Zuo, X., Xu, W., Xu, M., Tian, R., Moussalli, M.J., Mao, F., Zheng, X., Wang, J., Morris, J.S., Gagea, M., et al. (2017). Metastasis regulation by PPARD expression in cancer cells. JCI Insight *2*, e91419.

FIGURE LEGENDS

Figure 1. Induction of EMT-like phenotype in PDAC cells. (**A**) **Left**: Representative images illustrating morphological changes for PDAC-354 cells in response to treatment for 72h with the complex I inhibitor Metformin (3mM), the ß-oxidation inhibitor Etomoxir (20μM), complex II inhibitor Malonate (5mM), the pyruvate carrier inhibitor UK5099 (100μM), or tumor-like conditions (low pH (HCl 50 µM) + low glucose concentration (1 mM) + 3% O_2). **Right**: Expression of EMT-associated genes (*VIM* [vimentin], *SNAIL*, *SLUG*, *ZEB1* and *LOXL2*) was determined by rtQPCR after cells were treated for 48h as indicated. Pooled data for PDAC-185, A6L, 215, 253, and 354 ($n \leq 4$ for each cell type). Data are normalized to *HPRT* (**lower left panel**). (**B-C**) PDAC-215, 253, and 354 cells were treated with macrophage-conditioned medium (MCM) or 20μM Etomoxir (Eto) for 48h and expression of EMT-associated genes (*VIM*, *SNAIL*, *ZEB1, SLUG* and *LOXL2*) was determined by rtQPCR ($n \leq 4$ for each cell type). Data are normalized to *HPRT*. (**D**) Cells were treated as indicated above and seeded in modified Boyden invasion chambers containing 20% FBS in the lower compartment. The number of invasive cells was analyzed after 16h. (**E**) GFP^+ $Luciferase^+$ PDAC-354 cells were treated with control, MCM, or 20μM Eto for 48h and then injected intrasplenically to assess their metastatic capacity. Representative photographs of liver metastasis and subsequent H&E staining. All data are represented as mean ± SEM. * $p<0.05$, ** $p<0.01$, *** $p<0.001$. See also Figure S1.

Figure 2. Single-cell RNAseq analysis identifies metabolic switch during EMT induction. (**A**) **Left panel**: PDAC-003 cells were treated with control vehicle (CTRL), macrophage-conditioned medium (MCM), or 20μM Etomoxir (ETO) for 48h to induce an EMT-like state and were then subjected to single-cell RNAseq (10X Genomics Chromium platform). Unsupervised clustering of viable PDAC cells exposed to CTRL, MCM or ETO, represented as UMAP plots. Different clusters are color coded. **Right panel**: Boxplots illustrating gene set enrichment results for the *EMT* and *Glycolysis* (Hallmark data set) for different clusters in CTRL versus MCM and ETO treatment, respectively. Differences in enrichment scores between treatments were assessed using the Mann-Whitney U test. (**B**) Expression of EMT hallmark signature and PPARD family members in single

cancer cells (PDAC-002 and 021) displayed as unsupervised clusters and color-coded for allocated treatment.

Figure 3. *PPARD* expression is linked to metabolic switch and invasiveness in PDAC patients. (**A**) Expression levels for PPAR family members in PDAC tumors (T) versus surrounding normal tissue (N) included in the TCGA and GTEx projects. (**B**) Patients were dichotomized for the tumor expression levels for PPAR family members (higher and lower expression compared to the mean; RNA Seq V2 RSEM values). Kaplan Meier survival curves for disease-free survival are shown. Dotted lines denote the confidence interval. (**C**) Correlation between tumor expression levels for PPAR family members and an EMT-associated signature composed of *SLUG*, *SNAIL*, and *ZEB1*. (**D**) Gene sets enriched in the transcriptional profile of tumors belonging to the top *PPARD* high-expression group, compared with the bottom expression group in the TCGA data series. Shown are the NES (normalized enrichment score) values for each pathway using the Hallmark gene sets, meeting the significance criteria: nominal p-value of <0.05, FDR < 25%. (**E**) Enrichment plot for EMT, Glycolysis, Hypoxia and OXPHOS hallmarks in *PPARD* high versus low samples, showing values of NES and FRD q-values.

Figure 4. Activation of PPAR-δ initiates invasiveness and metastasis. (**A**) *PPARD* expression upon 48h of treatment with the complex I inhibitor Metformin (3mM), the ß-oxidation inhibitor Etomoxir (20μM), complex II inhibitor Malonate (5mM), the pyruvate carrier inhibitor UK5099 (100μM), or tumor-like conditions (HCl 50 μM + 1 mM Glc+ 3% O2) with the indicated stimuli in PDAC-215, 253, and 354 cells. (**B**) PPAR-δ activity, measured as binding to its specific DNA sequence, following stimulation with MCM, Eto, and PPAR-δ agonist GW0742 for 24 hours. (**C**) Invasive capacity of cells treated for 48h with the PPAR-δ agonists L-165 and GW0742, respectively. Cells were placed in modified Boyden invasion chambers containing 20% FBS in the lower compartment and the number of invasive cells was assessed after 16h. (**D**) *In vivo* metastatic activity of PDAC-354-GFP-luc cells pretreated with GW0742 for 48h. After surgery, mice received three more daily doses of GW0742 (0.3mg/kg i.v.). IVIS imaging (**left panel**) and quantification of the total CK19 area in the livers 9 weeks after implantation (**right panel**). (**E**) PDAC-215, 253, and

354 cells were stably transduced with inducible lentiviral vectors expressing either a non-targeting shRNA (NT) or three different shRNAs against PPARD (sh#1, sh#2, sh#3). Transduced cells were pre-treated with doxycycline for 24h, then incubated with MCM, Eto, or L-165 for 48h. (**F**) ZsGreen expression by rt-QPCR in liver homogenates from an *in vivo* metastasis assay of PDAC-354 cells stably expressing either the NT or the sh#1 against PPARD. Cells were pretreated with doxycycline and/or 20 Eto μM for 48h. After intrasplenic implantation, mice were treated with oral doxycycline (2mg/ml drinking water) and Etomoxir (15 mg/kg, i.p. every day) for 7 days, when splenectomies were performed. Table indicates the percentage and total number of micrometastases in each experimental group. All data are represented as mean ± SEM. * p<0.05, ** p<0.01, *** p<0.001. See also Figures S3 and S4.

Figure 5. A common PPAR-δ-initiated metabolic program drives invasiveness. (**A**) Gene expression profile as assessed by a Carbohydrate metabolism PCR array in PDAC-354 cells. Heatmap showing only genes whose expression was significantly altered. Cells were treated with vehicle (Cont), macrophage-conditioned medium (MCM), 20μM Etomoxir (Eto), or 100μM of the pyruvate carrier inhibitor UK5099 for 48h. (**B**) Representative Extracellular Acidification Rate (ECAR) profile for PDAC-253 cells (Glycolysis test) (**upper panel**). G, Glucose; O, ATP synthase inhibitor Oligomycin; 2DG, Glycolysis inhibitor 2-deoxy-glucose. Representative Oxygen Consumption Rate (OCR) profile for PDAC-253 cells (Mitochondrial stress test) (**lower panel**). O, ATP synthase inhibitor Oligomycin; F, mitochondrial oxidative phosphorylation uncoupler FCCP (Carbonyl cyanide-4 [trifluoromethoxy] phenylhydrazone); A+R, complex III inhibitor Antimycin A + Electron transport change inhibitor Rotenone. (**C**) Glycolysis, glycolytic capacity, and reserve in adherent vs sphere-derived cells (**upper panel**). Pooled data from PDAC-215, 253, and 354. Maximal and ATP-linked respiration in non-CSCs vs CSCs (**lower panel**). Pooled data for PDAC-215, 253, and 354. All data are represented as mean ± SEM. * p<0.05, ** p<0.01, *** p<0.001. See also Figure S3.

Figure 6. PPAR-δ controls the balance between OXPHOS and glycolysis, linked to EMT and metastasis. (**A**) PDAC-215, 253, and 354 cells were stably transduced with inducible lentiviral vectors expressing either a non-targeting shRNA (NT) or three different shRNAs against PPARD

(sh#1, sh#2, sh#3). Transduced cells were pre-treated with doxycycline for 24h, then incubated with macrophage-conditioned medium (MCM), Etomoxir (Eto), or L-165 and tested for glycolytic capacity (**upper panel**) and ATP-linked respiration (**lower panel**) after additional 24h. (**B**) Mitochondrial stress test (**upper row**) and glycolysis test (**lower row**) following treatment with control (Cont) or the PPAR-δ agonists L-165 or GW0742. **Left column**, representative OCR and ECAR profiles for PDAC-253. **Right column**, pooled data for PDX-215, 253, and 354 cells. O, ATP synthase inhibitor Oligomycin; F, mitochondrial oxidative phosphorylation uncoupler FCCP (Carbonyl cyanide-4 [trifluoromethoxy] phenylhydrazone); A+R, complex III inhibitor Antimycin A + Electron transport change inhibitor Rotenone. G, Glucose; 2DG, Glycolysis inhibitor 2-deoxy-glucose. * $p<0.05$, ** $p<0.01$. (**C**) ATP-linked respiration (**left panel**) and maximal respiration (**right panel**) for control versus GW0742-treated cells following treatment with or without Palmitate-BSA (FAO assay). Cells were treated with 10 μM GW0742 for 48 hours prior to the assay. Pooled data from PDAC-215, 253 and 354 cells. All data are represented as mean ± SEM. *** $p<0.001$ vs Control, &&& $p<0.001$ vs Palmitate.

Figure 7. PPAR-δ rewires cellular metabolism regulating *MYC*/*PGC1A* balance. (**A**) Expression of *MYC*, *PGC1A* and *MYC*/*PGC1A* ratio in PDX-354 after mitochondrial energy deprivation during 48-72h. (**B**) MYC and PGC-1α expression measured by Western Blot following 48 h treatment with macrophage-conditioned medium (MCM), Etomoxir (Eto), or the PPAR-δ agonist GW0742 (5μM). Vinculin was used as loading control. (**C**) *MYC* and *PGC1A* promoter activity at the indicated times following treatment with PPAR-δ agonist GW0742 or *PPARD* overexpression (*PPARD* OE). (**D**) PDAC- 354 cells were transduced with inducible lentiviral vectors expressing either a non-targeting shRNA (NT) or two different shRNAs against MYC (sh#1, sh#2) or the complete cDNA of *PGC1A*. Effect of MYC knockdown (shMYC, pooled data for sh#1 and sh#2) or PGC-1α overexpression (PGC1A OE) on invasiveness in response to treatment with 5μM PPAR-δ agonist L-165 for 48h. (**E-H**) PDAC-215 and 354 cells were transduced with inducible lentiviral vectors expressing either a non-targeting shRNA (NT) or two different shRNAs against MYC (sh#1, sh#2). Transduced cells were pre-treated with doxycycline for 48h and then incubated with MCM or

Eto. (**E**) OCR changes for maximal respiration (left) and ATP-linked respiration (right). (**F**) Glycolytic capacity (left) and reserve (right). (**G**) *ZEB1* gene expression. (**H**) Invasive capacity. (**I**) PDAC-354 cells were treated with MCM or 20μM Eto for 48h in the presence or absence of the MYC/Max interaction inhibitor Mycro3 (25µM). Cells were then seeded in modified Boyden invasion chambers containing 20% FBS in the lower compartment and the number of invasive cells was assessed after 16h. All data are represented as mean ± SEM. # p<0.05, ## p<0.01, ### p<0.001 vs unstimulated control. * p<0.05, ** p<0.01, *** p<0.001 versus NT. See also Figure S.

Figure 8. Therapeutic targeting of PPAR-δ impairs invasion *in vitro* and metastasis *in vivo*. (**A**) PDAC-215 and 354 cells were pre-treated with PPAR-δ antagonists GSK0660 (10μM) and GSK3787 (10μM) and inverse agonist DG172 (2.5μM) for 1h and then treated with MCM or Etomoxir for 48h. Invasion over 16h was assessed in modified Boyden invasion chambers. (**B**) Highly metastatic PDAC-265 cells were incubated with the PPAR-δ antagonists GSK0660 (10µM) and GSK3787 (10µM) and the PPAR-δ inverse agonist DG172 (1µM) for 48h and invasion was assessed after additional 16 hours. (**C, D**) Spontaneous metastasis upon orthotopic injection of 10^5 metastatic PDAC-265-GFP-luc cells. Following implantation, mice were treated daily with either vehicle, the PPAR-δ agonist GW0724 (0.3mg/kg i.p.) or the PPAR-δ antagonist GSK3887 (3mg/kg i.p.) until termination of the experiment at week 9, when mice showed signs of disease. Tumor and onset of metastasis were assessed by weekly IVIS. (**C**) Expression of *PPARD* in pancreatic tumors measured by rt-QPCR. (**D**) Metastasis onset evaluated as *hGAPDH* absolute copy number. (**E**) Percentage of macro and micrometastases in the liver (**upper panel**). Expression levels of CK-19 in liver sections (**middle panel**, representative images), or c-MYC (brown) and VIM (purple) in pancreatic tumors was measured by IHQ (**bottom panel**, representative images). All data are represented as mean ± SEM. * p<0.05, ** p<0.01, *** p<0.001 vs NT cells; # p<0.05, ## p<0.01, ### p<0.001 vs control or single treatment.

EXPERIMENTAL PROCEDURES

Primary human PDAC cells. For primary cultures, PDAC tissue fragments were minced, enzymatically digested with collagenase (Stem Cell Technologies) for 90 min at 37°C (Mueller et al., 2009), and after centrifugation for 5 min at 1,200 rpm the pellets were resuspended and cultured in RPMI, 10% FBS, and 50 units/ml penicillin/streptomycin. For experiments, cells were cultured in DMEM:F12 supplemented with B-27, L-Glutamine (all from Gibco, Life Technologies), 50 U/mL penicillin–streptomycin (Sigma) and β-FGF (PeproTech). PDXs tissues were obtained through the Biobank of the Spanish National Cancer Research Centre (CNIO), Madrid, Spain (references M-20/002-1, I409181220BSMH, 1204090835CHMH) and the ARC-NET Biobank at the 'Rossi' University of Verona Hospital, Italy (reference 6.B.04 - Samples PDAC-10953). Cancer cells from advanced PDAC patients were isolated and expanded from peripheral blood (Shanghai Jiaotong University School of Medicine, Protocol No 20130905), as previously described (Agerbæk et al., 2018).

Primary human macrophages and conditioned media. Leucocyte cones from anonymous healthy donors were obtained from the National Blood Transfusion Service (UK) according to City and East London Research Ethics Committee (17/EE/0182). Cones were stored at 4°C and used within 24 hours of delivery to maintain cell viability. Monocyte-derived human macrophage culture, polarization into M2-like macrophages and generation of conditioned medium were as previously described (Sainz et al., 2014, 2015). Monocyte-derived human macrophage cultures were maintained in IMDM (Gibco) supplemented with 10% human AB serum and polarized by incubation with 0.5ng/ml of macrophage colony-stimulating factor for 48 hours (MCSF; PeproTech). To generate conditioned media, macrophages were then washed with PBS and cultured for additional 48 hours in supplemented DMEM:F12 (see previous section). Media was then collected, centrifuged and supernatant stored at -80°C.

Single-cell capture, library Preparation, and RNA-seq. The samples (ETO-treatment vs CTRL, MCM-treatment vs CTRL) were labeled with Cell Hashing antibodies following the manufacturer's instruction (BioLegend), cells were counted on Countess II automated cell counter

(Thermo Fisher) after staining, and up to 25,000 cells were loaded per lane on 10X Chromium microfluidic chips (10X Genomics). Single-cell capture, barcoding, and library preparation were performed using the 10X Chromium Single Cell 3' Reagent Kits version 3 chemistry, and according to the manufacturer's protocol (#CG000185). cDNA and HTO libraries were checked for quality on the Agilent 4200 Tapestation, and quantified by KAPA qPCR before sequencing on a single lane of a NovaSeq 6000 S4 flow cell (Illumina) to an average depth of 100,000 reads per cell.

Single-Cell Data Processing, Quality Control, and Analysis. The Cell Ranger pipeline (v1.3, 10X Genomics) was used to firstly convert Illumina base call files to FASTQ files, then demultiplexing was conducted before aligning FASTQs to the GRCh38 genome reference and producing the digital gene-cell counts matrix. Samples were combined using the Cell Ranger aggregate function, which merges output from multiple runs to normalized to the same sequencing depth before generating a gene-barcode (cell) expression matrix. Potential doublets were identified by DoubletFinder (McGinnis et al., 2019) and removed before proceeding to downstream analysis. Quality control, normalization, clustering, dimensionality reduction and visualization were performed using R toolkit Seurat package (Butler et al., 2018). Gene-cell matrices were filtered to remove cells with fewer than 500 unique molecular identifiers (UMI) counts and 500 detected genes, and cells with more than 15% mitochondrial gene counts were also filtered. The gene set enrichment analysis was conducted using ssgsea function from GSVA package. RNA-seq data are available at NCBI dbGaP under the accession number GSE184871.

XF extracellular flux analysis. Single-cell suspensions from trypsinized secondary spheres/adherent cultures were plated in XF96 Cell Culture Microplates previously coated with Cell-Tak (BD Biosciences) at a cellular density of 30,000 cells/well. For OCR determination, cells were incubated in base assay medium supplemented with 2mM glutamine, 10mM glucose, and 1mM pyruvate for 1h, prior to the measurements using the XF Cell Mito Stress Kit. Concentrations of oligomycin and FCCP were adjusted for each primary cell type. For glycolytic metabolism measurements, cells were incubated in basal media supplemented with 2mM glutamine and 1mM pyruvate prior to injections using the Glycolysis Stress Test kit. Experiments were run in a XF96^{e}

analyzer, and raw data were normalized to protein content. Unless indicated otherwise, all reagents and materials were from Agilent Seahorse XF Technologies (Agilent Technologies).

Invasion assay. Invasion assays were performed using 24-well 8.0µm PET membrane invasion chambers coated with growth factor reduced Matrigel^{TM} (Corning). After 48h of pre-treatment, 10^5 primary PDAC cells were seeded to coated inserts in serum free media. Invasion towards 20% FBS was tested after 12-24h incubation at 37°C in a humidified atmosphere of 5% CO_2. Invaded cells were fixed with 4% paraformaldehyde, stained with DAPI and imaged on the Olympus Fluorescence microscope (model BX51). Cell number was analyzed using automated ImageJ particle analysis software.

***In vivo* metastasis and treatments.** For classical metastasis assay upon intrasplenic injection, pre-treated PDAC-354 CMV-Luciferase-RFP-TK expressing cells were re-suspended in 50µl of Matrigel and injected in the spleen of NSG mice (NOD Scid interleukin (IL)-2 receptor γ chain knockout mice; Charles Rivers) at a concentration of $0.5x10^5$ cells per injection. After 7 days, splenectomy was performed. For spontaneous metastasis assay, PDAC-265 cells were re-suspended in 30µl of Matrigel and injected orthotopically to NSG mice at a concentration of $1x10^5$ cells per injection. Mice were then imaged weekly using the IVIS Spectrum Imaging System (Caliper Life Sciences). Mice were anaesthetized with isoflurane (2%) and injected intraperitoneally with 150 mg/kg of luciferin (Caliper Life Sciences) diluted at 15 mg/mL in PBS. For the experiment shown in Figure 5D, mice were treated for three consecutive days with GW0742 (0.3 mg/kg i.v.) after surgery. For the experiment shown in Figure 5F, mice were treated with oral doxycycline (2mg/ml drinking water) and Etomoxir (15 mg/kg, i.p. every day) for 7 days after intrasplenic implantation. For the experiment shown in Figure 8E, mice were treated daily with either vehicle (PBS), the PPAR-δ agonist GW0724 (0.3 mg/kg i.p.) or the PPAR-δ antagonist GSK8337 (3 mg/kg i.p.) until termination of the experiment. Once a minimum of $1x10^6$ ROI bioluminescence in liver was achieved in at least 3 mice after 5 minutes following injection, or if signs of ascites developed, all experimental mice were sacrificed (9 weeks). Livers and pancreas were harvested, imaged on collection and fixed in 4% PFA. Procedures were conducted in accordance with institutional and national regulations (Animals in

Science Regulation Unit, Home Office Science, London, UK; Project License PPL70/8129; Ethical Conduct in the Care and Use of Animals as stated in The International Guiding Principles for Biomedical Research involving Animals (Council for International Organizations of Medical Sciences (CIOMS)); Universidad de Zaragoza Ethics Committee; project licenses PI22/17 and PI41/20).

Statistical analysis. Results for continuous variables are presented as means ± SEM unless stated otherwise. Treatment groups were compared with the independent samples t test. Pair-wise multiple comparisons were performed with the one-way ANOVA (two-sided) with Bonferroni adjustment. p values < 0.05 were considered statistically significant. All analyses were performed using Prism GraphPad (version 5.04).

Further description of experimental procedures is provided as supplemental information.

Figure 1 – Induction of EMT-like phenotype in PDAC

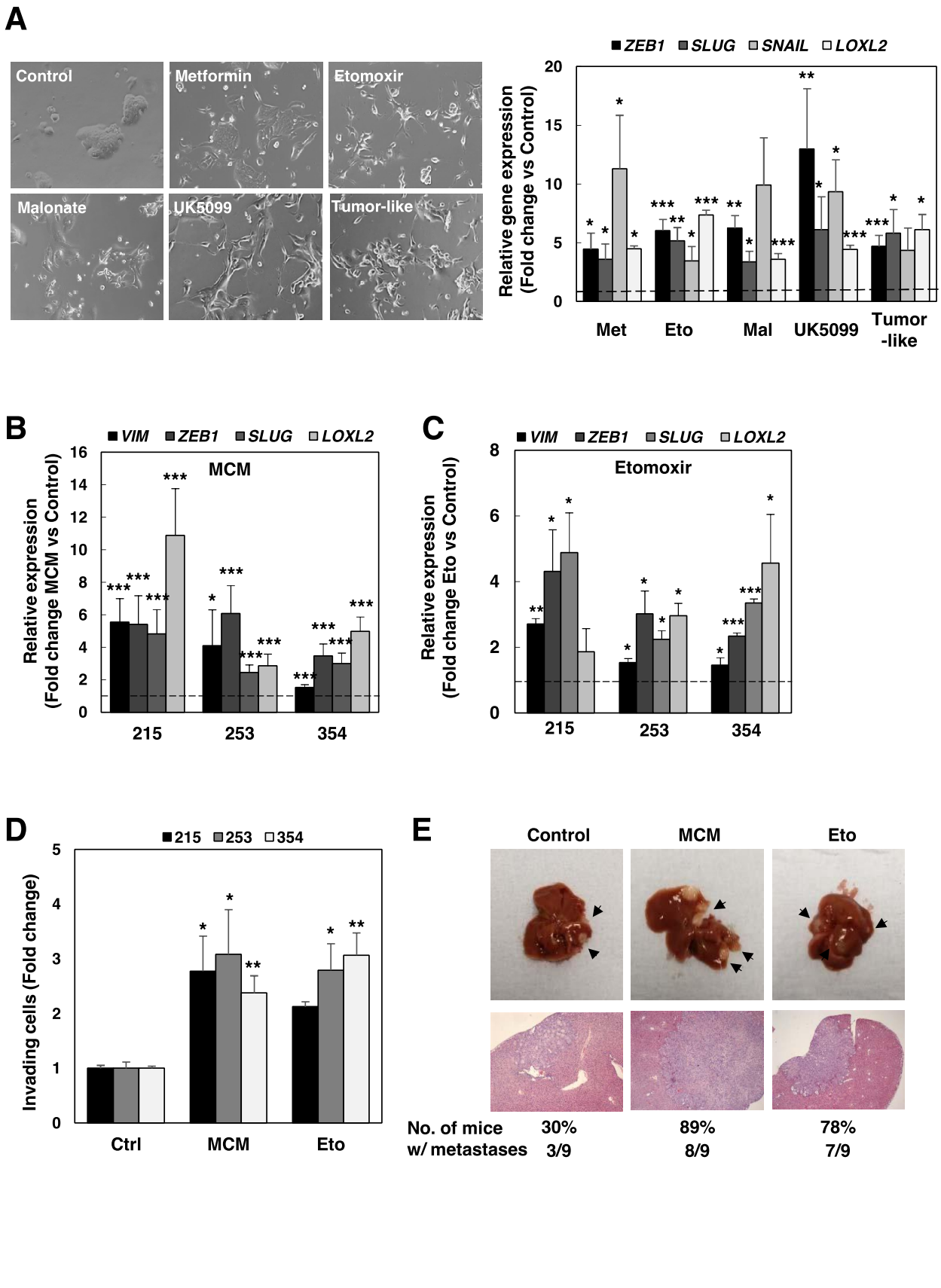

Figure 2 – Single-cell RNAseq analysis

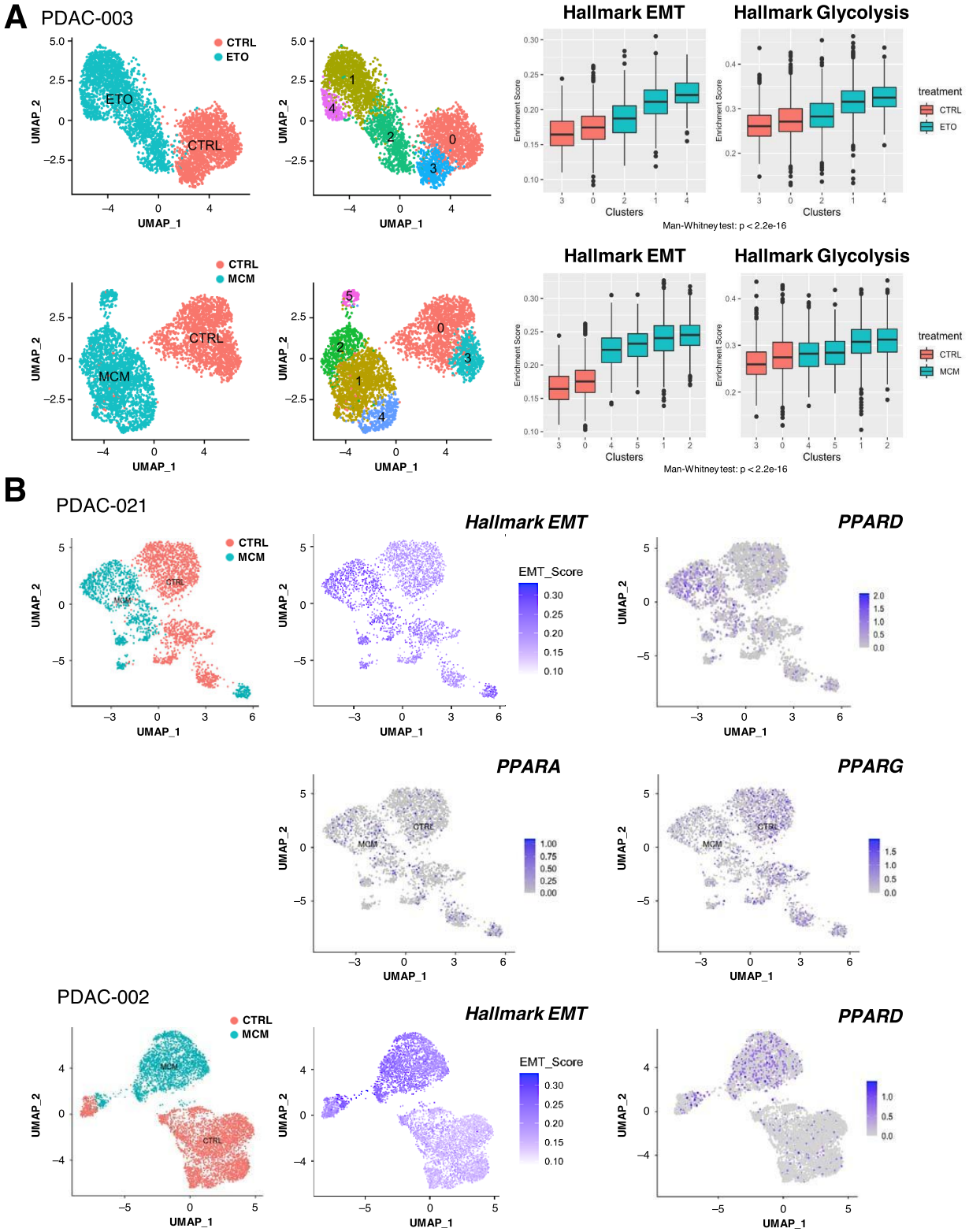

Figure 3 – *PPARD* expression is linked to EMT and metabolic switch

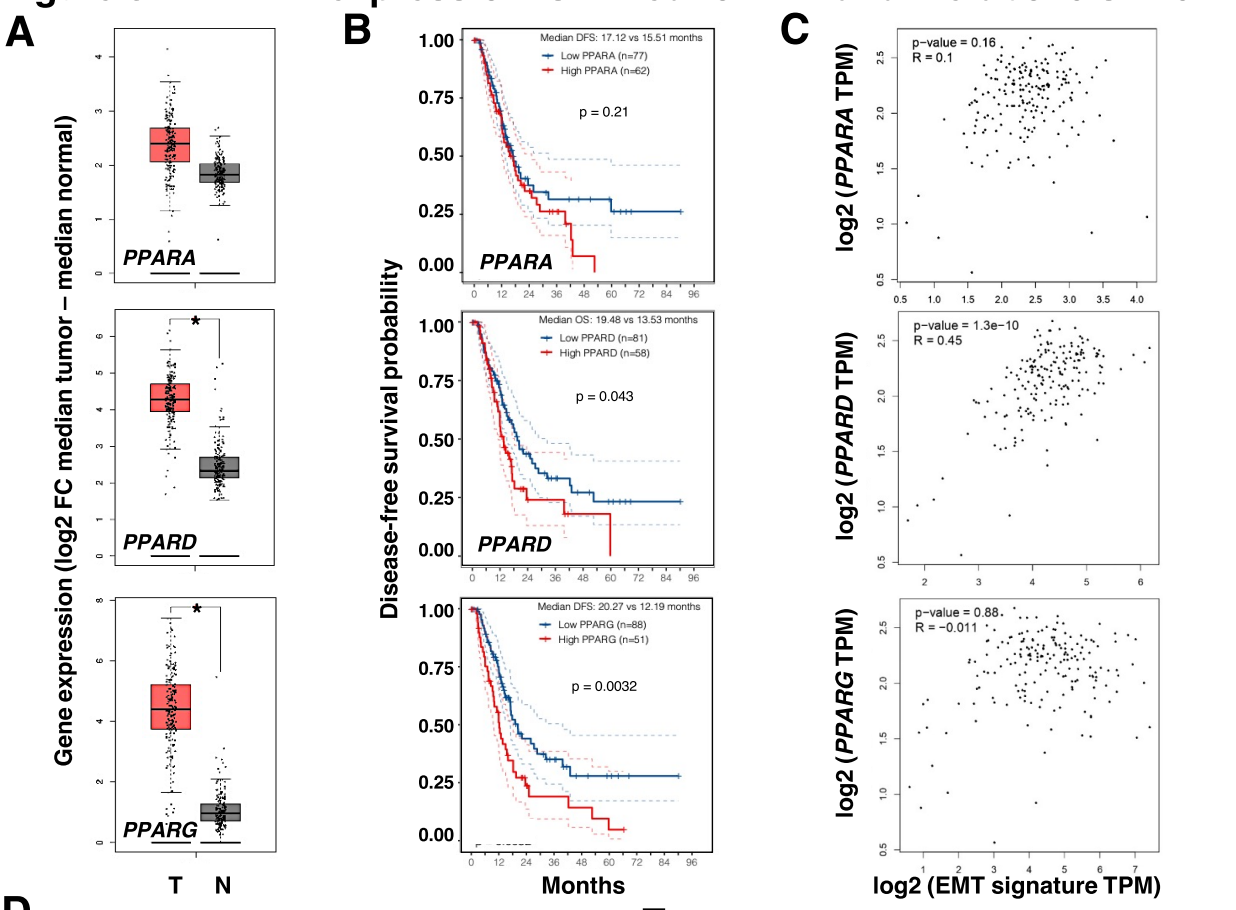

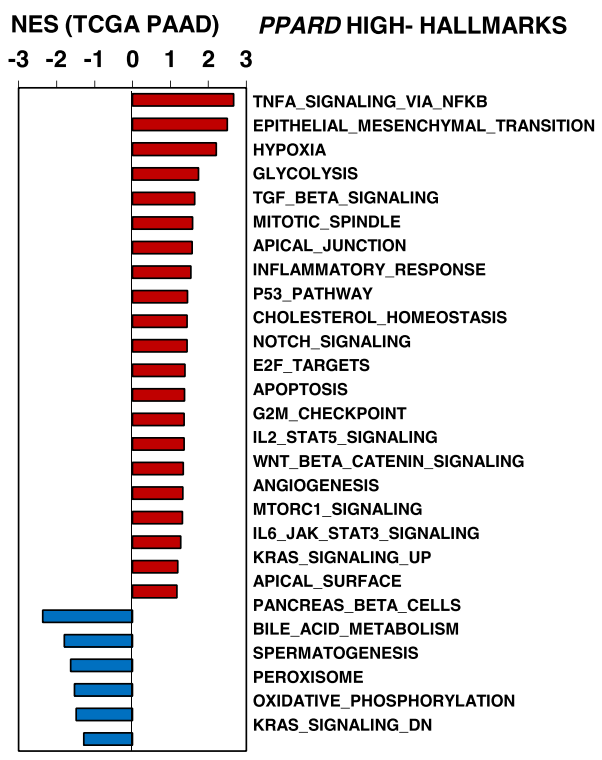

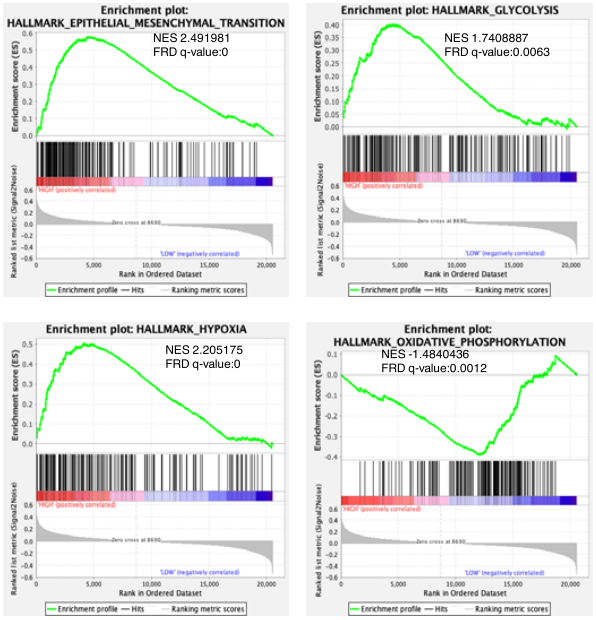

Figure 4 – PPARD promotes invasion and metastasis

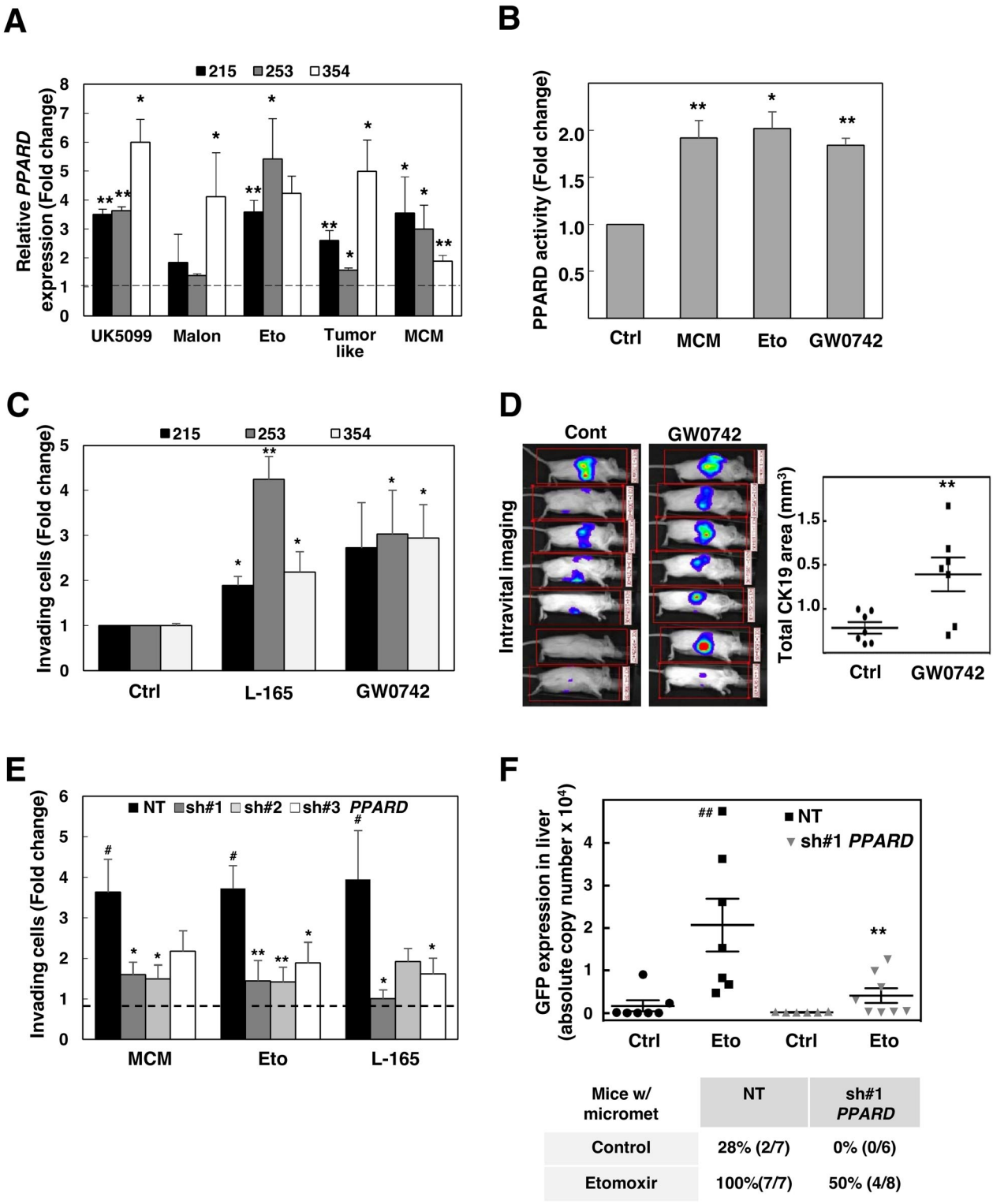

Mice w/ micromet	NT	sh#1 *PPARD*
Control	28% (2/7)	0% (0/6)
Etomoxir	100%(7/7)	50% (4/8)

Figure 5 – A common metabolic program induced in EMT

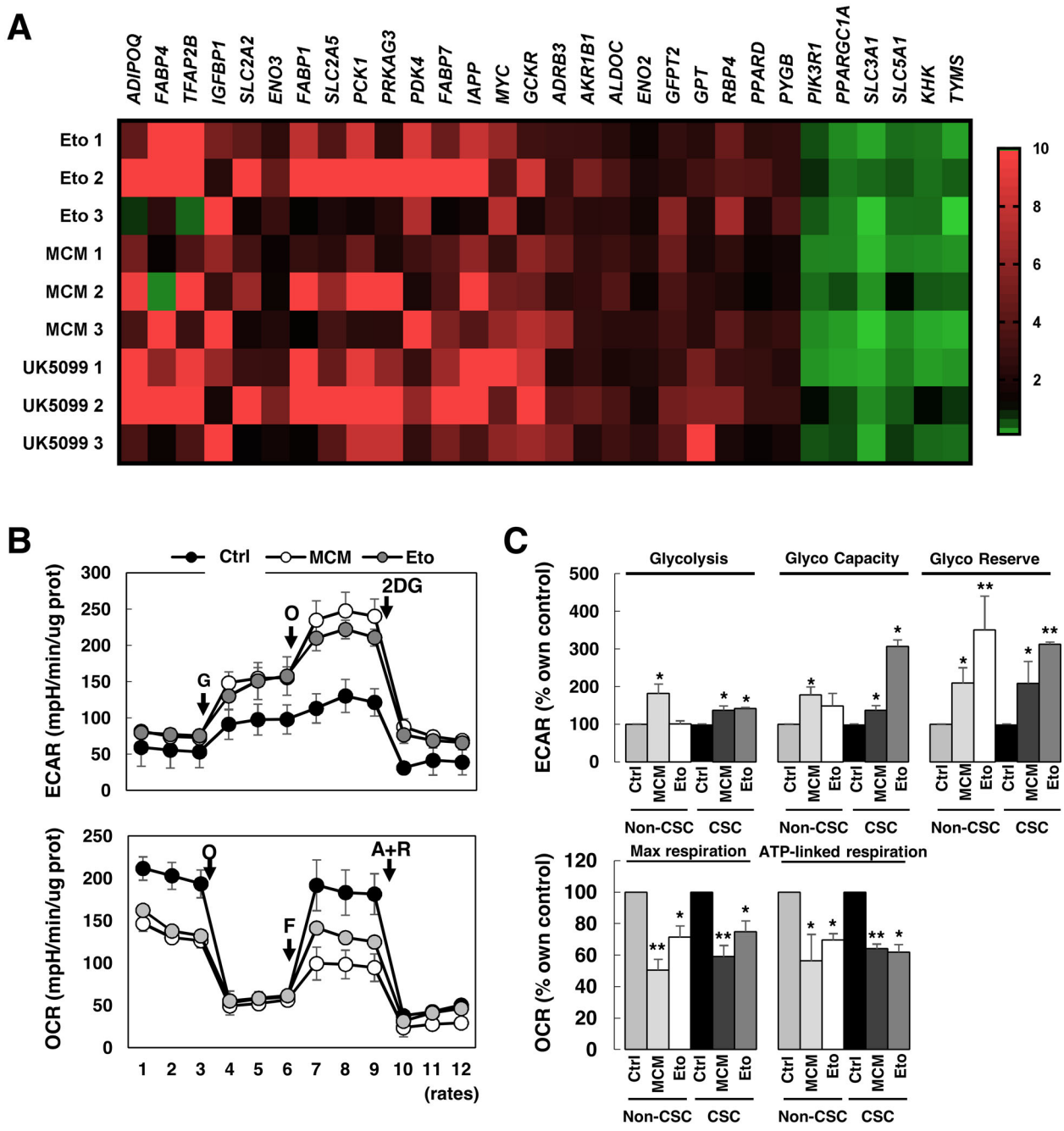

Figure 6 – PPARD-induced metabolic changes

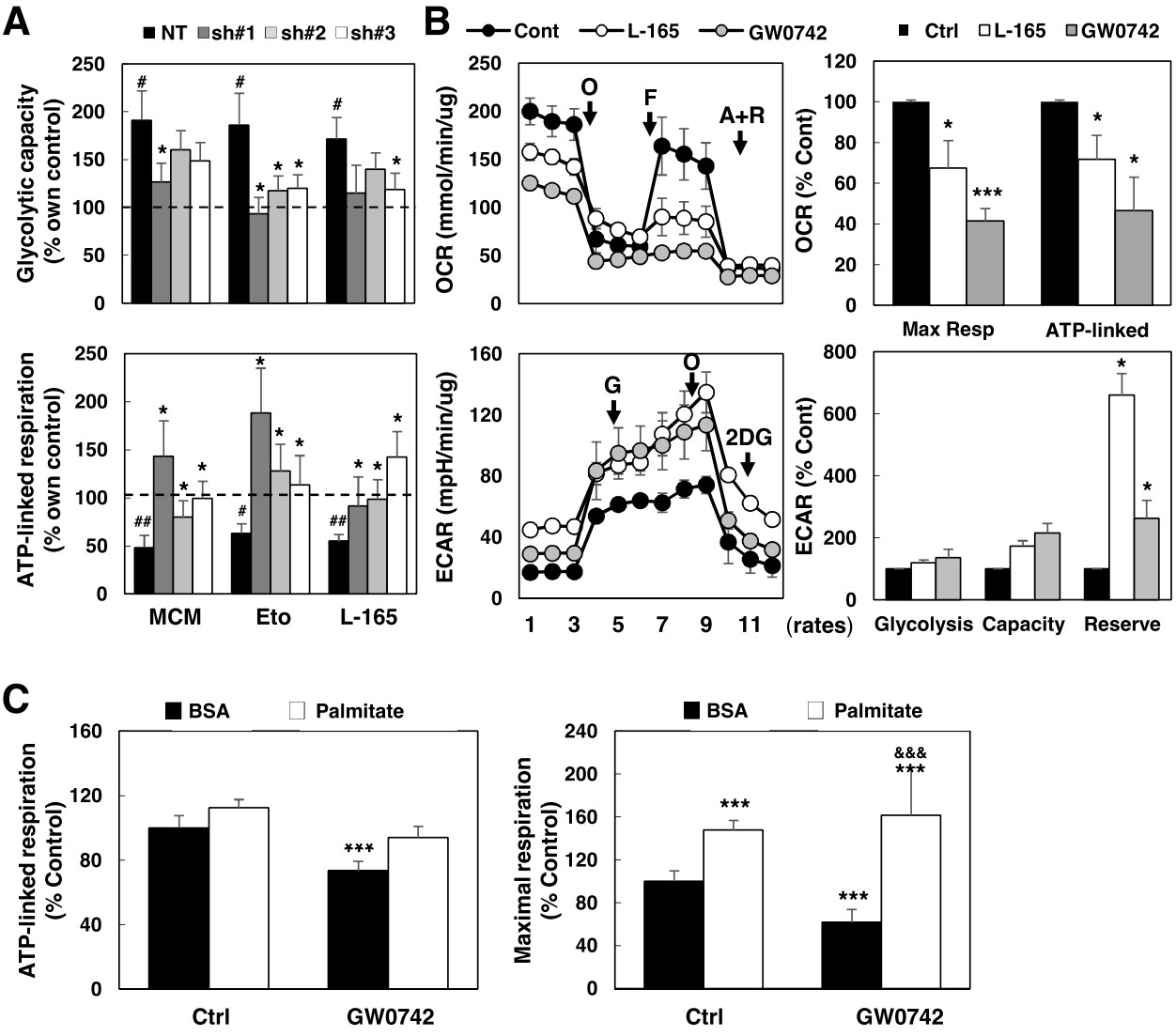

Figure 7 – PPARD-induced downstream signaling

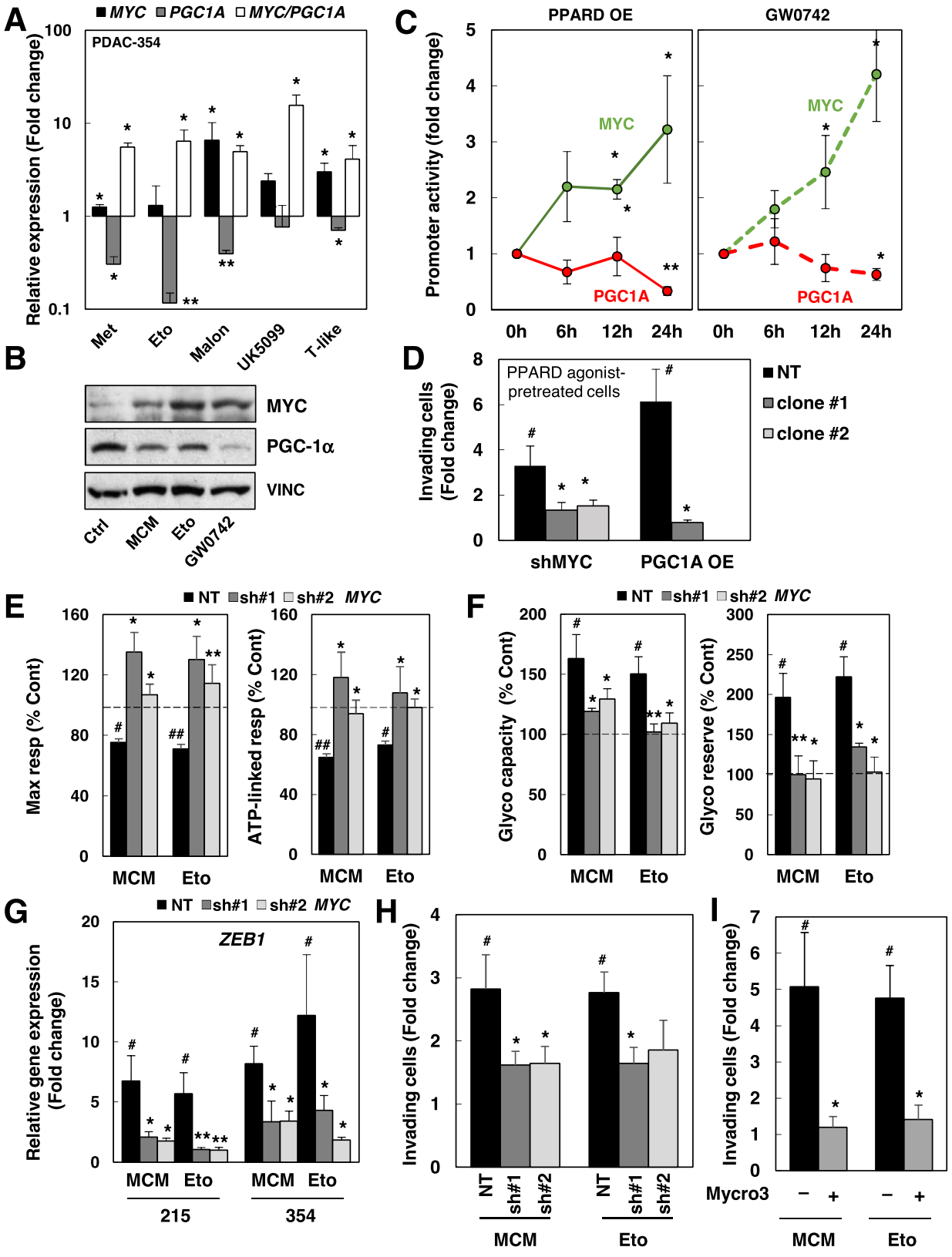

Figure 8 – Therapeutic targeting of PPARD

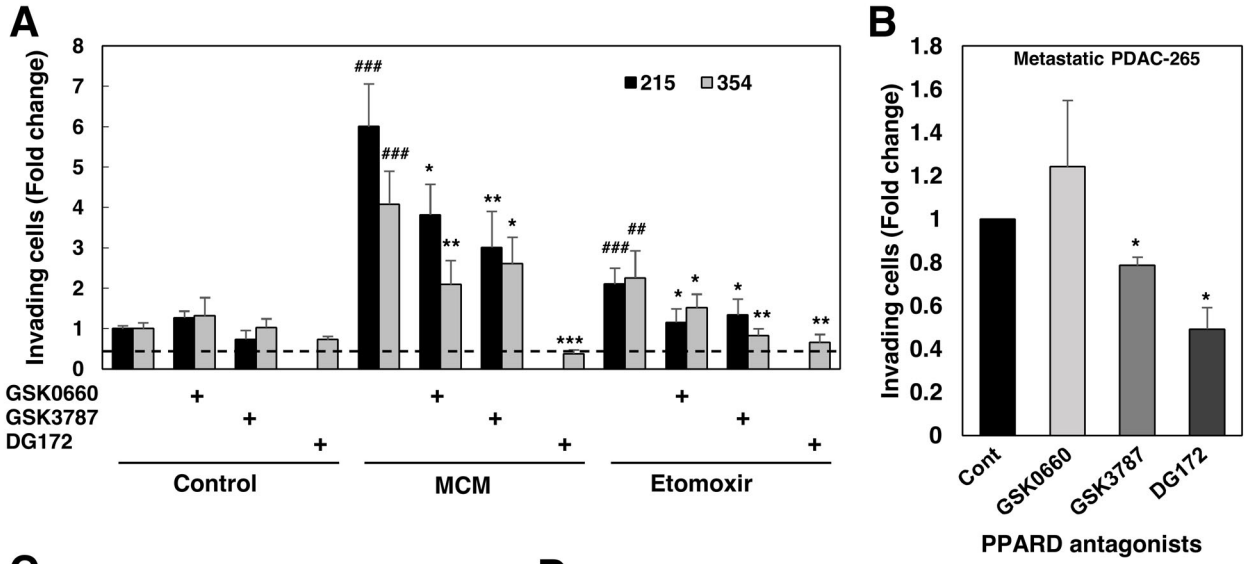

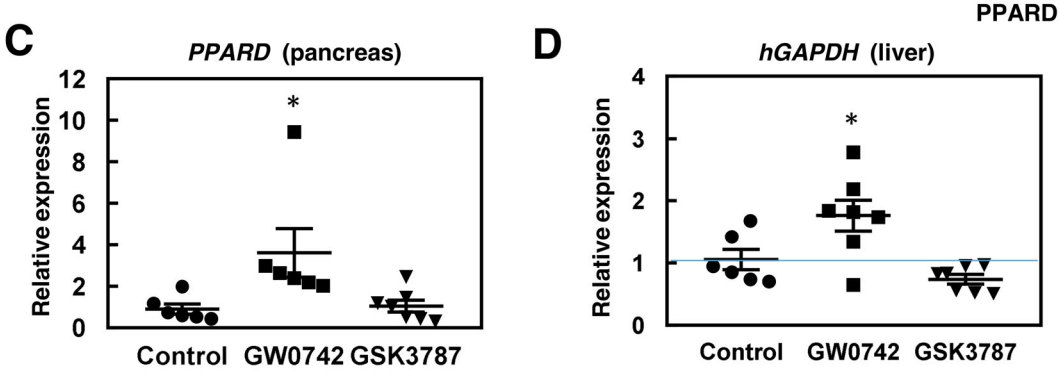

E

	Control	GW0742	GSK3887
Macromet	22%	66%	10%
Micromet	33%	87.5%	10%

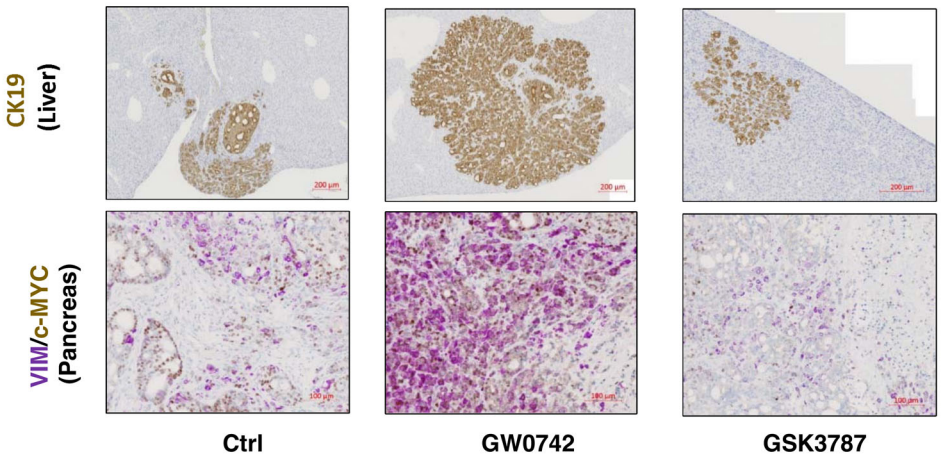

Figure S1, related to Figure 1

Mitochondrial energy deprivation promotes epithelial-to-mesenchymal transition in PDAC cells. (A) Left panel: representative micrographs of parental PDAC-215 and their metformin-resistant counterparts. **Right panel**: *Vimentin* (*VIM*) and *ZEB1* expression in Metformin-resistant cells (215M, 253M, 354M) *vs* treatment naïve parental cells (PDAC-215, 253, 354). (**B**) PDAC-215, 253, and 354 cells were treated for 48h with the indicated concentrations of Metformin, Malonate, UK5099, or hypoxia (3% O_2) with or without glutamine deprivation (low Q, 0.2 mM) and low pH (50 µM HCl). Expression of EMT-associated genes was determined by rtPCR. Data were normalized to HPRT. (**C**) Cells were exposed for 72h to normoxia (20% O_2) or hypoxia (3% O_2) ± the following metabolic stress conditions : low glutamine (low Q, 0.2mM), low glucose (low Glc, 1mM), low pH (50µM HCl) or combinations thereof (low Q & low pH; low Glc & low pH). Pooled data for PDAC-185, A6L, 215, 253, and 354 (n≤4 for each cell type). (**D**) *VIM* and *ZEB1* expression in cells co-cultured for 72 h with M2-differentiated human primary macrophages (M0) or human primary pancreatic stellate cells (PSC). Pooled data from PDAC-253 and 354 (n=2 for each cell type). (**E**) *ZEB1* expression for cells sorted for CD133 and mitochondrial content (MitoTracker) and treated for 48h as indicated. Pooled data from PDAC-253 and 354. (**F**) Sphere formation after 7 days of treatment with Control, MCM, and Etomoxir. Some of the data shown here are also included in the pooled data graphs represented in Figure 1. Data are represented as mean ± SEM. * p<0.05, ** p<0.01. *** p<0.001. & p<0.05 *vs* M0

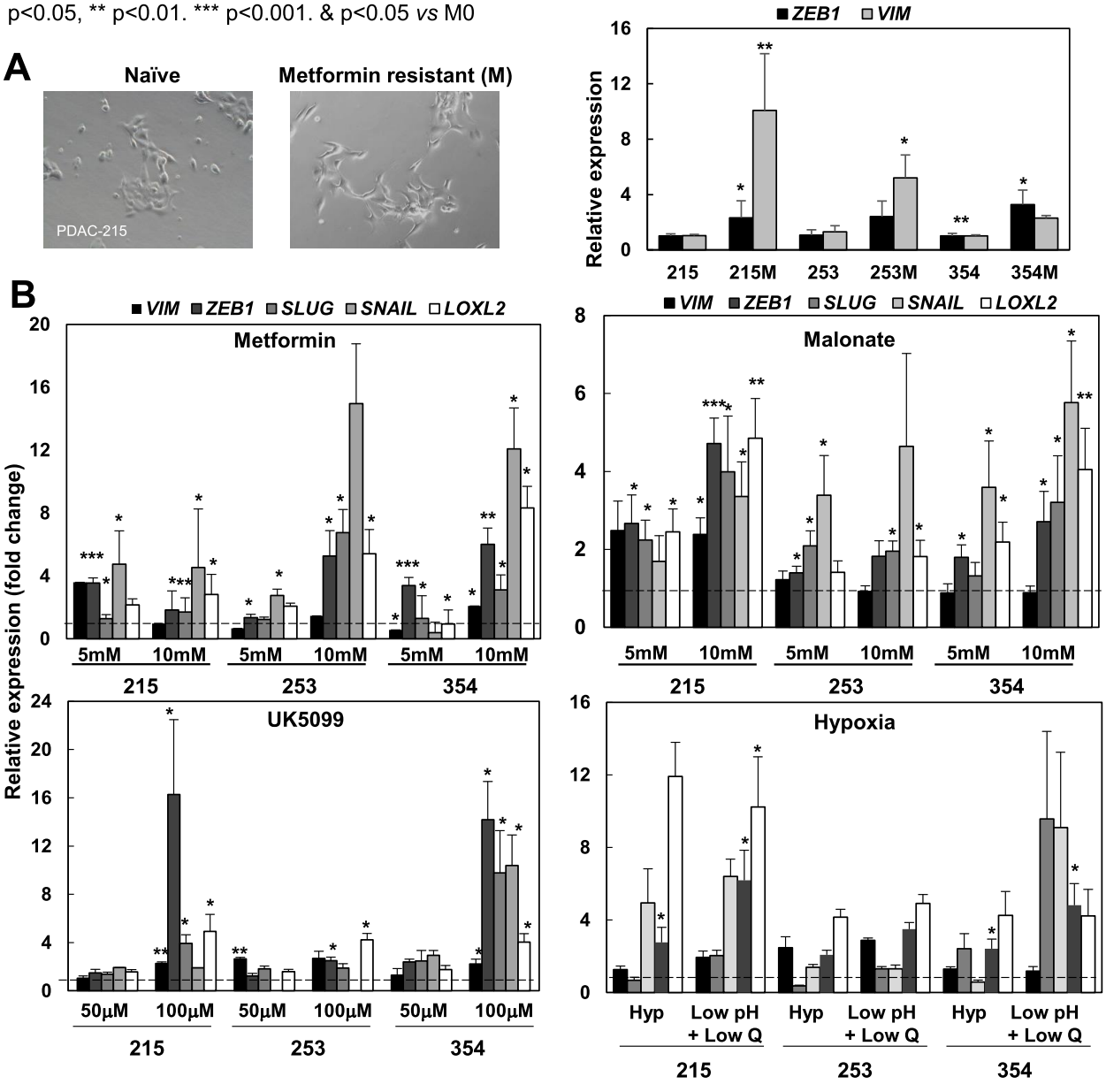

Figure S1, related to Figure 1

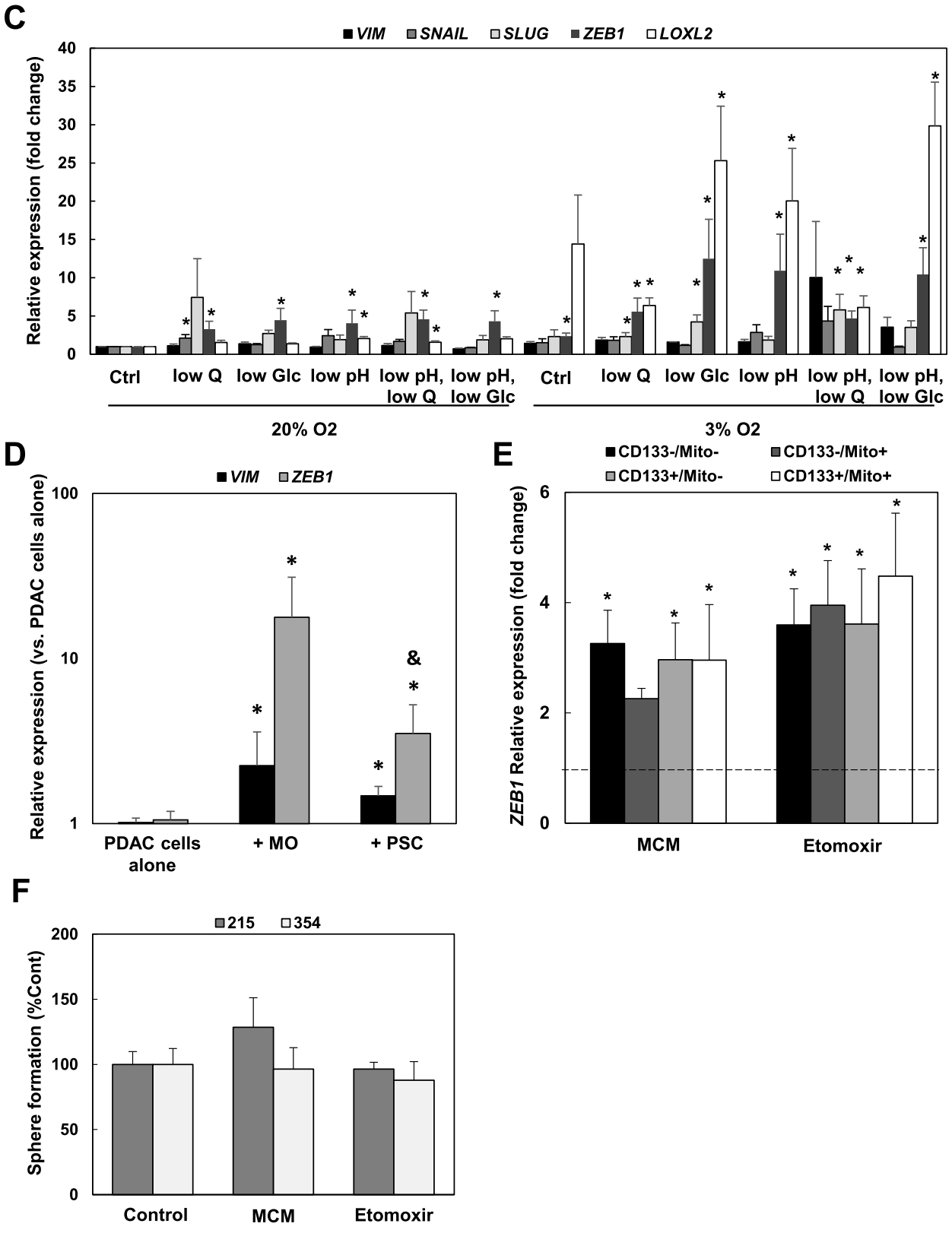

Figure S2, related to Figure 2

Transcriptomic analyses reveals a common transcriptional program associated to EMT. Cells were treated with control vehicle (CTRL), macrophage-conditioned medium (MCM), or 20µM Etomoxir (ETO) for 48h. (**A**) representative images. (**B**) Unsupervised clustering of viable PDAC cells exposed to CTRL, MCM or ETO, subjected to single-cell RNAseq (10X Chromium platform) and represented as UMAP plots. (**C**) Gene set enrichment analysis (GSEA, Hallmark gene set) for the Hallmark Hypoxia in the different transcriptional clusters identified by single-cell RNAseq. (**D**) Heat map showing scaled normalized expression of differentially expressed genes between control and MCM cells, with cells as columns and genes as rows. Genes were selected based on absolute log2FoldChange > 0.8 and p<0.05. (**E**) Heatmap of top differentially expressed genes (absolute log2FoldChange > 1.5, padj < 0.1) after analysis by bulk RNAseq. Hierarchical clustering of genes differentially expressed in control cells versus treated cells. (**F**) Commonly up-regulated and metabolism-related pathways as determined by GSEA (Hallmark gene set) for Etomoxir-treated PDAC cells.

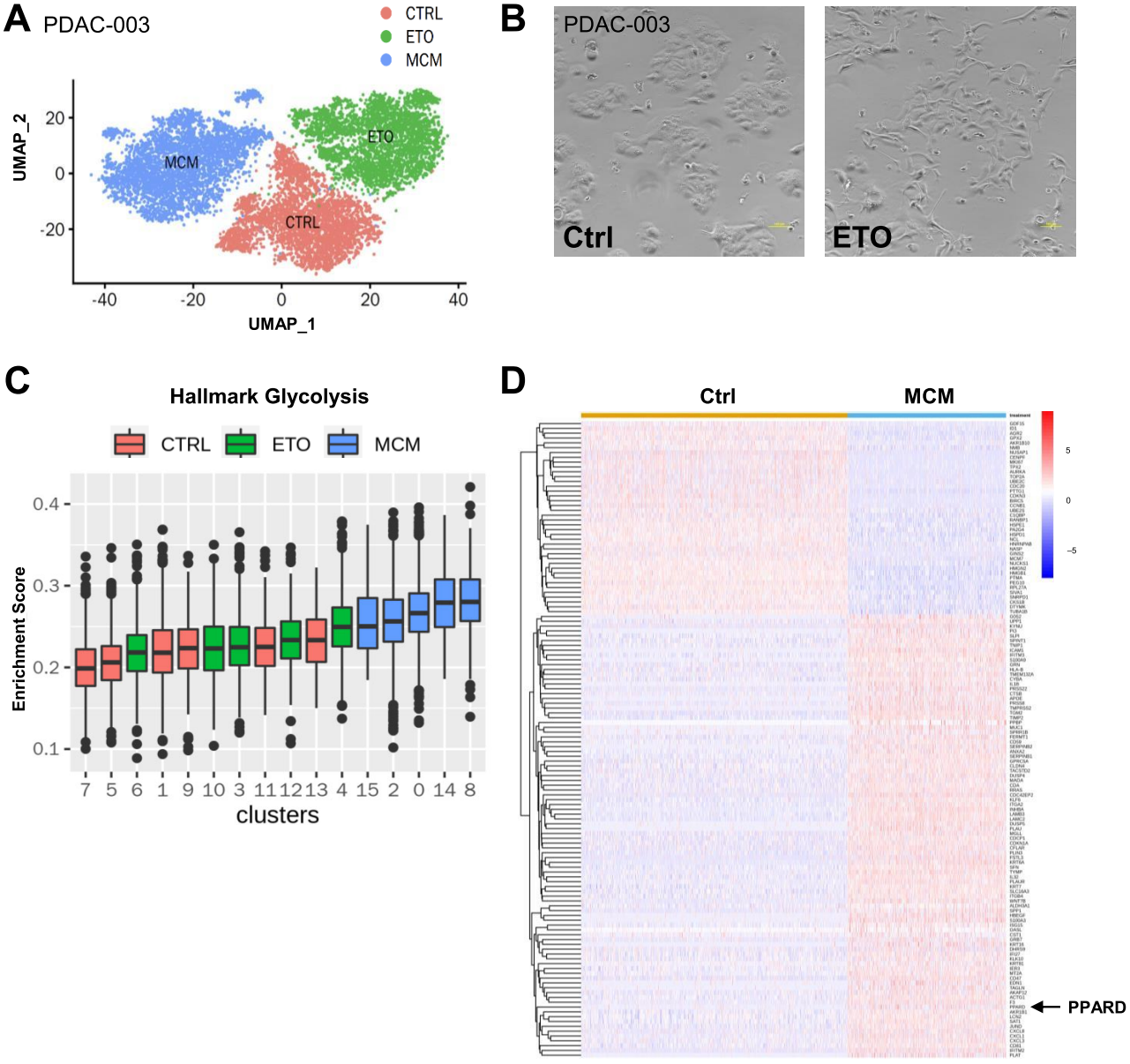

Figure S2, related to Figure 2

E

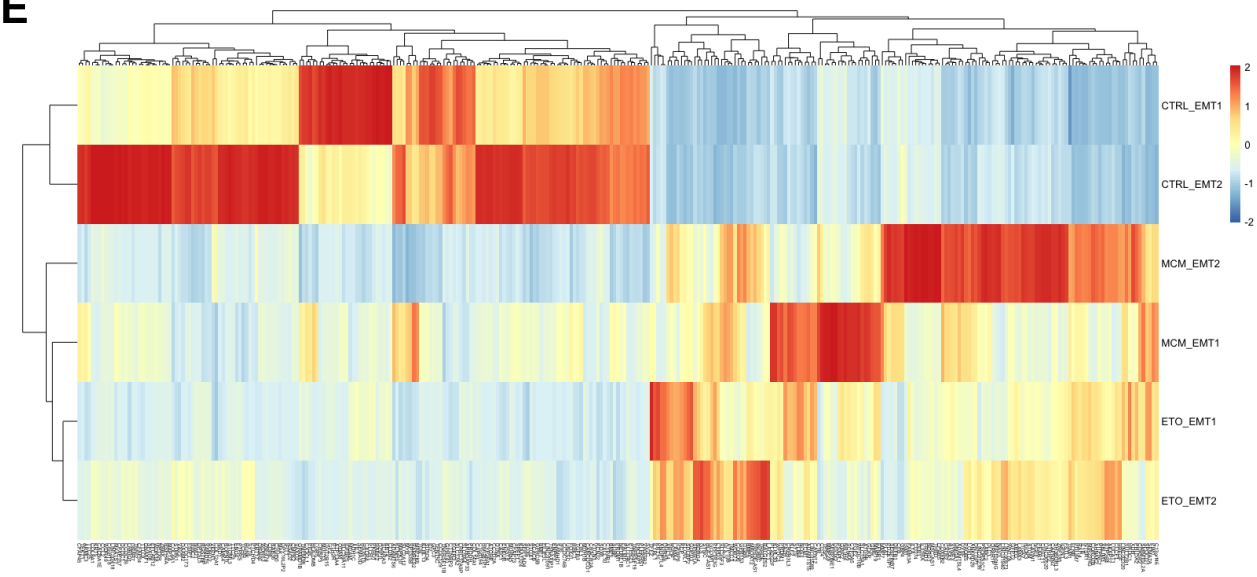

F

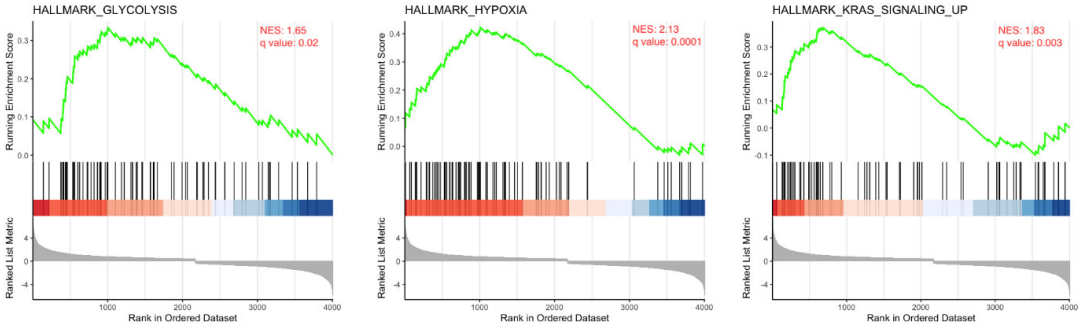

Figure S3, related to Figure 4

Activation of PPARD induces EMT and metastasis. (**A**) Gene (24 & 48h; left panel) and protein (48h; right panel) expression for the PPAR family members following treatment with macrophage-conditioned medium (MCM), Etomoxir (Eto), or the PPAR-δ agonist GW0742 (5 μM). (**B**) Representative gene expression kinetics of the indicated genes after treatment with MCM (left) of Etomoxir (right) in PDAC-215 cells. (**C**) Induction of PPAR targets after 24h of treatment with MCM, Etomoxir or the PPARD agonist GW0742 (10μM). (**D**) Preferential induction of PPARD after 72h of treatment with the PPARD agonists GW0742, GW501516, and L-165 (each 10μM). Pooled data from PDAC-A6L, 185, 215, 253, and 354 cells.

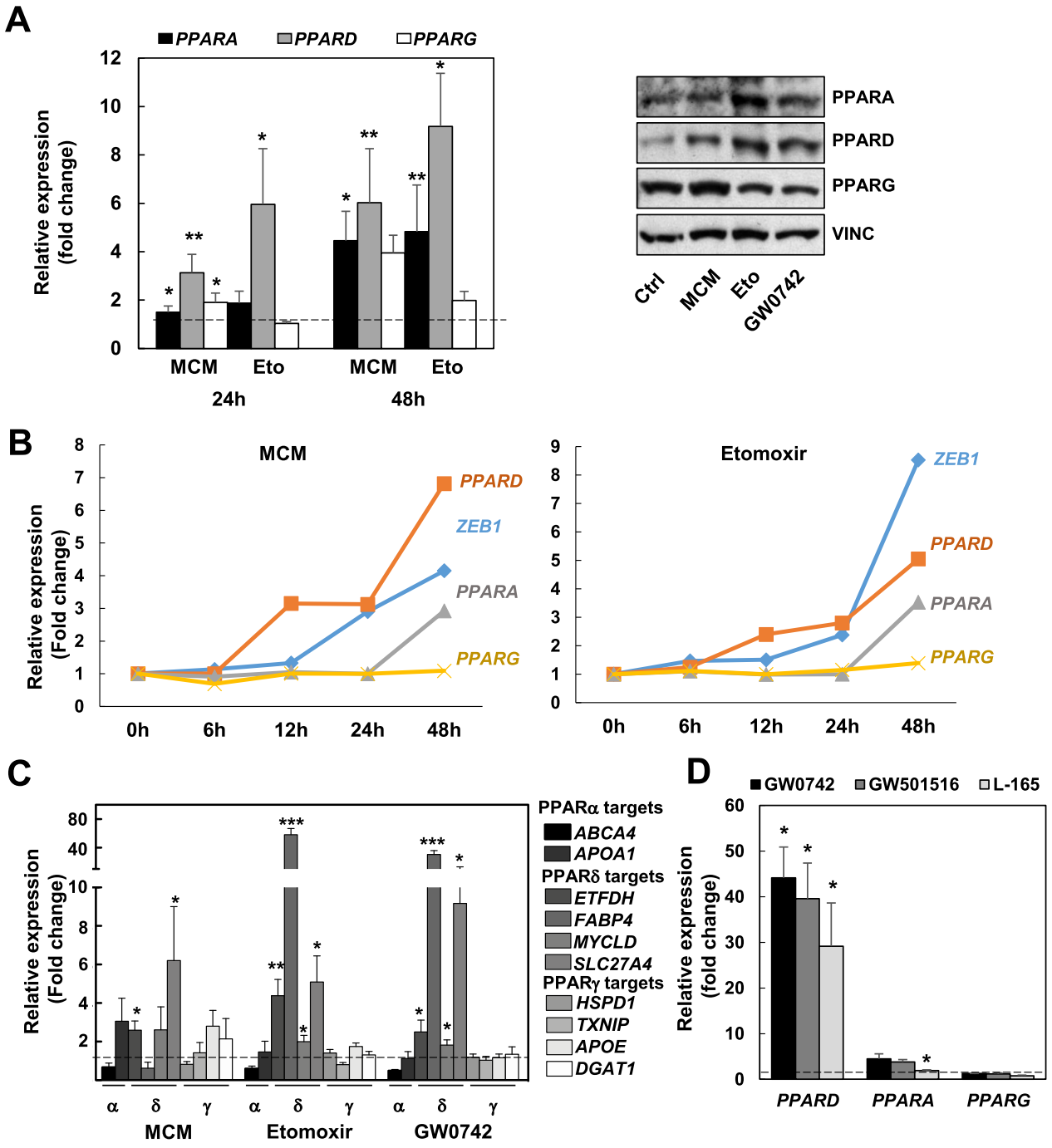

Figure S4, related to Figure 4

PPAR-δ controls the EMT program induced by microenvironmental and nutrient-sensing signals. (**A**) Changes in *PPARD* and EMT-associated genes after 72h of treatment with the indicated concentrations of the PPAR-δ agonists GW0742, GW501516, and L-165. Pooled data from PDAC-A6L, 185, 215, 253, and 354 cells. (**B**) Lack of changes in gene expression (left panel, pooled data for PDAC-215, 253, and 354) and morphology (right panel, PDAC-354 cells) treated with WY14643 (PPAR-α agonist), Rosiglitazone (PPAR-γ agonist), and GW0742 (PPAR-δ agonist) (each 10μM). (**C, D**) PDAC-253, 215, and 354 cells transduced with inducible lentiviral vectors expressing either a non-targeting shRNA (NT) or three different shRNA against PPARD (sh#1, sh#2, sh#3). Cells were pre-treated with doxycycline for 24 hours to induce shRNA expression and subsequently incubated with macrophage-conditioned medium (MCM), Etomoxir (Eto) or the PPAR-δ agonist L-165. Changes in expression of *PPARD* (**C**) and EMT-related genes (**D**) for PDAC-253 (upper panel), 215 (middle panel) and 354 (lower panel) cells. Data are represented as mean ± SEM. # p<0.05, ## p<0.01, ### p<0.001 vs respective NT control.

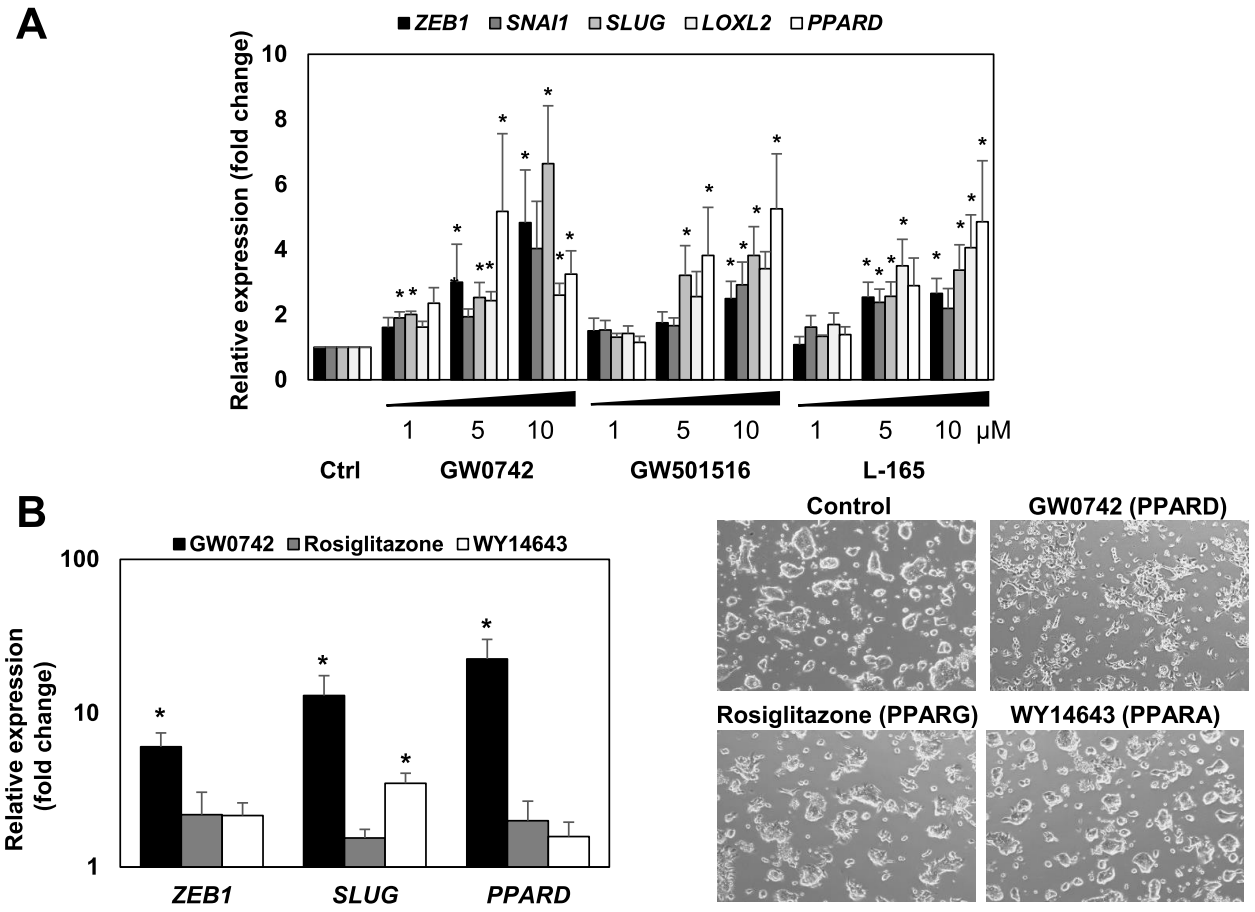

Figure S4, related to Figure 4

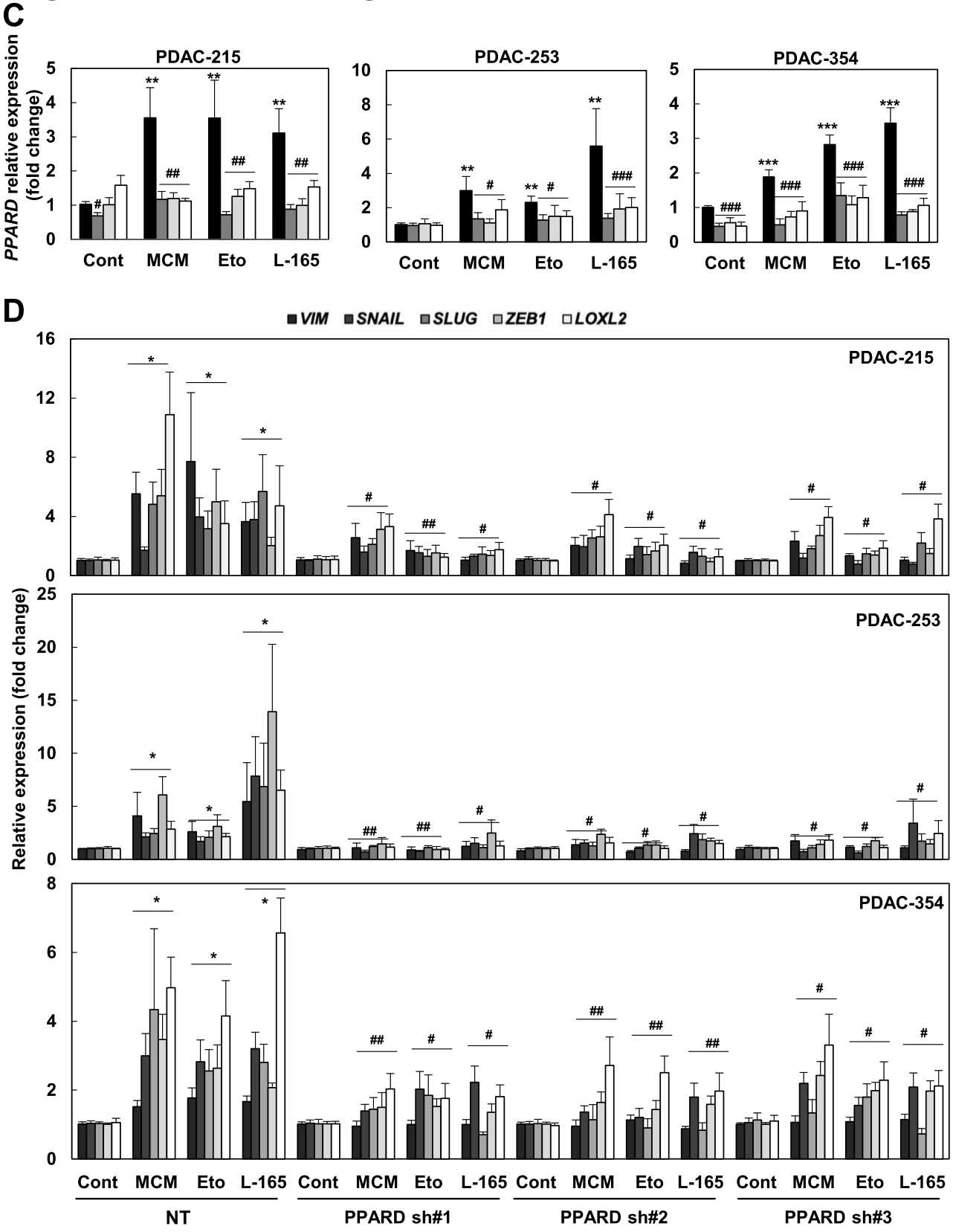

Figure S5, related to Figure 5

EMT induced by microenvironmental and nutrient-sensing signals relates to common metabolic changes. **(A)** OCR and (**B**) ATP-linked OCR for PDAC spheres cultured alone (alone), together with M2 macrophages (+MO) or with PSC (+PSC). Pooled data for sphere-derived PDAC-253 and 354 cells. (**C**) Maximal and ATP-linked respiration in non-CSC or CSC alone or co-cultured with MO. Pooled data from PDAC-253 and 354 cells. (**D**) Cells incubated for 48h with macrophage-conditioned medium (MCM) or 20mM Etomoxir (Eto). Representative FACS for NBDG uptake in PDAC-253 cells, (**E**) Lactate concentration in supernatants, (**F**) ^{13}C-Lactate and ^{13}C-Alanine in supernatants as measured by GCMS after incubation with ^{13}C-Glucose for 12h. All data are represented as mean ± SEM. * p<0.05, ** p<0.01, *** p<0.001.

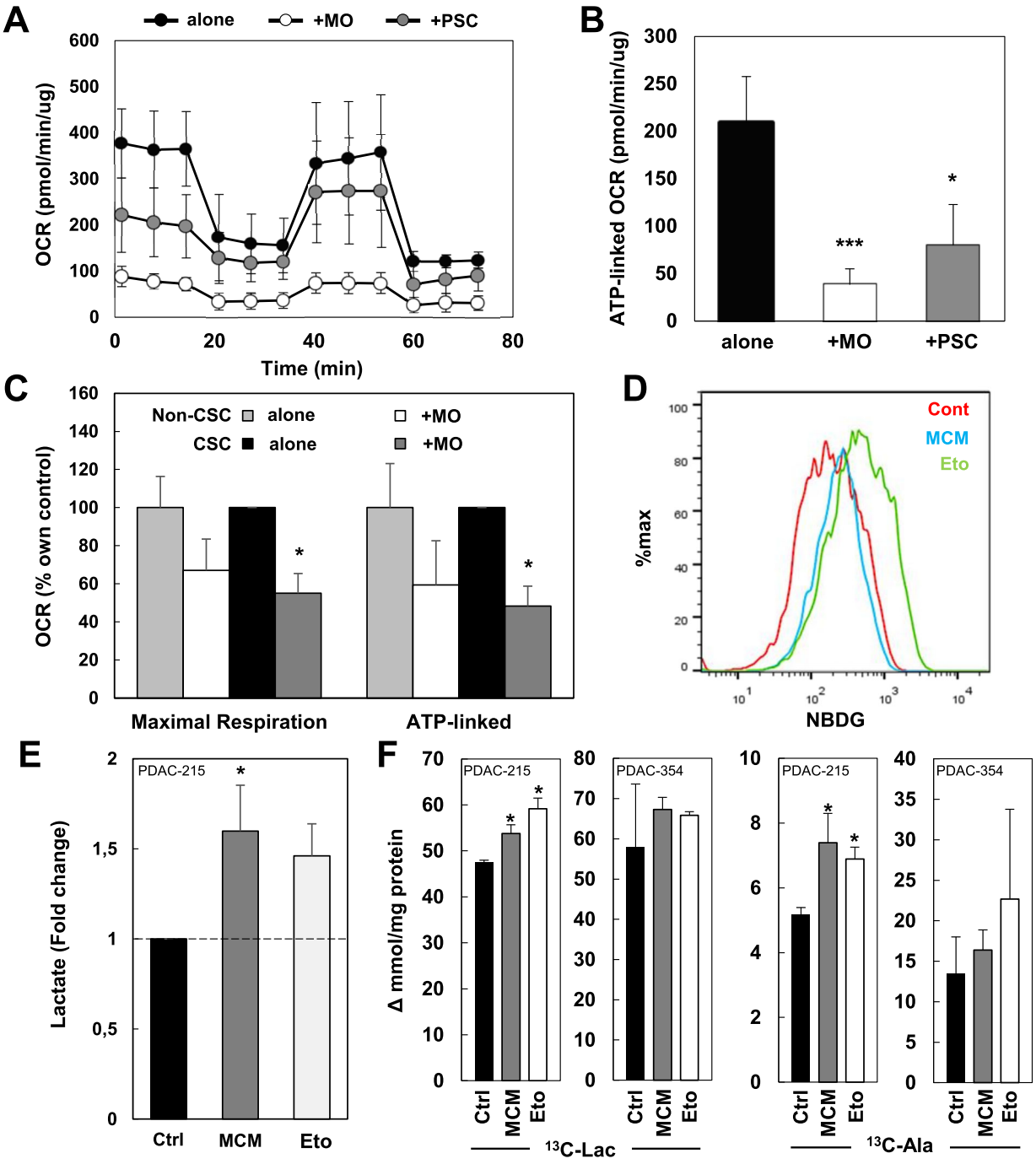

Figure S6, related to Figure 7

***PPARD* controls cellular metabolism via *MYC/PGC1A* ratio to promote EMT and metastasis**. Where indicated, cells were treated with macrophage-conditioned medium (MCM) or Etomoxir 20 μM (Eto) for 48h. Cells transduced with lentiviral constructs were pretreated with doxycycline for 48h before treatments. (**A**) MYC overexpression promotes EMT-like phenotype**.** Left panel: representative images of parental and MYC-overexpressing PDAC-215 cells (MYC OE). Right panel: *MYC*, *VIM*, and *ZEB1* expression. (**B**) Expression of *MYC*, *PGC1A* and *MYC/PGC1A* ratio in PDAC-253 (**left**) and PDAC-215 (**right**) after mitochondrial energy deprivation during 48-72h. (**C**) PDAC-253, 215, and 354 cells transduced with a non-targeting shRNA (NT) or three different shRNA against PPARD (sh#1, sh#2, sh#3) were incubated with MCM or Eto or the PPARD agonist L-165 to determine *MYC*/*PGC1A* expression. (**D**) Patients from the TCGA dataset were dichotomized for the tumor expression levels for *MYC*, *PGC1A* and *MYC/PGC1A* ratio. Kaplan Meier survival curves for disease-free survival are shown. (**E**) EMT-related gene expression of cells that had transmigrated towards 20% FBS for 16h versus gene expression of non-transmigrated cells. Pooled data from PDAC-253, 10953, and 354 (n=2 for each cell type). (**F**) *MYC*, *PGC1A* and *MYC/PGC1A* ratio comparing six local disease PDX (A6L, 185, 215, 253, 354, 10953) vs 5 metastatic PDX (SiC-002, 004, 006, 021, and 023). (**G, H**) Single GFP+ PDAC-354 cells sorted from the blood (CTC) and pancreas (primary) of mice bearing orthotopic tumors were analyzed for the expression of *MYC* and *PGC1A* (**G**) or stratified into CSC versus non-CSC based on their expression of pluripotency-related genes (*NANOG*, *KLF4*, *SOX2*, *OCT4*) (**H**). (**I**) *MYC*, *PGC1A* and *MYC/PGC1A* in primary tumors and liver metastasis from mice bearing orthotopic tumors. (**J**) *In vivo* metabolomics data after ^{13}C-Glucose injection comparing primary tumors with liver metastases. (**K**) PDAC-215 and 354 cells transduced a non-targeting shRNA (NT) or two different shRNAs against MYC (sh#1, sh#2) were incubated with MCM or Eto to measure *MYC* (**left**) and *PGC1A* (**right**) expression. (**L**) *VIM* and *ZEB1* expression in PDAC-354 cells treated with MCM (**left**) or Eto (**right**) in the presence or absence of the MYC/MAX interaction inhibitor Mycro3 (25μM). (**M**) PDAC-354 cells transduced with an inducible construct for PGC-1α overexpression were incubated with MCM or Eto to test maximal respiration (**left**) or invasion (**right**). All data are represented as mean ± SEM. * p<0.05, ** p<0.01, *** p<0.001 vs NT cells; # p<0.05, ## p<0.01, ### p<0.001 vs control or single treatment.

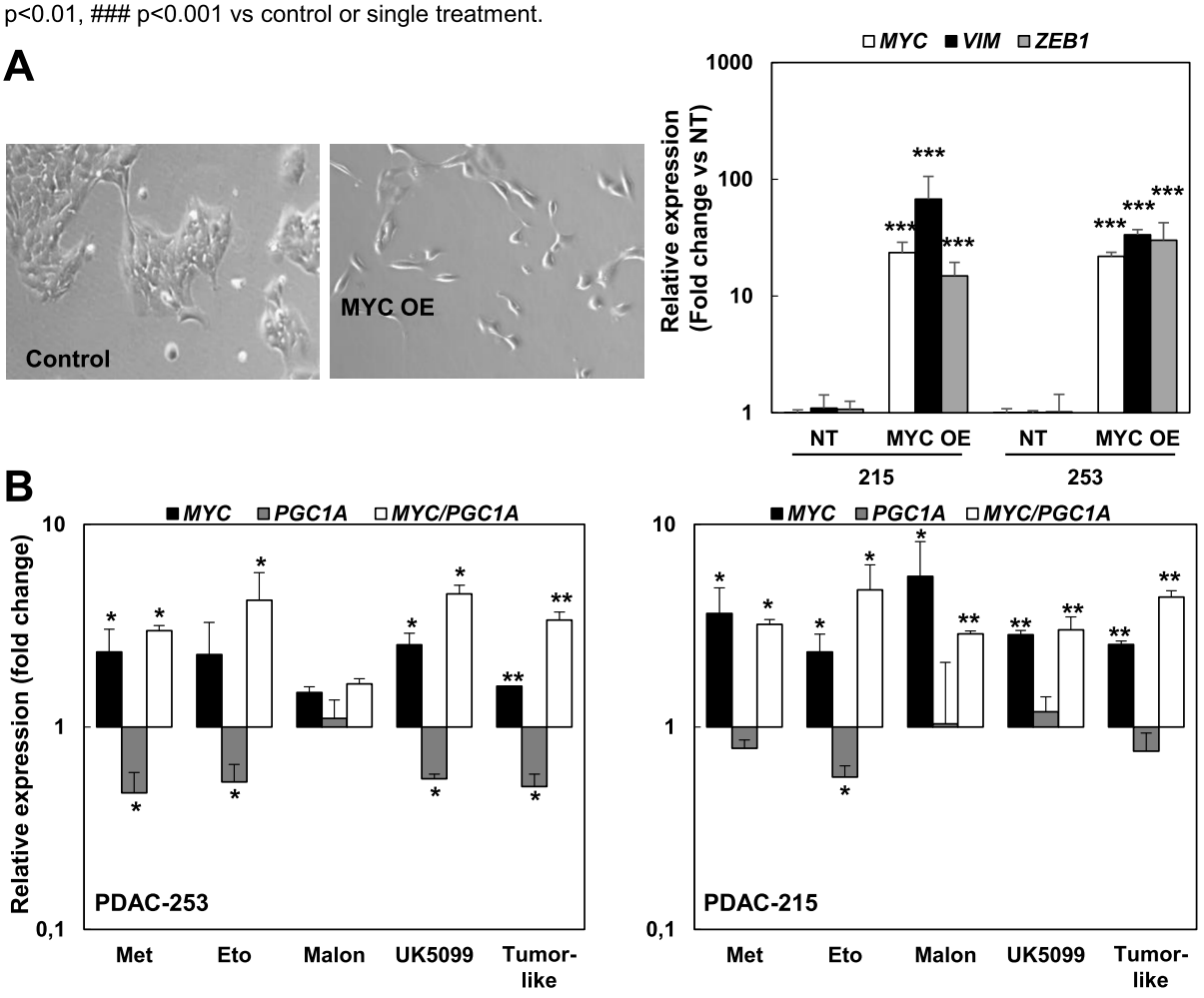

Figure S6, related to Figure 7

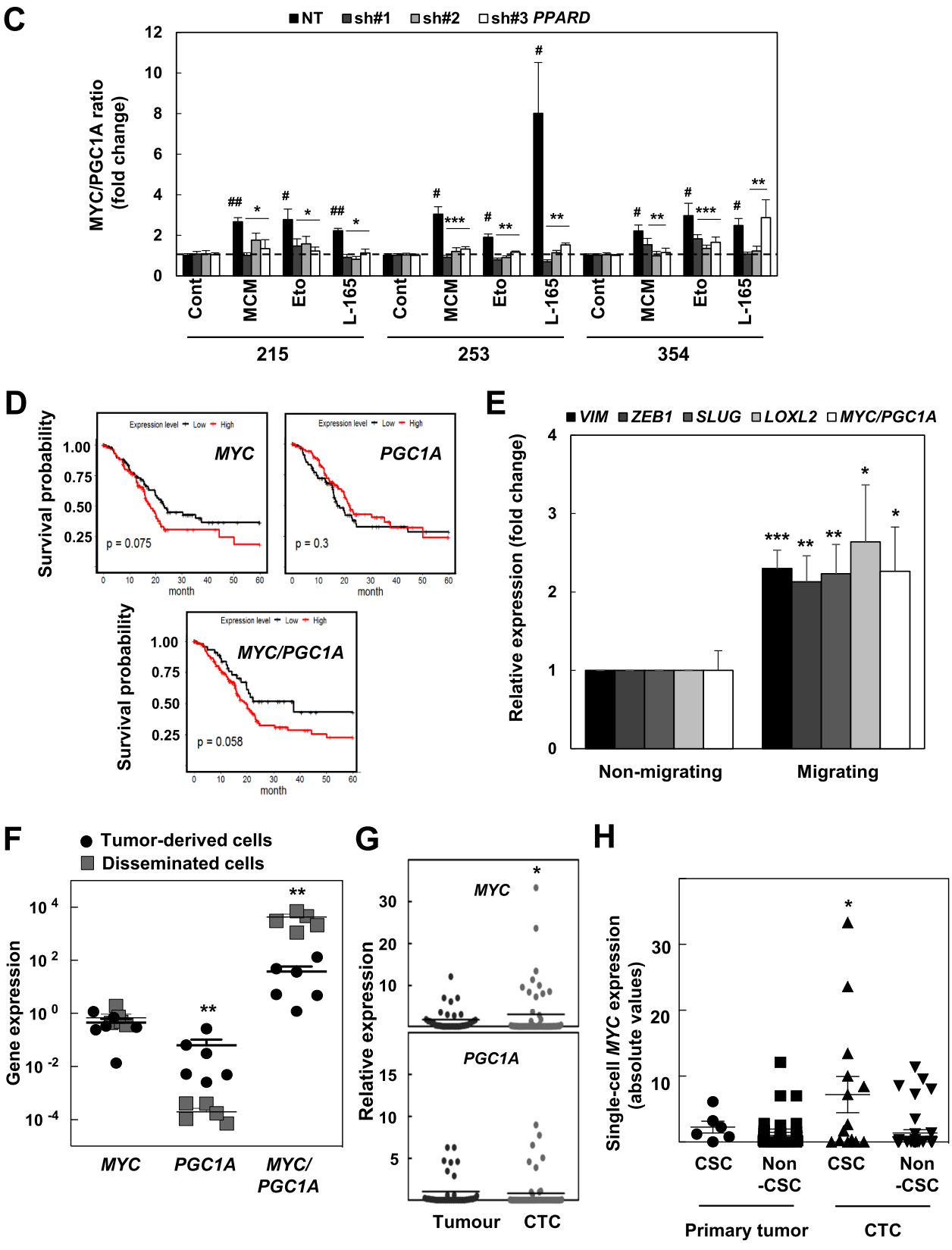

Figure S6, related to Figure 7

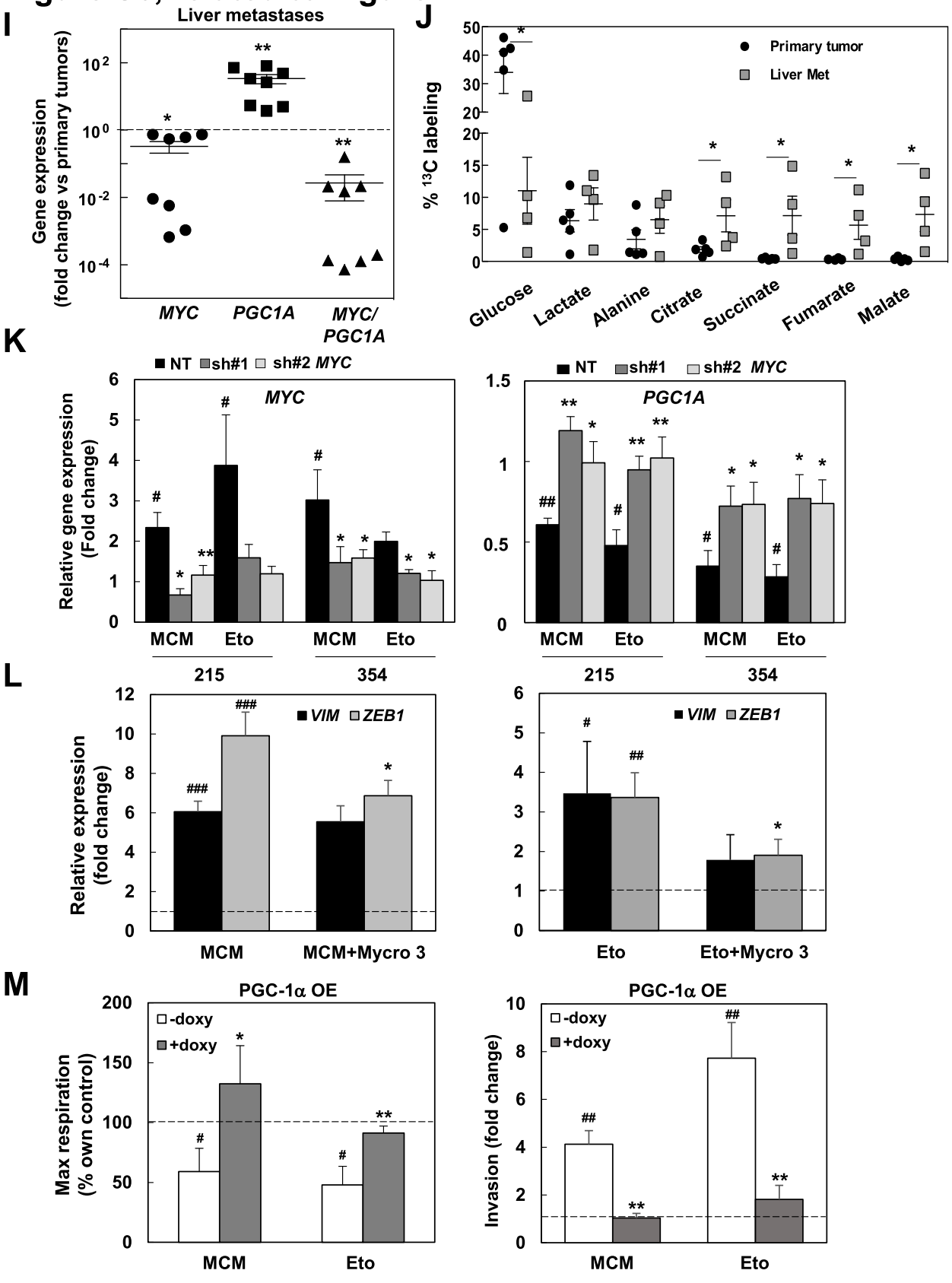

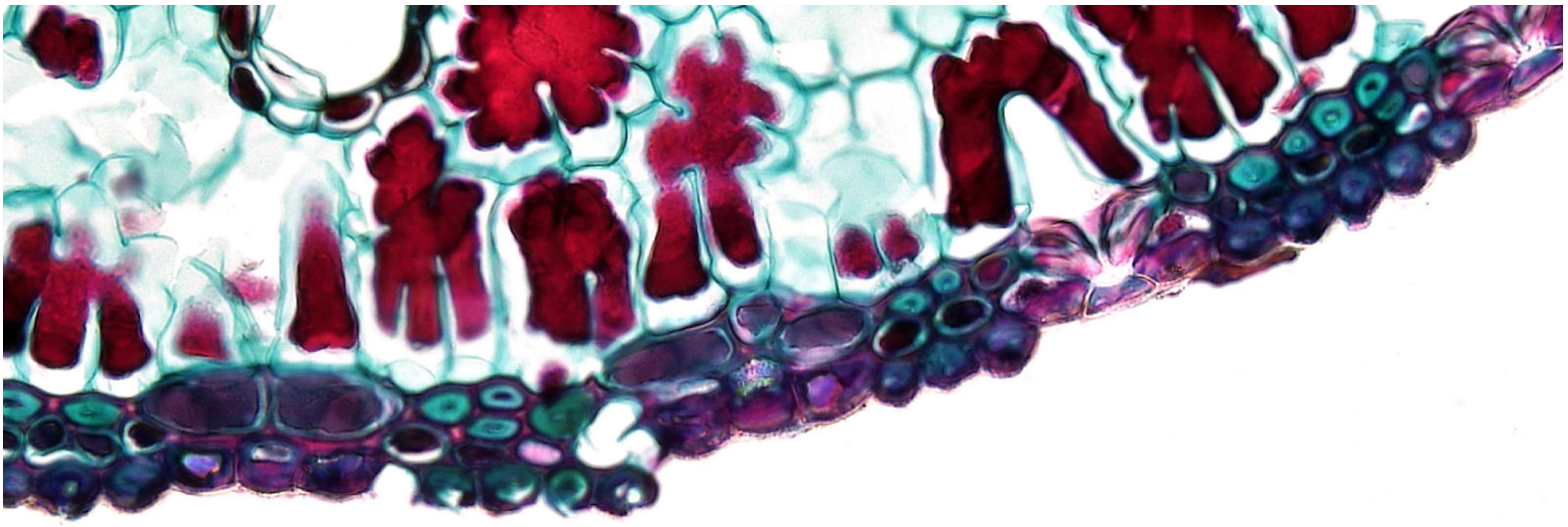

ANNEX II

Biomedicine & Pharmacotherapy 158 (2023) 114162

Contents lists available at ScienceDirect

Biomedicine & Pharmacotherapy

journal homepage: www.elsevier.com/locate/biopha

Pharmacological targeting of the receptor ALK inhibits tumorigenicity and overcomes chemoresistance in pancreatic ductal adenocarcinoma

Beatriz Parejo-Alonso [a], Alba Royo-García [a], Pilar Espiau-Romera [a], Sarah Courtois [a], Álvaro Curiel-García [b], Sladjana Zagorac [c], Isabel Villaoslada [a,d], Kenneth P. Olive [b], Christopher Heeschen [e,f], Patricia Sancho [a,*]

[a] Instituto de Investigación Sanitaria Aragón (IIS Aragón), Hospital Universitario Miguel Servet, Zaragoza, Spain
[b] Department of Medicine, Division of Digestive Liver Diseases and Herbert Irving Comprehensive Cancer Center, Columbia University Irving Medical Center, New York, NY, USA
[c] Center for Stem Cells in Cancer & Ageing (Barts Cancer Institute), London, UK
[d] Aragon Institute of Engineering Research, Department of Mechanical Engineering, University of Zaragoza, Zaragoza, Spain
[e] Center for Single-Cell Omics and Key Laboratory of Oncogenes and Related Genes, Shanghai Jiao Tong University School of Medicine, China
[f] Pancreatic Cancer Heterogeneity, Candiolo Cancer Institute - FPO – IRCCS, Candiolo (Torino), Italy

ARTICLE INFO

Keywords:
Pancreatic Ductal Adenocarcinoma
ALK
Receptor Tyrosine Kinases
Cancer Stem Cells
Chemoresistance

ABSTRACT

Pancreatic ductal adenocarcinoma (PDAC) is an extremely aggressive disease characterized by its metastatic potential and chemoresistance. These traits are partially attributable to the highly tumorigenic pancreatic cancer stem cells (PaCSCs). Interestingly, these cells show unique features in order to sustain their identity and functionality, some of them amenable for therapeutic intervention. Screening of phospho-receptor tyrosine kinases revealed that PaCSCs harbored increased activation of anaplastic lymphoma kinase (ALK). We subsequently demonstrated that oncogenic ALK signaling contributes to tumorigenicity in PDAC patient-derived xenografts (PDXs) by promoting stemness through ligand-dependent activation. Indeed, the ALK ligands midkine (MDK) or pleiotrophin (PTN) increased self-renewal, clonogenicity and CSC frequency in several *in vitro* local and metastatic PDX models. Conversely, treatment with the clinically-approved ALK inhibitors Crizotinib and Ensartinib decreased PaCSC content and functionality *in vitro* and *in vivo,* by inducing cell death. Strikingly, ALK inhibitors sensitized chemoresistant PaCSCs to Gemcitabine, as the most used chemotherapeutic agent for PDAC treatment. Consequently, ALK inhibition delayed tumor relapse after chemotherapy *in vivo* by effectively decreasing the content of PaCSCs. In summary, our results demonstrate that targeting the MDK/PTN-ALK axis with clinically-approved inhibitors impairs *in vivo* tumorigenicity and chemoresistance in PDAC suggesting a new treatment approach to improve the long-term survival of PDAC patients.

1. Introduction

Pancreatic ductal adenocarcinoma (PDAC) is the most common form of pancreatic cancer, with an increasing incidence and an extremely poor five-year overall survival of less than 9 % [1,2]. Despite PDAC low incidence rate compared to other malignancies, its mortality rate continues to rise [3]. Importantly, PDAC aggressiveness mainly relies on two key factors: delayed detection, since symptoms are mild and/or unspecific even at advanced disease stage, and its intrinsic resistance to current treatment regimens [1]. Regarding the latter, PDAC is a considerably heterogeneous disease organized hierarchically, with mounting evidence of a small but unique subpopulation of cancer cells with self-renewal capacity and tumor-initiating properties. These pancreatic cancer stem cells (PaCSCs) are capable of symmetrical and

Abbreviations: ALK, anaplastic lymphoma kinase; PDAC, pancreatic ductal adenocarcinoma; PaCSCs, pancreatic cancer stem cells; PDXs, patient-derived xenografts; MDK, midkine; PTN, pleiotrophin; TK, tyrosine kinase; TKi, tyrosine kinase inhibitor; RTK, receptor tyrosine kinase; CTC, circulating tumor cell; Fluo, autofluorescence-sorted cells; GSEA, gene set enrichment analysis; *ALK* OE, *ALK* overexpression; TCGA, The Cancer Genome Atlas; GTEx, Genotype-Tissue Expression; EMT, epithelial-to-mesenchymal transition; scRNAseq, single-cell RNA sequencing; ELDA, extreme limiting dilution assay; nRTKs, non-receptor tyrosine kinases; NSCLC, non-small-cell lung cancer; FDA, Food and Drug Administration.

* Correspondence to: IIS Aragón, Hospital Universitario Miguel Servet, Zaragoza, Spain.
E-mail address: psancho@iisaragon.es (P. Sancho).

https://doi.org/10.1016/j.biopha.2022.114162
Received 3 November 2022; Received in revised form 14 December 2022; Accepted 21 December 2022
Available online 24 December 2022

asymmetrical divisions [4], the former giving rise to identical CSCs to perpetuate its lineage, and the latter to differentiated progenies that form the bulk of the tumor [4,5]. As such, PaCSCs have the capacity to initiate and sustain tumor growth, in addition to promoting recurrence after treatment due to their intrinsic chemoresistance [6]. Therefore, new treatment strategies for pancreatic cancer are urgently needed.

One of the most explored avenues to design new treatment strategies is the inhibition of tyrosine kinases (TKs), which are hyperactivated in many cancer types and control basic functions such as cell differentiation, proliferation and metabolism [7,8]. Notably, several TK inhibitors (TKi) are currently under evaluation in clinical trials for PDAC, including Erlotinib (EGFR inhibitor, phase III) or Masitinib (c-kit/PDGFR inhibitor, phase III) [9]. Interestingly, several receptor TKs (RTKs) have been shown to promote stemness in different tumor types, such as EGFR in breast cancer [10,11], FGFR in prostate cancer [12], EphR in brain tumors [13,14], melanoma [15] and lung cancer [16], as well as the non-receptor TK (nRTK) SRC in pancreatic cancer [17]. Hence, RTKs may also be potential candidates for targeting PaCSCs and thereby improve patient long-term survival.

Here, we show now that the RTK anaplastic lymphoma kinase (ALK) and its downstream signaling pathways are overactivated in PaCSCs-enriched conditions. Mechanistically, we demonstrate that ALK can be exogenously activated by midkine (MDK) and promotes essential stemness functions such as self-renewal and tumorigenicity. Crucially, we found that pathway blockade with clinically-approved ALK inhibitors rescue Gemcitabine resistance in PDAC, thereby providing a new perspective for a more effective treatment regimen against this deadly disease.

2. Methods

2.1. Cell culture

Patient-Derived Xenografts (PDXs) and Circulating Tumor Cells (CTCs): PDX185, PDX215, PDX253 and PDX354 were obtained through the Biobank of the Spanish National Cancer Research Center (CNIO, Madrid, Spain; CNIO20–027). Tumor pieces underwent several amplification passages in mice prior to establishing primary cultures. Tumor dissociation and establishment of *in vitro* primary cultures was performed as previously described [18]. The metastatic model CTCA was established from circulating tumor cells and obtained through the Barts Pancreas Tissue Bank of the Barts Cancer Institute (https://www.bartspancreastissuebank.org.uk/; BCI, London, United Kingdom; 2019/02/IISA/PS/E/Cell-cultures). Cells were submitted to a maximum of 15 passages in complete RPMI 1640 GlutaMAX™ medium supplemented with 10 % FBS and 50 U/mL penicillin/streptomycin (all from Gibco, Life Technologies, Carlsbad, CA, USA). For experiments, the medium was changed to DMEM/F-12 GlutaMAX™ supplemented with 2 % B27 (Gibco), 50 U/mL penicillin/streptomycin, and 20 ng/mL FGF-basic (Pan-Biotech, Aidenbach, Germany). All PDXs were grown in a humidified incubator at 37º C with 5 % CO_2 and regularly tested for mycoplasma at the Technical and Scientific Services Unit from the Health Sciences Institute of Aragón (IACS).

Cell Lines: AsPC1, BxPC3, MiaPaCa2, Panc1 and Su8686 were purchased from the American Type Culture Collection (ATCC, Manassas, VA, USA). Cells were submitted to a maximum of 30 passages in the same conditions as the primary cultures described above.

Spheroids: Cells were cultured in anchorage-independent conditions at 10^5 cells/mL with complete DMEM/F-12 GlutaMAX™ medium. First generation spheroids were grown up to seven days, dissociated with trypsin (Corning, Oneonta, NY, USA) and regrown at 10^5 cells/mL for five more days. Flasks were coated with 10 % poly(2-hydroxyethyl methacrylate) (Sigma-Aldrich, Saint Louis, MO, USA) in 96 % ethanol and left at 37 ºC until all the liquid was evaporated. Flasks were rinsed once with 1X PBS prior to their utilization.

2.2. In vitro Treatments

ALK inhibitors: Crizotinib and Ensartinib were purchased from Selleckchem (Munich, Germany) and dissolved in DMSO (Sigma-Aldrich) following the manufacturer's instructions. Cells were treated for 24–72 h at concentrations ranging 0.5–10 μM, with DMSO compensation when needed.

Chemotherapy: Gemcitabine 0.9 % sodium chloride (Eli Lilly and Company, IN, USA) was used at concentrations ranging from 1 to 750 nM for 24–72 h.

2.3. Flow cytometry

Apoptosis: Cell pellets were rinsed once with 1X PBS and incubated on ice for 15 min in 2 % FBS-0.5 % BSA-1X PBS blocking solution. PE-conjugated CD133 antibody or the corresponding control immunoglobulin G1 were added at 1:400 in blocking solution. Cells were stained on ice for 30 min and protected from light. Then, the antibody or IgG1 excess was rinsed and pellets were resuspended in APC-conjugated Annexin V at 1:20 in Annexin V buffer solution plus Zombie Violet dye at 1:400 (all antibodies and probes are from Biolegend, San Diego, CA, USA). Samples were transferred into FACS tubes and incubated for 20 min at room temperature protected from light prior to their analysis by FACS Canto II (BD, Franklin Lakes, NJ, USA). Flowing 2 software (Turku Bioscience Centre, Turku, Finland) was used for data analysis.

Fluorescence Activated Cell Sorting (FACS): Cells were blocked and stained for CD133 as described above. For autofluorescence sorting, a previously described protocol was followed [19]. After staining, pellets were resuspended in Zombie Violet dye at 1:400 in 1X PBS and incubated for 20 min at room temperature protected from light. Viable cells corresponding to CD133 or autofluorescence negative and positive populations were sorted using the SH800S Cell Sorter (Sony Biotechnology, San José, CA, USA) and collected into 5 mL tubes containing complete RPMI medium. Pellets were stored at −80 ºC for further processing.

2.4. Proteome profiler™ array

Cells were sorted by autofluorescence and CD133 expression using the SH800S Cell Sorter as described above and pellets were lysed according to manufacturer's instructions. The samples were further processed following the Human Phospho-Receptor Tyrosine Kinase Kit (R&D Systems Europe, Ltd., Abingdon OX14 3NB, UK) manufacturer's instructions. Pierce™ ECL Western Blotting Substrate was used to detect protein-antibody complexes prior to visualization on CL-X Posure™ films (both from ThermoFisher Scientific, Waltham, MA, USA). The resulting dots were analyzed using ImageJ software (National Institutes of Health, Bethesda, MD, USA).

2.5. Western blot

Cell pellets were lysed in RIPA buffer (Sigma-Aldrich) plus protease and phosphatase inhibitors (both from Alfa Aesar, ThermoFisher Scientific). After extraction, proteins were quantified using the Pierce™ BCA Protein Assay Kit (ThermoFisher Scientific). Proteins were separated in Novex™ WedgeWell™ 10 % Tris-Glycine precast gels using BenchMark™ pre-stained protein ladder (both from Invitrogen, Carlsbad, CA, USA) and transferred into PVDF membranes (ThermoFisher Scientific). Membranes were blocked in 5 % BSA-1X PBS-0.1 % Tween 20 (ThermoFisher Scientific) for 1 h at room temperature and incubated overnight at 4º C with the following primary antibodies: ALK (1:1000), p-ALK (T1604, 1:1000), ERK 1/2 (1:3000) (all from Cell Signaling Technology, Danvers, MA, USA), p-ERK 1/2 (T202-Y204, 1:3000, Abgent, San Diego, CA, USA), and β-actin as loading control (clone AC-74, 1:10000, Sigma-Aldrich). After several washes with 1X PBS-0.5 % Tween 20, membranes were incubated with peroxidase-conjugated goat

anti-rabbit (1:5000) or goat anti-mouse (1:50000) (both from Invitrogen). Pierce™ ECL Western Blotting Substrate was used to detect protein-antibody complexes prior to visualization on CL-X Posure™ films. Band intensities were analyzed using ImageJ software. Likewise, protein from sorted CD133 and autofluorescence cells extracted for the RTK array were separated, transferred and visualized as described for normal Western Blot.

2.6. Real time quantitative polymerase chain reaction (RTqPCR)

Cell pellets were homogenized in TRIzol reagent (Invitrogen) and RNA was extracted according to manufacturer's instructions and quantified using Nanodrop™ 2000 (ThermoFisher Scientific). 1 μg of RNA was retrotranscribed into cDNA using Maxima H minus cDNA synthesis Master Mix with dsDNase kit (ThermoFisher Scientific). RTqPCR was performed using PowerUp™ SYBR Green Master Mix (Applied Biosystems, ThermoFisher Scientific) according to manufacturer's instructions. The primers used are listed below. *HPRT* was used as endogenous housekeeping gene. Table 1.

2.7. Bioinformatic analyses

Expression data from human PDAC tissue and normal pancreatic tissue were analyzed using the webserver GEPIA2 (TCGA and the GTEx project databases; http://gepia2.cancer-pku.cn/) [20]. The Pearson correlation coefficient was calculated to study the association of the individual genes corresponding to ALK ligands with a stemness signature defined by the combined expression of the pluripotency-related genes *KLF4*, *OCT3/4*, *NANOG* and *SOX2*. A publicly available human single-cell RNA sequencing (scRNAseq) dataset [21] was used to investigate the expression of *ALK*, *MDK* and *PTN* genes. Raw counts were obtained from the Genome Sequence Archive (#CRA001160). Raw counts from tumor samples were filtered excluding low-quality cells and normalized using CPM (counts per million). Transform function was used to obtain the final gene expression matrix. Cell types identified in the reference papers were also used to calculate and plot the expression and percentage of cells in each group for *ALK*, *MDK* and *PTN* genes using ggplot2 package. All analyses were performed using R v.4.2.1 (University of Auckland, Auckland, New Zealand). The PDAC samples of the TCGA dataset were classified into high and low *ALK* expression and compared in gene set enrichment analyses (GSEA). The GSEA module of the GenePattern suite from the Broad Institute was used with 1000 permutations and FDR < 25 % was considered statistically significant. The signatures for stemness and *ALK* overexpression (OE) were previously described in Ai et al. [22] and Mazzeschi et al. [23], respectively. *ALK* mutational status was assessed using the webserver cBioPortal (Pancreas UTSW, Pancreas TCGA PanCan 2018, Pancreas TCGA, Pancreas ICGC and Pancreas QCMG 2016 project datasets; https://www.cbioportal.org) [24].

2.8. Enzyme-linked immunosorbent assay (ELISA)

MDK levels in supernatants from cell cultures and fresh tumor pieces, as well as plasma from mice bearing orthotopic tumors were determined using the MDK DuoSet ELISA kit (R&D systems, Minneapolis, MN, USA) as per manufacturer's instructions. For MDK determination in tumor pieces, freshly extracted subcutaneous or orthotopic tumors were minced, and pieces of around 1 mm^3 were incubated for 24 h in 1 mL of complete DMEM/F12 medium.

2.9. Sphere formation assay (SFA)

10^4 cells were seeded in triplicate in complete DMEM/F-12 medium using polyhema-coated 24-well plates in the presence of different treatments. When indicated, cells were pre-treated in adherence for 48 h in complete DMEM/F-12 medium prior to being seeded without treatments in anchorage-independent conditions as described above. In both cases, the spheroids were counted after seven days using an inverted microscope at 20X magnification.

2.10. Colony formation assay (CFA)

Cells were seeded in complete RPMI medium in 6-well plates at a density of 500 or 1000 cells/well. After 24 h, treatments were added in complete DMEM/F-12 medium. Medium and treatments were changed every seven days. After 21 days, colonies were stained with crystal violet dye (Acros Organics, ThermoFisher Scientific). Colonies were then counted manually, dissolved in 1 % sodium dodecyl sulfate (SDS, ThermoFisher Scientific) and the absorbance at 590 nm was read using the plate reader Synergy HT (BioTek Instruments, Santa Clara, CA, USA).

2.11. Extreme limiting dilution assay (ELDA)

In vitro ELDA: 10^3 cells per condition were mixed with DMEM/F-12 medium plus treatments and serial dilutions were then seeded in sextuplicate in polyhema-coated 96-well plates. After seven days, the presence or absence of, at least, one spheroid was assessed using an inverted microscope. Further analysis was done by the Walter+Eliza Hall Bioinformatics online tool for ELDA analysis (http://bioinf.wehi.edu.au/software/elda/) [25].

In vivo ELDA (Tumorigenicity Assay): Cells were pre-treated *in vitro* for 48 h. Two cell densities (10^4 and 10^3) diluted in 50:50 complete DMEM/F-12 medium:Matrigel™ (Corning) were subcutaneously injected into both the top and bottom flanks of six weeks-old $Foxn1^{nu}$ nude mice of both sexes (n = 4 mice per group, n = 8 injections per group). Tumor size was monitored once a week using a caliper and volumes were calculated using the formula (length*$width^2$)/2. After six weeks, when control mice had reached humane endpoint criteria, mice were euthanized, tumors were collected and pictures were taken. The number of tumors at end point was analyzed using the Walter+Eliza Hall Bioinformatics online tool, considering tumors > 50 mm^3 that were growing for 3 weeks in a row, the rest were excluded from the analysis. Tumors corresponding to the injections with 10^4 cells from PDX354 were dissociated and stained with EpCAM-FITC, CD133-PE and CD44-APC antibodies for FACS analysis as described above.

2.12. Viability assay

Cells were seeded in triplicate in 96-well plates 24 h before

Table 1
List of primers used for the RTqPCR assays.

Gene	Forward primer	Reverse primer
HPRT	TGACCTTGATTTATTTTGCATACC	CGAGCAAGACGTTCAGTCCT
ALK	CGAGCTGTTCAGTTGGTGGA	AGGAGCTATGACCAGTCCCG
MDK	GGTCCCGCGGGTTATACAG	CCGCCCTTCTTCACCTTATCTTT
KLF4	ACCCACACAGGTGAGAAACC	ATGTGTAAGGCGAGGTGGTC
OCT3/4	CTTGCTGCAGAAGTGGGTGGAGGAA	CTGCAGTGTGGGTTTCGGGCA
NANOG	AGAACTCTCCAACATCCTGAACCT	TGCCACCTCTTAGATTTCATTCTCT
SOX2	AGAACCCCAAGATGCACAAC	CGGGGCCGGTATTTATAATC

treatment. At zero and 72 h, medium was discarded and Resazurin (Alfa Aesar) was added to the cells at 10 μM in 1X PBS and incubated for one hour in a humidified incubator at 37ºC with 5 % CO_2. Fluorescence was then read according to manufacturer's instructions by using a Synergy HT plate reader. The IC_{50} was calculated using GraphPad Prism 8.

2.13. MultiTox-fluor multiplex cytotoxicity assay

Cells were seeded in triplicate in 96-well plates 24 h before treatment. At zero and 72 h, assay was performed by incubating with Multitox reagents (Promega, Madison, WI, USA) and fluorescence was then read according to manufacturer's instructions by using a Synergy HT plate reader.

2.14. Proliferation assay

After Resazurin or MultiTox technique, the cells were rinsed once with 1X PBS and incubated for 30 min with crystal violet. The plates were rinsed carefully with tap water and dried for at least 24 h. After dissolution in 1 % SDS, the absorbance at 590 nm was read using a Synergy HT plate reader. The IC_{50} was calculated using GraphPad Prism 8.

2.15. In vivo treatment

Tumor pieces of about 15 mm^3 were soaked in Matrigel™ prior subcutaneous implantation in both flanks of six weeks-old Foxn1^{nu} nude female mice (n = 4 mice per group, n = 8 implants per group) under isofluorane-induced anesthesia. When tumor size was about 300 mm^3, mice were treated with one cycle of chemotherapy as follows: 30 mg/kg Abraxane (i.v.) twice a week plus 70 mg/kg Gemcitabine (i.p) once a week during three weeks and one week of rest. After the chemotherapy cycle, mice were randomized and treated with 25 mg/kg Crizotinib or the corresponding dose of vehicle (hydroxypropyl methyl cellulose, Sigma Aldrich) (oral gavage) twice a day until end point. Tumor size was monitored twice a week using a caliper and volumes were calculated using the formula (length*width^2)/2. After 10.5 weeks, when control tumors had reached humane end point criteria, mice were euthanized, tumors were collected and weighted and pictures were taken. A small piece of the tumors was processed for RNA to assess pluripotency gene expression by RTqPCR as described above. The rest of the tumors was dissociated as previously reported[18] and stained with EpCAM-FITC, CD133-PE and CD44-APC antibodies for FACS analysis as described above.

2.16. Statistical analysis

Data are represented as mean ± SEM of, at least, three independent experiments unless otherwise specified. Data were analyzed using GraphPad Prism 8. Student's *t*-test or Mann-Whitney test were performed for two-group comparisons, while one-way ANalysis Of VAriance (ANOVA) or Kruskal-Wallis tests were performed for multiple group comparisons. Differences were considered significant when $p < 0.05$.

3. Results

3.1. ALK receptor expression and activation are linked to stemness in PDAC patients

In order to identify pharmacologically targetable RTKs specifically activated in stem-like cells, we ran a series of RTK arrays using different CSC-enriching conditions *versus* differentiated cells (autofluorescence, Fig. 1A, top and middle panel; CD133, Fig. 1A, bottom panel). Among the differentially phosphorylated RTKs, the receptor anaplastic lymphoma kinase (ALK) showed the most consistent upregulation in both CSC-enriching conditions across the panel of tested PDXs (Fig. 1A and S1A). ALK receptor was shown to be aberrantly expressed and/or activated in several cancer types [26–29], but its expression had been previously reported to be very low or even absent in PDAC tissues [30]. For this reason, we decided to verify its expression by western blot in a panel of PDAC patient-derived xenografts (PDXs) and established cell lines. Surprisingly, all of them showed considerable ALK expression and phosphorylation (Fig. S1B). We further validated our initial findings by western blot (Fig. 1B), where CSC-enriching conditions such as Fluo$^+$, CD133$^+$ and spheroids (sph) showed further enhanced ALK phosphorylation. Notably, CSC-enriched samples also showed increased ALK mRNA (Fig. S1C) and protein expression (Fig. 1B, C).

As mentioned above, *ALK* expression is low in PDAC tissues and chromosomal translocations are very rare [30–32]. Indeed, although we detected a positive trend, bioinformatic analyses showed no significant differences in *ALK* expression in PDAC patients as compared to healthy pancreatic tissue from The Cancer Genome Atlas (TCGA) and Genotype-Tissue Expression (GTEx) datasets(Fig. S1D) and revealed a low percentage of genetic alterations in this gene (Fig. S1E). Despite its low expression, we were able to classify these PDAC patients into high and low *ALK* expression groups for gene set enrichment analysis (GSEA). Interestingly, while *ALK*^{LOW} patients did not show any enrichment, patients with higher *ALK* expression exhibited significant enrichment of pathways related to CSC properties and functionality such as epithelial-to-mesenchymal transition (EMT) and xenobiotic metabolism (Fig. 1D), as well as a stemness signature previously described in PDAC (Fig. 1E, left panel) [22]. On the other hand, besides pathways related to ALK downstream signaling such as K-Ras or JAK/STAT, *ALK*^{HIGH} samples also showed enrichment of an *ALK* overexpression (OE) gene signature described in breast cancer cells [23] (Fig. 1E, right panel). Interestingly, this *ALK* OE signature was significantly overexpressed in human PDAC samples (Fig. 1F) and correlated with the expression of our validated set of pluripotency genes (*KLF4*, *NANOG*, *OCT3/4* and *SOX2*) [33] (Fig. 1G).

In summary, our results indicate that ALK expression and activation is enhanced in PaCSC-enriched conditions from different PDXs, and its expression is linked to stemness and CSC-related pathways in human PDAC samples.

3.2. Ligand-dependent activation of ALK contributes to PDAC stemness

Several molecules have been proposed as ALK activators, including midkine (MDK), pleiotrophin (PTN), and family with sequence similarity 150 members A (FAM150A) and B (FAM150B)[27,34]. Interestingly, bioinformatic analyses revealed that *MDK* and *PTN*, but not *FAM150A* nor *FAM150B*, were significantly overexpressed in human PDAC samples when compared to normal pancreas (Fig. S2A). Moreover, only *MDK* expression showed a significant positive correlation with both our well-stablished pluripotency gene set and the *ALK* OE signature mentioned above (Fig. S2B). These results obtained in bulk tumor samples were confirmed in a PDAC single-cell transcriptomic dataset[21], where *MDK* showed the strongest positive correlation with three out of the four of the stemness genes separately (*KLF4*=0.37, *OCT3/4*=0.9, *NANOG*=0.78, *SOX2*=0.81) (Fig. 2A). Further analyses of this single-cell dataset revealed that *MDK* was expressed by a wide range of cell types, including ductal, acinar and tumor cells as well as fibroblasts (Fig. 2B), whereas *PTN* was mainly expressed by stromal cells (Fig. 2B). Moreover, these analyses further corroborated the low expression of *ALK* mRNA in PDAC tumors, as it was undetectable at single-cell level in the different PDAC cell populations included in this dataset (Fig. 2B).

Importantly, we confirmed that MDK was secreted by both subcutaneous and orthotopic PDX tumors *ex vivo* (Fig. 2C, left and middle panel, respectively) and *in vivo*, since we detected human MDK in the plasma of mice bearing orthotopic PDXs (Fig. 2C, right panel). Although CSC-enriched samples showed increased levels of *MDK* expression at the

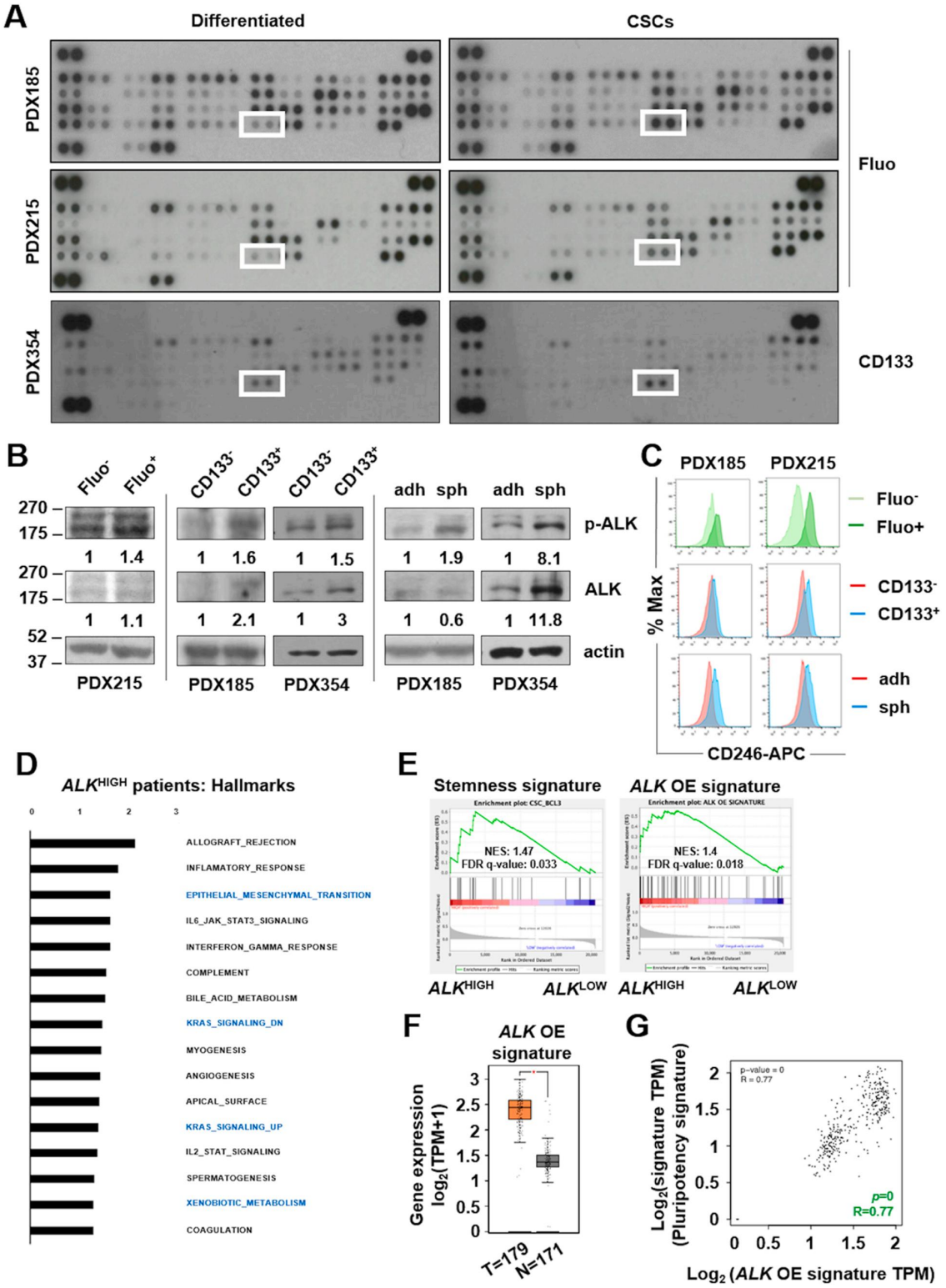

(caption on next page)

Fig. 1. ALK is preferentially activated and overexpressed in PaCSC-enriched conditions. A) Proteome Profiler Human Phospho-RTK Array in cells sorted by autofluorescence (Fluo) and CD133 content as CSC-enriching conditions for the indicated PDXs. Dots corresponding to pALK are indicated with a white square. B) Western blot of cell lysates from different CSC settings (sorted cells by autofluorescence (Fluo) and CD133 content; cells grown in adherent (adh) *versus* anchorage-independent conditions as spheroids (sph)). The numbers represent the quantification of the band intensity of each protein normalized by actin, shown as the fold change of each differentiated cell condition. C) Flow cytometry histograms of CD246 (ALK) expression (percentage of maximal fluorescence) in the CSC-enriching conditions shown in B. D) Gene set enrichment analysis (GSEA) comparing the top 50 % *ALK* expression group (ALK^{HIGH}) with the bottom 50 % expression group in the TCGA data series. NES (normalized enrichment score) values of the Hallmark gene sets meeting the significance criteria: nominal *p*-value of < 0.05, FDR < 25 %. E) Enrichment plot of stemness (left panel) and *ALK* overexpression (OE) (right panel) signatures in ALK^{HIGH} *versus* ALK^{LOW}. F, G) Transcriptomic bioinformatic analyses comparing normal (N) to PDAC (T) human tissues from GTEx and TCGA datasets, respectively (webserver: GEPIA2): F) *ALK* OE signature expression; **G)** Correlation of *ALK* OE signature with a stemness gene signature composed by *KLF4*, *OCT3/4*, *NANOG* and *SOX2*. TPM: transcripts per million.

mRNA level (Fig. 2D), no significant differences were found in terms of MDK secretion (Fig. 2E). Treatment with recombinant human MDK induced ALK phosphorylation in the short term (Fig. 2F, left panel). Later on, phosphorylation was observed in its well-described downstream signaling partner ERK1/2 [35] (Fig. 2F, right panel), corroborating ligand-dependent ALK activation. This activation resulted in improved CSC functionality, as exogenous treatment with MDK enhanced self-renewal (Fig. 2G) and clonogenic capacity (Fig. 2H), and increased CSC frequency *in vitro* (Fig. 2I). Interestingly, similar results were obtained after treatment with PTN (Fig. S2C-E). These results confirm that ligand-dependent activation of the ALK pathway enhances PDAC aggressiveness by boosting CSCs properties.

3.3. ALK inhibition abrogates CSC functionality in vitro and in vivo

The use of small compounds, like Crizotinib or Ensartinib, to inhibit ALK signaling is a common approach to treat ALK^+ malignancies, such as non-small-cell lung cancer (NSCLC) [36]. Considering ALK contribution to stemness in PDAC, we decided to test the effects of these compounds on our PDXs, including a model of metastatic PDAC established from circulating tumor cells (CTCA).

First, both Crizotinib and Ensartinib inhibited cell proliferation, with IC_{50} ranging from 0.7 to 3.8 and 0.4–1.8 μM, respectively (Fig. S3A). Importantly, both compounds inhibited ALK phosphorylation and downstream signaling at the selected concentrations (Fig. 3A). Since ALK inhibition with Crizotinib induced cell toxicity (Fig. S3B), we measured next cell death after treatment with both compounds. Treatment with both Crizotinib and Ensartinib induced apoptosis in the tumor bulk (Fig. S3C, S3D) and, most importantly, in the $CD133^+$ population (Fig. 3B, C), thus decreasing the CD133 content (Fig. 3D, E).

Afterwards, since these findings suggested that ALK inhibition particularly targets $CD133^+$ cells, we assessed the efficacy of these compounds in impairing stemness-related functionality. Indeed, both Crizotinib and Ensartinib diminished self-renewal (Fig. 4A and S4A) and clonogenic capacity (Fig. 4B and S4B). Likewise, pretreatment with both Crizotinib and Ensartinib treatment decreased CSC frequency *in vitro* (Fig. 4C and S4C). These effects on CSC functionality could be validated *in vivo*, where pretreatment with the compounds decreased the number and size of tumors (Fig. 4D and S4D), the percentage of tumorigenicity (Fig. 4E) and the CSC frequency (Fig. 4F). Importantly, even though the percentage of epithelial tumor cells remained unchanged (Fig. S4E), the number of $CD133^+/CD44^*$ cells decreased in the tumors obtained from Crizotinib-pretreated cells (Fig. S4F). These results demonstrate that ALK inhibition targets $CD133^+$ stem-like cells, by inducing cell death and effectively impairing their functionality.

3.4. ALK inhibition prevents chemoresistance in vitro and in vivo

One of the main contributors to chemotherapy failure in PDAC is its intrinsic chemoresistance [37]. Indeed, conventional chemotherapy usually targets just the tumor bulk, thus enriching the content of chemoresistant CSCs and causing tumor relapse. Considering the toxic effect of ALK inhibitors on stem-like $CD133^+$ cells, we decided to test if either Crizotinib or Ensartinib were able to sensitize our cells to Gemcitabine treatment *in vitro*. Interestingly, the combination of Gemcitabine with Crizotinib or Ensartinib at low doses decreased considerably the IC_{50} for this chemotherapeutic agent (Fig. 5A and S5A), resulting in enhanced cell death (Fig. S5B). Certainly, co-treatment with Ensartinib significantly increased cell death in the $CD133^+$ population (Fig. 5B) and decreased CD133 content (Fig. 5C) when compared to Gemcitabine alone. Importantly, both Crizotinib and Ensartinib prevented Gemcitabine-induced self-renewal (Fig. 5D) and clonogenic capacity (Fig. S5C), indicating the effectiveness of this combined treatment.

Considering these results, we decided next to transfer this approach into the *in vivo* setting by treating mice bearing subcutaneous PDAC implants with Crizotinib after a chemotherapy cycle with Gemcitabine and Abraxane, the most commonly used chemotherapy combination to treat PDAC nowadays. We first confirmed that treatment with Crizotinib was not toxic to the animals by showing that their body weight remained essentially unchanged (Fig. S5D). Strikingly, treatment with Crizotinib significantly delayed tumor growth after chemotherapy (Fig. 5E, F). Crizotinib-treated tumors were significantly smaller (Fig. S5E) and lighter (Fig. S5F) than tumors in the control group, and in some cases disappeared completely after treatment (Fig. 5F). Importantly, while no difference was found in the expression of the epithelial marker EpCAM (Fig. S5G), Crizotinib-treated tumors showed decreased content of $CD133^+/CD44^+$ cells (Fig. 5G) and reduced expression of stemness genes (Fig. 5H). These results confirmed our hypothesis that blocking ALK using small molecule inhibitors delays tumor growth after chemotherapy by targeting $CD133^+$ cells in PDAC.

4. Discussion

Despite current efforts to improve treatment outcomes, life expectancy of pancreatic cancer patients remains terribly brief. This is, at least in part, due to the presence of aggressive pancreatic cancer stem cells (PaCSCs) that survive after conventional chemotherapy, eventually regrow the tumor and migrate to colonize secondary organs. For this reason, targeting stem-like cells in combination with conventional therapies may be the only way to ensure long-term survival of pancreatic ductal adenocarcinoma (PDAC) patients.

Previous studies from our group and others have shown that $CD133^+$ PaCSCs bear unique features, essential to maintain their properties and functionality and, in principle, are amenable for therapeutic intervention. Indeed, we have provided proof-of-concept for the efficacy of metabolic inhibition for PaCSCs targeting in animal models [33,38–40], but further clinical translation has remained challenging due to lack of clinically effective compounds. In contrast, receptor and non-receptor tyrosine kinases (RTKs and nRTKs, respectively) represent a much more approachable strategy since they can be targeted by a plethora of specific and clinical-grade compounds. In addition, RTKs and nRTKs control essential cellular mechanisms dysregulated in cancer, such as metabolism, proliferation, survival and, most importantly, stemness [10,11,13,14]. Several clinical trials in PDAC are currently exploring the potential benefit of diverse TK inhibitors in PDAC [41].

In order to find novel pharmacologically amenable targets hyperactivated in PaCSCs, we decided to focus on RTKs, since their expression in the cellular membrane allows for targeting by both small molecules and blocking antibodies. Screening of RTKs revealed that the receptor anaplastic lymphoma kinase (ALK) was consistently overexpressed and

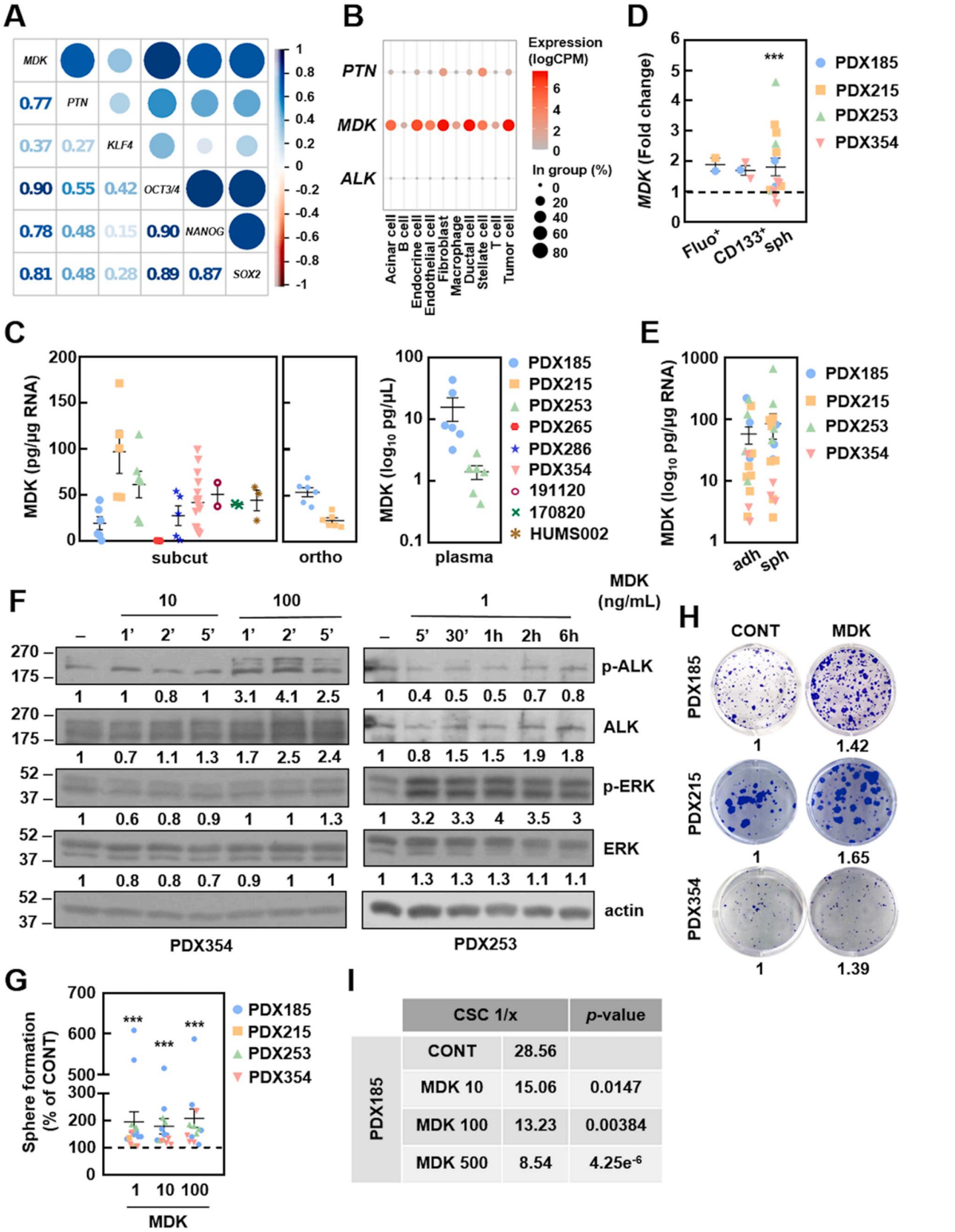

(caption on next page)

Fig. 2. Ligand-dependent ALK activation supports self-renewal in PDAC. A) Correlation matrix of the indicated genes in single tumor cells from the Peng single cell RNA sequencing (scRNAseq) dataset. The numbers and dot sizes indicate the r value of each correlation. The blue color indicates a positive correlation, whereas the red color represents a negative correlation. B) Single-cell expression analysis of the indicated genes in the different cellular populations included in the Peng scRNAseq dataset. The dot size represents the percentage of cells expressing each gene per population, while the color scale denotes the expression level. C) MDK in supernatants from subcutaneous (subcut, left panel) and orthotopic (ortho, middle panel) PDX implants *ex vivo* and in plasma (right panel) from orthotopic tumor-bearing mice by ELISA. D) RTqPCR of *MDK* mRNA levels in the indicated CSC settings: autofluorescence-sorted cells (Fluo), CD133-sorted cells and spheroids (sph). Pooled data showing the individual values for the indicated PDXs. E) MDK detection in supernants from adherent (adh) and spheroid (sph) cultures by ELISA. Pooled data showing the individual values for the indicated PDXs. F) Kinetics of ALK activation by western blot at the indicated times after treatment with 10 or 100 ng/mL of recombinant MDK. Numbers represent the quantification of the band intensity of each protein normalized by actin, shown as fold change from the control group. G) Sphere formation assay after pre-treatment with recombinant MDK for 72 h at the indicated concentrations (ng/mL) in adherent conditions. Pooled data from PDX185 and 354. The dashed lines represent the value of the differentiated cells (D) or control (G) groups. Data are represented as mean ± SEM and analyzed using one-way ANOVA or Kruskal-Wallis tests of, at least, three independent experiments, unless otherwise specified. * $p < 0.05$, * * $p < 0.01$, * ** $p < 0.005$. **H)** Representative colony formation assay after 21 days of treatment with 10 ng/mL of recombinant MDK. The numbers represent the absorbance of crystal violet shown as the fold change from the control group. I) Estimation of the CSC frequency by *in vitro* extreme limiting dilution assay (ELDA) after treatment with the indicated concentrations of recombinant MDK for seven days. The numbers indicate one CSC every x number of cells.

hyperactivated in PaCSCs-enriched conditions, using different CSC enrichment methods and PDAC patient-derived xenograft (PDX) models (Fig. 1A, B, C and S1A, S1C) to account for intrinsic intra- and intertumoral heterogeneity. Although the ALK receptor plays an important physiological role in neural development [26,42], it was first discovered in lymphoma as the fusion protein NPL-ALK following chromosomal rearrangement [43]. Subsequently, ALK was shown to be aberrantly expressed and/or activated in several cancer types [26–29]. ALK receptor activation triggers different intracellular signaling pathways involved in proliferation, survival and metabolism, including JAK/STAT and Ras/ERK [35,44]. Importantly, some studies suggested that ALK acts as a regulator of stemness in several cancers [45–48]. However, our results were certainly unexpected, since this receptor has been overlooked in PDAC. The possible cause points to the lack of mRNA overexpression in tumor bulk cells when compared with normal pancreas or the low level of chromosomal rearrangement of the *ALK* gene in PDAC [30] (Fig. S1D, S1E), which is the main pathogenic mechanism associated to ALK in non-small-cell lung cancer (NSCLC) and brain tumors [26–29]. The low *ALK* expression at the mRNA level detected in bulk transcriptomic analysis of The Cancer Genome Atlas (TCGA) dataset (Fig. S1D) was further evidenced in the single-cell expression analysis (scRNAseq, Fig. 2B), where *ALK* was undetectable in the different populations of the pancreatic niche, including tumor cells. In fact, detection of *ALK* mRNA levels proved challenging even in our primary cultures (Fig. S1C and data not shown). However, we detected considerable ALK expression and phosphorylation in different PDAC PDX models and established cell lines by western blot (Fig. 1B, C and S1B). Our data further reinforces the importance of considering protein post-translational regulation and modifications over purely transcriptomic studies for target discovery screenings.

Nevertheless, further bioinformatic analyses of transcriptomic datasets supported our initial results *in vitro*. Indeed, we were able to link the mRNA expression of both *ALK* and an *ALK* overexpression (OE) signature previously described [23] with pathways related with CSCs in PDAC patients, such as epithelial-to-mesenchymal transition (EMT), drug metabolism and stemness (Fig. 1D, E, G). In addition, these analyses allowed us to propose the cytokines midkine (MDK) and, to a lesser extent, pleiotrophin (PTN), as the main putative ligands triggering ALK activation in stem-like cells. Indeed, the identification of the actual ALK ligand is a matter of great controversy: while some studies point to MDK and PTN [27,49], others suggest the cytokines FAM150A and B (family with sequence similarity 150 members A and B) [34,50] as main activators of the ALK pathway. While the results obtained for *FAM150A* and *FAM150B* were inconsistent, both *MDK* and *PTN* were overexpressed in PDAC patient samples, although only *MDK* correlated with the expression of pluripotency genes in both bulk and scRNAseq data and with the *ALK* OE signature mentioned above (Fig. 2A and S2B).

MDK and PTN are heparin-binding growth factors with multiple regulatory functions in biological processes such as proliferation, differentiation and development through binding to different receptors, including ALK [51,52]. Interestingly, functional assays with recombinant MDK and PTN demonstrated that ligand-dependent ALK activation increased self-renewal, clonogenicity and CSC frequency in our PDX models (Fig. 2F-I and S2C-E), indicating that the axis MDK/PTN-ALK enhances stemness in PDAC. Although we cannot discard side effects of MDK/PTN on proliferation, the observed increase in the number of spheres and colonies, as well as the estimated CSC frequency indicates that the impact of ALK ligands in our models is on self-renewal capacity. Indeed, ALK activation *via* MDK or PTN has been shown to regulate self-renewal and tumorigenicity in glioblastoma [45,46], while PTN knockdown favored chemosensitivity and inhibited clonogenic capacity in osteosarcoma [53].

Our results point to different modes of ALK ligand-dependent activation in PaCSC-like cells. On the one hand, *PTN* was barely expressed in tumor cells according to our analysis of the scRNAseq PDAC dataset (Fig. 2B) and was undetectable in PDXs (data not shown). In contrast, *PTN* was expressed by stromal cells, such as fibroblasts and stellate cells (Fig. 2B), revealing a potential paracrine regulatory loop in which cells from the tumor microenvironment may sustain PaCSCs through ALK activation *via* PTN. On the other hand, analysis of the scRNAseq dataset indicated that *MDK* was expressed by a wide range of cells present in the pancreatic niche, including tumor cells (Fig. 2B, D, E). We confirmed high levels of human MDK secretion in supernatants of both subcutaneous and orthotopic tumor pieces, plasmas from orthotopic tumor-bearing mice (Fig. 2C) and primary tumor cells in culture regardless of their pluripotency status (Fig. 2E). Strikingly, a recent study revealed that melanoma cells secrete MDK to promote an immune-suppressive microenvironment involving tumor associated macrophages and cytotoxic T cells [54], suggesting that MDK secretion by PaCSCs could also play a role in immunoediting in PDAC.

Importantly, we have demonstrated the crucial role of ALK for PDAC stemness not only by exogenous activation of the receptor, but also through pharmacological inhibition strategies using clinically-approved compounds. Crizotinib is a trivalent ALK, c-Met and ROS1 inhibitor approved by the Food and Drug Administration (FDA) to treat cancers expressing oncogenic ALK fusion proteins [55,56] and, later on, those depending on c-Met and/or ROS1 signaling [57]. On the other hand, Ensartinib is a potent and specific next-generation ALK inhibitor currently evaluated in a phase III trial [58], included in our study to discard off-target effects induced by Crizotinib. Treatment with both Crizotinib and Ensartinib inhibited proliferation (Fig. S3A), and induced cell death *in vitro* (Fig. 3B, C and S3C, S3D), suggesting that ALK signaling contributes to cell survival. ALK inhibition was effective in our PDX models derived from both local (PDXs) and metastatic PDAC (CTCA), suggesting this therapeutic approach may be effective in advanced and metastatic patients. Notably, ALK inhibition drastically decreased the CSC content (Fig. 3D, E) and stemness features *in vitro* and *in vivo* (Fig. 4 and S4), demonstrating that ALK is functionally necessary for PaCSC-like cells maintenance.

Chemotherapy failure remains a major issue in PDAC management

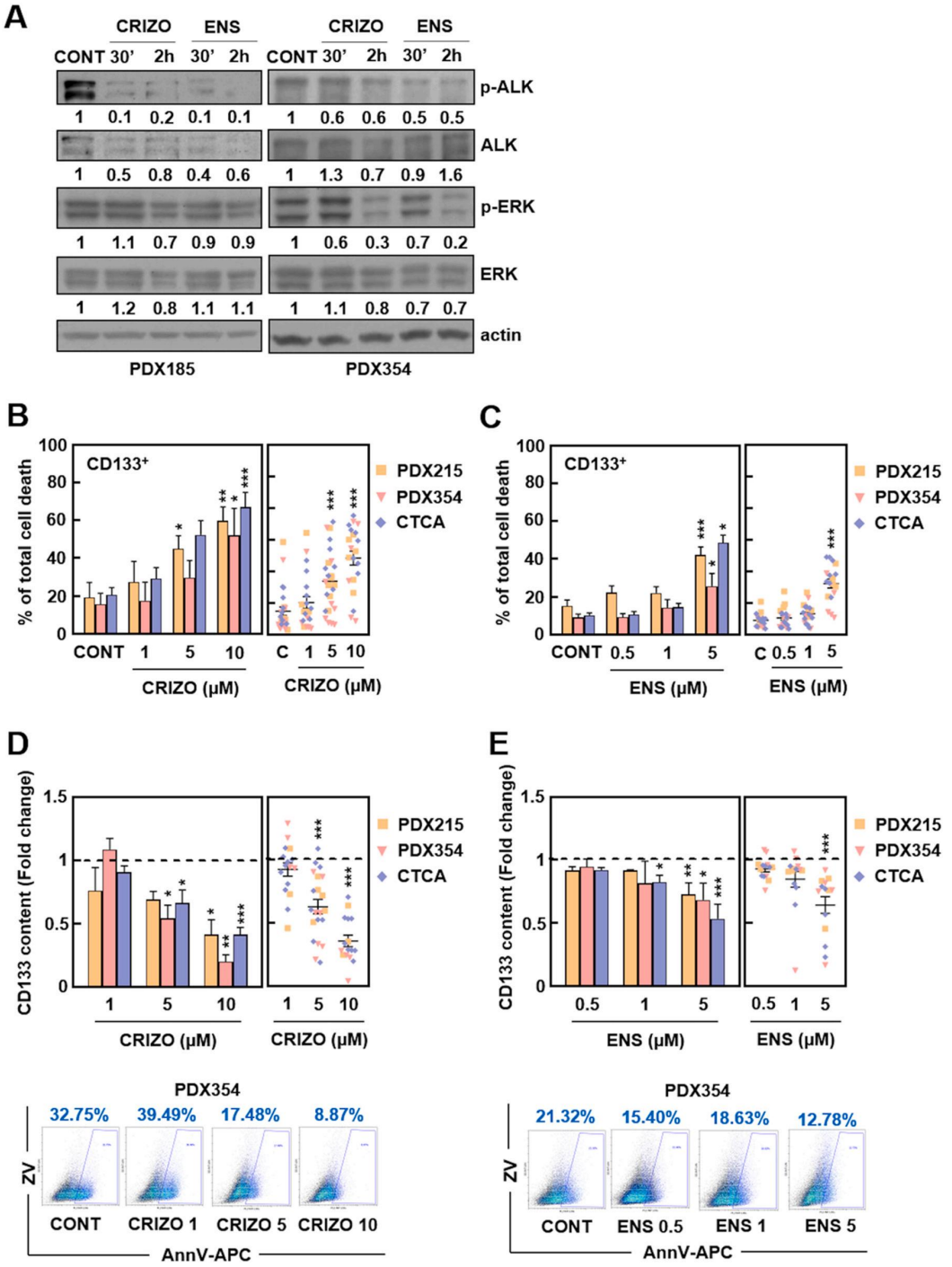

Fig. 3. ALK pharmacologic inhibition targets CD133^{+} cells. A) Kinetics of ALK inhibition after the indicated times of treatment with 10 μM Crizotinib and 5 μM Ensartinib. The numbers represent the quantification of the band intensity of each protein normalized by actin, shown as the fold change from control group. B, C) Percentage of total cell death measured as the sum of Annexin V^{+}, Zombie Violet^{+} and double positive staining in CD133^{+} cells after 48 h of treatment with Crizotinib (B) and Ensartinib (C). Left panels: mean value of each PDX separately; right panels: pooled data showing the individual values of each PDX. D, E) CD133 content in samples from B (D) and C (E). Top panels: mean of the CD133^{+} content of each PDX separately (left) and pooled data showing the individual values of each PDX (right); bottom panels: representative flow cytometry density plots of PDX354. Data are shown as the fold change from control group, which is represented with the dashed line. Data are represented as mean ± SEM and analyzed using one-way ANOVA or Kruskal-Wallis test of, at least, three independent experiments. * $p < 0.05$, * * $p < 0.01$, * ** $p < 0.005$.

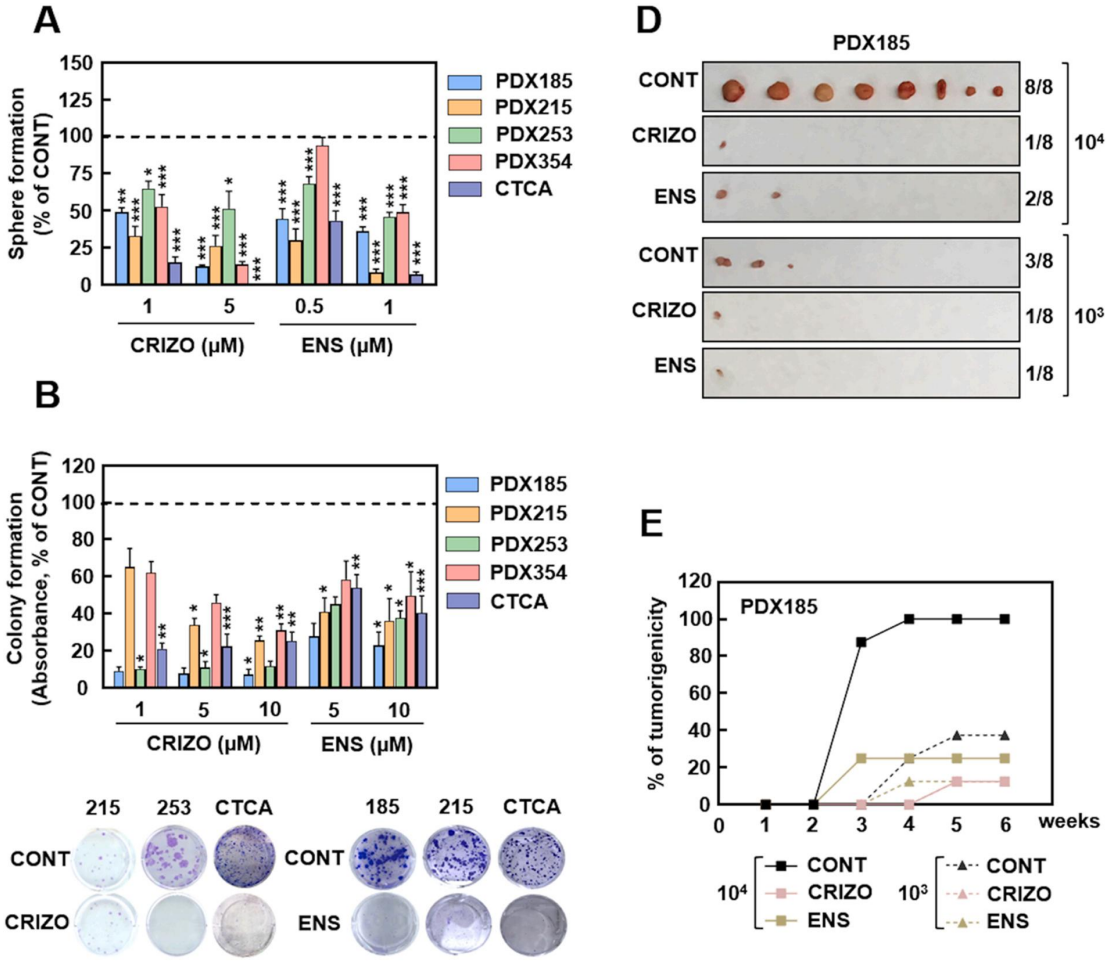

C

	PDX185		CTCA	
	CSC 1/x	*p*-value	CSC 1/x	*p*-value
CONT	28.6		8.39	
CRIZO 1	206.7	$1.69e^{-9}$	6.33	0.474
CRIZO 5	103.2	$1.69e^{-6}$	18.82	0.0455
CRIZO 10	85.6	0.00044	35.34	0.0004
ENS 0.5	75.1	0.0032	18.26	0.0491
ENS 1	315.3	$2.99e^{-13}$	16.55	0.084
ENS 5	183.2	$1.48e^{-8}$	130.51	$3.05e^{-12}$

F

	CSC 1/x		*p*-value
PDX185	CONT	1961	
	CRIZO	41148	$1.75e^{-5}$
	ENS	25616	0.0001

Fig. 4. ALK pharmacologic targeting abrogates CSC features *in vitro* and *in vivo*. A) Sphere formation assay after seven days of treatment with Crizotinib and Ensartinib. B) Colony formation assay after 21 days of treatment with Crizotinib and Ensartinib. Top panel: absorbance of crystal violet; bottom panel: images of a representative experiment of each PDX treated with either 1 μM Crizotinib or Ensartinib. C) CSC frequency after treatment with Crizotinib or Ensartinib for seven days estimated by *in vitro* ELDA. D-F) *In vivo* ELDA of cells pre-treated *in vitro* with 10 μM Crizotinib or 5 μM Ensartinib for 48 h and subcutaneously injected into the flanks of nude mice at decreasing cell densities. D) Pictures of tumors at end point (week six). E) Percentage of tumorigenicity over time. Note that the curves representing the Crizotinib conditions 10^3 and 10^4 cells overlap. F) Estimated CSC frequency. Data are represented as mean ± SEM and analyzed using one-way ANOVA or Kruskal-Wallis tests of, at least, three independent experiments. * $p < 0.05$, * * $p < 0.01$, * ** $p < 0.005$.

A

		Gemcitabine absolute IC_{50} (nM)	
		PDX185	PDX215
Proliferation	Gem	38.3	246.8
	+CRIZO	12.4	226.6
	+ENS	3.3	38.1
Viability	Gem	31.3	26.9
	+CRIZO	9.7	8.9
	+ENS	10.7	6.0

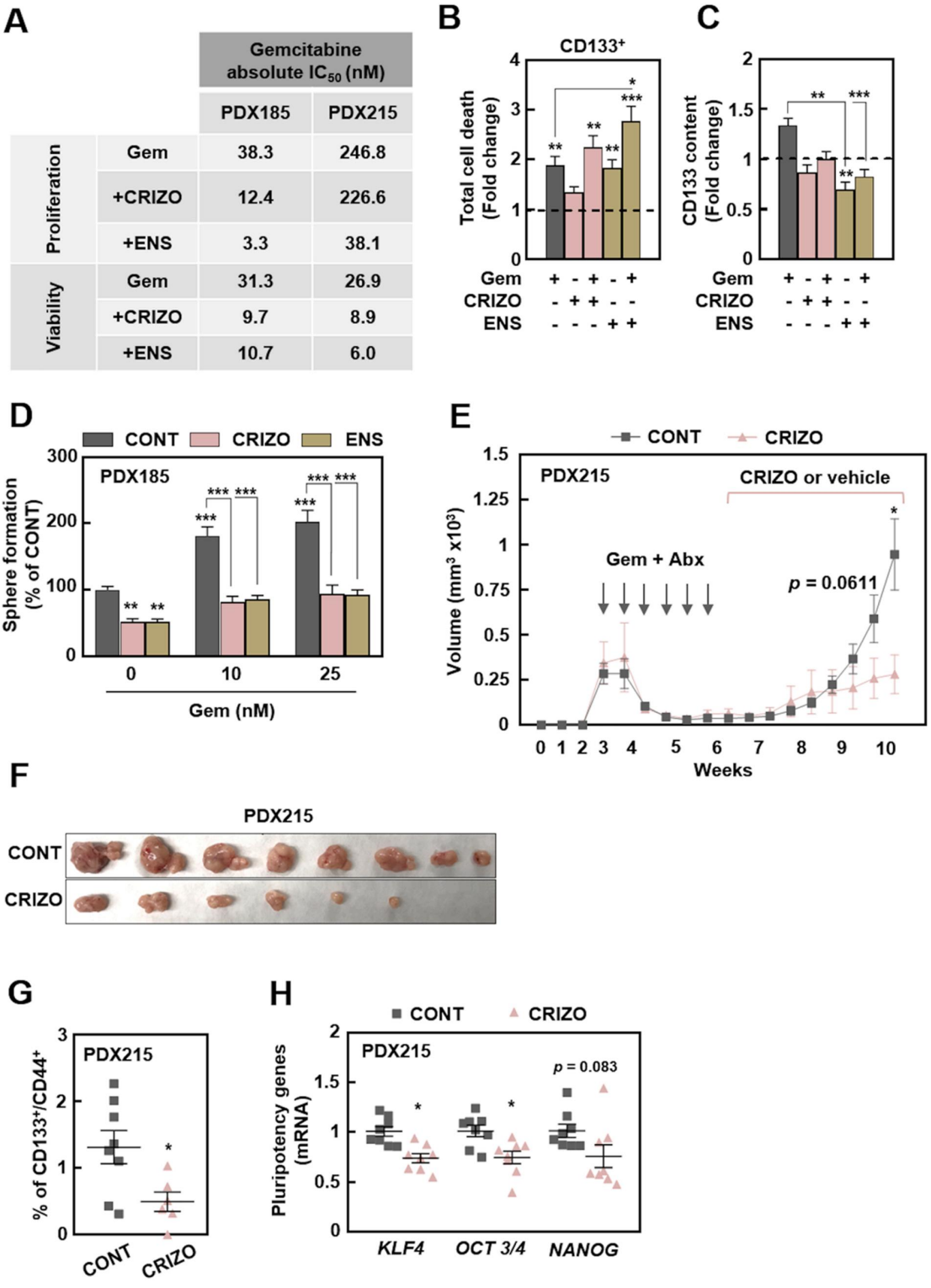

(caption on next page)

Fig. 5. ALK inhibition synergizes with Gemcitabine treatment *in vitro* and *in vivo*. The combined effect of Gemcitabine and ALK inhibitors was studied using low doses of the compounds (Gem 50 nM unless otherwise specified, Crizotinib 1 μM, Ensartinib 1 μM). A) IC_{50} of Gemcitabine at 72 h of treatment alone and in combination with Crizotinib or Ensartinib. B) Total cell death measured as the sum of Annexin V^+, Zombie $Violet^+$ and double positive staining in $CD133^+$ cells after 48 h of treatment as indicated. Pooled data from PDX185, 253 and 354. C) CD133 content of the samples shown in B. Data are shown as the fold change from control group, which is represented with the dashed line (B and C). D) Sphere formation assay after 48 h of Gemcitabine pre-treatment in adherent conditions prior to seven days of treatment with Crizotinib or Ensartinib in anchorage-independent conditions as indicated. E-H) *In vivo* treatment of mice subcutaneously implanted with PDX215 tumour pieces. When tumors reached around 300 mm^3, mice were treated with 30 mg/kg of Abraxane (i.v., twice a week) in combination with 70 mg/kg of Gemcitabine (i.p., once a week) for 21 days. After seven days of rest, mice were randomized and treated with either vehicle or 25 mg/kg of Crizotinib (oral gavage, twice a day) until end point. E) Tumor volume over time. F) Pictures of tumors at end point (week 10). G) Percentage of $CD133^+/CD44^+$ cells of tumors shown in F. H) Pluripotency gene expression of tumors shown in F. Data are represented as mean ± SEM and analyzed using one-way ANOVA or Kruskal-Wallis tests of, at least, three independent experiments. * $p < 0.05$, * * $p < 0.01$, * ** $p < 0.005$.

due to its intrinsic chemoresistance. In addition, conventional treatments target the tumor bulk and enriches the CSC content, responsible for tumor relapse. Here, we demonstrate that both Crizotinib and Ensartinib decreased the IC_{50} of Gemcitabine more than half (Fig. 5A and S5A) with stronger effects by Ensartinib treatment. Importantly, both ALK inhibitors in combination with Gemcitabine decreased $CD133^+$ content (Fig. 5B, C) and abrogated Gemcitabine-induced self-renewal (Fig. 5D) and clonogenicity (Fig. S5C). Importantly, Crizotinib treatment significantly delayed tumor relapse *in vivo* (Fig. 5E) and some tumors even disappeared after treatment (Fig. 5F). Moreover, tumors treated with Crizotinib showed reduced stemness markers (Fig. 5G, H), indicating a successful targeting *in vivo*. Since development of resistance to Crizotinib has been reported already [59], further *in vivo* experiments would be needed in order to test Ensartinib, a compound still in the process of approval by the FDA. Besides its improved specificity, this inhibitor was more potent than Crizotinib either alone or in combination with Gemcitabine *in vitro*. Considering our results, we would expect a reduction of the required dosage *in vivo* to obtain a positive response, further translated into minimal side effects when applied as combinatory treatment.

In summary, our results demonstrate that PaCSC-like cells sustain their stemness program through MDK (and PTN)-dependent activation of the ALK signaling pathway. Importantly, this pathway can be pharmacologically targeted with small molecule inhibitors that, combined with conventional chemotherapy, show promising effects for an effective long-term treatment of PDAC.

5. Conclusions

In this study, we have linked ALK signaling pathway to PDAC aggressiveness by promoting CSC features, such as tumorigenicity and chemoresistance. On the one hand, activation of ALK pathway with MDK or PTN enhanced self-renewal, clonogenicity and estimated CSC frequency. On the other hand, pharmacological inhibition of this receptor with clinically-approved compounds targeted $CD133^+$ cells by inducing cell death, thus inhibiting self-renewal, clonogenicity, estimated CSC frequency and *in vivo* tumorigenicity. Most importantly, the use of chemotherapeutic agents in combination with ALK inhibitors delayed tumor relapse in mice. Taken together, our findings demonstrate an important role of ALK receptor in stem-like cells contributing to PDAC aggressiveness, thus showing the potential for mitigating the otherwise inevitable tumor relapse after chemotherapy and improving treatment outcome in PDAC patients.

Funding

The research was supported by the Instituto de Salud Carlos III through the Miguel Servet Program (CP16/00121 to P.S.), a PFIS predoctoral contract (FI21/00031 to P. E-R) and Fondo de Investigaciones Sanitarias (PI17/00082 and PI20/00921, to P.S.) (all co-financed by European funds (FSE: "El FSE invierte en tu futuro" and FEDER: "Una manera de hacer Europa", respectively), the Worldwide Cancer Research (WCR) Charity together with Asociación Española contra el Cáncer (AECC) (19-0250, to P.S.). BP-A was supported by crowdfunding through Precipita-Fecyt and a predoctoral contract from Apadrina la Ciencia-Ford Motor Company. ACG received support from Charles H. Revson Senior Fellowship in Biomedical Science (Grant No. 22-22). IV was supported by the Government of Aragon (LMP29_21).

Ethics approval

Mice were housed according to institutional guidelines and all experimental procedures were performed in compliance with the institutional guidelines for the welfare of experimental animals as approved by the Universidad of Zaragoza Ethics Committee (CEICA PI22/17) and in accordance with the guidelines for Ethical Conduct in the Care and Use of Animals as stated in The International Guiding Principles for Biomedical Research involving Animals, developed by the Council for International Organizations of Medical Sciences (CIOMS).

CRediT authorship contribution statement

B. Parejo-Alonso: conceptualization, investigation, formal analysis, visualization, writing-original draft, writing-review and editing. **A. Royo-García**: investigation, writing-review and editing. **P. Espiau-Romera**: investigation, writing-review and editing. **S. Courtois**: investigation, writing-review and editing. **A. Curiel-García**: formal analysis, visualization, writing-review and editing. **S. Zagorac**: investigation, writing-review and editing. **I. Villaoslada**: investigation, writing-review and editing. **K. P. Olive**: resources, writing-review and editing. **C. Heeschen**: resources, writing-review and editing. **P. Sancho**: conceptualization, project administration, supervision, funding acquisition, investigation, writing-original draft, writing-review and editing.

Conflict of Interest Statement

The authors declare no conflicts of interest.

Data Availability

Data will be made available on request.

Acknowledgements

Authors would like to acknowledge the use of the CIBA (Centro de Investigación Biomédica de Aragón) Flow Cytometry, Pathology and Microscopy Facilities (Servicios Científico-T é cnicos, IACS-Universidad de Zaragoza). We also thank Laura Sancho Andrés for proofreading the manuscript. We are grateful to patients with pancreatic cancer who donated samples to the Barts Pancreatic Tissue Bank (http://www.bartspancreastissuebank.org.uk) funded by the Pancreatic Cancer Research Fund.

Appendix A. Supporting information

Supplementary data associated with this article can be found in the online version at doi:10.1016/j.biopha.2022.114162.

References

[1] M. Hidalgo, Pancreatic cancer, N. Engl. J. Med. 362 (2010) 1605–1617, https://doi.org/10.1056/NEJMra0901557.

[2] P. Rawla, T. Sunkara, V. Gaduputi, Epidemiology of pancreatic cancer: global trends, etiology and risk factors, World J. Oncol. 10 (2019) 10–27, https://doi.org/10.14740/wjon1166.

[3] F. Bray, J. Ferlay, I. Soerjomataram, R.L. Siegel, L.A. Torre, A. Jemal, Global cancer statistics 2018: GLOBOCAN estimates of incidence and mortality worldwide for 36 cancers in 185 countries, Ca. Cancer J. Clin. 68 (2018) 394–424, https://doi.org/10.3322/caac.21492.

[4] P.C. Hermann, S.L. Huber, T. Herrler, A. Aicher, J.W. Ellwart, M. Guba, C.J. Bruns, C. Heeschen, Distinct populations of cancer stem cells determine tumor growth and metastatic activity in human pancreatic cancer, Cell Stem Cell 1 (2007) 313–323, https://doi.org/10.1016/j.stem.2007.06.002.

[5] C. Li, D.G. Heidt, P. Dalerba, C.F. Burant, L. Zhang, V. Adsay, M. Wicha, M. F. Clarke, D.M. Simeone, Identification of pancreatic cancer stem cells, Cancer Res 67 (2007) 1030–1037, https://doi.org/10.1158/0008-5472.CAN-06-2030.

[6] P. Sancho, S. Alcala, V. Usachov, P.C. Hermann, B. Sainz, The ever-changing landscape of pancreatic cancer stem cells, Pancreatology 16 (2016) 489–496, https://doi.org/10.1016/j.pan.2016.04.004.

[7] R. Sever, J.S. Brugge, Signal transduction in cancer, Cold Spring Harb. Perspect. Med. 5 (2015), https://doi.org/10.1101/cshperspect.a006098.

[8] Z. Du, C.M. Lovly, Mechanisms of receptor tyrosine kinase activation in cancer, Mol. Cancer 17 (2018) 58, https://doi.org/10.1186/s12943-018-0782-4.

[9] E.S. Katayama, J.J. Hue, D.L. Bajor, L.M. Ocuin, J.B. Ammori, J.M. Hardacre, J. M. Winter, A comprehensive analysis of clinical trials in pancreatic cancer: what is coming down the pike, Oncotarget 11 (2020) 3489–3501, https://doi.org/10.18632/oncotarget.27727.

[10] Z. Zheng, N. Shao, H. Weng, W. Li, J. Zhang, L. Zhang, L. Yang, S. Ye, Correlation between epidermal growth factor receptor and tumor stem cell markers CD44/CD24 and their relationship with prognosis in breast invasive ductal carcinoma, Med. Oncol. North. Lond. Engl. 32 (2015) 275, https://doi.org/10.1007/s12032-014-0275-2.

[11] X. Wang, M.E. Reyes, D. Zhang, Y. Funakoshi, A.P. Trape, Y. Gong, T. Kogawa, B. L. Eckhardt, H. Masuda, D.A. Pirman, P. Yang, J.M. Reuben, W.A. Woodward, C. Bartholomeusz, G.N. Hortobagyi, D. Tripathy, N.T. Ueno, EGFR signaling promotes inflammation and cancer stem-like activity in inflammatory breast cancer, Oncotarget 8 (2017) 67904–67917, https://doi.org/10.18632/oncotarget.18958.

[12] J. Ko, A.N. Meyer, M. Haas, D.J. Donoghue, Characterization of FGFR signaling in prostate cancer stem cells and inhibition via TKI treatment, Oncotarget 12 (2021) 22–36, https://doi.org/10.18632/oncotarget.27859.

[13] E. Binda, A. Visioli, F. Giani, G. Lamorte, M. Copetti, K.L. Pitter, J.T. Huse, L. Cajola, N. Zanetti, F. DiMeco, L. De Filippis, A. Mangiola, G. Maira, C. Anile, P. De Bonis, B.A. Reynolds, E.B. Pasquale, A.L. Vescovi, The EphA2 receptor drives self-renewal and tumorigenicity in stem-like tumor-propagating cells from human glioblastomas, Cancer Cell 22 (2012) 765–780, https://doi.org/10.1016/j.ccr.2012.11.005.

[14] B.W. Day, B.W. Stringer, F. Al-Ejeh, M.J. Ting, J. Wilson, K.S. Ensbey, P. R. Jamieson, Z.C. Bruce, Y.C. Lim, C. Offenhäuser, S. Charmsaz, L.T. Cooper, J. K. Ellacott, A. Harding, L. Leveque, P. Inglis, S. Allan, D.G. Walker, M. Lackmann, G. Osborne, K.K. Khanna, B.A. Reynolds, J.D. Lickliter, A.W. Boyd, EphA3 maintains tumorigenicity and is a therapeutic target in glioblastoma multiforme, Cancer Cell 23 (2013) 238–248, https://doi.org/10.1016/j.ccr.2013.01.007.

[15] M.L. Taddei, E. Giannoni, A. Morandi, L. Ippolito, M. Ramazzotti, M. Callari, P. Gandellini, P. Chiarugi, Mesenchymal to amoeboid transition is associated with stem-like features of melanoma cells, Cell Commun. Signal. Ccs. 12 (2014) 24, https://doi.org/10.1186/1478-811X-12-24.

[16] W. Song, Y. Ma, J. Wang, D. Brantley-Sieders, J. Chen, JNK signaling mediates EPHA2-dependent tumor cell proliferation, motility, and cancer stem cell-like properties in non-small cell lung cancer, Cancer Res. 74 (2014) 2444–2454, https://doi.org/10.1158/0008-5472.CAN-13-2136.

[17] S. Alcalá, V. Mayoral-Varo, L. Ruiz-Cañas, J.C. López-Gil, C. Heeschen, J. Martín-Pérez, B. Sainz, Targeting SRC kinase signaling in pancreatic cancer stem cells, Int. J. Mol. Sci. 21 (2020) 7437, https://doi.org/10.3390/ijms21207437.

[18] M. Mueller, P.C. Hermann, J. Witthauer, B. Rubio–Viqueira, S.F. Leicht, S. Huber, J.W. Ellwart, M. Mustafa, P. Bartenstein, J.G. D'Haese, M.H. Schoenberg, F. Berger, K. Jauch, M. Hidalgo, C. Heeschen, Combined targeted treatment to eliminate tumorigenic cancer stem cells in human pancreatic cancer, Gastroenterology 137 (2009) 1102–1113, https://doi.org/10.1053/j.gastro.2009.05.053.

[19] I. Miranda-Lorenzo, J. Dorado, E. Lonardo, S. Alcala, A.G. Serrano, J. Clausell-Tormos, M. Cioffi, D. Megias, S. Zagorac, A. Balic, M. Hidalgo, M. Erkan, J. Kleeff, A. Scarpa, B. Sainz, C. Heeschen, Intracellular autofluorescence: a biomarker for epithelial cancer stem cells, Nat. Methods 11 (2014) 1161–1169, https://doi.org/10.1038/nmeth.3112.

[20] Z. Tang, B. Kang, C. Li, T. Chen, Z. Zhang, GEPIA2: an enhanced web server for large-scale expression profiling and interactive analysis, (n.d.) 5.

[21] J. Peng, B.-F. Sun, C.-Y. Chen, J.-Y. Zhou, Y.-S. Chen, H. Chen, L. Liu, D. Huang, J. Jiang, G.-S. Cui, Y. Yang, W. Wang, D. Guo, M. Dai, J. Guo, T. Zhang, Q. Liao, Y. Liu, Y.-L. Zhao, D.-L. Han, Y. Zhao, Y.-G. Yang, W. Wu, Single-cell RNA-seq highlights intra-tumoral heterogeneity and malignant progression in pancreatic ductal adenocarcinoma, Cell Res. 29 (2019) 725–738, https://doi.org/10.1038/s41422-019-0195-y.

[22] J. Ai, S.M. Wörmann, K. Görgülü, M. Vallespinos, S. Zagorac, S. Alcala, N. Wu, D. Kabacaoglu, A. Berninger, D. Navarro, E. Kaya-Aksoy, D.A. Ruess, K. J. Ciecielski, M. Kowalska, I.E. Demir, G.O. Ceyhan, I. Heid, R. Braren, M. Riemann, S. Schreiner, S. Hofmann, M. Kutschke, M. Jastroch, J. Slotta-Huspenina, A. Muckenhuber, A.M. Schlitter, R.M. Schmid, K. Steiger, K. N. Diakopoulos, M. Lesina, B. Sainz, H. Algül, Bcl3 couples cancer stem cell enrichment with pancreatic cancer molecular subtypes, Gastroenterology 161 (318–332) (2021), e9, https://doi.org/10.1053/j.gastro.2021.03.051.

[23] M. Mazzeschi, M. Sgarzi, D. Romaniello, V. Gelfo, C. Cavallo, F. Ambrosi, A. Morselli, C. Miano, N. Laprovitera, C. Girone, M. Ferracin, S. Santi, K. Rihawi, A. Ardizzoni, M. Fiorentino, G. D'Uva, B. Győrffy, R. Palmer, M. Lauriola, The autocrine loop of ALK receptor and ALKAL2 ligand is an actionable target in consensus molecular subtype 1 colon cancer, J. Exp. Clin. Cancer Res. 41 (2022) 113, https://doi.org/10.1186/s13046-022-02309-1.

[24] J. Gao, B.A. Aksoy, U. Dogrusoz, G. Dresdner, S.O. Sumer, Y. Sun, A. Jacobsen, R. Sinha, E. Larsson, E. Cerami, C. Sander, N. Schultz, Integrative Analysis of Complex Cancer Genomics and Clinical Profiles Using the cBioPortal, (2014) 34.

[25] Y. Hu, G.K. Smyth, ELDA: Extreme limiting dilution analysis for comparing depleted and enriched populations in stem cell and other assays, J. Immunol. Methods 347 (2009) 70–78, https://doi.org/10.1016/j.jim.2009.06.008.

[26] R.H. Palmer, E. Vernersson, C. Grabbe, B. Hallberg, Anaplastic lymphoma kinase: signalling in development and disease, Biochem. J. 420 (2009) 345–361, https://doi.org/10.1042/BJ20090387.

[27] A. Wellstein, ALK receptor activation, ligands and therapeutic targeting in glioblastoma and in other cancers, Front. Oncol. 2 (2012), https://doi.org/10.3389/fonc.2012.00192.

[28] A. García-Regalado, C.H. González-De la Rosa, The role of anaplastic lymphoma kinase in human cancers, Oncol. Hematol. Rev. Us. 09 (2013) 149, https://doi.org/10.17925/OHR.2013.09.2.149.

[29] H. Huang, Anaplastic lymphoma kinase (ALK) receptor tyrosine kinase: a catalytic receptor with many faces, Int. J. Mol. Sci. 19 (2018), https://doi.org/10.3390/ijms19113448.

[30] S. Ormanns, G. Assmann, S. Reu, E. Gallmeier, D.C. Bader, A. Kleespies, M. Haas, S. Kruger, V. Heinemann, T. Kirchner, S. Boeck, ALK expression is absent in pancreatic ductal adenocarcinoma, J. Cancer Res. Clin. Oncol. 140 (2014) 1625–1628, https://doi.org/10.1007/s00432-014-1774-4.

[31] A.D. Singhi, S.M. Ali, J. Lacy, A. Hendifar, K. Nguyen, J. Koo, J.H. Chung, J. Greenbowe, J.S. Ross, M.N. Nikiforova, H.J. Zeh, I.S. Sarkaria, A. Dasyam, N. Bahary, Identification of targetable *ALK* rearrangements in pancreatic ductal adenocarcinoma, J. Natl. Compr. Canc. Netw. 15 (2017) 555–562, https://doi.org/10.6004/jnccn.2017.0058.

[32] Y. Shimada, T. Kohno, H. Ueno, Y. Ino, H. Hayashi, T. Nakaoku, Y. Sakamoto, S. Kondo, C. Morizane, K. Shimada, T. Okusaka, N. Hiraoka, An oncogenic ALK fusion and an RRAS mutation in KRAS mutation-negative pancreatic ductal adenocarcinoma, Oncologist 22 (2017) 158–164, https://doi.org/10.1634/theoncologist.2016-0194.

[33] S. Courtois, B. de Luxán-Delgado, L. Penin-Peyta, A. Royo-García, B. Parejo-Alonso, P. Jagust, S. Alcalá, J.A. Rubiolo, L. Sánchez, B. Sainz, C. Heeschen, P. Sancho, Inhibition of mitochondrial dynamics preferentially targets pancreatic cancer cells with enhanced tumorigenic and invasive potential, Cancers 13 (2021) 698, https://doi.org/10.3390/cancers13040698.

[34] J. Guan, G. Umapathy, Y. Yamazaki, G. Wolfstetter, P. Mendoza, K. Pfeifer, A. Mohammed, F. Hugosson, H. Zhang, A.W. Hsu, R. Halenbeck, B. Hallberg, R. H. Palmer, FAM150A and FAM150B are activating ligands for anaplastic lymphoma kinase, ELife 4 (2015), e09811, https://doi.org/10.7554/eLife.09811.

[35] B. Hallberg, R.H. Palmer, The role of the ALK receptor in cancer biology, Ann. Oncol. 27 (2016) iii4–iii15, https://doi.org/10.1093/annonc/mdw301.

[36] A.T. Shaw, D.-W. Kim, K. Nakagawa, T. Seto, L. Crinó, M.-J. Ahn, T. De Pas, B. Besse, B.J. Solomon, F. Blackhall, Y.-L. Wu, M. Thomas, K.J. O'Byrne, D. Moro-Sibilot, D.R. Camidge, T. Mok, V. Hirsh, G.J. Riely, S. Iyer, V. Tassell, A. Polli, K. D. Wilner, P.A. Jänne, Crizotinib versus chemotherapy in advanced *ALK* -positive lung cancer, N. Engl. J. Med 368 (2013) 2385–2394, https://doi.org/10.1056/NEJMoa1214886.

[37] S. Zeng, M. Pöttler, B. Lan, R. Grützmann, C. Pilarsky, H. Yang, Chemoresistance in pancreatic cancer, Int. J. Mol. Sci. 20 (2019) 4504, https://doi.org/10.3390/ijms20184504.

[38] P.C. Hermann, P. Sancho, M. Cañamero, P. Martinelli, F. Madriles, P. Michl, T. Gress, R. de Pascual, L. Gandia, C. Guerra, M. Barbacid, M. Wagner, C.R. Vieira, A. Aicher, F.X. Real, B. Sainz, C. Heeschen, Nicotine promotes initiation and progression of KRAS-induced pancreatic cancer via Gata6-dependent dedifferentiation of acinar cells in mice, Gastroenterology 147 (1119–1133) (2014), e4, https://doi.org/10.1053/j.gastro.2014.08.002.

[39] P. Sancho, E. Burgos-Ramos, A. Tavera, T. Bou Kheir, P. Jagust, M. Schoenhals, D. Barneda, K. Sellers, R. Campos-Olivas, O. Graña, C.R. Viera, M. Yuneva, B. Sainz, C. Heeschen, MYC/PGC-1α balance determines the metabolic phenotype and plasticity of pancreatic cancer stem cells, Cell Metab. 22 (2015) 590–605, https://doi.org/10.1016/j.cmet.2015.08.015.

[40] P. Jagust, S. Alcalá, B.S. Jr, C. Heeschen, P. Sancho, Glutathione metabolism is essential for self-renewal and chemoresistance of pancreatic cancer stem cells, World J. Stem Cells 12 (2020) 1410–1428, https://doi.org/10.4252/wjsc.v12.i11.1410.

[41] B.V.K.S. Lakkakula, B. Farran, S. Lakkakula, S. Peela, N.S. Yarla, P.V. Bramhachari, M.A. Kamal, M.S. Saddala, G.P. Nagaraju, Small molecule tyrosine kinase inhibitors and pancreatic cancer—trials and troubles, Semin. Cancer Biol. 56 (2019) 149–167, https://doi.org/10.1016/j.semcancer.2018.09.011.

[42] T. Iwahara, J. Fujimoto, D. Wen, R. Cupples, N. Bucay, T. Arakawa, S. Mori, B. Ratzkin, T. Yamamoto, Molecular characterization of ALK, a receptor tyrosine

kinase expressed specifically in the nervous system, Oncogene 14 (1997) 439–449, https://doi.org/10.1038/sj.onc.1200849.
[43] S.W. Morris, M.N. Kirstein, M.B. Valentine, K.G. Dittmer, D.N. Shapiro, D. L. Saltman, A.T. Look, Fusion of a kinase gene, *ALK*, to a nucleolar protein gene, *NPM*, in non-Hodgkin's lymphoma, Science 263 (1994) 1281–1284, https://doi.org/10.1126/science.8122112.
[44] B. Hallberg, R.H. Palmer, Mechanistic insight into ALK receptor tyrosine kinase in human cancer biology, Nat. Rev. Cancer 13 (2013) 685–700, https://doi.org/10.1038/nrc3580.
[45] R. Koyama-Nasu, R. Haruta, Y. Nasu-Nishimura, K. Taniue, Y. Katou, K. Shirahige, T. Todo, Y. Ino, A. Mukasa, N. Saito, M. Matsui, R. Takahashi, A. Hoshino-Okubo, H. Sugano, E. Manabe, K. Funato, T. Akiyama, The pleiotrophin-ALK axis is required for tumorigenicity of glioblastoma stem cells, Oncogene 33 (2014) 2236–2244, https://doi.org/10.1038/onc.2013.168.
[46] I. López-Valero, D. Dávila, J. González-Martínez, N. Salvador-Tormo, M. Lorente, C. Saiz-Ladera, S. Torres, E. Gabicagogeascoa, S. Hernández-Tiedra, E. García-Taboada, M. Mendiburu-Eliçabe, F. Rodríguez-Fornés, R. Sánchez-Domínguez, J. C. Segovia, P. Sánchez-Gómez, A. Matheu, J.M. Sepúlveda, G. Velasco, Midkine signaling maintains the self-renewal and tumorigenic capacity of glioma initiating cells, Theranostics 10 (2020) 5120–5136, https://doi.org/10.7150/thno.41450.
[47] B.-S. Xu, H.-Y. Chen, Y. Que, W. Xiao, M.-S. Zeng, X. Zhang, A.L.K. ATI, interacts with c-Myc and promotes cancer stem cell-like properties in sarcoma, Oncogene 39 (2020) 151–163, https://doi.org/10.1038/s41388-019-0973-5.
[48] T. Matsumoto, Y. Oda, Y. Hasegawa, M. Hashimura, Y. Oguri, H. Inoue, A. Yokoi, M. Tochimoto, M. Nakagawa, Z. Jiang, M. Saegusa, Anaplastic lymphoma kinase overexpression is associated with aggressive phenotypic characteristics of ovarian high-grade serous carcinoma, Am. J. Pathol. 191 (2021) 1837–1850, https://doi.org/10.1016/j.ajpath.2021.06.009.
[49] G.E. Stoica, A. Kuo, C. Powers, E.T. Bowden, E.B. Sale, A.T. Riegel, A. Wellstein, Midkine binds to anaplastic lymphoma kinase (ALK) and acts as a growth factor for different cell types, J. Biol. Chem. 277 (2002) 35990–35998, https://doi.org/10.1074/jbc.M205749200.
[50] C. Moog-Lutz, J. Degoutin, J.Y. Gouzi, Y. Frobert, N.B. Carvalho, J. Bureau, C. Créminon, M. Vigny, Activation and Inhibition of anaplastic lymphoma kinase receptor tyrosine kinase by monoclonal antibodies and absence of agonist activity of pleiotrophin, J. Biol. Chem. 280 (2005) 26039–26048, https://doi.org/10.1074/jbc.M501972200.
[51] T. Muramatsu, Midkine, a heparin-binding cytokine with multiple roles in development, repair and diseases, Proc. Jpn. Acad. Ser. B Phys. Biol. Sci. 86 (2010) 410–425, https://doi.org/10.2183/pjab.86.410.
[52] X. Wang, Pleiotrophin: activity and mechanism, in: Adv. Clin. Chem., Elsevier, 2020, pp. 51–89, https://doi.org/10.1016/bs.acc.2020.02.003.
[53] D. Wu, L. Liu, X. Yan, C. Wang, Y. Wang, K. Han, S. Lin, Z. Gan, D. Min, Pleiotrophin promotes chemoresistance to doxorubicin in osteosarcoma by upregulating P-glycoprotein, Oncotarget 8 (2017) 63857–63870, https://doi.org/10.18632/oncotarget.19148.
[54] D. Cerezo-Wallis, M. Contreras-Alcalde, K. Troulé, X. Catena, C. Mucientes, T. G. Calvo, E. Cañón, C. Tejedo, P.C. Pennacchi, S. Hogan, P. Kölblinger, H. Tejero, A.X. Chen, N. Ibarz, O. Graña-Castro, L. Martinez, J. Muñoz, P. Ortiz-Romero, J. L. Rodriguez-Peralto, G. Gómez-López, F. Al-Shahrour, R. Rabadán, M.P. Levesque, D. Olmeda, M.S. Soengas, Midkine rewires the melanoma microenvironment toward a tolerogenic and immune-resistant state, Nat. Med. 26 (2020) 1865–1877, https://doi.org/10.1038/s41591-020-1073-3.
[55] E.L. Kwak, Y.-J. Bang, D.R. Camidge, A.T. Shaw, B. Solomon, R.G. Maki, S.-H.I. Ou, B.J. Dezube, P.A. Jänne, D.B. Costa, M. Varella-Garcia, W.-H. Kim, T.J. Lynch, P. Fidias, H. Stubbs, J.A. Engelman, L.V. Sequist, W. Tan, L. Gandhi, M. Mino-Kenudson, G.C. Wei, S.M. Shreeve, M.J. Ratain, J. Settleman, J.G. Christensen, D. A. Haber, K. Wilner, R. Salgia, G.I. Shapiro, J.W. Clark, A.J. Iafrate, Anaplastic lymphoma kinase inhibition in non–small-cell lung cancer, N. Engl. J. Med. 363 (2010) 1693–1703, https://doi.org/10.1056/NEJMoa1006448.
[56] D.E. Gerber, J.D. Minna, ALK inhibition for non-small cell lung cancer: from discovery to therapy in record time, Cancer Cell 18 (2010) 548–551, https://doi.org/10.1016/j.ccr.2010.11.033.
[57] A. Puccini, N.I. Marín-Ramos, F. Bergamo, M. Schirripa, S. Lonardi, H.-J. Lenz, F. Loupakis, F. Battaglin, Safety and tolerability of c-MET inhibitors in cancer, Drug Saf. 42 (2019) 211–233, https://doi.org/10.1007/s40264-018-0780-x.
[58] L. Horn, Z. Wang, G. Wu, E. Poddubskaya, T. Mok, M. Reck, H. Wakelee, A. A. Chiappori, D.H. Lee, V. Breder, S. Orlov, I. Cicin, Y. Cheng, Y. Liu, Y. Fan, J. G. Whisenant, Y. Zhou, V. Oertel, K. Harrow, C. Liang, L. Mao, G. Selvaggi, Y.-L. Wu, Ensartinib vs crizotinib for patients with anaplastic lymphoma kinase–positive non–small cell lung cancer, JAMA Oncol. 7 (2021) 1–9, https://doi.org/10.1001/jamaoncol.2021.3523.
[59] I. Dagogo-Jack, A.T. Shaw, Crizotinib resistance: implications for therapeutic strategies, Ann. Oncol. 27 (2016) iii42–iii50, https://doi.org/10.1093/annonc/mdw305.

Figure S1: ALK is preferentially activated and overexpressed in PaCSCs. A) Mean of the quantification of the dots corresponding to p-ALK from Fig. 1A. DOP: density of pixels, Diff: differentiated, CSCs: cancer stem cells. **B)** Western blot of cell lysates comparing PDXs and cell lines. Numbers represent the quantification of the band intensity for each protein normalized by actin. Bx: BxPC3; Mia: MiaPaCa2; Su: Su8686. **C)** RT-qPCR for *ALK* mRNA levels in different CSC settings. Pooled data from PDX185 and 215. Sph: spheroids. Fluo n=1, CD133 n=2. Data are shown as the fold change to differentiated cells, which are represented as the dashed line. Data are represented as mean ± SEM and analyzed using one-way ANOVA or Kruskal-Wallis tests of, at least, three independent experiments, unless otherwise specified. * $p<0.05$, ** $p<0.01$, *** $p<0.005$. **D)** Transcriptomic bioinformatic analyses of *ALK* comparing normal (N) and PDAC (T) human tissues from GTEx and TCGA datasets, respectively (webserver: GEPIA2). **E)** Mutational status of *ALK* from different datasets: 1. Pancreas UTSW, 2. Pancreas TCGA PanCan 2018, 3. Pancreas TCGA, 4. Pancreas ICGC and 5. Pancreas QCMG 2016. Mut: mutation, Amp: amplification, DDel: deep deletion (webserver: cBioPortal).

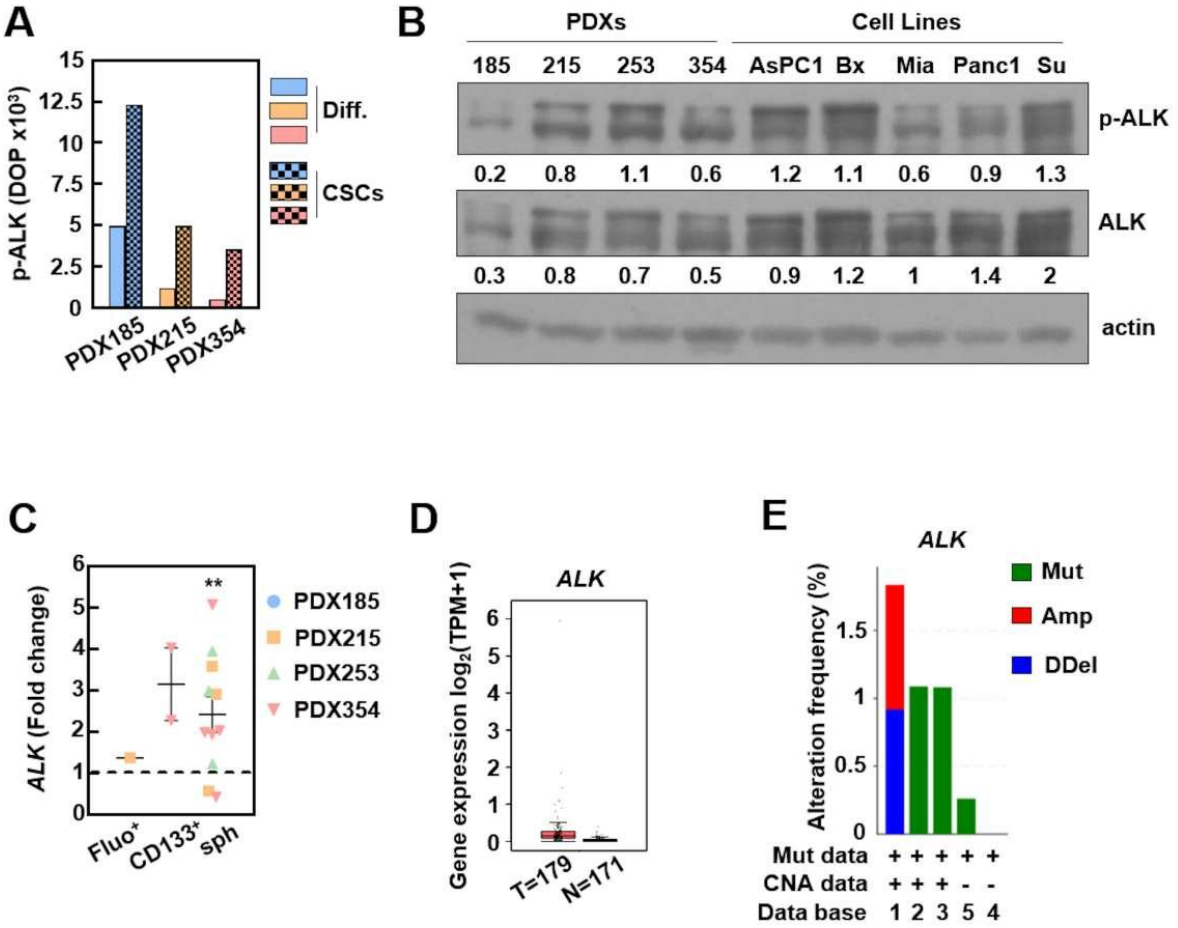

Figure S2: Ligand-dependent ALK activation supports self-renewal in PDAC. A) Expression of ALK ligands comparing normal (N) and PDAC (T) human tissues from TCGA and GTEx datasets. **B)** Correlation expression of ALK ligands with a pluripotency signature composed by *KLF4*, *OCT3/4*, *NANOG* and *SOX2* (top row or an ALK overexpression (OE) signature (bottom row) in human tissues from TCGA and GTEx datasets. The Pearson correlation coefficient (R) is calculated and interpreted as follows together with the *p*-value: the color green represents a *p*-value<0.05 and a R>0.5, the color orange represents a *p*-value<0.05 and a R<0.5, while the color red represents either a *p*-value>0.05 or a R<0 (negative correlation). TPM: transcripts per million. **C)** Kinetics of ALK activation after the indicated times of treatment with 1 ng/mL of recombinant PTN measured by Western Blot. Numbers represent the quantification of the band intensity for each protein normalized by actin, shown as the fold change to control condition. **D)** Sphere formation assay after pre-treatment with recombinant PTN for 72 hours at the indicated concentrations (ng/mL) in adherent conditions (pooled data showing the individual values for the indicated PDXs). The dashed line represents the value of the control condition. Data are represented as mean ± SEM and analyzed using one-way ANOVA or Kruskal-Wallis tests of, at least, three independent experiments. * p<0.05, ** p<0.01, *** p<0.005. **E)** Representative colony formation assay after 21 days of treatment with 10 ng/mL recombinant PTN. The numbers represent the crystal violet staining absorbance, shown as the fold change to control condition.

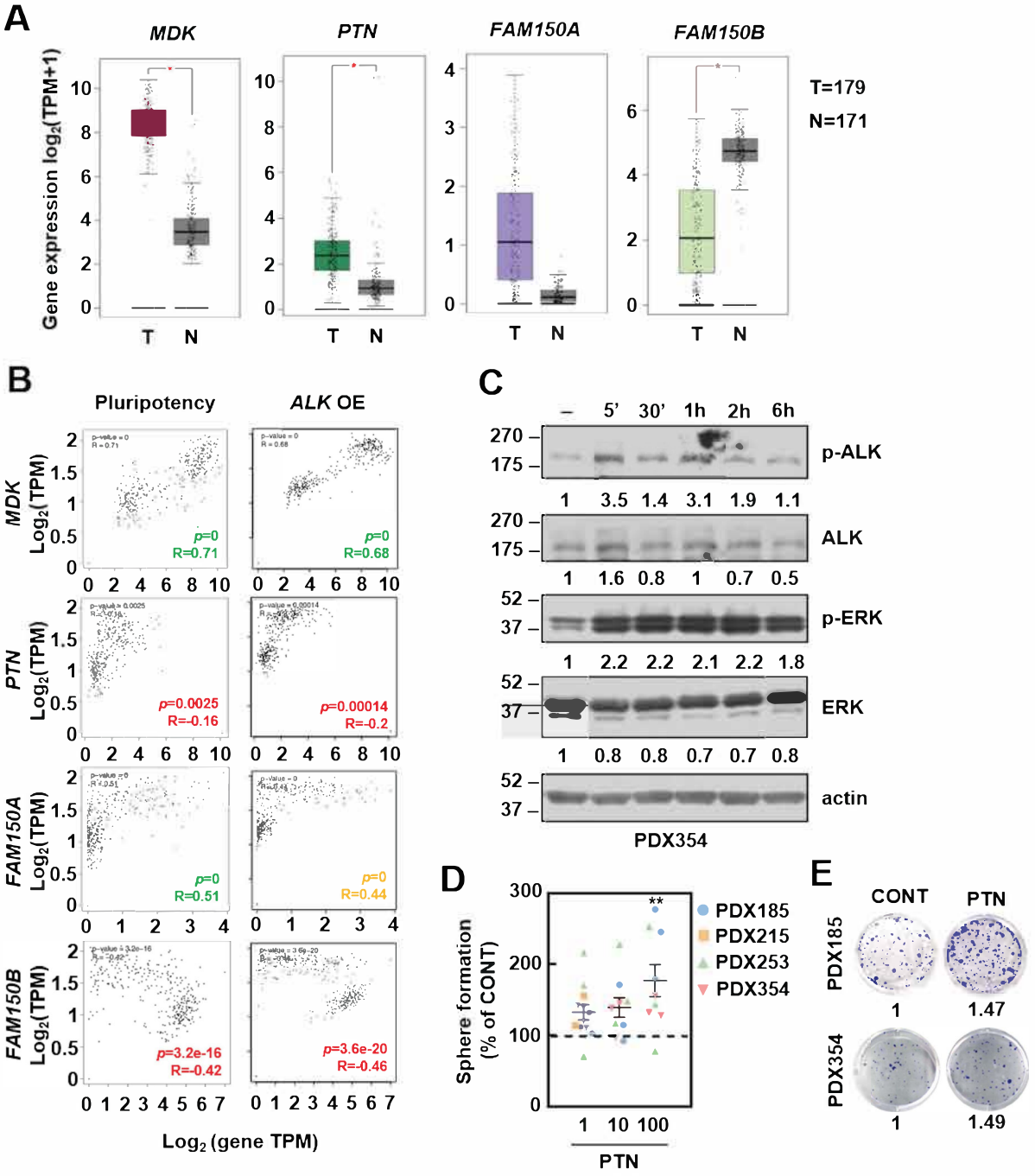

Figure S3: ALK pharmacologic inhibition targets PaCSCs. A) IC_{50} of Crizotinib and Ensartinib at 72 hours of treatment. Left panel: IC_{50} values for each cell type and inhibitor; right panel: representative proliferation rate graph of PDX185 and CTCA. **B)** Toxicity of Crizotinib for each cell type measured as relative fluorescence units normalized by crystal violet. Left panel: mean value for each cell type separately, right panel: pooled data showing the individual values for each cell type. Data are shown as the fold change to control condition which is represented as the dashed line (A and B). **C, D)** Percentage of total cell death measured as the sum of Annexin V^+, Zombie $Violet^+$ and double positive staining in the whole population after 48 hours of treatment with Crizotinib (C) or Ensartinib (D). Top panels: mean value for each PDX separately (left) and pooled data showing the individual values for each PDX (right); bottom row: representative flow cytometry density plots of PDX354. Data are represented as mean ± SEM and analyzed using one-way ANOVA or Kruskal-Wallis tests of, at least, three independent experiments. * $p<0.05$, ** $p<0.01$, *** $p<0.005$.

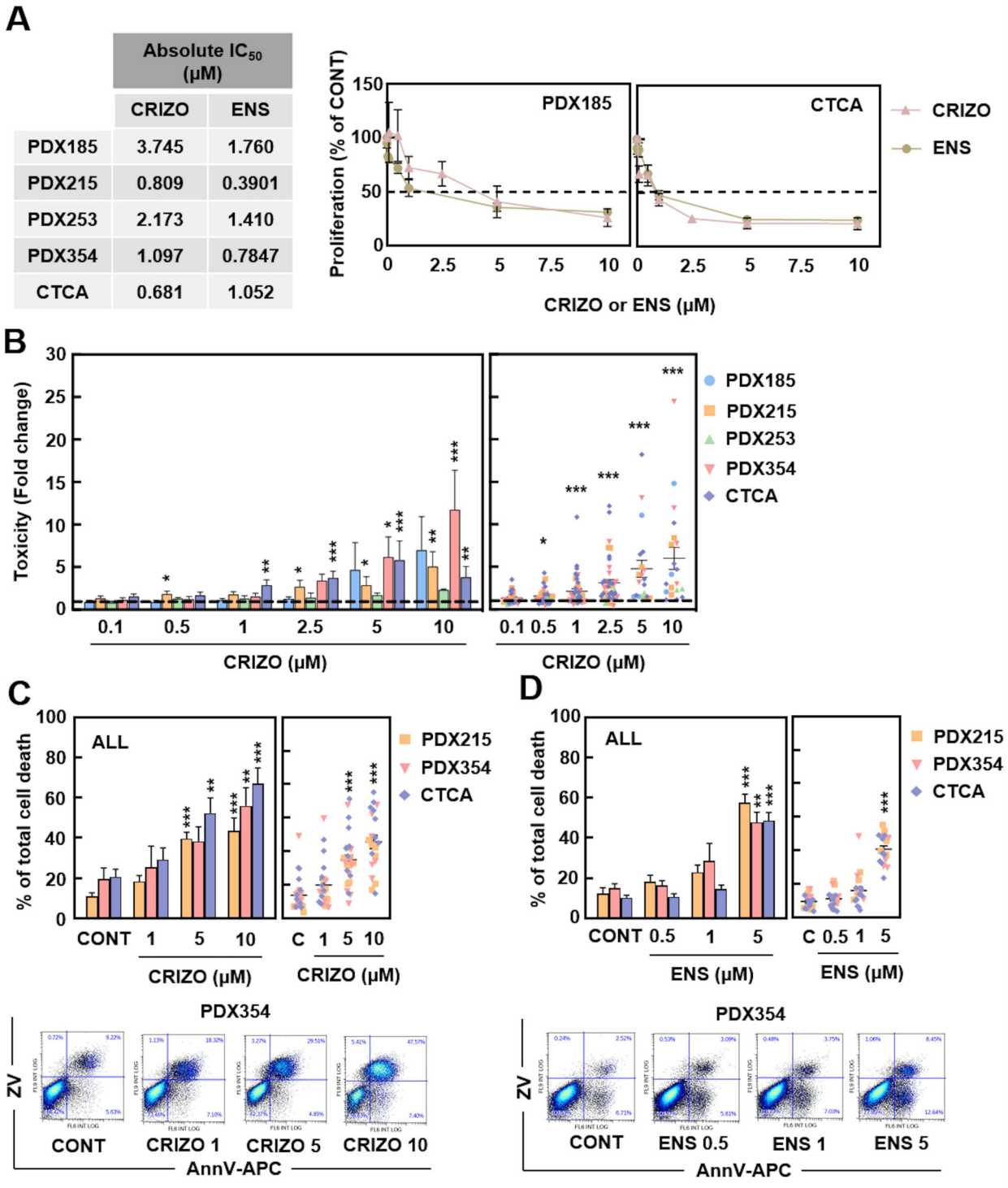

Figure S4. ALK pharmacologic targeting abrogates CSC features *in vitro* and *in vivo*. A) Sphere formation assay from Fig. 4A. Left panel: individual values for each PDX; right panel: representative images of PDX185. **B)** Sphere formation assay after pre-treatment with Crizotinib for 48 hours in adherent conditions. Left panel: percentage of spheres for each PDX; right panel: pooled data showing the individual values for each PDX. ND: not determined. **C)** Colony formation assay after 21 days of treatment with Crizotinib or Ensartinib. Pooled data showing the individual values for each PDX. Data are shown as the percentage of control condition which is represented as the dashed line. **D-F)** *In vivo* ELDA of cells pre-treated *in vitro* with 5 µM Crizotinib for 48 hours and subcutaneously injected in the flanks of nude mice at decreasing cell densities. **D)** Tumors at end point (week 6); **E)** percentage of $EpCAM^+$ cells in the 10^4 tumors showed in D; **F)** $CD133^+/CD44^+$ content in the 10^4 tumors showed in D. Data are represented as mean ± SEM and analyzed using one-way ANOVA or Kruskal-Wallis tests of, at least, three independent experiments. * $p<0.05$, ** $p<0.01$, *** $p<0.005$.

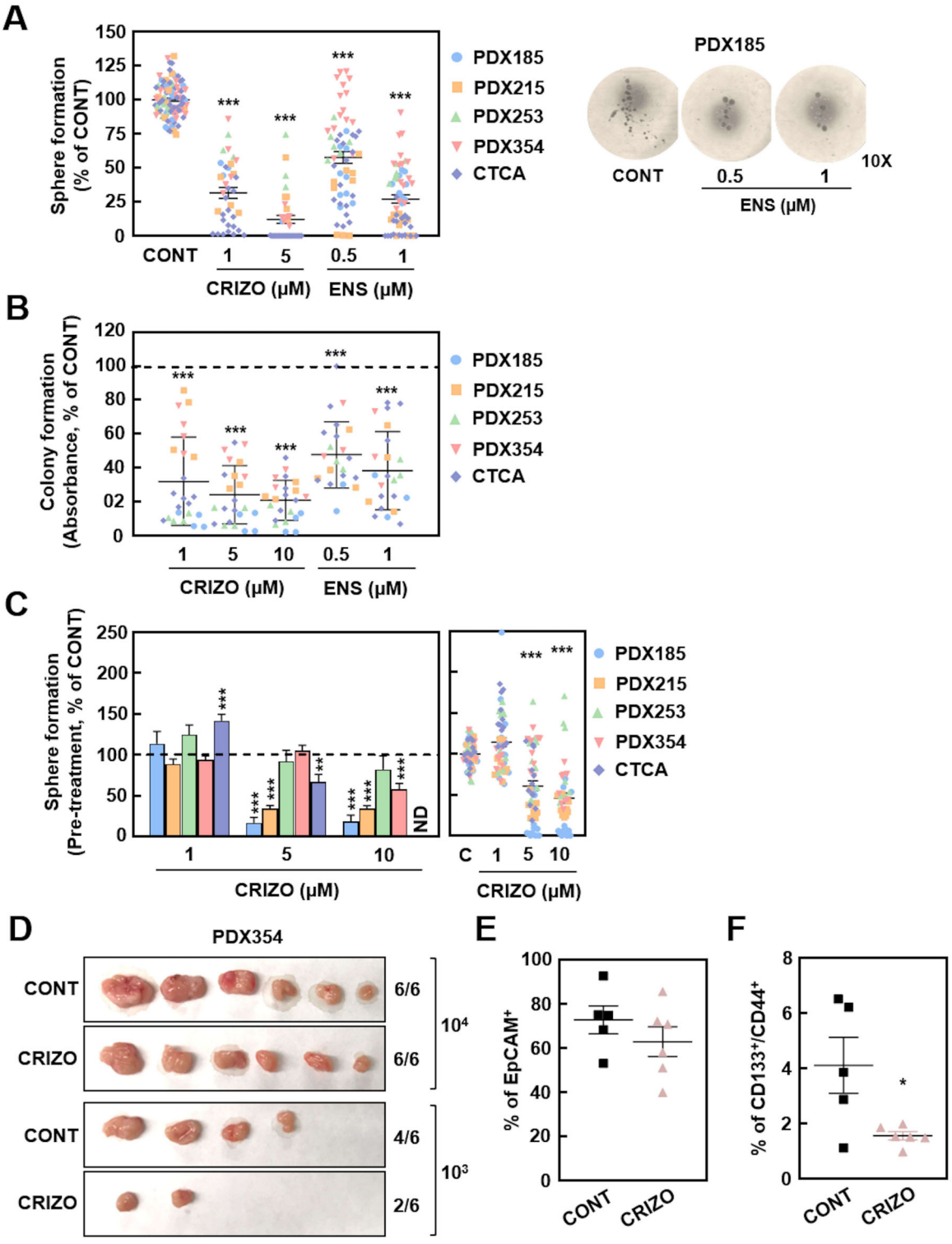

Figure S5: ALK inhibition synergizes with Gemcitabine treatment *in vitro* and *in vivo*. The combined effect of Gemcitabine and ALK inhibitors was studied using low doses of the compounds (Gem 50 nM unless otherwise specified, Crizotinib 1 µM, Ensartinib 1 µM). **A)** Representative proliferation rate graph of PDX185 and 215 from Fig. 5A. **B)** Total cell death measured as the sum of Annexin V$^+$, Zombie Violet$^+$ and double positive staining in the whole population after 48 hours of treatment with Gemcitabine alone or in combination with Crizotinib or Ensartinib. Pooled data from PDX185, 253 and 354. **C)** Colony formation assay after 21 days of treatment with Gemcitabine alone or in combination with Crizotinib or Ensartinib. **D-G)** *In vivo* treatment from Fig. 5E-H. **D)** Mice weight over time; **E)** tumor volume at end point (week 10); **F)** tumor weight at end point (10 weeks); **G)** percentage of EpCAM$^+$ cells of tumors shown in Fig. 5F. Data are represented as mean ± SEM and analyzed using one-way ANOVA or Kruskal-Wallis tests of, at least, three independent experiments. * p<0.05, ** p<0.01, *** p<0.005.